Studies of Semiconducting Ladder Polymers for Organic Electronics

Sarah Marie West

A dissertation

submitted in partial fulfillment of the

requirements for the degree of

Doctor of Philosophy

University of Washington

2024

Reading Committee:

Samson A. Jenekhe, Chair

Alshakim Nelson

Gojko Lalic

Program Authorized to Offer Degree:

Chemistry

University of Washington

Abstract

Studies of Semiconducting Ladder Polymers for Organic Electronics

Sarah Marie West

Chair of the Supervisory Committee:

Samson A. Jenekhe

Department of Chemical Engineering

Organic semiconducting polymers have garnered much interest over the last several decades due to their potential to be fabricated on a large scale for use in low-cost, flexible electronic devices. A key feature of semiconducting polymers is their synthetic tunability though molecular design that allows fine-tuning of their properties and enables the study of their structure-property relationships. The goal of the research presented in this thesis is to synthesize and study the structure-property relationships of semiconducting polymers that feature a double-stranded architecture, called π-conjugated ladder polymers. π-Conjugated ladder polymers by design have properties beneficial for organic electronics including planar and rigid backbones, low conformational disorder, large persistence lengths, and tight intermolecular contacts. However, these polymers are rarely studied due to their difficult synthesis and processing.

My first approach to studying the structure-property relationships of semiconducting ladder polymers was to synthesize functionalized and derivatized poly(benzimidazobenzophenanthroline) (BBL) polymers and then compare their properties to those of BBL. Towards this goal, I report the synthesis and properties of BBL-P, a phenazine derivative of BBL (Chapter 2), and two series of electron-deficient random copolymers, BBL-*x*CN and BBL-*x*TCN (x = 0, 0.2, 0.35, 0.5) featuring

known and novel electron-deficient, cyanated monomers (Chapter 3). Compared to BBL, I found that while phenazine substitution in BBL-P does not impact the lowest unoccupied molecular orbital (LUMO) energy level, the thin films have decreased crystallinity with preferential *face-on* molecular orientations on substrates, which contributed to a decreased field-effect electron mobility of 1.2×10^{-4} cm^2/V s.

The random copolymer series BBL-*x*2CN and BBL-*x*TCN discussed in Sections 3.1 and 3.2, respectively, demonstrate that as little as 20 mol% of the electron-deficient monomers increased the speed of the polycondensations compared to BBL. Additionally, I found that while 20-50 mol% of the cyanated monomers had little impact on the optical bandgaps, 50 mol% reduced the LUMO levels by ~ 0.2 eV and facilitated the reduction processes. The n-doped conductivity of the BBL-*x*2CN series was found to decrease with increasing 2CN content. These studies provide important insights into the synthesis and structure-property relationships of electron-deficient BBL derivatives.

My second approach focused on N-alkyl side chain engineering of p-type ladder poly(pyrrolobenzothiazine)s (Chapter 4). Here, I found that polymer with N-methyl (LPBT-Me) and N-H (LPBT) groups both have strong intramolecular charge transfer (ICT) character when protonated, and N-methylation does not effect the narrow optical bandgaps of ~1.5 eV. Moreover, temperature-dependent absorption spectroscopy and theoretical calculations revealed that both polymers show planar/non-planar conformations that vary with the degree of protonation; this conformational variation was enhanced by N-methylation, which contributed to a decreased field-effect hole mobility in LPBT-Me.

My third approach involved the synthesis and studies of a new p-type thiophene-containing ladder polymer (LTBT) that I discussed in Chapter 5. Although the solubility in strong acids is limited, the polymer demonstrated excellent film-forming properties evidenced by the high quality freestanding and thin films that I used to characterize the molecular structure using infrared and Raman spectroscopies. I found that this polymer has a narrow optical bandgap of 1.28 eV, enhanced

protonation-enhanced ICT character extending out into the infrared region, and a modest average electrical conductivity of $(3.31 \pm 0.31) \times 10^{-1}$ S/cm when p-doped with $FeCl_3$.

Table of Contents

List of Figures. iv

List of Charts. ix

Lists of Schemes. x

List of Tables. xi

Acknowledgements. X

Chapter 1. Introduction. 1

1.1 Semiconducting Polymers in Organic Electronic and Optoelectronic Devices. 1

1.2 Conjugated Polymer Chain Topology. 3

1.3 π-Conjugated Ladder Polymers. 4

1.3.1 Synthetic Routes to form π-Conjugated Ladder Polymers. 5

1.3.2. n-Type Ladder Polymers. 7

1.3.3. p-Type Ladder Polymers. 9

1.4 Challenges and Objectives. 9

1.5 References. 12

Chapter 2. Phenazine-Substituted Poly(benzimidazobenzophenanthrolinedione): Electronic Structure, Thin Film Morphology, Electron Transport, and Mechanical Properties of an n-Type Semiconducting Ladder Polymer. 23

2.1 Introduction. 23

2.2 Experimental Methods. 26

2.3 Results and Discussion. 29

2.4 Conclusions. 48

2.5 References. 49

Chapter 3. Studies of Random Copolymers of Poly(benzimidazobenzophenanthrolinedione) Featuring Electron-deficient Cyanated Comonomers for Organic Electronics 58

3.1 Cyanated and Noncyanated Conjugated Ladder Copolymers and Model Compound of Poly(benzimidazobenzophenanthroline): Synthesis, Electronic Structure, and n-Doped Electrical Conductivity. 58

3.1.1 Introduction. 58

3.1.2 Experimental Methods. 61

3.1.3 Results and Discussion. 66

3.1.4 Conclusions. 82

3.1.5 References. 82

3.2 Random Copolymers and Model Compound of Ladder Poly(benzimidazobenzophenanthroline) Featuring Dithiinotetracarbonitrile Groups: Synthesis and Electronic Structure. 90

3.2.1 Introduction. 90

3.2.2 Experimental Methods. 92

3.2.3 Results and Discussion. 96

3.2.4 Conclusions. 111

3.2.5 References. 112

Chapter 4. p-Type Semiconducting Ladder Poly(pyrrolobenzothiazine)s: Effects of N-Alkyl Side Chains on the Chain Conformation, Electronic Structure, and Charge Transport Properties. 119

4.1 Introduction. 119

4.2 Experimental Methods. 122

4.3 Results and Discussion. 125

4.4 Conclusions. 148

4.5 References. 149

Chapter 5. Ladder Poly(Thienobenzothiazine): Synthesis, Electronic Structure, Optical Properties, and p-Doped Electrical Conductivity of a Narrow Bandgap Ladder Polymer. 157

5.1 Introduction. 157

5.2 Experimental Methods. 160

5.3 Results and Discussion. 164

5.4 Conclusions. 181

5.5 References. 182

Chapter 6. Conclusions and Outlook. 190

6.1 Conclusions. 190

6.2 Outlook. 194

Appendix A 197

Appendix B 207

Appendix C 232

Appendix D. 248

Appendix E. 255

List of Figures

Figure 1.1. Chemical structures of a few well-known ladder polymers and semi-flexible polymers 4

Figure 1.2. Synthetic routes used to synthesize π-conjugated ladder polymers. (a) Single-step polymerization/ladderization method that creates the polycyclic fused structure simultaneously with chain growth, and the (b) multi-step polymerization method where a single-stranded polymer is first synthesized followed by post-polymerization modification. 5

Figure 1.3. Molecular structures of known n-type and p-type ladder polymers. 8

Figure 2.1. (a) BBL-P film floating on water after peeling off from the initial supporting substrate, (b) Freestanding BBL-P film with a diameter of 1 cm, (c) Raman spectrum of BBL-P freestanding film with an excitation laser of 532 nm, (d) Fourier-transform infrared (FTIR) spectrum of BBL-P freestanding film, and (e) Optical absorption spectrum of BBL-P freestanding film 33

Figure 2.2. DFT calculations of (a) The optimized ground state molecular geometry of BBL-P oligomer, and (b) Pictorial representation of ground state frontier molecular orbitals. Calculations were performed at the ωB97XD/6-31G(d,p) level of theory 37

Figure 2.3. Cyclic voltammograms for the (a) reduction and (b) oxidation processes of BBL-P thin films measured in 0.1 M Bu_4NPF_6 electrolyte solution using $Ag/AgNO_3$ as the reference electrode. The scan rate was 100 mV/s 39

Figure 2.4. Absorption spectrum of BBL-P (red) and BBL (gray) in (a) dilute methanesulfonic acid solution; and (b) thin film on glass substrate 41

Figure 2.5. (a) 2D-GIWAXS diffraction pattern of BBL-P thin film, and (b) 1D line cuts of GIWAXS patterns in the out-of-plane (OOP) direction and the in-plane (IP) direction 42

Figure 2.6. (a) Representative output curves of BBL-P n-channel organic field-effect transistor with a channel length/channel width of 100 μm/1000 μm. (b) Representative transfer curve of BBL-P transistor 45

Figure 2.7. (a) Elastic modulus of BBL-P thin films at various indent depths measured by nanoindentation tests. (b-d) Dynamic mechanical properties of BBL-P thin films as a function of frequency measured at room temperature by nano(dynamic mechanical analysis): (b) Storage modulus, (c) Loss modulus, and (d) Loss tangent (tan δ) 46

Figure 3.1. Single crystal structure analysis of the monomer NTE-2CN. (a) Skeletal structure with atoms placed at the center of the thermal ellipsoids that were calculated at the 50% probability level. (b) Side view and (c) top view of the unit cell showing face-to-face π-π stacking with an intermolecular distance of 3.9 Å. The hydrogens and ester group disorder have been eliminated for clarity. 68

Figure 3.2. (a) The FTIR spectrum of the model compound PCN. (b) The FTIR and (c) Raman spectra of the copolymers. 72

Figure 3.3. High-resolution XPS N 1s spectra for (a) NTE-2CN, (b) PCN, (c) BBL, (e) BBL-202CN, (e) BBL-352CN, and (f) BBL-502CN and their optimal fits. 74

Figure 3.4. The reduction processes and energy levels of PCN and the BBL-*x*2CN random copolymers as thin films in anhydrous acetonitrile with $Ag/AgNO_3$ as the reference electrode and plotted vs. Fc/Fc^+. The scan rate was 15 mV/s. Note that the *HOMO level of PCN was out of range of the CV oxidation scan in acetonitrile and therefore was calculated using HOMO = LUMO – $E_g^{opt.}$ 76

Figure 3.5. Normalized optical absorption spectra of (a) PCN thin film and TFA solution, and BBL-x2CN copolymers as (b) MSA solutions and (c) thin films on glass. 79

Figure 3.6. FTIR and Raman spectra of (a-b) the PTCNMe model compound and (c-d) the freestanding films of the BBL-*x*TCN random copolymers. The Raman spectra were collected with an excitation laser of 532 nm. 100

Figure 3.7. XPS spectra of the optimally fit high-resolution N 1s emissions of the PTCNMe model compound and BBL-*x*TCN random copolymers. 103

Figure 3.8. DFT calculations of the optimized ground state geometry and frontier molecular orbital distributions of (a) PTCNMe and (b) the representative BBL-50TCN oligomer comprised of 6 repeat units. The calculations were performed at the wB97XD-631G(d,p) level of theory. 105

Figure 3.9. (a) Cyclic voltammograms for the reduction processes of PTCNMe and the BBL-*x*TCN random copolymers as thin films measured in 0.1 M Bu_4NPF_6 electrolyte solution using $Ag/AgNO_3$ as the reference electrode and plotted vs. Fc/Fc^+. The scan rate was 15 mV/s. (b) Energy levels of PTCNMe and the BBL-*x*TCN series. 106

Figure 3.10. (a) Normalized optical absorption spectra of the PTCNMe model compound as a thin film on glass and in MSA solution. Optical absorption spectra of the BBL-*x*TCN copolymers as (b) MSA solutions, and (c) as thin films on glass substrates. 110

Figure 4.1. Normalized (a) FTIR and (c) Raman spectra for the free-standing films of LPBT, and normalized (b) FTIR and (d) Raman spectra for the free-standing films of LPBT-Me 127

Figure 4.2. DFT calculations using ωB97XD/6-31G(d,p) level of theory for the optimized ground state geometry and molecular orbital distributions for single oligomers comprising 3 repeat units each for (a) LPBT-Me and (b) LPBT. The molecular geometry top and side views are of the same single oligomer 131

Figure 4.3. Cyclic voltammograms for the oxidation and reduction processes of (a) LPBT and (b) LPBT-Me thin films measured in 0.1 M Bu_4NPF_6 electrolyte solution using $Ag/AgNO_3$ as the reference electrode. The scan rate was 100 mV/s. The arrows indicate the direction of charging 132

Figure 4.4. Electrostatic potential (ESP) map calculated using DFT ωB97XD/6-31G(d,p) level of theory for (a) LPBT, (b) LPBT-Me, and (c) a theoretical oligomer with a methoxy group, LPBT-A. 135

Figure 4.5. Optical absorption spectra of the ladder polymers (a) in MSA solution. Normalized absorption spectra in dilute (10^{-6} M) protic acid solutions of varying pKa values: (b) LPBT-Me and (c) LPBT. 136

Figure 4.6. DFT-calculated optimized geometries of oligomers bearing +1, +2, and +6 protonation states for (a) LPBT and (b) LPBT-Me, where both oligomers were protonated on the imine nitrogens. Calculations performed at the ωB97XD/6-31G(d,p) level of theory. 139

Figure 4.7. Variable temperature optical absorption spectra of LPBT in (a) MSA and (b) triflic acid solutions (10^{-5} M), LPBT-Me in (c) MSA and (d) triflic acid solutions (10^{-5} M), (e) BBL in MSA solution (10^{-5} M), (f) the blue-shifts of the maximum wavelengths with increasing temperature for LPBT, LPBT-Me, and BBL in MSA solutions and LPBT and LPBT-Me in triflic acid solutions. 141

Figure 4.8. Optical absorption spectrum of the ladder polymers spin-coated from MSA solutions onto glass substrates. 142

Figure 4.9. 2D-GIWAXS diffraction patterns of LPBT (a) and LPBT-Me (b) thin films; 1D line cuts of GIWAXS patterns in the out-of-plane (OOP) direction (c) and the in-plane (IP) direction (d). 145

Figure 4.10. (a, b) Output curves of p-channel organic field-effect transistor (OFET) devices of LPBT (a) and LPBT-Me (b) ladder polymers; (c, d) Transfer curves of p-channel OFET devices of LPBT (c) and LPBT-Me (d) ladder polymers measured in saturated regimes (V_{ds} = -80V). 147

Figure 5.1. (a) LTBT freestanding film with an edge of 2 cm. (b) Fourier-transform infrared (FTIR) spectrum of the LTBT freestanding film and (c) Raman spectrum of the LTBT freestanding film with an excitation laser of 532 nm. 168

Figure 5.2. (a) Skeletal structure with atoms placed at the center of the thermal ellipsoids that were calculated at the 50% probability level with atom numbering scheme. (b) Organization of the molecules in a single unit cell. (c) Packing of the molecules along the *c*-axis with an intermolecular distance of 3.8 Å. 170

Figure 5.3. DFT calculated optimized ground-state geometry and the pictoral representation of the frontier molecular orbital distributions of (a) the neutral oligomer and (b) the protonated (+1) oligomer. Calculations performed at the ωB97XD/6-31G(d,p) level of theory. 172

Figure 5.4. Cyclic voltammograms measured in 0.1 M Bu_4NPF_6 electrolyte solution using $Ag/AgNO_3$ as the reference electrode of the oxidation processes of (a) LTBT thin films coated on platinum wires, and (b) TBBT needles in solution. The scan rate was 100 mV/s. 174

Figure 5.5. Optical absorption spectra of TBBT and LTBT in (a) dilute MSA solution (10^{-5} M), and (b) as thin films on glass substrates. (c) The thin film absorption spectrum of LTBT plotted vs. electron volts to determine the optical bandgap. 176

Figure 5.6. (a) Dc-electrical conductivity (σ_{dc}) of $FeCl_3$ doped LTBT thin films at various annealing temperatures; (b) Stability of electrical conductivity of LTBT doped films in ambient stability; (c) Thin film optical absorption spectra of undoped and $FeCl_3$ doped LTBT thin films; (d) Optical absorption spectra of LTBT doped films in energy space. 180

Figure 6.1. Examples of potential ladder polymers featuring alkyl chains. R = long alkyl chain. 196

Figure A.1. (a) TGA of BBL-P (at 10˚C/min under N_2) taken after 48 hours drying (orange), 96 hours drying (blue) at 200˚C under vacuum, and drying to 400˚C in the TGA, cooling to 50˚C, and ramping up to 880˚C (red). (b) DSC heating and cooling scans of BBL-P with a heating and cooling rate of 10˚C/min under N_2 gas flow. 200

Figure A.2. Proton NMR spectrum of (a) BBL-P and (b) BBL in $GaCl_3$/nitromethane-d3, and (c) possible structural isomers of the BBL-P monomeric repeat unit. 201

Figure A.3. Pictorial representation of the DFT-calculated ground state frontier molecular orbitals of BBL oriented in a trans-cis-trans geometry. Calculations were performed at the ωB97XD/6-31G(d,p) level of theory. 202

Figure A.4. (a) Simulated absorption spectrum of the gas phase BBL-P oligomer calculated at the time-dependent (TD) ωB97XD/6-31G(d,p) level of theory calculated with 12 excited states (λ_{max} = 527 nm), (b) The pictorial representation of hole and electron orbital distributions for the lowest energy transition (π-π^*) at 527 nm, and (c) The anionic BBL-P oligomer showing polaron orbital distribution calculated at the same ωB97XD/6-31G(d,p) level of theory. 203

Figure A.5. (a) AFM height image of BBL-P thin film (2 μm x 2 μm) and (b) AFM phase image of BBL-P thin film (2 μm x 2 μm). 204

Figure A.6. Transfer curve of BBL-P transistors with reverse and forward scans. The inset shows a zoomed-in region with gate voltage varying between 60 V and 120 V. 204

Figure A.7. (a-e) AFM topography images of BBL-P films after nanoindentation tests at various indent depths (60 nm (a), 90 nm (b), 110 nm (c), 130 nm (d), and 150 nm (e)), (f) Indent depth as a function of time, and (g) Load-displacement response curve of BBL-P films (thickness = 650 nm) at various indent depths. 205

Figure B.1. Proton NMR of NTCDA-2Br (**2**) in DMSO-d6. 210

Figure B.2. Proton NMR of NTE-2Br (**3**) in $CDCl_3$. 211

Figure B.3. Proton NMR of NTE-2CN (**4**) in $CDCl_3$. The inserts show the peak splitting. 212

Figure B.4. Carbon NMR of NTE-2CN (**4**) in $CDCl_3$. 213

Figure B.5. FTIR spectrum of the NTE-2CN (**4**) crystals. 214

Figure B.6. Proton NMR of PCN in DMSO-d6 and the possible isomers of PCN, which contribute to the overlapping resonances in the aromatic region. 215

Figure B.7. Carbon NMR of PCN in DMSO-d6. 216

Figure B.8. ESI mass spectrum of PCN in dilute methanol (10^{-6} M). 217

Figure B.9. TGA scans of the BBL-*x*2CN random copolymers under N_2 with a scan rate of 10˚C/min. 218

Figure B.10. DFT-calculated (a) FTIR spectrum of PCN, and the (b) FTIR and (c) Raman spectra of the BBL-502CN oligomer. Calculations were performed at the ωB97XD 6-31G(d,p) level of theory. 219

Figure B.11. Survey scans of the (a) NTE-2CN crystals on silicon substrates, and thin films on silicon substrates of (b) PCN, (c) BBL, (d) BBL-202CN, (e) BBL-352CN, and (f) BBL-502CN. 220

Figure B.12. XPS spectra of the C 1s peaks and their optimal fits of the (a) NTE-2CN monomer, (b) PCN model compound, and (c-f) the copolymers. N 1s spectra showing a two-peak fit with residual standard deviations (RSTD) for PCN (g) and (h-k) the copolymers. 221

Figure B.13. DFT calculations of the optimized ground-state molecular geometry of PCN, and the pictoral representation of the ground-state frontier molecular orbitals. Calculations were performed at the ωB97XD/6-31G(d,p) level of theory. 222

Figure B.14. DFT calculations of the optimized (a) ground-state molecular geometry of the representative BBL-502 oligomer comprised of 6 repeat units, and (b) the pictoral representation of the ground-state frontier molecular orbitals. Calculations were performed at the ωB97XD/6-31G(d,p) level of theory. 223

Figure B.15. Oxidation scans of (a) PCN (b) BBL-202CN, (c) BBL-352CN, and (d) BBL-502CN as thin films coated on platinum electrodes vs. Ag/Ag^+ in anhydrous acetonitrile. The scan rate was 15 mV/s. 224

Figure C.1. Proton NMR of the NTA-TCN monomer dissolved in D_2O+NaOH. 234

Figure C.2. FTIR spectrum of the NTA-TCN monomer in a Nujol mull. The peak at 2202 cm^{-1} is the nitrile stretch. 235

Figure C.3. Proton NMR of PTCNMe dissolved in DMSO-d6. The methyl groups are overlapping with the satellite peaks of DMSO-d6. 236

Figure C.4. Thermogravimetric analysis (TGA) scans of the BBL-*x*TCN random copolymers and model compound under N_2 at a heating rate of 10˚C/min. The dashed line marks 5% weight loss. 237

Figure C.5. The DFT-predicted (a,c) FTIR and (b,d) Raman spectra for PTCNMe and BBL-50TCN. The calculations were performed at the ωB97XD/6-31G(d,p) level of theory. 238

Figure C.6. XPS survey scans of thin films on silicon substrates of the (a) PTCNMe, (b) BBL, (c) BBL-20TCN, (d) BBL-352CN, and (e) BBL-50TCN. 239

Figure C.7. XPS spectra of optimally fit C 1s and S 2p emissions for (a,f) PTCNMe, (b) BBL, (c,g) BBL-20TCN, (d,h) BBL-352CN, and (e,i) BBL-502CN. The peaks at ~ 168 eV in the S 2p spectra are due to an oxidized sulfur species, likely from residual methanesulfonic acid. 240

Figure C.8. Electrostatic potential map of PTCNMe showing top and bottom views calculated at the DFT ωB97XD/6-31G(d,p) level of theory. 241

Figure C.9. TD-DFT calculations performed at the ωB97XD/6-31G(d,p) level of theory on the model compound showing (a) the excited state geometry, (b) simulated absorption spectra, and (c) the pictoral representations of the hole and electron orbital distributions show the lowest energy transition (π-π*) at 576 nm. The calculations were run for n = 12 excited states. 242

Figure C.10. Cyclic voltammetry oxidation scans for (a) BBL-20TCN, (b) BBL-35TCN, (c) BBL-50TCN, and (d) PTCNMe vs. $Ag/AgNO^3$ in acetonitrile with 0.1 M Bu_4NPF_6 at a scan rate of 15 mV/s. 243

Figure C.11. Normalized optical absorption spectra of PTCNMe and the BBL-*x*TCN random copolymers (a) in dilute MSA solutions (10^{-5}M) and (b) as thin films on glass substrates. 244

Figure D.1. DFT ωB97XD/6-31G(d,p) level of theory calculated IR spectra for (a) LPBT and (b) LPBT-Me. DFT-calculated Raman spectra for (c) LPBT and (d) LPBT-Me. The peak assignments and corresponding vibrational modes are in Tables D.1 and D.2. 250

Figure D.2. Proton NMR spectra of (a) LPBT and (b) LPBT-Me in $GaCl_3$/nitromethane-d3. 251

Figure D.3. (a) TGA (at 10˚C/min under N_2) of LPBT and LPBT-Me under nitrogen with 5% weight loss of 475˚C and 508˚C for LPBT and LPBT-Me, respectively, and (b) DSC heating and cooling scans of LPBT and LPBT-Me with a heating and cooling rate of 10˚C/min under N_2 gas flow. 252

Figure D.4. TD-DFT-calculated vertical electronic transitions and excited state geometries of LPBT and LPBT-Me oligomers. Calculated at the TD-DFT ωB97XD/6-31G(d,p) level of theory for n=12 excited states. 253

Figure D.5. Additional CV scans of the LPBT and LPBT-Me thin films measured in 0.1 M Bu_4NPF_6 electrolyte solution using $Ag/AgNO_3$ as the reference electrode. The scan rate was 100 mV/s and the arrow indicates the direction of charging. 253

Figure D.6. HOMO and LUMO orbital distributions calculated using DFT at the ωB97XD/6-31G(d,p) level of theory for (a) LPBT and (b) LPBT-Me for oligomers bearing +1 and +6 charges. The oligomers were protonated at the same imine nitrogens. 254

Figure E.1. Proton NMR of the monomer 3,4-dibromothiophene-2,5-dione in DMSO-d6. 258

Figure E.2. Carbon NMR of monomer 3,4-dibromothiophene-2,5-dione in DMSO-d6. 259

Figure E.3. Attenuated Total Reflectance Fourier-transform Infrared **(**ATR-FTIR) spectrum of the neat monomer, 3,4-dibromothiophene-2,5-dione. 260

Figure E.4. Proton NMR of TBBT in TFA-d. Insert shows the peak integration for the benzene moiety. 261

Figure E.5. FTIR spectrum of TBBT. 262

Figure E.6. Thermal gravimetric analysis (TGA) scans of (a) TBBT and (c) LTBT under nitrogen at a scan rate of 10˚C/min. Differential scanning calorimetry (DSC) scans of (b) TBBT and (d) LTBT at a scan rate of 10˚C/min under nitrogen. 263

Figure E.7. Ground state geometry and molecular orbital distributions of TBBT calculated using DFT ωB97XD/6-31G(d,p) level of theory. 264

Figure E.8. Excited state geometry and simulated vertical excitations of the gas phase LTBT oligomer, and the corresponding hole and electron wavefunctions for the lowest energy transition (π-π^*) at 1170 nm calculated using TD-DFT ωB97XD/6-31G(d,p) level of theory for n=12 excited states (λ_{max} = 1170 nm). 265

Figure E.9. Cationic LTBT oligomer geometry and polaron orbital distribution calculated at the DFT ωB97XD/6-31G(d,p) level of theory. 266

Figure E.10. The reduction scans of (a) LTBT and (b) TBBT in 0.1 M Bu_4NPF_6 acetonitrile solution vs. Ag/Ag^+. The scan rate was 100 mV/s. 267

Figure E.11. Thin film absorption spectra of TBBT plotted vs. eV to determine the optical bandgap from the onset of absorption. 268

Figure E.12. Optical absorption spectra of LTBT in (a) dilute (10^{-5} M) MSA solution (λ_{max} = 1151 nm) and (b) triflic acid solution (λ_{max} = 1192 nm). 268

Figure E.13. (a-c) Atomic force microscopy (AFM) height images of neat LTBT thin films deposited on glass; (d-f) AFM phase images of neat LTBT films. 269

List of Charts

Chart 2.1. Molecular structures of π-conjugated ladder polymers BBL and BBL-P. 24

Chart 2.2. Different linkage positions for incorporating phenazine (phen) into π-conjugated polymer backbones. 25

Chart 3.1. Molecular structures of the (a) representative 2CN-functionalized n-type polymeric building blocks, and (b) the new model compound PCN and ladder polymers BBL-2CN and BBL-*x*2CN random copolymers. 59

Chart 3.2. Molecular structures of the n-type polymer BBL, the random copolymers featuring dithiinotetracarbonitrile groups BBL-*x*TCN (x = 0.2, 0.35, 0.5), and BBL-TCN. 91

Chart 4.1. Molecular structures of π-conjugated ladder polymers BBL, LPBT and LPBT-Me, and ladder molecule PBBTZ. 120

Chart 5.1. Molecular structures of model compound TBBT and conjugated p-type ladder polymer LTBT. 159

List of Schemes

Scheme 2.1. Synthesis of BBL-P (PPA = polyphosphoric acid, 84% free P_2O_5). 29

Scheme 3.1. Synthesis of (a) the new NTE-2CN monomer, (b) PCN model compound, and (c) conjugated random copolymers, BBL-*x*2CN. (DBH = dibromohydrantoin, EtI = ethyl iodide, EtOH = ethanol, DMF = dimethylformamide, PPA = polyphosphoric acid, 84% free P_2O_5). 67

Scheme 3.2. Synthesis of (a) the model compound PTCNMe, and (b) the BBL-*x*TCN random copolymers (PPA= Polyphosphoric acid, 84% free P_2O_5). 97

Scheme 4.1. Synthesis of LPBT and LPBT-Me (PPA = polyphosphoric acid, 84% free P_2O_5; PhPA = phenylphosphonic acid). 126

Scheme 5.1. Synthesis of TBBT and LTBT (HNO_3 = fuming nitric acid, DCM = dichloromethane, AcOH = glacial acetic acid, PPA = polyphosphoric acid (84% free P_2O_5), and PPA/Sulfolane 1:1 w/w). 164

List of Tables

Table 2.1. FTIR and Raman Absorption Bands of Freestanding BBL-P Film and Their Peak Assignments. 35

Table 2.2 Optical Properties and Electronic Structure of BBL-P and BBL. 42

Table 3.1. Electronic and Optical Properties of the model compound PCN and the BBL-*x*2CN Random Copolymers. 77

Table 3.2. XPS Parameters Including the Combined Full-width at Half-maximum (FWHM) for N 1s Peaks, and Sulfur/Nitrogen Ratios of the BBL-*x*TCN Random Copolymers. 102

Table 3.3. Electronic Structure Parameters and Optical Properties of the model compound PTCNMe and the BBL-*x*TCN polymers. 108

Table 4.1. Electronic Structure Parameters and Optical Properties of LPBT and LPBT-Me. 133

Table 4.2. Summary of Diffraction Peak Position (q), Interplanar Spacing (d), Crystalline Coherence Length (L_c), Number of Stacked Layers Within a Crystallite (N), and Paracrystallinity Disorder (g) of LPBT and LPBT-Me Thin Films. 146

Table 4.3. Hole Transport Properties of LPBT and LPBT-Me Conjugated p-Type Ladder Polymers Measured by Organic Field-Effect Transistors. 147

Table 5.1. Electronic Structure Parameters and Optical Properties of LTBT and TBBT. 174

Table 5.2. Dc-Electrical Conductivity (σ_{dc}) of $FeCl_3$-Doped LTBT Thin Films as a Function of Annealing Temperature and Storage Duration. 179

Table A.1. Summary of Diffraction Peak Positions (q), d-Spacings, and Crystalline Coherence Length (L_c) in the In-Plane (IP) and Out-of-Plane (OOP) Directions of BBL-P. 206

Table A.2. Charge Transport Properties of BBL-P Ladder Polymer Characterized by Organic Field-Effect Transistor (OFET) with Channel Length/Channel Width of 100 μm/1000 μm. 206

Table B.1. Crystal Data and Structure Refinement for NTE-2CN. 225

Table B.2. Atomic Coordinates (x 10^4) and Equivalent Isotropic Displacement Parameters (Å^2 x 10^3) for NTE-2CN. U(eq) is Defined as One Third of the Trace of the Orthogonalized U^{ij} Tensor. 226

Table B.3. FTIR Absorption Bands and Their Peak Assignments for the Monomer NTE-2CN and the Model Compound PCN. 227

Table B.4. FTIR and Raman Absorption Bands and Their Peak Assignments for the Random Copolymers. 228

Table B.5. C 1s Binding Energies (B.E.) of the High-resolution Scans in Figure B.12. 229

Table B.6. N 1s Binding Energies (B.E.), Full-Width at Half-Maximum (FWHM), and the Residual Standard Deviation (RSTD) of the 2 Peak and 3 Peak Fits of the High-resolution Scans in Figures 3.3 and B.12. 230

Table C.1. FTIR and Raman Absorption Bands and Peak Assignments for PTCNMe. 245

Table C.2. FTIR and Raman Absorption Bands for the BBL-*x*TCN Random Copolymer Freestanding Films. 245

Table C.3. C 1s Binding Energies (B.E.) and the Corresponding Full-width at Half-maximum (FWHM) for the Fitted Peaks for PTCNMe, BBL, and the BBL-*x*TCN Random Copolymers. 246

Table C.4. N 1s, S 2p, and O 1s Binding Energies for PTCNMe and the BBL-*x*TCN Random Copolymers Calibrated to the Lowest Energy Carbon Peak at 285.0 eV. 247

Table D.1. Fourier-Transform Infrared Spectroscopy (FT-IR) and Raman Absorption Bands of LPBT Free Standing Films and Their Peak Assignments. 255

Table D.2. Fourier-Transform Infrared Spectroscopy (FT-IR) and Raman Absorption Bands of LPBT-Me Free Standing Film and Their Peak Assignments. 255

Table E.1. Fourier-Transform Infrared Spectroscopy (FTIR) and Raman Absorption Bands of LTBT Freestanding Films and Their Peak Assignments. 270

Table E.2. Fourier-Transform Infrared Spectroscopy (FTIR) Absorption Bands of TBBT Needles and Their Peak Assignments. 270

Table E.3. Crystallographic Data for TBBT. 271

Table E.4. Atomic Coordinates (x 10^4) and Equivalent Isotropic Displacement Parameters ($Å^2$x 10^3) for TBBT. U(eq) is Defined as One Third of the Trace of the Orthogonalized U^{ij} Tensor. 272

Acknowledgments

First, I would like to express my gratitude towards my thesis advisor and primary mentor, Professor Samson A. Jenekhe, for his valuable advice and guidance and providing me with the opportunity to pursue my research interests in the field of semiconducting polymers. His valued advice in areas of scientific research and writing, participation in collaborations, and interaction with the scientific community in general has been instrumental for the completion of this dissertation.

I would like to thank Professors Alshakim Nelson, Gojko Lalic and Bruce Hinds for taking the time to serve on my committee and provide me with value feedback during the course of my studies. I would also like to think my past committee members, Professors Matthew Golder and Eleftheria Roumeli.

Of course, I could not have succeeded without my lab members both past and present. Specifically, I would like to thank Dr. Nagesh B. Khole for getting me starting with the synthesis of π-conjugated systems and helping improve my column chromatography skills. I would also like to thank Mary Nguyen and Dr. Xiaomei Ding for their collaborative discussions about my projects and the field in general. I would like to give a special thank you to Dr. Duyen Tran who was not only fabricated all of my solar cell and transistor devises, but was also a good friend in and outside of the lab. She was my forefront collaborator on all my projects with whom I could discuss my results and setbacks and always provided valuable insights. We also supported each other's coffee addiction and shared frequent coffee breaks together.

I would like to thank my collaborators, including Professor David A. Ginger, Dr. Shinya E. Chen, and Dr. Jiajie Guo who helped with GIWAXS data collection for my polymers. Additionally, I would like to thank Professor Theodore Goodson III and Meghan Orr at the University of Michigan for their interest and study of my small molecule acceptors and productive discussions. I would like to thank all the support staff in the Department of Chemistry at the University of Washington for

assisting me with experiments and niche requests, including teaching me how to rebuild a diaphragm pump.

I would like to acknowledge all the funding agencies for supporting my research including the US. Department of Energy, the Office of Naval Research, the National Science Foundation, and the Clean Energy Institute at the University of Washington.

Finally, I would like to thank all my friends and family for their continued support during my graduate studies. My parents have always been supportive of my goals and I am eternally grateful to them for giving me the opportunity to be the first, first-generation college student in my family. My sisters, childhood friends, and new friends made while in graduate school have supported me fiercely throughout my undergraduate and graduate college career. Lastly, I would like to thank my favorite person in the world, my husband Lee West. Without him, I would not have considered graduate school as a feasible pathway for someone with humble beginnings. He has been my biggest supporter through the years, and he has always pushed me to reach for goals I thought were unobtainable.

Chapter 1. Introduction

1.1. Semiconducting Polymers in Organic Electronic and Optoelectronic Devices

Organic semiconductors are of broad and fundamental interest for applications in electronic and optoelectronic devices including; organic photovoltaics (OPVs),[1–3] organic field-effect transistors (OFETs),[4–6] organic electrochemical transistors (OECTs),[7–11] and organic thermoelectric devices.[12–14] Contrary to their inorganic counterparts, they have potential for applications in low-cost flexible displays, integrated circuits for logic and memory, and high-throughput processing of large area electronic devices such as spin-coating and roll-to-roll printing. Significant progress has been made towards wide-spread applications of organic electronics including the commercialization of organic light-emitting diodes (OLEDs) in small-area flexible displays,[15] OPVs with power conversion efficiencies > 18%,[16,17] and OFETs that have charge transport mobilities beyond that of amorphous silicon.[18,19] Understanding the structure-property relationships of the organic semiconductors have allowed these technologies by enabling rational design of high-performance organic materials to suit a given application.[20–27]

Since the discovery of doped conducting polyacetylene in 1977,[28,29] there has been widespread interest and research into the field of π-conjugated semiconducting polymers for organic electronics. The backbone of π-conjugated polymers is comprised of alternating single (sigma, σ) and double (pi, π) bonds that creates their $sp^2 + p_z$ hybrid orbitals that act as a pathway for charge transport, thus endowing them with unique semiconducting properties. As the π-conjugation length or delocalization of the electrons increases, the gap between the occupied valence band, or the highest occupied molecular orbital (HOMO), and the empty conduction band, or the lowest unoccupied molecular orbital (LUMO), decreases. This bandgap (E_g) of semiconducting polymers (4 eV > E_g > 1.0 – 1.2 eV) distinguishes them from insulating (E_g > 4 eV) materials such as Kevlar, or conducting (E_g < 0.4 eV) materials like metals.

The optical properties, electrochemical properties and the electronic structure of semiconducting polymers are all highly tunable via molecular design and synthesis. For example, the optical bandgap of π-conjugated polymers can be decreased by introducing a double-stranded architecture[30–32] or a noncovalent conformational lock[33,34] that reduces conformational disorder and enhances π-electron delocalization.[35–37] Another strategy to manipulate the properties of π-conjugated polymers is to utilize a donor-acceptor (D-A) motif whereby careful selection of the electron-donating (electron rich) and electron-accepting (electron deficient) moieties in the polymer backbone can dramatically influence the electronic structure (HOMO and LUMO energy levels), optical properties and intramolecular charge transfer (ICT) interactions.[38,39]

π-Conjugated polymers can be classified as either p-type (hole conducting)[3,27,40–42] or n-type (electron conducting)[13,22,43–45] materials depending on their electronic structure and majority charge carriers. In some cases, π-conjugated polymers have been reported to be ambipolar, or capable of transporting both electrons and holes.[46–50] The type of charge carriers in π-conjugated polymers can be readily manipulated by tuning their HOMO and LUMO energy levels with respect to vacuum by rational monomer design and synthesis. Although parity in both hole and electron transport is necessary to develop high-performing organic electronic devices, the development of n-type semiconducting polymers still lags behind that of p-type.[22,44] This is primary due to difficult synthesis of n-type moieties and their poor ambient stability in air[22,46,51] since a common strategy to realize n-type building blocks is to incorporate electron-deficient moieties into the hydrocarbon backbone such as halogens,[52–55] nitriles,[56–58] carbonyls,[59–61] and imine groups.[62–64] Increasing the molecular diversity of n-type building blocks is necessary to establish structure-property relationships to realize high-performance n-type π-conjugated polymers to match those of p-type polymers.

Despite the aforementioned advantages of semiconducting polymers for organic electronics and optoelectronics, there are notable disadvantages. Device reproducibility can be a challenge

owing to the fact that polymers are polydisperse materials with broad molecular-weight distributions (polydispersity > 1). Moreover, typical polymerization routes such as Stille,[65,66] Suzuki,[67,68] and Negishi couplings,[69,70] Knoevenagel and Aldol polycondensations,[71–73] and C-H activation polymerizations[74] are not specific enough to achieve a target molecular weight. This can lead to polymers with ambiguous properties because many, including charge transport, are largely determined by the degree of polymerization (DP).[11,75,76] Moreover, purification of polymer semiconductors for organic electronics is often limited to large-scale precipitation which can be insufficient to afford electronic device grade materials.

1.2. π-Conjugated Polymer Chain Topology

π-Conjugated polymers can be generally divided into two main classes based off of polymer chain topology: *semi-flexible* and *rigid-rod ladder* polymers. Examples of polymers that feature a *semi-flexible* and *rigid-rod ladder* chain topologies are shown in Figure 1.1. The *semi-flexible* class of π-conjugated polymers feature a single bond that link the repeat units in the polymer backbone, which give the polymers intrinsic flexibility.[30,77] This class of polymer chain topology represents the vast majority of semiconducting polymers that have been synthesized for organic electronics due to the large diversity of single-stranded polymerization techniques and ubiquity of available monomers.[30,78] However, the commonly observed dihedral fluctuations in single-stranded polymers can disrupt the π-conjugation, widen the bandgap, create charge carrier trap states, and decrease intermolecular interactions.[49,79,80] A popular approach to circumvent the inherent flexibility of single-stranded polymers is to utilize noncovalent interactions to establish conformational locks. For example, noncovalent interactions including sulfur-nitrogen, sulfur-oxygen, sulfur-halogen, and hydrogen bonding are attributed to the observed planarity of many π-conjugated polymers such as those containing (acylimino)thiadiazoline,[81] 2-alkoxythiophene,[82,83] isoindigo,[84–86] diketopyrrolopyrrole[87,88] building blocks.

The second class of polymer chain topology is *rigid-rod ladder* polymers, which are exceedingly rare due to difficult synthesis of the double-stranded ladder architecture, and consequently these polymers have seldom been used in organic electronic devices.[30,78] However, the ladder polymer design features many properties that benefit organic electronic devices originating from their decreased conformational disorder; these include enhanced π-conjugation lengths, fast intra-chain charge transport, long exciton diffusion lengths, and tight intermolecular contacts.[30–32,77,89–91] Additionally, ladder polymers have superior thermal, mechanical, and chemical stability.[92–94]

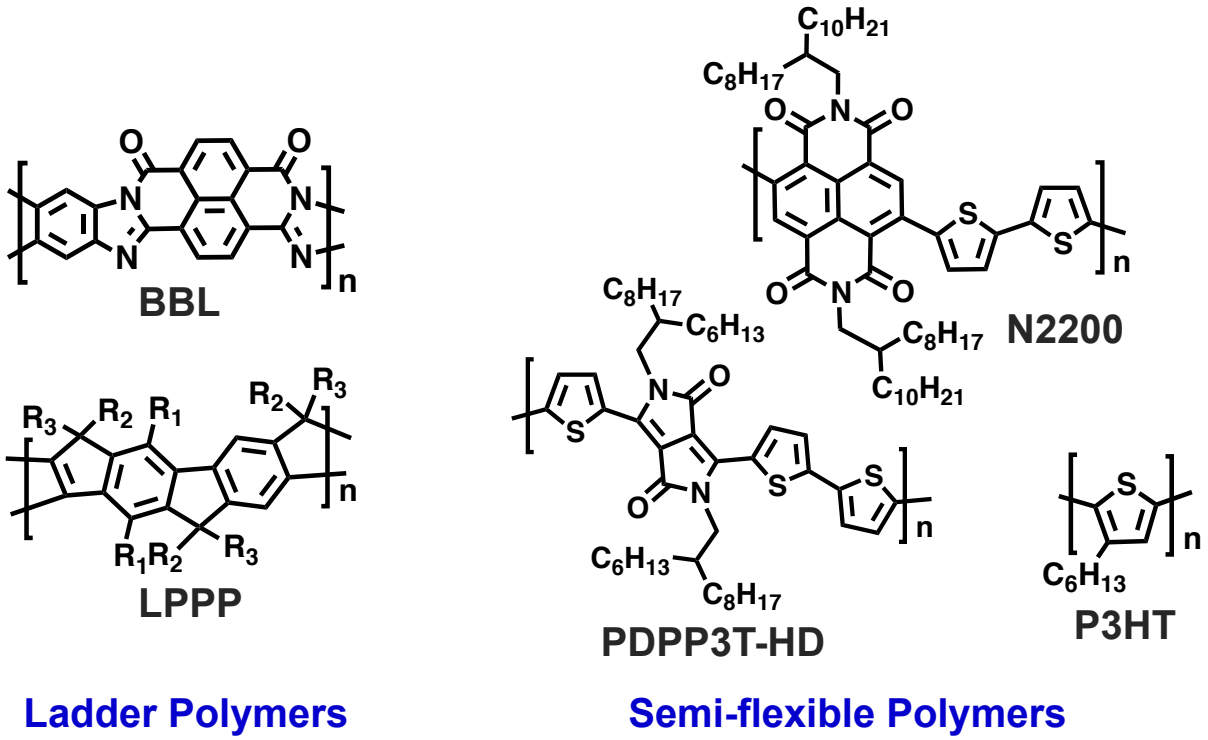

Figure 1.1 Chemical structures of a few well-known ladder polymers and semi-flexible polymers.

1.3. π-Conjugated Ladder Polymers

The double-stranded architecture of π-conjugated ladder polymers creates unique challenges in the synthesis, processing, and characterization that have prevented elucidation of the structure-property relationships of ladder polymers. For example, their rigid ribbon-type structure affords the polymer very low solubility in organic solvents such that they can only be processed in strong protic

acids or air sensitive Lewis-acid complexes.[77,95,96] However, the aforementioned benefits of the π-conjugated ladder architecture including their exceptional thermal stability and unique electronic properties have prompted investigation into various electronic and optoelectronic applications including OFETs,[21,25,31] OPVs,[97] and organic thermoelectrics.[55,98] In order to be able to rationally design new ladder polymers for electronic device applications, the diversity of both p-type and n-type π-conjugated ladder polymers must be increased, and their structure-property relationships must be elucidated.

1.3.1. Synthetic Routes to Form π-Conjugated Ladder Polymers

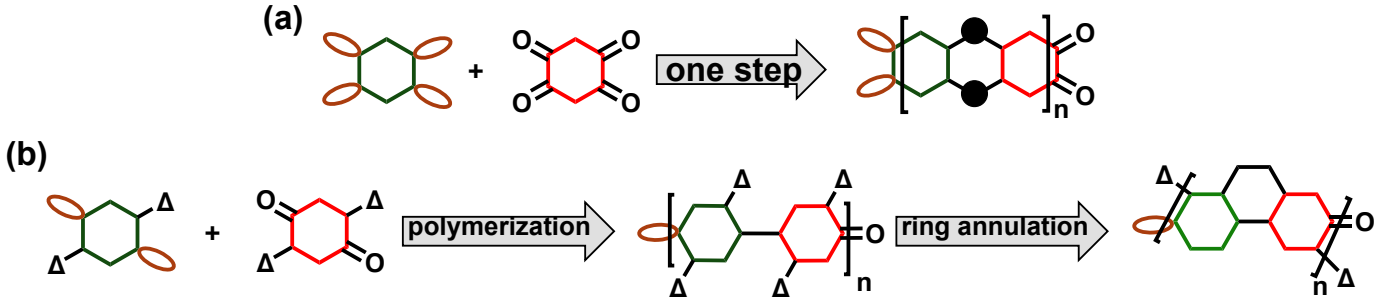

Figure 1.2. Synthetic routes used to synthesize π-conjugated ladder polymers. (a) Single-step polymerization/ladderization method that creates the polycyclic fused structure simultaneously with chain growth, and the (b) multi-step polymerization method where a single-stranded polymer is first synthesized followed by post-polymerization modification.

The two different polymerization routes to form π-conjugated ladder polymers are shown in Figure 1.2. Synthetic routes to form fully fused ladder structures can be classified as (i) a single-step polymerization/ladderization that constructs the double-stranded, fused ring simultaneously with chain growth; and (ii) the two-step polymerization followed by ladderization where the non-fused polymer chain is first synthesized and followed by ring closure, which is typically done using differing synthetic conditions.[30,78] Although the latter approach encompasses a larger scope of building blocks, the resulting polymers are prone to defects because of inefficient post-annulation, leading to poor device performance.[30,78,99] Therefore, the simplified single-step ladderization method is preferred such that the polymers are more likely to be defect-free.

The synthetically simple way to form a double-stranded ladder polymers is though single-step polycondensations in highly acidic solvents such as polyphosphoric acid (PPA). Early examples of polymers synthesized by this method include poly(benzimidazobenzophenanthroline) (BBL),[92] poly(quinoxaline),[100,101] poly(phenothiazine),[102] and poly(phenooxazine).[102] In 1966, Van Deusen reported the synthesis of BBL through a single-step polycondensation of monomers 1,4,5,8-naphthalenetetracarboxylic acid (NTCA) and 1,2,4,5-tetraaminobenzene hydrochloride (TABH) in PPA solvent.[92] The intrinsic viscosity ([η]) of ladder polymers are often used as a proxy for molecular weight given their low solubility in organic solvents;[103] this first BBL polymer had [η] = 0.3 dL/g in conc. sulfuric acid (H_2SO_4).[92] A few years later, Van Deusen improved the synthetic method to synthesize ladder polymers including BBL with higher [η] values by liberating the salt of the amine monomers to improve their reactivity.[93] This approach afforded BBL with an improved intrinsic viscosity of 6.12 dL/g in methanesulfonic acid (MSA). More than a decade later, Wolfe, Loo and Arnold discovered a unique feature of the rigid-rod π-conjugated polymers poly(benzobizthiazole) (PBT) and poly(benzobisoxazole) (PBO): polycondensation occurs more efficiently in the liquid crystalline phase formed at low polymer conversion, which allows for higher molecular weights vs. polymerization in the isotropic phase.[104] Using this liquid-crystalline phase polycondensation technique, a BBL polymer with an intrinsic viscosity of 32.0 dL/g in MSA at 30˚C was synthesized in our lab, which is the highest known [η] value reported for BBL. These finding mean that effort should be taken to achieve liquid crystallinity during the polycondensation of ladder polymers.

Another example of a single-step polycondensation reaction was reported for the ladder poly(pyrrolobenzothiazine) (LPBT), which utilized kinetic control to create a fully-fused ladder backbone.[105] At low temperatures < 100˚C, the nucleophilic attack of the thiol and amine groups creates the C-S and C-NH bond, respectively, that create the non-conjugated ladder polymer backbone. Upon reaching higher temperatures > 150˚C, the imine condensation forms the π-

conjugated ladder backbone. Overall, the single-step approach benefits from synthetic simplicity and a low rate of defects, both of which are critical for polymers used in organic electronics and optoelectronics. However, the major drawback for this approach is that tetra-functionalized monomers are difficult to synthesize and purify on a gram scale.

The two-step ladderization approach has been used successfully to create a variety of organic-solvent soluble ladder polymers. The most famous example is the polymer ladder poly(para-phenylene) (LPPP) first synthesized in 1991.[106] The synthesis of LPPP starts with a Suzuki polymerization to form the pre-polymer followed by reduction with lithium aluminum hydride and finally a Friedel-Crafts ring annulation reaction. This polymerization scheme has been utilized frequently to form many π-conjugated ladder polymers.[30,78] However, as evidenced in the careful analysis of the LPPP molecular structure,[99] this synthetic route usually produces structural defects simply because no chemical reaction has 100% efficiency across dozens/hundreds of repeat units. In the case of LPPP, the ketone defects result from incomplete reduction of the pre-polymer. Even still, the benefits of the two-step polymerization scheme has continued to inspire research into reducing the molecular defects during the post-annulation reactions; however, is only one known examples of π-conjugated ladder polymers synthesized using this two-step approach that have shown potential for organic electronics or optoelectronics,[107] because defects as low as parts-per-million can negatively impact electronic device performance.[108–110]

1.3.2. n-Type π-Conjugated Ladder Polymers

Examples of reported n-type π-conjugated ladder polymers are shown in Figure 1.3. The most well-known n-type π-conjugated ladder polymer is the polymer BBL. Since the 1980s, BBL has been widely studied as an n-type semiconducting polymer when its highly conductive doped state was first described.[111] Notably, BBL was the first n-type polymer to be used in OFET devices where a high field-effect electron mobility (μ_e) of ~ 0.03 – 0.1 cm^2/Vs in air was reported.[21,25] Since then, BBL has continued to be the gold standard for all n-type ladder polymers and has found use in a wide variety

of organic electronic devices. Of importance to this thesis, our group studied the effects of BBL molecular weight on field-effect electron mobility and we found that the μ_e values scale linearly with the degree of polymerization, which emphasizes the need to maximize the molecular weight of π-conjugated ladder polymers.[76]

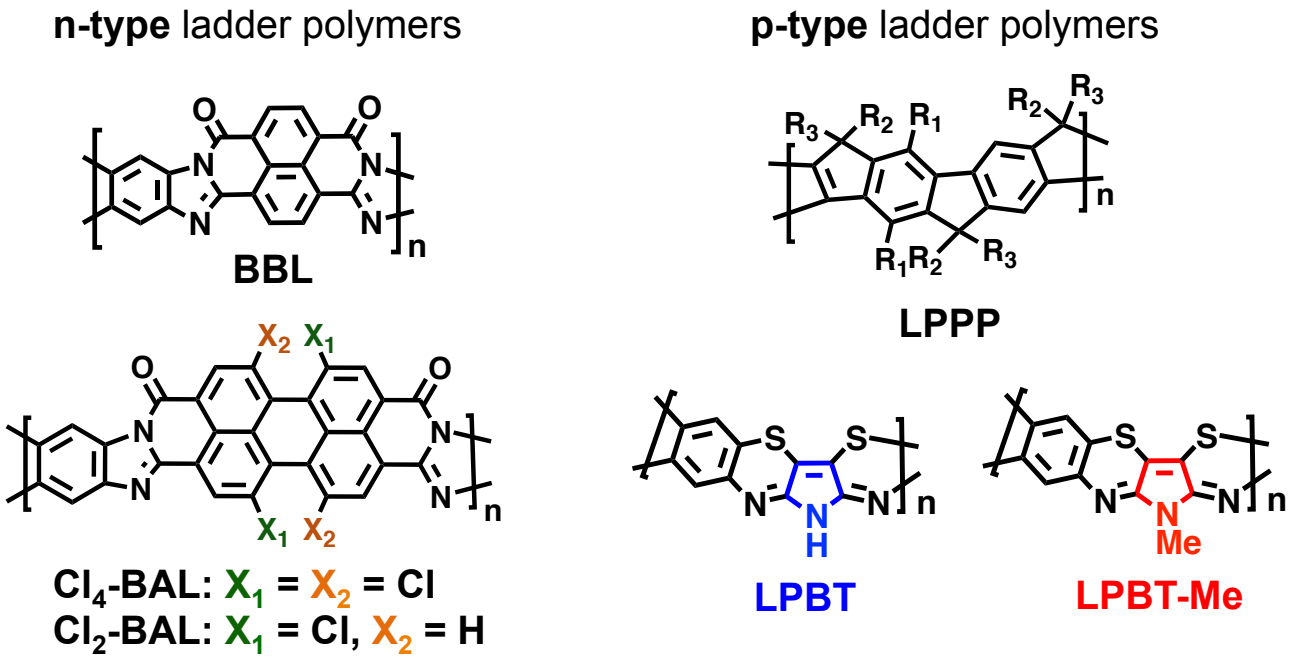

Figure 1.3. Molecular structures of known n-type and p-type ladder polymers.

Other than BBL and its phenazine-substituted derivative BBL-P,[112,113] there are two other reported n-type π-conjugated ladder polymers that show promise as n-type semiconductors: a tetrachloro-substituted perylene derivative poly(benzimidazoanthradiisoquinolinedione) (Cl_4-BAL),[54] and a dichloro-substituted perylene derivative poly(benzimidazoanthradiisoquinolinedione) (Cl_2-BAL)[55] which are shown in Figure 1.3. The addition of the chloride groups in Cl_4-BAL resulted in a non-rigid and twisted backbone that improved the solubility of the polymer in protic acids. Furthermore, Cl_4-BAL was found to have good air-stability and conductivity when n-doped, and a low LUMO energy level of -4.55 eV was reported.[54] However, the out-of-plane twisting conformations of the polymer backbone are likely to negatively impact the intrinsic electron mobility, which was never reported. To create a more planar and rigid n-type ladder polymer, a

derivative featuring two chlorine atoms (Cl_2-BAL) was reported (Figure 1.3).[55] Compared to Cl_4-BAL, this polymer exhibited a lesser degree of backbone torsions (28˚ vs. 40˚ based off of DFT calculations), although the marginal solubility of this polymer limited to intrinsic viscosity to 1.2 dL/g in MSA at 25˚C. Additionally, the placement of the chlorine atoms at the bay positions of the perylene monomer created an isomeric mixture of chlorine placements that was carried into the polymer backbone. Even still, Cl_2-BAL showed good electrical conductivity when n-doped, although no intrinsic electron mobility studies were reported.

1.3.3. p-Type π-Conjugated Ladder Polymers

Besides LPPP, the only reported solution-processable p-type π-conjugated ladder polymers feature a pyrrolobenzothiazine backbone and are shown in Figure 1.3. The ladder poly(pyrrolobenzothiazine) (LPBT) backbone featuring a hydrogenated pyrrole moiety showed modest p-type conductivity when doped with $FeCl_3$,[105] and promising performance in OECTs[98] that demonstrated the potential of this ladder backbone in electronic device applications. However, polymer chain topology studies were not reported, which complicates elucidating structure-property relationships since polymer chain topology directly impacts the electronic structure, thin film morphology, and ultimately performance in electronic devices.[30,75,77] In 2023, the pyrrolobenzothiazine ladder polymer featuring methylated (LPBT-Me) pyrrole groups was also reported.[42,114] Doping[114] and OECT device studies[42] showed that N-methylation can improve performance in organic electronics, although no intrinsic hole mobility or polymer chain topology information was reported.

1.4. Challenges and Objectives

Recent years have seen a resurgence of interest in π-conjugated ladder polymers because of the remarkable success of BBL over the past several decades. There are several challenges that need to be addressed in order to be able to rationally design new n-/p-type ladder polymers for organic electronics. Firstly, the synthetic method of choice must be able to form a fused ring ladder system

repeated reliably over tens or hundreds of times without incurring linear defects, branching, or crosslinking. This means that the monomers must be have excellent selectivity and efficiency in the reaction medium of choice. Additionally, the reaction medium must also be able to solubilize high molecular weight ladder polymers such that the polymer is not prematurely precipitated out of the reaction mixture. The only known example of such a system is demonstrated in the polycondensation of BBL. In this case, polyphosphoric acid (PPA) solubilizes very high molecular weight polymers (DP > 300), selectively phosphorylates the acid and amine groups of the tetrafunctionalized monomers which activates them for condensation,[115] and absorbs the water of condensation that shifts the equilibrium of the condensation towards the product.

Another major challenge is the inherent insolubility of ladder polymers that stems from their fused rigid backbones and strong intermolecular interactions. Adequate solubility of polymers in organic solvents is necessary in order to unambiguously characterize the molecular structure, elucidate defects in the backbone, and enable solution-phase processing for electronic device applications. The reported ladder polymers that have shown promise in organic electronic devices are selectively soluble in protic acids or as Lewis-acid complexes.[95] Creative workarounds must often be developed to enable characterization or processing in protic acids, which are often complicated and non-trivial. Furthermore, the strong aggregation tendencies and rigidity of ladder polymers means that the conformation and dynamics of ladder polymers in solution differ significantly from those of linear, semi-flexible polymers.[30,77] Therefore, solving the issue of solubility is not enough to allow characterization by standard techniques such as SEC, which is typically calibrated against polystyrene. As such, a variety of techniques have been used to analyze the molecular weight and chain conformation, all with varying effectiveness.[30]

As a result of these challenges, the development of new π-conjugated ladder polymers lags behind that of semi-flexible polymers, and the studies of ladder polymers in organic electronics are limited to reports of BBL and the few recently developed polymers previously discussed. To

understand the structure-property relationships of ladder polymers for organic electronic devices, new defect-free p-type and n-type ladder polymers must be developed.

The primary aim of my research is to synthesize both known and new n-/p-type π-conjugated ladder polymers using robust, metal-free, one-pot polycondensations with low synthetic complexity in order to study their fundamental structure-property relationships that govern performance in electronic devices. This objective will help address the current challenges in the field and will be implemented using three different approaches as outlined:

(i) Functionalizing and derivatizing BBL with electron-deficient monomers. One strategy to increase the molecular diversity of n-type semiconducting ladder polymers is to incorporate more electron-deficient building blocks in the backbone of the known polymer BBL. In Chapter 2, I report the polycondensation of a ladder polymer BBL-P, in which I replaced the benzene tetraamine with the electron-deficient phenazine tetraamine moiety. In Chapter 3, I describe the synthesis and comprehensive characterizations of two different series of random copolymers of BBL using both known and novel electron-deficient monomers. Detailed characterizations including electronic structure, optical properties, and field-effect electron mobility or n-doped electrical conductivities are described and compared to those of BBL. Information gained from these studies not only provide important insights into structure-property relationships of BBL and its derivatives, but also provides guidelines for designing and synthesizing new electron-deficient n-type ladder polymers for organic electronics.

(ii) N-alkyl side chain engineering of p-type ladder polymers. The unalkylated p-type ladder polymer LPBT featuring a pyrrolobenzothiazine backbone reported in 2022 showed potential in organic electronic devices, though the intrinsic charge transport properties and chain topology were not reported. In this study (Chapter 4), I synthesized and characterized a new methylated p-type ladder polymer LPBT-Me and compared its properties to those of LPBT. The small methyl group fostered stark changes in the electronic structure, optical properties, polymer

chain topology, and OFET charge carrier mobility. This study demonstrates the effects of alkylation and molecular disorder on the optical properties, thin film morphology, and charge transport properties of p-type ladder polymers.

(iii) Synthesis and studies of a new narrow bandgap p-type ladder polymer. There has been longstanding interest in narrowing the bandgap of semiconducting polymers to improve their photon harvesting capabilities and performance in optoelectronic devices such as solar cells and photodetectors. In Chapter 5, I discuss the design and synthesis of a new p-type ladder polymer ladder poly(thienobenzothiazine) (LTBT) and its model compound thienobis(benzothiazine) (TBBT). Single-crystal X-ray analysis of TBBT showed the model compound crystallizes into a planar topology. I discovered that incorporation of the thiophene into the benzothiazine backbone enabled a narrow optical bandgap of 1.28 eV, strong protonation-enhances intramolecular charge transfer character, and modest average electrical conductivities of (3.31 ± 0.31) x 10^{-1} S/cm when p-doped with $FeCl_3$.

1.5. References

1. Solak, E. K.; Irmak, E. Advances in Organic Photovoltaic Cells: A Comprehensive Review of Materials, Technologies, and Performance. *RSC Adv.* **2023**, *13* (18), 12244–12269. DOI: 10.1039/D3RA01454A.

2. Chen, L. X. Organic Solar Cells: Recent Progress and Challenges. *ACS Energy Lett.* **2019**, *4* (10), 2537–2539. DOI: 10.1021/acsenergylett.9b02071.

3. Li, Y.; Huang, W.; Zhao, D.; Wang, L.; Jiao, Z.; Huang, Q.; Wang, P.; Sun, M.; Yuan, G. Recent Progress in Organic Solar Cells: A Review on Materials from Acceptor to Donor. *Molecules* **2022**, *27* (6), 1800. DOI: 10.3390/molecules27061800.

4. Yao, Z.-F.; Wang, J.-Y.; Pei, J. High-Performance Polymer Field-Effect Transistors: From the Perspective of Multi-Level Microstructures. *Chem. Sci.* **2021**, *12* (4), 1193–1205. DOI: 10.1039/D0SC06497A.

5. Yang, J.; Zhao, Z.; Wang, S.; Guo, Y.; Liu, Y. Insight into High-Performance Conjugated Polymers for Organic Field-Effect Transistors. *Chem.* **2018**, *4* (12), 2748–2785. DOI: 10.1016/j.chempr.2018.08.005.

6. Liu, K.; Ouyang, B.; Guo, X.; Guo, Y.; Liu, Y. Advances in Flexible Organic Field-Effect Transistors and Their Applications for Flexible Electronics. *npj Flex. Electron* **2022**, *6* (1), 1–19. DOI: 10.1038/s41528-022-00133-3.

7. Yu, S.; Kousseff, C. J.; Nielsen, C. B. n-Type Semiconductors for Organic Electrochemical Transistor Applications. *Synth. Met.* **2023**, *293*, 117295. DOI: 10.1016/j.synthmet.2023.117295.

8. Marks, A.; Chen, X.; Wu, R.; Rashid, R. B.; Jin, W.; Paulsen, B. D.; Moser, M.; Ji, X.; Griggs, S.; Meli, D.; Wu, X.; Bristow, H.; Strzalka, J.; Gasparini, N.; Costantini, G.; Fabiano, S.; Rivnay, J.; McCulloch, I. Synthetic Nuances to Maximize N-Type Organic Electrochemical Transistor and Thermoelectric Performance in Fused Lactam Polymers. *J. Am. Chem. Soc.* **2022**. DOI: 10.1021/jacs.2c00735.

9. Zeglio, E.; Inganäs, O. Active Materials for Organic Electrochemical Transistors. *Adv. Mater.* **2018**, *30* (44), 1800941. DOI: 10.1002/adma.201800941.

10. Rivnay, J.; Inal, S.; Salleo, A.; Owens, R. M.; Berggren, M.; Malliaras, G. G. Organic Electrochemical Transistors. *Nat. Rev. Mater.* **2018**, *3* (2), 1–14. DOI:10.1038/natrevmats.2017.86.

11. Wu, H.-Y.; Yang, C.-Y.; Li, Q.; Kolhe, N. B.; Strakosas, X.; Stoeckel, M.-A.; Wu, Z.; Jin, W.; Savvakis, M.; Kroon, R.; Tu, D.; Woo, H. Y.; Berggren, M.; Jenekhe, S. A.; Fabiano, S. Influence of Molecular Weight on the Organic Electrochemical Transistor Performance of Ladder-Type Conjugated Polymers. *Adv. Mater.* **2011**, *34* (4), 2106235. DOI: 10.1002/adma.202106235.

12. Lee, S.; Kim, S.; Pathak, A.; Tripathi, A.; Qiao, T.; Lee, Y.; Lee, H.; Woo, H. Y. Recent Progress in Organic Thermoelectric Materials and Devices. *Macromol. Res.* **2020**, *28* (6), 531–552. DOI: 10.1007/s13233-020-8116-y.

13. Sun, Y.; Di, C.-A.; Xu, W.; Zhu, D. Advances in N-Type Organic Thermoelectric Materials and Devices. *Adv. Electron. Mater.* **2019**, *5* (11), 1800825. DOI: 10.1002/aelm.201800825.

14. Zhao, Y.; Liu, L.; Zhang, F.; Di, C.; Zhu, D. Advances in Organic Thermoelectric Materials and Devices for Smart Applications. *SmartMat.* **2021**, *2* (4), 426–445. DOI: 10.1002/smm2.1034.

15. Hong, G.; Gan, X.; Leonhardt, C.; Zhang, Z.; Seibert, J.; Busch, J. M.; Bräse, S. A Brief History of OLEDs—Emitter Development and Industry Milestones. *Adv. Mater.* **2021**, *33* (9), 2005630. DOI: 10.1002/adma.202005630.

16. Chen, S.; Feng, L.; Jia, T.; Jing, J.; Hu, Z.; Zhang, K.; Huang, F. High-Performance Polymer Solar Cells with Efficiency over 18% Enabled by Asymmetric Side Chain Engineering of Non-Fullerene Acceptors. *Sci. China Chem.* **2021**, *64* (7), 1192–1199. DOI: 10.1007/s11426-021-1013-0.

17. He, C.; Chen, Z.; Wang, T.; Shen, Z.; Li, Y.; Zhou, J.; Yu, J.; Fang, H.; Li, Y.; Li, S.; Lu, X.; Ma, W.; Gao, F.; Xie, Z.; Coropceanu, V.; Zhu, H.; Bredas, J.-L.; Zuo, L.; Chen, H. Asymmetric Electron Acceptor Enables Highly Luminescent Organic Solar Cells with Certified Efficiency over 18%. *Nat. Commun.* **2022**, *13* (1), 2598. DOI: 10.1038/s41467-022-30225-7.

18. Wu, Y.; Zhao, Y.; Liu, Y. Toward Efficient Charge Transport of Polymer-Based Organic Field-Effect Transistors: Molecular Design, Processing, and Functional Utilization. *Acc. Mater. Res.* **2021**, *2* (11), 1047–1058. DOI: 10.1021/accountsmr.1c00149.

19. Sirringhaus, H. 25th Anniversary Article: Organic Field-Effect Transistors: The Path Beyond Amorphous Silicon. *Adv. Mater.* **2014**, *26* (9), 1319–1335. DOI: 10.1002/adma.201304346.

20. Mei, J.; Diao, Y.; Appleton, A. L.; Fang, L.; Bao, Z. Integrated Materials Design of Organic Semiconductors for Field-Effect Transistors. *J. Am. Chem. Soc.* **2013**, *135* (18), 6724–6746. DOI: 10.1021/ja400881n.

21. Babel, A.; Jenekhe, S. A. High Electron Mobility in Ladder Polymer Field-Effect Transistors. *J. Am. Chem. Soc.* **2003**, *125* (45), 13656–13657. DOI: 10.1021/ja0371810.

22. Griggs, S.; Marks, A.; Bristow, H.; McCulloch, I. N-Type Organic Semiconducting Polymers: Stability Limitations, Design Considerations and Applications. *J. Mater. Chem. C* **2021**, *9* (26), 8099–8128. DOI: 10.1039/D1TC02048J.

23. Kim, M.; Ryu, S. U.; Park, S. A.; Choi, K.; Kim, T.; Chung, D.; Park, T. Donor–Acceptor-Conjugated Polymer for High-Performance Organic Field-Effect Transistors: A Progress Report. *Adv. Funct. Mater.* **2020**, *30* (20), 1904545. DOI: 10.1002/adfm.201904545.

24. Fratini, S.; Nikolka, M.; Salleo, A.; Schweicher, G.; Sirringhaus, H. Charge Transport in High-Mobility Conjugated Polymers and Molecular Semiconductors. *Nat. Mater.* **2020**, *19* (5), 491–502. DOI: 10.1038/s41563-020-0647-2.

25. Babel, A.; Jenekhe, S. Electron Transport in Thin-Film Transistors From an n-Type Conjugated Polymer. *Adv. Mater.* **2002**, *14* (5), 371–374. DOI: 10.1002/1521-4095(20020304)14:5<371::AID-ADMA371>3.0.CO;2-5.

26. Chen, S. E.; Flagg, L. Q.; Onorato, J. W.; Richter, L. J.; Guo, J.; Luscombe, C. K.; Ginger, D. S. Impact of Varying Side Chain Structure on Organic Electrochemical Transistor Performance: A Series of Oligoethylene Glycol-Substituted Polythiophenes. *J. Mater. Chem. A* **2022**, *10* (19), 10738–10749. DOI: 10.1039/D2TA00683A.

27. Feng, K.; Guo, H.; Wang, J.; Shi, Y.; Wu, Z.; Su, M.; Zhang, X.; Son, J. H.; Woo, H. Y.; Guo, X. Cyano-Functionalized Bithiophene Imide-Based n-Type Polymer Semiconductors: Synthesis, Structure–Property Correlations, and Thermoelectric Performance. *J. Am. Chem. Soc.* **2021**, *143* (3), 1539–1552. DOI: 10.1021/jacs.0c11608.

28. Shirakawa, H.; Louis, E. J.; MacDiarmid, A. G.; Chiang, C. K.; Heeger, A. J. Synthesis of Electrically Conducting Organic Polymers: Halogen Derivatives of Polyacetylene, (CH)x. *J. Chem. Soc., Chem. Commun.* **1977**,16, 578–580. DOI: 10.1039/C39770000578.

29. Chiang, C. K.; Fincher, C. R.; Park, Y. W.; Heeger, A. J.; Shirakawa, H.; Louis, E. J.; Gau, S. C.; MacDiarmid, A. G. Electrical Conductivity in Doped Polyacetylene. *Phys. Rev. Lett.* **1977**, *39* (17), 1098–1101. DOI: 10.1103/PhysRevLett.39.1098.

30. Lee, J.; Kalin, A. J.; Yuan, T.; Al-Hashimi, M.; Fang, L. Fully Conjugated Ladder Polymers. *Chem. Sci.* **2017**, *8* (4), 2503–2521. DOI: 10.1039/c7sc00154a.

31. Kim, F. S.; Park, C. H.; Na, Y.; Jenekhe, S. A. Effects of Ladder Structure on the Electronic Properties and Field-Effect Transistor Performance of Poly(Benzobisimidazobenzophenanthroline). *Org. Electron.* **2019**, *69*, 301–307. DOI: 10.1016/j.orgel.2019.03.049.

32. Scherf, U. Ladder-Type Materials. *J. Mater. Chem.* **1999**, *9* (9), 1853–1864. DOI: 10.1039/a900447e.

33. Huang, H.; Yang, L.; Facchetti, A.; Marks, T. J. Organic and Polymeric Semiconductors Enhanced by Noncovalent Conformational Locks. *Chem. Rev.* **2017**, *117* (15), 10291–10318. DOI: 10.1021/acs.chemrev.7b00084.

34. Liu, B.; Rocca, D.; Yan, H.; Pan, D. Beyond Conformational Control: Effects of Noncovalent Interactions on Molecular Electronic Properties of Conjugated Polymers. *JACS Au* **2021**, *1* (12), 2182–2187. DOI: 10.1021/jacsau.1c00284.

35. Brédas, J. L. Relationship Between Band Gap and Bond Length Alternation in Organic Conjugated Polymers. *J. Chem. Phys.* **1985**, *82* (8), 3808–3811. DOI: 10.1063/1.448868.

36. Kawabata, K.; Saito, M.; Osaka, I.; Takimiya, K. Very Small Bandgap π-Conjugated Polymers with Extended Thienoquinoids. *J. Am. Chem. Soc.* **2016**, *138* (24), 7725–7732. DOI: 10.1021/jacs.6b03688.

37. Kim, Y.; Kim, Y.-J.; Kim, Y.-A.; Jung, E.; Mok, Y.; Kim, K.; Hwang, H.; Park, J.-J.; Kim, M.-G.; Mathur, S.; Kim, D.-Y. Open-Shell and Closed-Shell Quinoid–Aromatic Conjugated Polymers: Unusual Spin Magnetic and High Charge Transport Properties. *ACS Appl. Mater. Interfaces* **2021**, *13* (2), 2887–2898. DOI: 10.1021/acsami.0c15893.

38. Jenekhe, S. A.; Lu, L.; Alam, M. M. New Conjugated Polymers with Donor−Acceptor Architectures: Synthesis and Photophysics of Carbazole−Quinoline and Phenothiazine−Quinoline Copolymers and Oligomers Exhibiting Large Intramolecular Charge Transfer. *Macromolecules* **2001**, *34* (21), 7315–7324. DOI: 10.1021/ma0100448.

39. Zhu, Y.; Champion, R. D.; Jenekhe, S. A. Conjugated Donor−Acceptor Copolymer Semiconductors with Large Intramolecular Charge Transfer: Synthesis, Optical Properties, Electrochemistry, and Field Effect Carrier Mobility of Thienopyrazine-Based Copolymers. *Macromolecules* **2006**, *39* (25), 8712–8719. DOI: 10.1021/ma061861g.

40. Zhu, P.; Fan, B.; Ying, L.; Huang, F.; Cao, Y. Recent Progress in All-Polymer Solar Cells Based on Wide-Bandgap p-Type Polymers. *Chem. Asian. J.* **2019**, *14* (18), 3109–3118. DOI: 10.1002/asia.201900827.

41. Chen, X.; Jenekhe, S. Bipolar Conducting Polymers: Blends of p-Type Polypyrrole and an n-Type Ladder Polymer. *Macromolecules* **1997**, *30* (6), 1728–1733. DOI: 10.1021/ma961121f.

42. Wu, H.-Y.; Huang, J.-D.; Jeong, S. Y.; Liu, T.; Wu, Z.; Pol, T. van der; Wang, Q.; Stoeckel, M.-A.; Li, Q.; Fahlman, M.; Tu, D.; Woo, H. Y.; Yang, C.-Y.; Fabiano, S. Stable Organic Electrochemical Neurons Based on P-Type and n-Type Ladder Polymers. *Mater. Horiz.* **2023**. 10, 4213-4223. DOI:10.1039/D3MH00858D.

43. Liao, M.; Duan, J.; Peng, P.; Zhang, J.; Zhou, M. Progress in the Synthesis of Imide-Based n-Type Polymer Semiconductor Materials. *RCS Adv.* **2020**, *10* (68), 41764–41779. DOI: 10.1039/D0RA04972G.

44. Sun, H.; Guo, X.; Facchetti, A. High-Performance n-Type Polymer Semiconductors: Applications, Recent Development, and Challenges. *Chem.* **2020**, *6* (6), 1310–1326. DOI: 10.1016/j.chempr.2020.05.012.

45. Kolhe, N. B.; West, S. M.; Tran, D. K.; Ding, X.; Kuzuhara, D.; Yoshimoto, N.; Koganezawa, T.; Jenekhe, S. A. Designing High Performance Nonfullerene Electron Acceptors with Rylene Imides for Efficient Organic Photovoltaics. *Chem. Mater.* **2019**, *32* (1), 195-204. DOI: 10.1021/acs.chemmater.9b03329.

46. Babel, A.; Wind, J.; Jenekhe, S. A. Ambipolar Charge Transport in Air-Stable Polymer Blend Thin-Film Transistors. *Adv. Funct. Mater.* **2004**, *14* (9), 891–898. DOI: 10.1002/adfm.200305180.

47. Chen, X. L.; Bao, Z.; Schön, J. H.; Lovinger, A. J.; Lin, Y.-Y.; Crone, B.; Dodabalapur, A.; Batlogg, B. Ion-Modulated Ambipolar Electrical Conduction in Thin-Film Transistors Based on Amorphous Conjugated Polymers. *Appl. Phys. Lett.* **2001**, *78* (2), 228–230. DOI: 10.1063/1.1339849.

48. Babel, A.; Zhu, Y.; Cheng, K.; Chen, W.; Jenekhe, S. A. High Electron Mobility and Ambipolar Charge Transport in Binary Blends of Donor and Acceptor Conjugated Polymers. *Adv. Funct. Mater.* **2007**, *17* (14), 2542–2549. DOI: 10.1002/adfm.200600312.

49. Ortiz, R. P.; Herrera, H.; Seoane, C.; Segura, J. L.; Facchetti, A.; Marks, T. J. Rational Design of Ambipolar Organic Semiconductors: Is Core Planarity Central to Ambipolarity in Thiophene–Naphthalene Semiconductors? *Eur. J. Chem.* **2012**, *18* (2), 532–543. DOI: 10.1002/chem.201101715.

50. Fan, J.; Yuen, J. D.; Wang, M.; Seifter, J.; Seo, J.-H.; Mohebbi, A. R.; Zakhidov, D.; Heeger, A.; Wudl, F. High-Performance Ambipolar Transistors and Inverters from an Ultralow Bandgap Polymer. *Adv. Mater.* **2012**, *24* (16), 2186–2190. DOI: 10.1002/adma.201103836.

51. Briseno, A.; Kim, F.; Babel, A.; Xia, Y.; Jenekhe, S. A. n-Channel Polymer Thin Film Transistors with Long-Term Air-Stability and Durability and Their Use in Complementary Inverters. *J. Mater. Chem.* **2011**, *21* (41), 16461–16466. DOI: 10.1039/c1jm12953h.

52. Lu, S.; Li, F.; Zhang, K.; Zhu, J.; Cui, W.; Yang, R.; Yu, L.; Sun, M. Halogenation on Terminal Groups of ITIC Based Electron Acceptors as an Effective Strategy for Efficient Polymer Solar Cells. *Sol. Energy* **2020**, *195*, 429–435. DOI: 10.1016/j.solener.2019.11.074.

53. Lai, H.; Chen, H.; Zhou, J.; Qu, J.; Wang, M.; Xie, W.; Xie, Z.; He, F. 3D Interpenetrating Network for High-Performance Nonfullerene Acceptors via Asymmetric Chlorine Substitution. *J. Phys. Chem. Lett.* **2019**, *10* (16), 4737–4743. DOI: 10.1021/acs.jpclett.9b01931.

54. He, Q.; Tam, D.; T. L.; Lin, T.; Chien, S. W.; Lin, M.; Meng, H.; Huang, W.; Xu, J. π-Extended Poly(Benzimidazoanthradiisoquinolinedione) Ladder-Type Conjugated Polymer. *ACS Macro. Lett.* **2022**, *11* (9), 1136–1141. DOI: 10.1021/acsmacrolett.2c00438.

55. He, Q.; Zhang, X.; Tam, T. L. D.; Wang, J.; Chen, H.; Chien, S. W.; Tham, N. N.; Koh, X. Q.; Lee, J. J. C.; Lin, M.; Soh, P. X.; Meng, H.; Huang, W.; Xu, J. Balancing Solubility and Thermoelectric Performance in π-Extended Poly(Benzimidazoanthradiisoquinolinedione) Ladder-Type Conjugated Polymer. *ACS Appl. Electron. Mater.* **2023**. DOI: 10.1021/acsaelm.3c00294.

56. Weitz, R. T.; Amsharov, K.; Zschieschang, U.; Villas, E. B.; Goswami, D. K.; Burghard, M.; Dosch, H.; Jansen, M.; Kern, K.; Klauk, H. Organic n-Channel Transistors Based on Core-Cyanated Perylene Carboxylic Diimide Derivatives. *J. Am. Chem. Soc.* **2008**, *130* (14), 4637–4645. DOI: 10.1021/ja074675e.

57. Yang, L.; Xiao, C.; Jiang, W.; Wang, Z. Conjugated Donor-Acceptor Copolymers from Dicyanated Naphthalene Diimide. *Tetrahedron* **2014**, *70* (36), 6265–6270. DOI: 10.1016/j.tet.2014.04.002.

58. Yang, M.; Tan, X.; Yin, B.; Kim, S.; Pang, S.; Chen, Z.; Yang, X.; Yang, C.; Liu, Z.; Duan, C. Near-Infrared Electron Acceptors with Cyano-Substituted 2-(3-Oxo-2,3-Dihydroinden-1-Ylidene)Malononitrile End-Groups for Organic Solar Cells. *ACS Energy Lett.* **2023**, *8* (6), 2641–2651. DOI: 10.1021/acsenergylett.3c00664.

59. Karpov, Y.; Erdmann, T.; Stamm, M.; Lappan, U.; Guskova, O.; Malanin, M.; Raguzin, I.; Beryozkina, T.; Bakulev, V.; Günther, F.; Gemming, S.; Seifert, G.; Hambsch, M.; Mannsfeld, S.; Voit, B.; Kiriy, A. Molecular Doping of a High Mobility Diketopyrrolopyrrole–Dithienylthieno[3,2-b]Thiophene Donor–Acceptor Copolymer with F6TCNNQ. *Macromolecules* **2017**, *50* (3), 914–926. DOI: 10.1021/acs.macromol.6b02452.

60. Ray, S.; Sharma, S.; Salzner, U.; Patil, S. Synthesis and Characterization of Quinoidal Diketopyrrolopyrrole Derivatives with Exceptionally High Electron Affinities. *J. Phys. Chem. C* **2017**, *121* (30), 16088–16097. DOI: /10.1021/acs.jpcc.7b04085.

61. Zhao, X.; Cai, H.; Deng, Y.; Jiang, Y.; Wang, Z.; Shi, Y.; Han, Y.; Geng, Y. Low-Band Gap Conjugated Polymers with Strong Absorption in the Second Near-Infrared Region Based on Diketopyrrolopyrrole-Containing Quinoidal Units. *Macromolecules* **2021**, *54* (7), 3498-3506. DOI: 10.1021/acs.macromol.1c00124.

62. Chen, S.; Zhao, Y.; Bolag, A.; Nishida, J.; Liu, Y.; Yamashita, Y. Solution-Processed and Air-Stable n-Type Organic Thin-Film Transistors Based on Thiophene-Fused Dicyanoquinonediimine (DCNQI) Deriatives. *ACS Appl. Mater. Interfaces* **2012**, *4* (8), 3994–4000. DOI: 10.1021/am300822z.

63. Yang, C. J.; Jenekhe, S. A. Conjugated Aromatic Polyimines. 2. Synthesis, Structure, and Properties of New Aromatic Polyazomethines. *Macromolecules* **1995**, *28* (4), 1180–1196. DOI: 10.1021/ma00108a054.

64. Zhang, Q. T.; Tour, J. M. Imine-Bridged Planar Poly(Phenylenethiophene)s and Polythiophenes. *J. Am. Chem. Soc.* **1997**, *119* (41), 9624–9631. DOI: 10.1021/ja964223u.

65. Scott, W. J.; Stille, J. K. Palladium-Catalyzed Coupling of Vinyl Triflates with Organostannanes. Synthetic and Mechanistic Studies. *J. Am. Chem. Soc.* **1986**, *108* (11), 3033–3040. DOI: 10.1021/ja00271a037.

66. Carsten, B.; He, F.; Son, H. J.; Xu, T.; Yu, L. Stille Polycondensation for Synthesis of Functional Materials. *Chem. Rev.* **2011**, *111* (3), 1493–1528. DOI: /10.1021/cr100320w.

67. Miyaura, Norio.; Suzuki, Akira. Palladium-Catalyzed Cross-Coupling Reactions of Organoboron Compounds. *Chem. Rev.* **1995**, *95* (7), 2457–2483. DOI: 10.1021/cr00039a007.

68. Farhang, M.; Akbarzadeh, A. R.; Rabbani, M.; Ghadiri, A. M. A Retrospective-Prospective Review of Suzuki–Miyaura Reaction: From Cross-Coupling Reaction to Pharmaceutical Industry Applications. *Polyhedron* **2022**, *227*, 116124. DOI: 10.1016/j.poly.2022.116124.

69. Negishi, E.; Baba, S. Novel Stereoselective Alkenyl–Aryl Coupling via Nickel-Catalysed Reaction of Alkenylanes with Aryl Halides. *J. Chem. Soc., Chem. Commun.* **1976**, 15, 596b–597b. DOI: 10.1039/C3976000596B.

70. Haas, D.; Hammann, J. M.; Greiner, R.; Knochel, P. Recent Developments in Negishi Cross-Coupling Reactions. *ACS Catal.* **2016**, *6* (3), 1540–1552. DOI: 10.1021/acscatal.5b02718.

71. Guo, Y.; Yang, X.; Wang, L.; Duan, J.; Zhou, Y.; Nielsen, C. B.; Yu, Y.; Yang, J.; Guo, Y.; Li, Z.; Yue, W.; Liu, Y.; McCulloch, I. Aldol Polymerization to Construct Half-Fused Semiconducting Polymers. *Macromolecules* **2021**, *54* (22), 10312-10320. DOI: 10.1021/acs.macromol.1c01740.

72. Onwubiko, A.; Yue, W.; Jellett, C.; Xiao, M.; Chen, H.-Y.; Ravva, M. K.; Hanifi, D. A.; Knall, A.-C.; Purushothaman, B.; Nikolka, M.; Flores, J.-C.; Salleo, A.; Bredas, J.-L.; Sirringhaus, H.; Hayoz, P.; McCulloch, I. Fused Electron Deficient Semiconducting Polymers for Air Stable Electron Transport. *Nat. Commun.* **2018**, *9* (1), 416. DOI: 10.1038/s41467-018-02852-6.

73. Holliday, S.; Donaghey, J. E.; McCulloch, I. Advances in Charge Carrier Mobilities of Semiconducting Polymers Used in Organic Transistors. *Chem. Mater.* **2014**, *26* (1), 647–663. DOI: 10.1021/cm402421p.

74. Dalton, T.; Faber, T.; Glorius, F. C–H Activation: Toward Sustainability and Applications. *ACS Cent. Sci.* **2021**, *7* (2), 245–261. DOI: 10.1021/acscentsci.0c01413.

75. K. Tran, D.; Robitaille, A.; Jo Hai, I.; Ding, X.; Kuzuhara, D.; Koganezawa, T.; Chiu, Y.-C.; Leclerc, M.; A. Jenekhe, S. Elucidating the Impact of Molecular Weight on Morphology, Charge Transport, Photophysics and Performance of All-Polymer Solar Cells. *J. Mater. Chem. A* **2020**, *8* (40), 21070–21083. DOI: 10.1039/D0TA08195G.

76. Tran, D. K.; West, S. M.; Guo, J.; Chen, S. E.; Ginger, D. S.; Jenekhe, S. A. Chain Length Dependence of Electron Transport in an N-Type Conjugated Polymer with a Rigid-Rod Chain Topology. *J. Am. Chem. Soc.* **2024**. *146* (2), 1435-1446. DOI: 10.1021/jacs.3c10650.

77. Cao, Z.; Leng, M.; Cao, Y.; Gu, X.; Fang, L. How Rigid Are Conjugated Non-Ladder and Ladder Polymers? *J. Polym. Sci.* **2022**, *60* (3), 298.DOI: 10.1002/pol.20210550.

78. Lee, J. Recent Progress in Synthesis of Conjugated Ladder Polymers. *Asian J. Org. Chem.* **2023**, 12, e202300104. DOI: 10.1002/ajoc.202300104.

79. Nijegorodov, N.; Luhanga, P. V. C.; Nkoma, J. S.; Winkoun, D. P. The Influence of Planarity, Rigidity and Internal Heavy Atom Upon Fluorescence Parameters and the Intersystem Crossing Rate Constant in Molecules with the Biphenyl Basis. *Spectrochim. Acta A Mol. Biomol. Spectrosc.* **2006**, *64* (1), 1–5. DOI: 10.1016/j.saa.2005.06.032.

80. Wedler, S.; Bourdick, A.; Athanasopoulos, S.; Gekle, S.; Panzer, F.; McDowell, C.; Nguyen, T.-Q.; Bazan, G. C.; Köhler, A. What Is the Role of Planarity and Torsional Freedom for Aggregation in a π-Conjugated Donor–Acceptor Model Oligomer? *J. Mater. Chem. C* **2020**, *8* (14), 4944–4955. DOI: 10.1039/D0TC00217H.

81. Nagao, Y.; Hirata, T.; Goto, S.; Sano, S.; Kakehi, A.; Iizuka, K.; Shiro, M. Intramolecular Nonbonded S···O Interaction Recognized in (Acylimino)Thiadiazoline Derivatives as Angiotensin II Receptor Antagonists and Related Compounds. *J. Am. Chem. Soc.* **1998**, *120* (13), 3104–3110. DOI: 10.1021/ja973109o.

82. Guo, X.; Quinn, J.; Chen, Z.; Usta, H.; Zheng, Y.; Xia, Y.; Hennek, J. W.; Ortiz, R. P.; Marks, T. J.; Facchetti, A. Dialkoxybithiazole: A New Building Block for Head-to-Head Polymer Semiconductors. *J. Am. Chem. Soc.* **2013**, *135* (5), 1986–1996. DOI: 10.1021/ja3120532.

83. Meille, S. V.; Farina, A.; Bezziccheri, F.; Gallazzi, M. C. The Influence of Alkoxy Side Chains on the Conformational Flexibility of Oligo- and Polythiophenes. *Adv. Mater.* **1994**, *6* (11), 848–851. DOI: 10.1002/adma.19940061109.

84. Larsen, S.; Wätjen, F.; Niinistö, L.; Tuhtar, D.; Sjöblom, J.; Strand, T. G.; Sukhoverkhov, V. F. The Crystal and Molecular Structures of Tyrian Purple (6,6'-Dibromoindigotin) and 2,2'-Dimethoxyindigotin. *Acta Chem. Scand.* **1980**, *34a*, 171–176. DOI: 10.3891/acta.chem.scand.34a-0171.

85. Głowacki, E. D.; Leonat, L.; Voss, G.; Bodea, M.-A.; Bozkurt, Z.; Ramil, A. M.; Irimia-Vladu, M.; Bauer, S.; Sariciftci, N. S. Ambipolar Organic Field Effect Transistors and Inverters with the Natural Material Tyrian Purple. *AIP Advances* **2011**, *1* (4), 042132. DOI: 10.1063/1.3660358.

86. Irimia-Vladu, M.; Głowacki, E. D.; Troshin, P. A.; Schwabegger, G.; Leonat, L.; Susarova, D. K.; Krystal, O.; Ullah, M.; Kanbur, Y.; Bodea, M. A.; Razumov, V. F.; Sitter, H.; Bauer, S.; Sariciftci, N. S. Indigo - A Natural Pigment for High Performance Ambipolar Organic Field Effect Transistors and Circuits. *Adv. Mater.* **2012**, *24* (3), 375–380. DOI: 10.1002/adma.201102619.

87. Li, Y.; Sonar, P.; Murphy, L.; Hong, W. High Mobility Diketopyrrolopyrrole (DPP)-Based Organic Semiconductor Materials for Organic Thin Film Transistors and Photovoltaics. *Energy Environ. Sci.* **2013**, *6* (6), 1684–1710. DOI: 10.1039/C3EE00015J.

88. Yi, Z.; Wang, S.; Liu, Y. Design of High-Mobility Diketopyrrolopyrrole-Based π-Conjugated Copolymers for Organic Thin-Film Transistors. *Adv. Mater.* **2015**, *27* (24), 3589–3606. DOI: 10.1002/adma.201500401.

89. Fazzi, D.; Negri, F. Addressing the Elusive Polaronic Nature of Multiple Redox States in a π-Conjugated Ladder-Type Polymer. *Adv. Electron. Mater.* **2021**, *7* (1), 2000786. DOI: 10.1002/aelm.202000786.

90. Fazzi, D.; Fabiano, S.; Ruoko, T.; Meerholz, K.; Negri, F. Polarons in Pi-Conjugated Ladder-Type Polymers: A Broken Symmetry Density Functional Description. *J. Mater. Chem. C* **2019**, *7* (41), 12876–12885. DOI: 10.1039/c9tc03283e.

91. Ghosh, S.; Berggren, M.; Zozoulenko, I. Electronic Structures and Optical Properties of P-Type/n-Type Polymer Blend: A Density Functional Theory Study. *J. Phys. Chem. C.* **2020,** *124* (17), 9203-9214. DOI: 10.1021/acs.jppc.0c01336.

92. Deusen, R. L. V. Benzimidazo-Benzophenanthroline Polymers. *J. Polym. Sci. B Polym. Lett.* **1966**, *4* (3), 211–214. DOI: 10.1002/pol.1966.110040310.

93. Arnold, F. E.; Van Deusen, R. L. Preparation and Properties of High Molecular Weight, Soluble Oxobenz[de]Imidazobenzimidazoisoquinoline Ladder Polymer. *Macromolecules* **1969**, *2* (5), 497–502. DOI: 10.1021/ma60011a009.

94. Berry, G. C.; Yen, S. P. Structure and Properties of a Heterocyclic Polymer. *Addition and Condensation Polymerization Processes*. **1969**, 734–756. DOI: 10.1021/ba-1969-0091.ch048.

95. Roberts, M. F.; Jenekhe, S. A. Lewis-Acid Coordination-Complexes of Polymers .3. Poly(Benzimidazobenzophenanthroline) Ladder and Semiladder Polymers. *Polymer* **1994**, *35* (20), 4313–4325. DOI: 10.1016/0032-3861(94)90088-4.

96. Jenekhe, S. A.; Johnson, P. O. Complexation-Mediated Solubilization and Processing of Rigid-Chain and Ladder Polymers in Aprotic Organic Solvents. *Macromolecules* **1990**, *23* (20), 4419–4429. DOI: 10.1021/ma00222a015.

97. Alam, M. M.; Jenekhe, S. A. Efficient Solar Cells from Layered Nanostructures of Donor and Acceptor Conjugated Polymers. *Chem. Mater.* **2004**, *16* (23), 4647–4656. DOI: 10.1021/cm0497069.

98. He, Q.; Tam, T. L. D.; Koh, X. Q.; Tham, N. N.; Meng, H.; Huang, W.; Xu, J. P- and N-Dopable Ambipolar Bulk Heterojunction Thermoelectrics Based on Ladder-Type Conjugated Polymers. *J. Mater. Chem. C* **2022**, *11* (1), 204–210. DOI: 10.1039/D2TC03684C.

99. Hickl, P.; Ballauff, M.; Scherf, U.; Müllen, K.; Lindner, P. Characterization of a Ladder Polymer by Small-Angle X-Ray and Neutron Scattering. *Macromolecules* **1997**, *30* (2), 273–279. DOI: 10.1021/ma961038s.

100. Stille, J. K.; Mainen, E. L. Thermally Stable Ladder Polyquinoxalines. *Macromolecules* **1968**, *1* (1), 36–42. DOI: 10.1021/ma60001a007.

101. Stille, J. K.; Williamson, J. R. Polyquinoxalines. *J. Polym. Sci. A.* **1964**, *2* (9), 3867–3875. DOI: 10.1002/pol.1964.100020904.

102. Kim, O.-K. Electrical Conductivity of Heteroaromatic Ladder Polymers. 3. Phenothiazine and the Structurally Related Ladder Polymers. *J. Polym. Sci. Polym. Lett. Ed.* **1985**, *23* (3), 137–139. DOI: 10.1002/pol.1985.130230303.

103. Berry, G. C. Properties of an Optically Anisotropic Heterocyclic Ladder Polymer (BBL) in Dilute Solution. *J. Polym. Sci. Polym. Symp.* **1978**, *65* (1), 143–172. DOI: 10.1002/polc.5070650115.

104. Wolfe, J. F.; Loo, B. H.; Arnold, F. E. Rigid-Rod Polymers. 2. Synthesis and Thermal Properties of Para-Aromatic Polymers with 2,6-Benzobisthiazole Units in the Main Chain. *Macromolecules* **1981**, *14* (4), 915–920. DOI: 10.1021/ma50005a005.

105. Tam, T. L. D.; Lin, M.; Chien, S. W.; Xu, J. Facile Synthesis of Solubilizing a Group-Free, Solution-Processable p-Type Ladder Conjugated Polymer and Its Thermoelectric Properties. *ACS Macr. Lett.* **2022**, *11* (1), 110–115. DOI: 10.1021/acsmacrolett.1c00696.

106. Scherf, U.; Müllen, K. Polyarylenes and Poly(Arylenevinylenes), 7. A Soluble Ladder Polymer via Bridging of Functionalized Poly(p-Phenylene)-Precursors. *Makromol. Chem, Rapid Commun.* **1991**, *12* (8), 489–497. DOI: 10.1002/marc.1991.030120806.

107. Durban, M. M.; Kazarinoff, P. D.; Segawa, Y.; Luscombe, C. K. Synthesis and Characterization of Solution-Processable Ladderized n-Type Naphthalene Bisimide Copolymers for OFET Applications. *Macromolecules* **2011**, *44* (12), 4721–4728. DOI: 10.1021/ma2004822.

108. Cowan, S. R.; Leong, W. L.; Banerji, N.; Dennler, G.; Heeger, A. J. Identifying a Threshold Impurity Level for Organic Solar Cells: Enhanced First-Order Recombination Via Well-Defined PC84BM Traps in Organic Bulk Heterojunction Solar Cells. *Adv. Funct. Mater.* **2011**, *21* (16), 3083–3092. DOI: 10.1002/adfm.201100514.

109. Ashraf, R. S.; Schroeder, B. C.; Bronstein, H. A.; Huang, Z.; Thomas, S.; Kline, R. J.; Brabec, C. J.; Rannou, P.; Anthopoulos, T. D.; Durrant, J. R.; McCulloch, I. The Influence of Polymer Purification on Photovoltaic Device Performance of a Series of Indacenodithiophene Donor Polymers. *Adv. Mater.* **2013**, *25* (14), 2029–2034. DOI: 10.1002/adma.201300027.

110. Simatos, D.; Jacobs, I. E.; Dobryden, I.; Nguyen, M.; Savva, A.; Venkateshvaran, D.; Nikolka, M.; Charmet, J.; Spalek, L. J.; Gicevičius, M.; Zhang, Y.; Schweicher, G.; Howe, D. J.; Ursel, S.; Armitage, J.; Dimov, I. B.; Kraft, U.; Zhang, W.; Alsufyani, M.; McCulloch, I.; Owens, R. M.; Claesson, P. M.; Knowles, T. P. J.; Sirringhaus, H. Effects of Processing-Induced Contamination on Organic Electronic Devices. *Small Methods* **2023**, 7, 2300476. DOI: 10.1002/smtd.202300476.

111. Wilbourn, K.; Murray, R. W. The Electrochemical Doping Reactions of the Conducting Ladder Polymer Benzimidazobenzophenanthroline (BBL). *Macromolecules* **1988**, *21* (1), 89–96. DOI: 10.1021/ma00179a019.

112. West, S. M.; Tran, D. K.; Guo, J.; Chen, S. E.; Ginger, D. S.; Jenekhe, S. A. Phenazine-Substituted Poly(Benzimidazobenzophenanthrolinedione): Electronic Structure, Thin Film Morphology, Electron Transport, and Mechanical Properties of an n-Type Semiconducting Ladder Polymer. *Macromolecules* **2023**, *56* (5), 2081-2091. DOI: 10.1021/acs.macromol.2c01999.

113. Sicree, A. J.; Arnold, F. E.; Deusen, R. L. V. New Imidazoisoquinoline Ladder Polymers. *J. Polym. Sci. Polym. Chem.* **1974**, *12* (2), 265–272. DOI: 10.1002/pol.1974.170120202.

114. He, Q.; Wang, J.; Dexter Tam, T. L.; Zhang, X.; Jiang, Z.; Chien, S. W.; Tham, N. N.; Koh, X. Q.; Soh, P. X.; Meng, H.; Huang, W.; Xu, J. Thermoelectric Performance Enhancement of P-Type Pyrrolo[3,2-b:4,5-B′]Bis[1,4]Benzothiazine Conjugated Ladder Polymer by Pendant Group Engineering. *ACS Materials Lett.* **2023**, *5* (10), 2829–2835. DOI: 10.1021/acsmaterialslett.3c00758.

115. Krongauz, E. S.; Rusanov, A. L.; Renard, T. L. Polyphosphoric Acid in Cyclisation and Polycyclisation Reactions. *Russ. Chem. Rev.* **1970**, *39* (9), 747–765. DOI: 10.1070/RC1970v039n09ABEH002020.

Chapter 2. Phenazine-Substituted Poly(benzimidazobenzophenanthrolinedione): Electronic Structure, Thin Film Morphology, Electron Transport, and Mechanical Properties of an n-Type Semiconducting Ladder Polymer

2.1 Introduction

By virtue of their double-stranded or all-polycyclic architectures, π-conjugated ladder polymers have an ideal persistent ribbon-like conformation that is free of torsional disorders. They are thus promising for applications in organic electronics and optoelectronics as well as for basic understanding of structure-property relationships in semiconducting polymers. Among the most widely studied π-conjugated ladder polymers is the prototype *n-type* semiconducting polymer, ladder poly(benzimidazobenzophenanthroline) (BBL) (Chart 2.1).[1] Although first synthesized in 1966 by Van Deusen,[1] more than a decade before the discovery of doped conducting polymers in 1977,[2] the early chemical,[3] electrochemical,[4] and ion-implantation doping[5–7] of BBL to the highly conducting state were reported in the 1980s. Our group reported the n-type semiconducting charge transport properties of BBL in 2002,[8–10] leading to the demonstration of this ladder polymer as the first conjugated polymer-based high-performance, n-channel field-effect transistors (OFETs).[11] The n-type semiconducting properties of BBL have since been extensively investigated and successfully used in various device applications including organic photovoltaics (OPVs),[12,13] organic electrochemical transistors (OECTs),[14–16] OFETs,[8,17–19] organic thermoelectrics,[20–22] and supercapacitors.[23] Recently, ground-state charge transfer between neutral BBL and a neutral polythiophene derivative was observed, resulting in highly conducting polymer blend films without external doping.[24] However, unlike other classes

of n-type conjugated polymers such as perylene diimides,[25,26] naphthalene diimides,[27,28] and other arylene diimides[29–32] with numerous derivatives that enable understanding of structure-property relationships, very few derivatives of BBL have been reported.[33–37] Furthermore, very little is known about the electronic structure and properties of the few known BBL derivatives.

Chart 2.1. Molecular structures of π-conjugated ladder polymers BBL and BBL-P.

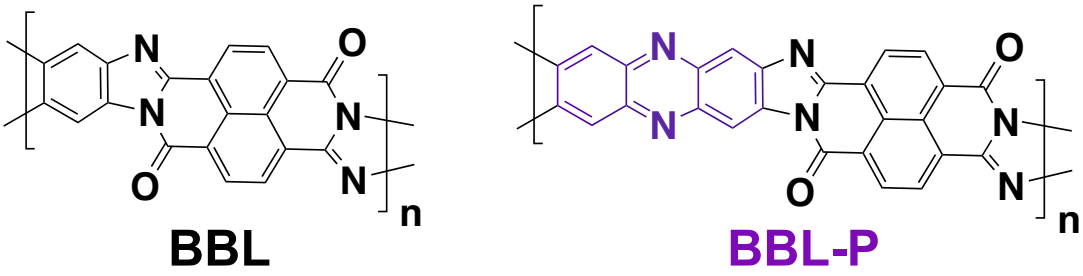

One intriguing derivative of BBL is the phenazine-substituted ladder polymer BBL-P, whose molecular structure is shown in Chart 2.1. Its synthesis was reported in 1974 in the context of thermally stable polymers for aerospace applications.[34] However, the electronic structure, field-effect charge transport and other physical properties of BBL-P have not been reported heretofore. Phenazine as a molecular building block has appealing features. The reduction potential of phenazine ($E_{1/2}$ = -1.19 V vs. SCE) is over 2 V more positive than benzene ($E_{1/2}$ = -3.42 V vs. SCE),[38,39] which suggests that its incorporation into conjugated polymers may enable achievement of high electron affinity and thus potential as n-type semiconducting polymers. Many p-type semiconducting polymers with donor-acceptor (D-A) architectures have incorporated phenazine-1,4-diyl (1,4-phen) unit (Chart 2.2) as the acceptor moiety with donor moieties such as indacenodithienothiophene,[40] indacenodithiophene,[41,42] benzodithiophene,[43–47] fluorene,[48] carbazole,[49–51] and dithienopyrrole.[52] These 1,4-phen-containing D-A copolymers have typical optical bandgaps of about 1.5 - 2.4 eV and space-charge limited current (SCLC)

hole mobilities of 10^{-2} - 10^{-5} cm^2/Vs, which have enabled their applications in polymer solar cells. π-Conjugated poly(phenazine-2,7-diyl) bearing 1,2,5,8-tetraalkyl side chains and two derivatives have been synthesized and shown to have high electron affinity (~ 4.1 eV) from cyclic voltammetry experiments and thus they were suggested to be n-type semiconducting polymers; however, electrical conductivity or charge transport properties were not reported for any of these polymers.[53]

Chart 2.2. Different linkage positions for incorporating phenazine (phen) into π-conjugated polymer backbones.

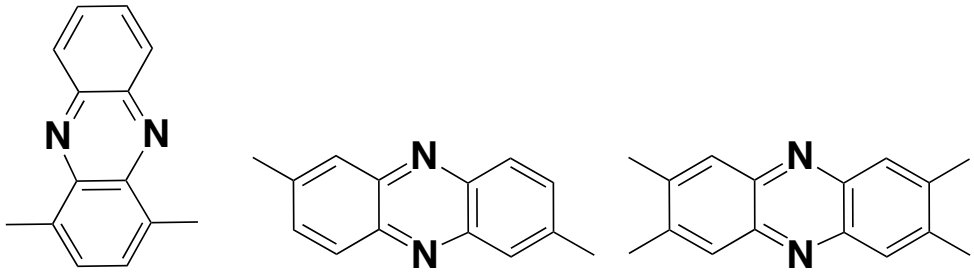

1,4-phen 2,7-phen 2,3,6,7-phen

Here, we report the synthesis and investigation of the electronic structure, thin film microstructure, and optical, electron transport, and mechanical properties of the conjugated ladder polymer, poly[7-oxo-7H,12H-benz[4',5']isoquino[2',1':1,2]imidazo[4,5-b]imidazo[4,5-i]phenazine-3,4:12.13-tetrayl)-12-carbonyl] (BBL-P). Although a moderate molecular weight was indicated by the measured intrinsic viscosity ([η]) (0.68 dL/g in methanesulfonic acid (MSA) and 1.1 dL/g in conc. H_2SO_4 at 30˚C), the BBL-P sample could form strong and flexible freestanding films. The molecular structure of BBL-P was confirmed by elemental analysis and FTIR and Raman spectroscopies. Unlike BBL which exhibits a relatively narrow absorption spectrum in MSA solution, we found that BBL-P has an unusually broad absorption spectrum in

MSA solution with a lowest energy absorption peak at 840 nm due to protonation-enhanced intramolecular charge transfer (ICT). We characterized the mechanical properties of BBL-P films and found the Young's modulus to be 11 GPa. BBL-P thin films have an optical bandgap of 1.6 eV and cyclic voltammetry derived LUMO energy level of -4.0 eV and HOMO energy level of -5.5 eV. As the n-channel material in organic field-effect transistors (OFETs), BBL-P showed an average electron mobility of ~ 1.0 x 10^{-4} cm^2/Vs. Our BBL-P results contribute important insights for the design of new high-performance BBL derivatives. We believe BBL-P will be an attractive n-type semiconducting polymer for various organic electronic applications including thermoelectric and OECT. In particular for OECT, n-type materials are rare,[16,54–56] with the performance lagging behind p-type materials.[57–59]

2.2 Experimental Methods

Materials and Methods. The monomer 1,4,5,8-naphthalenetetracarboxylic acid was purchased from TCI and purified according to a modified procedure.[60] 2,3,7,8-Tetraaminophenazine hydrochloride was synthesized according to the published procedures.[34] Sodium acetate, polyphosphoric acid (PPA, 84% P_2O_5), phosphorus pentoxide, and methanesulfonic acid (MSA) (> 99%) were purchased from Sigma-Aldrich and used as received. Methanol and concentrated sulfuric acid were purchased from Fisher Scientific and used as received.

Intrinsic viscosity of BBL-P in both MSA and H_2SO_4 was measured by an Ubbelohde viscometer suspended in a water bath at 30.0˚C. The concentrations of the polymer solutions were chosen such that the elution time of the polymer solution was 1.1 – 1.8 times that of the pure solvent. Thermogravimetric analysis (TGA) was conducted on a TA Instrument model Q50 TGA. A heating rate of 10°C /min under a flow of N_2 was used with runs conducted from room temperature to 880°C. Differential scanning calorimetry (DSC) analysis was performed on a TA

Discovery DSC 500 under N_2 by scanning from -10°C to 400°C at a heating rate and cooling rate of 10°C /min. The ^{1}H NMR spectrum was recorded on a Bruker AV500 (at 500 MHz) using deuterated nitromethane/$GaCl_3$ as the solvent. Optical absorption spectra were measured on a PerkinElmer model Lambda 900 UV-vis/near-IR spectrophotometer. Solution absorption spectrum was obtained from dilute (10^{-5} M) solutions in MSA.

Cyclic voltammetry (CV) experiments were done on an EG&G Princeton Applied Research potentiostat/galvanostat (model 273A). A three-electrode cell was used, using platinum wire as the counter electrode and BBL-P spin-coated onto indium tin oxide (ITO) substrates as the working electrode. The reference electrode was $Ag/AgNO_3$ in acetonitrile. The BBL-P working electrode was fabricated by coating BBL-P solution in MSA onto ITO substrates. The acidic solvent was removed by dipping the substrate in isopropanol (IPA) overnight and was subsequently dried in vacuum oven at 60˚C. The supporting electrolyte solution consists of 0.1 M tetrabutylammonium hexafluorophosphate (Bu_4NPF_6) in anhydrous acetonitrile. The electrolyte was purged with nitrogen for 15 minutes prior to the CV scans to ensure anerobic and anhydrous conditions. The reduction and oxidation potentials were referenced to the Fc/Fc^+ couple by using ferrocene as an internal standard. The LUMO energy level was estimated using a ferrocene value of -4.8 eV with respect to vacuum level. The LUMO and HOMO levels were determined by using the equations $E_{LUMO} = -(eE_{red}^{onset} + 4.8)$ and $E_{HOMO} = -(eE_{ox}^{onset} + 4.8)$.

Fourier-transform infrared (FTIR) spectroscopy experiments were performed on a Perkin Elmer Frontier spectrometer by using BBL-P freestanding films. The resolution was set at 1 cm^{-1} and a set of 16 scans was averaged. Raman spectroscopy of BBL-P freestanding films was carried out on a Thermo Scientific DXR2 Raman microscope. A 532-nm laser with a power of 5 mW was focused onto a sample through a 50x objective lens.

Atomic force microscopy (AFM) characterization of the surface morphology of the BBL-P films was done using a Bruker Dimension scanning probe microscope (SPM) system. Films of BBL-P were prepared as described earlier. Grazing incidence wide-angle X-ray scattering (GIWAXS) measurements were conducted at the Advanced Light Source (ALS) at Lawrence Berkley National Laboratory by using the beamlines 7.3.3 and a Pilatus 2M area detector. The images were taken with a beam energy of 10 keV and an incidence angle 0.14˚ with 5 s exposure time. Data were processed using Nika and WAXStools[61] in Igor Pro. Peak positions were determined by Lorentzian peak fittings. The crystal coherence length (L_c) of samples was determined by using the Scherrer equation[62]: $L_c = 2\pi K/\Delta q$, where K is a shape factor (typically 0.9) and Δq is the full width at half-maximum (FWHM) of the diffraction peak. Here, the L_c (100) and L_c (010) were obtained respectively from the FWHM of the (100) diffraction peak in the in-plane (q_{xy}) line-cut and the FWHM of the (010) diffraction peak in the out-of-plane (q_z) line-cut.

Gas-phase molecule density functional theory (DFT) calculations were performed using the Gaussian 16 suite of programs[63] at the ωB97XD/631-G(d,p) level of theory on the representative oligomer comprising three repeat units oriented in a *trans-cis-trans* geometry to represent the polymer backbone.

Synthesis of BBL-P. PPA (20.64 g) was added to a reaction vessel equipped with a mechanical stirrer and heated to 150˚C and purged with nitrogen overnight. The PPA was cooled to 40˚C, and 2,3,7,8-tetraaminophenazine HCl (1.606 g, 5.4 mmol) was added. The temperature was increased to 75˚C and stirred for 4 hours under dynamic vacuum. The temperature was then reduced to 65˚C and 1,4,5,8-naphthalenetetracarboxylic acid (1.656 g, 5.4 mmol) was added. The mixture was stirred for 45 minutes before P_2O_5 (3.090 g, 21.8 mmol) was added portionwise. The

temperature was increased to 100˚C and stirred overnight. The temperature was then slowly increased to 150˚C and stirred for 24 hours. The temperature was further increased to 180˚C and stirred for 3 days. The reaction mixture was cooled to room temperature, and water was added to quench the reaction. The polymer mass was added to a blender, cut into pieces, and washed with water by Soxhlet extraction for 3 days. The crude polymer was then added to 4 L of water and boiled for 24 h and dried under vacuum. The crude polymer was further purified by reprecipitation from H_2SO_4 into 1:1 water/methanol and thoroughly dried at 200˚C under vacuum (2.212 g, 82%). Intrinsic viscosity [η]: 1.1 dL/g (30.0˚C, conc. sulfuric acid). Anal. calcd for $C_{26}H_{14}N_6O_5$ (%) (BBL-P powder): C, 63.67; H, 2.88; N, 17.14; O, 16.31; found (%): C, 58.56; H, 3.21; N, 17.20; O, 16.17. Anal. cald for $C_{26}H_{12}N_6O_4$ (%) (BBL-P freestanding film): C, 66.10; H, 2.56; N, 17.79; O, 13.55; found (%): C, 63.39; H, 2.47; N, 18.74; O, 13.04

2.3 Results and Discussion

Scheme 2.1. Synthesis of BBL-P (PPA = polyphosphoric acid, 84% free P_2O_5).

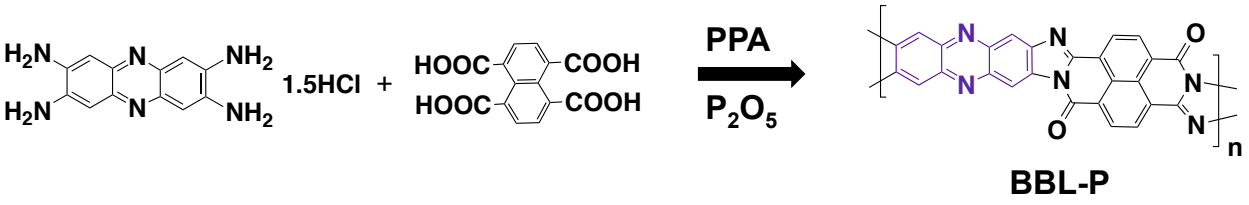

2.3.1. Synthesis and Characterization. The synthetic route to the ladder polymer BBL-P is shown in Scheme 2.1. The 2,3,7,8-tetraaminophenazine hydrochloride monomer was synthesized according to the published procedure which produced the monomer in high purity.[34] The 1,4,5,8-naphthalenetetracarboxylic acid co-monomer, purchased with 60% purity, was rigorously purified according to the published procedure before use.[60] A unique characteristic of rigid-rod polymers is that polymerization in the liquid crystalline phase yields higher molecular weights than polymerization in the isotropic phase.[64] Therefore, we modified the original synthetic

procedure in an attempt to induce liquid crystallinity during polymerization. However, we did not observe stir-opalescence or other evidence of liquid crystallinity. When first synthesized in 1974, the isotropic phase condensation in pure polyphosphoric acid (PPA) resulted in BBL-P with low intrinsic viscosity ([η]) of 1.1 dL/g in methanesulfonic acid (MSA) at 30˚C.[34] However, our BBL-P sample also gave a low [η] value of 1.1 dL/g in concentrated sulfuric acid (H_2SO_4) at 30˚C, which is nearly identical to that measured in 1974,[34] confirming that our synthesis of BBL-P also took place in the isotropic phase.

The BBL-P sample was isolated as a black solid powder and shows a purple color in either concentrated H_2SO_4 or MSA. In addition to the low [η] of BBL-P in concentrated H_2SO_4 (1.1 dL/g) at 30˚C, we found that [η] was 0.68 dL/g in MSA at 30˚C. The solvent-dependent viscosity of BBL-P solutions, which is in contrast with the constant [η] of BBL regardless of solvent,[65] may be due to the improved solubility of BBL-P in H_2SO_4 compared to MSA. The molecular structure of BBL-P was confirmed by elemental analysis and FTIR and Raman spectroscopies. The analytical data for each element match the calculated values except carbon, which was lower than calculated mainly due to incomplete combustion, which is a common problem in the elemental analyses of thermally stable polymers.[1,60,64,66] Interestingly, the elemental analysis of the BBL-P powder revealed a total of ~ 11 wt.% of water was retained, which is equivalent to approximately three water molecules per repeat unit, suggesting that BBL-P is intrinsically hygroscopic in marked contrast from the parent BBL.[67] The hygroscopic nature of BBL-P is likely to originate from the phenazine moieties whereby the imine nitrogen sites are free to hydrogen bond with absorbed water molecules from the atmosphere.[68]

The hygroscopic nature of BBL-P was further corroborated by thermogravimetric analysis (TGA) as shown in Figure A.1a An initial weight loss of ~ 8.1 % was observed at 80˚C -

110˚C, which can be attributed to water evaporation. Additional rigorous drying of BBL-P at 200˚C for 48 - 96 hours under vacuum was found to be insufficient to completely remove water. This result supports the elemental analysis that also showed residual water in BBL-P. To get a clear picture of the thermal stability, the TGA scans after drying by first scanning to 200˚C and 400˚C, respectively, then cooled down to 50˚C and heated to 880˚C under nitrogen (Figure A.1a). The results show that BBL-P is stable in high temperatures in agreement with similar ladder polymers,[34,69] showing 5% weight loss at 609˚C and 626˚C in inert atmosphere for samples dried at 200˚C and 400˚C, respectively. Differential scanning calorimetry (DSC) scans showed no detectable phase transitions in the 25˚C to 400˚C temperature range (Figure A.1b), which agrees with literature reports of the very high glass transition temperature (T_g) of ladder polymers (> 400˚C).[65] The observed excellent thermal stability and high T_g of BBL-P are comparable to those of BBL.[60] To further characterize the molecular structure of BBL-P, we collected ^{1}H NMR spectra for both BBL-P-$GaCl_3$ and BBL-$GaCl_3$ complexes in deuterated nitromethane[65] and they are shown in Figures A.2a-b. We note that soluble Lewis acid complexes of rigid-rod ladder polymers has allowed the study of both solution and solid-state properties of BBL in the last few several decades.[65,69] Solutions of both polymers were prepared in deuterated nitromethane containing $GaCl_3$ according to the known procedures.[65] However, the use of Lewis-acid complexes to acquire NMR spectra is known to produce multiple impurity peaks for benzimidazobenzophenanthroline polymers;[36,65.69] these impurities appear at ~ 7.3, 8.5, 9.1, and 10.5 ppm for BBL-P (Figure A.2a) and BBL (Figure A.2b). The broad overlapped resonances of both polymers are due to the presence of 6 possible *cis* and *trans* structural isomers[19] and are shown in Figure A.2c; these isomers make unambiguous peak assignments difficult. However, comparison of the two spectra does allow assignment of the resonances

associated with the co-monomers. The NMR spectra show unresolved peaks from the naphthalene protons at ~ 9.3 - 9.8 ppm for BBL-P and ~ 9.6 - 9.8 ppm for BBL. The phenazine protons in BBL-P are assigned to the four resonances centered at 7.2, 7.5, 8.6, and 8.9 ppm, whereas the benzene protons for BBL are assigned to the singlet within the naphthalene cluster at 9.8 ppm and the overlapped resonance at 9.0 ppm.[36,65]

To enable further characterization of the molecular structure, thin film microstructure and optical properties of BBL-P, we prepared freestanding films. The detailed procedure for the fabrication of BBL-P freestanding films is described in Appendix A. Briefly, the spin-coated BBL-P film on glass substrates was baked at 120˚C overnight on a hot plate in ambient atmosphere to evaporate most of the acidic solvent. The baked film was slowly cooled down to room temperature and subsequently submerged in water whereby the film swelled significantly due to the intrinsic hygroscopic nature of BBL-P. As a result, BBL-P thin films could be peeled off from the supporting glass substrates and lifted off from water (Figure 2.1a) to form freestanding films (Figure 2.1b) with surface area as large as 5-6 cm^2. We note that films of larger area can also be fabricated by extending the area of the initial supporting substrates. The freestanding films have good quality and were used to characterize the molecular structure through elemental analysis, UV-Vis optical absorption, Fourier-transform infrared (FTIR), and Raman spectra.

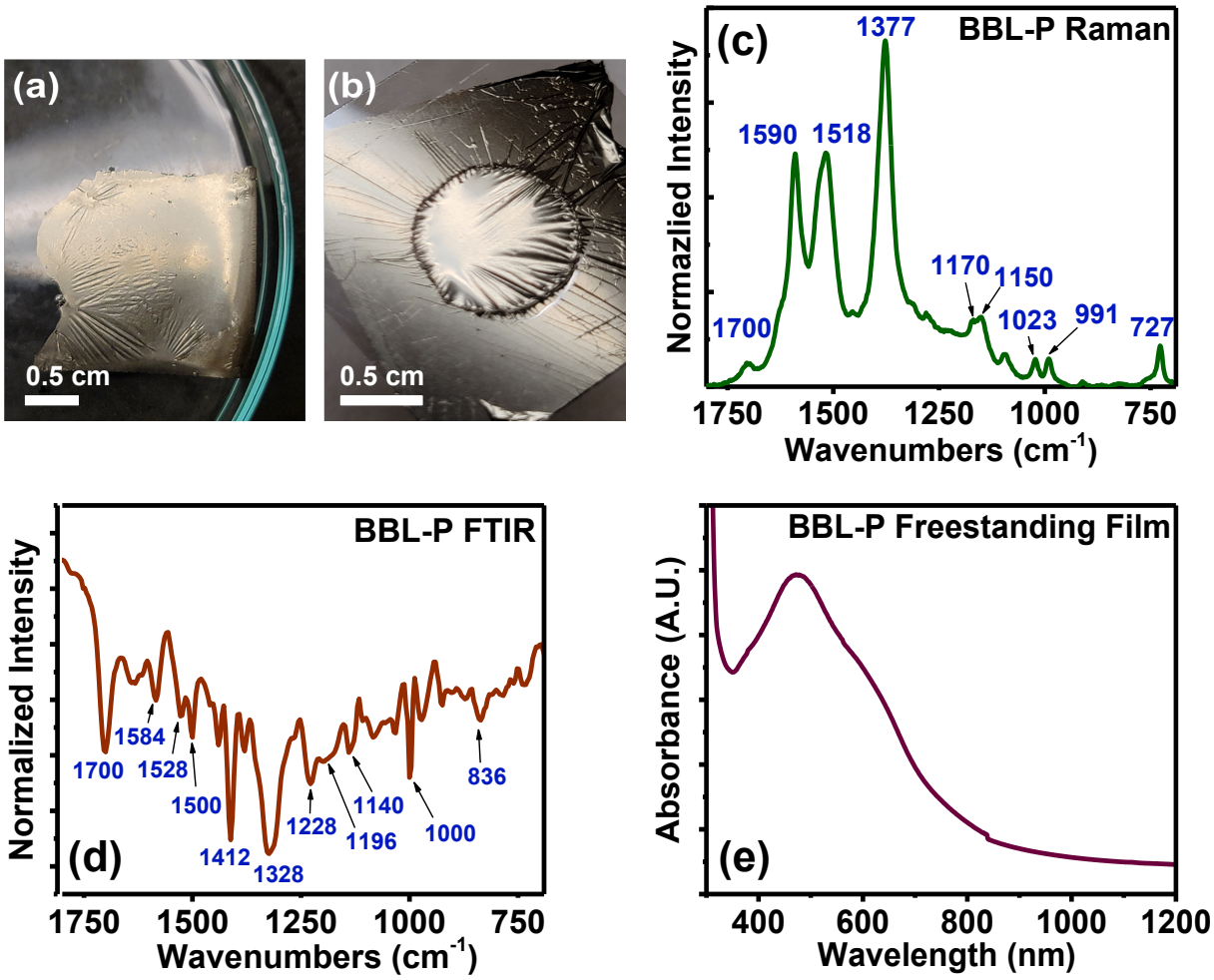

Figure 2.1. (a) BBL-P film floating on water after peeling off from the initial supporting substrate, (b) Freestanding BBL-P film with a diameter of 1 cm, (c) Raman spectrum of BBL-P freestanding film with an excitation laser of 532 nm, (d) Fourier-transform infrared (FTIR) spectrum of BBL-P freestanding film, and (e) Optical absorption spectrum of BBL-P freestanding film.

FTIR spectroscopy in conjunction with Raman spectroscopy was used to confirm the molecular structure of BBL-P in addition to the previously discussed elemental analysis. The FTIR and Raman spectra of freestanding BBL-P films collected in ambient atmosphere are shown in Figures 2.1c-d. The peak positions assigned to various vibration modes are summarized

in Table 2.1. The prominent ν(C=O) carbonyl carbon-oxygen stretch mode can be seen on both the FTIR and Raman spectra with distinct absorption peaks at 1700 cm^{-1} (Table 2.1). The imine carbon-nitrogen stretch mode, ν(C=N), can be identified by an intense Raman absorption band at 1590 cm^{-1} and a low intensity FTIR absorption band at 1584 cm^{-1}. At lower wavenumbers, there is an intense Raman absorption band at 1518 cm^{-1} and some weak-intensity FTIR bands at 1528 cm^{-1} and 1500 cm^{-1} which can be attributed to aromatic carbon-carbon and carbon-nitrogen skeletal vibrations (Table 2.1).[65] Moreover, a sharp and intense FTIR absorption band at 1412 cm^{-1} can be assigned to carbon-nitrogen amide bonds,[65] ν(C-N), which further supports backbone fusion. Additional FTIR absorption bands at 1380 cm^{-1} and 1328 cm^{-1} coupled with a Raman absorption band at 1377 cm^{-1} originate from the stretching of carbon-nitrogen single bonds,[65] ν(C-N) in the BBL-P polymer.

Skeletal vibrations also appeared in both the FTIR and Raman spectra respectively at 1228 cm^{-1} and 1000 cm^{-1} and at 1023 cm^{-1} and 991 cm^{-1} (Table 2.1).[65] In-plane C-H bending can be assigned to absorption bands centered at 1170 cm^{-1} and 1150 cm^{-1} in the Raman spectrum whereas out-of-plane C-H wagging can be seen at 972 cm^{-1} and 836 cm^{-1} in the FTIR spectrum (Table 2.1). A sharp Raman absorption band at 727 cm^{-1} can be attributed to the out-of-plane C-H wagging of the two adjacent carbon-hydrogen bonds on the naphthalene rings (Table 2.1). We note that no ν(O-H) peak was observed in the FTIR spectrum suggesting that the absorbed water seen in the BBL-P powder, which was used in TGA and elemental analysis, had been effectively removed in the BBL-P freestanding film. One possible explanation for the lack of observed water in the FTIR spectrum is that when processed into a freestanding film, water diffusion is kinetically limited. In particular, water is absorbed volumetrically (3D process) in the case of the powdered sample whereas the polymer film is subjected only to areal water uptake (2D process).

Thus, the films absorb significantly less water from the atmosphere compared to the powder sample. This was evidenced by elemental analysis of the freestanding films of BBL-P, which revealed a total of ~ 2 water molecules per repeat unit. This is in contrast to the powder sample which showed ~ 3 water molecules per repeat unit. The observed FTIR and Raman spectra data are in good agreement with previous reports of the parent BBL ladder polymer[65] and provide strong evidence for the molecular structure of BBL-P.

Table 2.1. FTIR and Raman Absorption Bands of Freestanding BBL-P Film and Their Peak Assignments.

FTIR Absorption Band (cm^{-1})	Raman Absorption Band (cm^{-1})	Assignment
1700	1700	ν(C=O), carbonyl carbon-oxygen stretch
1584	1590	ν(C=N), imine carbon-nitrogen stretch
1528, 1500	1518	Aromatic carbon-carbon, carbon-nitrogen skeletal vibrations
1412	-	ν(C-N), carbon-nitrogen amide bonds
1380, 1328	1377	ν(C-N), carbon-nitrogen single bonds
1228, 1000	1023, 991	Mixed skeletal vibrations
-	1170, 1150	In-plane C-H bending
972, 836	-	Out-of-plane C-H wagging
-	727	δ(C-H), out-of-plane wag of naphthalene C-H bonds

2.3.2 Electronic Structure and Optical Properties. We investigated the electronic structure of BBL-P by density functional theory (DFT) calculations, time-dependent DFT (TD-DFT) calculations and cyclic voltammetry in conjunction with optical absorption spectroscopy. The DFT calculations were performed at the ωB97XD/6-31G(d,p) level of theory for a BBL-P oligomer comprising three repeat units to gain insight into the polymer conformation and frontier

molecular orbital distribution (Figure 2.2). Note that a trimer was chosen to balance low computational costs and accuracy of simulation, and a *trans-cis-trans* conformation with respect to the imide was chosen to represent the polymer backbone, given that benzimidazobenzophenanthroline polymers are a statistical mixture of *cis* and *trans* repeat units.[19,70] The optimized geometry is completely planar with dihedral angle of 0.00˚ between the phenazine and naphthalene imide moieties (Figure 2.2a), which is similar to the observed molecular geometry of the parent BBL ladder polymer.[19] The molecular orbital distributions of the HOMO and LUMO are distributed along the backbone, where the HOMO is concentrated on the phenazine moieties and the LUMO on the naphthalene imide moieties (Figure 2.2b). This spatial distribution suggests enhanced intramolecular charge transfer (ICT) character in BBL-P compared to the parent polymer BBL that shows minimal spatial localizations of the HOMO molecular orbitals (Figure A.3).[71]

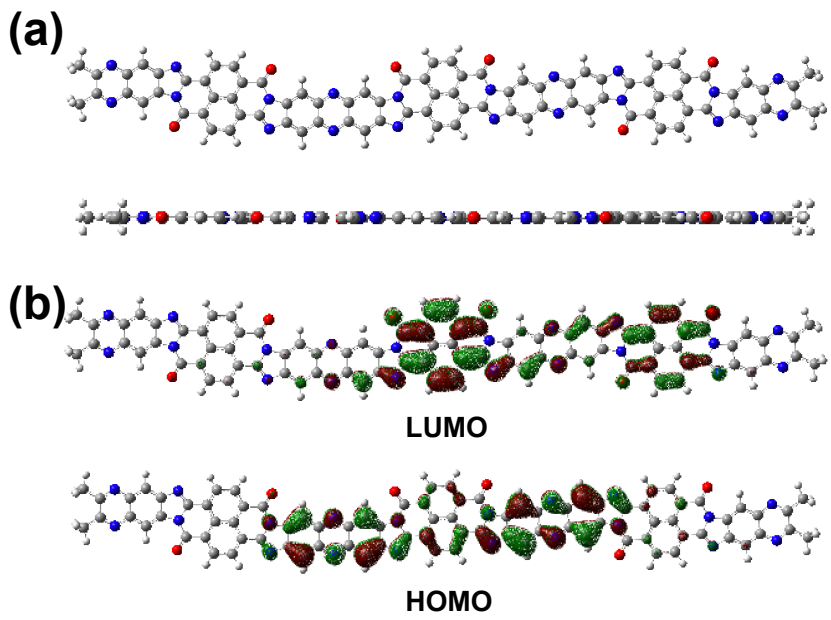

Figure 2.2. DFT calculations of (a) The optimized ground state molecular geometry of BBL-P oligomer, and (b) Pictorial representation of ground state frontier molecular orbitals. Calculations were performed at the ωB97XD/6-31G(d,p) level of theory.

Excited-state transitions were calculated using time-dependent (TD) DFT at the same ωB97XD/6-31G(d,p) level of theory. The calculated absorption spectrum in Figure A.4a closely resembles the experimental thin film absorption spectrum where the low-energy peak centered at 527 nm represents the π-π^* transition. The pictorial representations of both the electron and hole orbital distributions associated with the π-π^* transition is shown in Figure A.4b.

The reorganization energy (λ) of BBL-P was calculated from the sum of the relaxation energies in the neutral and anionic states.[71,72] The anionic geometry and orbital distribution of the oligomer is illustrated in Figure A.4c. Reorganization energy can be described as the energy corresponding to structural changes when going from the neutral to the charged-state geometry; typically, the lower the reorganizational energy, the higher the charge transfer rate.[71,73,74] A reorganization energy of 432 meV calculated for BBL-P is comparable to those calculated for conjugated rigid-rod polymers (327-427 meV) featuring isoindigo units using a similar level of

theory and number of monomer units.[71] Note that the calculated λ decreases with increasing number of monomers (n) and more accurate descriptions of the polymer chain would require $n >$ 12.[74]

We used cyclic voltammetry (CV) to measure the HOMO/LUMO energy levels of BBL-P and the results are summarized in Table 2.2. The CVs for reduction and oxidation processes (Figures 2.3a-b) of BBL-P thin films coated on indium tin oxide (ITO) glass substrates were taken in 0.1 M tetrabutylammonium hexafluorophosphate (Bu_4NPF_6) in degassed acetonitrile with $Ag/AgNO_3$ as the reference electrode. BBL-P thin films showed two quasi-reversible reduction waves in the CV scans (Figure 2.3a) and these were accompanied by observed color changes in the film during the scans. In particular, the initial dark brown BBL-P film changed to dark purple at the first reduction process at -0.99 V whereas the second reduction process at -1.22 V changed the film color to bright orange. These electrochromic effects were found to be relatively stable, which is similar to the previous results for BBL thin films.[75] The CV oxidation scans (Figure 2.3b) showed a non-reversible peak with no observable color changes. The onset oxidation potential and onset reduction potential of BBL-P are 0.85 V and -0.86 V, respectively, from which we estimated the HOMO level of -5.5 eV and LUMO level of -4.0 eV by using: $E_{LUMO} = -(eE_{red}^{onset} + 4.8)$ and $E_{HOMO} = -(eE_{ox}^{onset} + 4.8)$. While the LUMO value is identical to that of the parent BBL, the HOMO value of BBL-P is increased by 0.4 eV (HOMO = -5.9 eV for BBL).[10] Although the expansion of the repeat unit of BBL by phenazine substitution has little impact on the LUMO energy levels, it has a large effect on the HOMO energy level; this means that when electronically coupled to the strong electron-withdrawing naphthalene imide moiety, the phenazine acts as an electron donor, thereby enhancing ICT interactions. This correlates well

with the theoretical calculations showing localization of the HOMO wavefunctions on the phenazine core (Figure 2.2b).

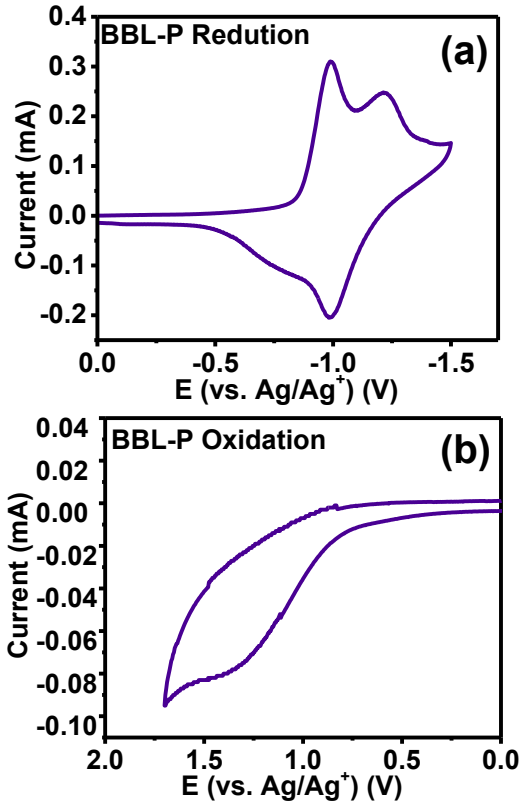

Figure 2.3. Cyclic voltammograms for the (a) reduction and (b) oxidation processes of BBL-P thin films measured in 0.1 M Bu_4NPF_6 electrolyte solution using $Ag/AgNO_3$ as the reference electrode. The scan rate was 100 mV/s.

The optical absorption spectrum of freestanding BBL-P film is shown in Figure 2.1e. It has a broad absorption band with a peak at 472 nm accompanied by weak vibronic features at 380 nm and 635 nm. We estimate the optical bandgap ($E_g^{opt.}$) of the freestanding film to be 1.62 eV (Table 2.2). The optical absorption spectra of BBL-P in dilute MSA solution and as a thin film on a glass substrate are shown in Figures 2.4a-b, and the optical properties (molar absorptivity (ε_{max}), absorption coefficient (α), and optical bandgap ($E_g^{opt.}$)) are summarized in Table 2.2. In solution (Figure 2.4a), BBL-P has a broad absorption band with a peak at 512 nm

(ε_{max} = 3.7 x 10^4 $M^{-1}cm^{-1}$) and a lower intensity peak at 840 nm (ε_{max}= 1.3 x 10^4 $M^{-1}cm^{-1}$). To help in understanding the unusual line shape of the absorption spectrum of BBL-P in MSA solution, we also show the absorption spectrum of BBL in MSA solution in Figure 2.4a. A relatively narrow absorption band with a peak at 545 nm (ε_{max}= 4.3 x 10^4 $M^{-1}cm^{-1}$) is seen in the parent BBL. We propose that the 840-nm absorption band in the MSA solution spectrum of BBL-P is due to intramolecular charge transfer (ICT),[76] enhanced by protonation of the imine nitrogens of the phenazine moieties. This interpretation is in agreement with similar observations in acid solutions of imine nitrogen-containing π-conjugated polymers[77] as well as with the previously discussed DFT calculations.

The thin film absorption spectrum of BBL-P (Figure 2.4b) is a broad band in the 300 – 700 nm range with a peak centered at 474 nm and an absorption coefficient of 1.4 x 10^5 cm^{-1}. The optical bandgap ($E_g^{opt.}$) measured from the onset of the BBL-P thin film absorption spectrum is 1.64 eV, which is identical to the bandgap measured from the freestanding BBL-P film (Figure 2.1e). Compared to the solution absorption spectrum, the thin film absorption spectrum is markedly different in lineshape. Notably, the 840-nm absorption peak observed in the solution spectrum is absent in the solid state, confirming its protonation-induced ICT origin. The main absorption peak of BBL-P, which is due to the π-π* transition, centered at 512 nm in the solution spectrum is significantly blue shifted to 474 nm in the solid state (Table 2.2). It is tempting to interpret the blue shift of the thin film absorption spectrum of BBL-P relative to its solution as a consequence of H-aggregation in the solid state.[78,79] However, an alternative interpretation is that the difference originates in differences in backbone conformation in solution and solid state;[80] in this case, the protonated polymer chains in solution would presumably be more planar than the neutral polymer chains in thin film.

The MSA solution and thin film optical absorption spectra of BBL, the parent ladder polymer, are shown in Figures 2.4a and 2.4b, respectively, for comparison with those of BBL-P. There are clearly dramatic differences in both the solution and solid-state absorption spectra. It is to be noted that BBL does not absorb above 600 nm in MSA solution and this further confirms that the 840-nm absorption band in BBL-P solution originates from protonation of the phenazine moieties. Furthermore, in solution, the BBL-P absorption maximum (λ_{max} = 512 nm) is 33 nm blue-shifted relative to BBL but the two ladder polymers have comparable ε_{max} (Table 2.2). Although BBL-P has a slightly narrower optical bandgap ($E_g^{opt.}$ = 1.64 eV) than BBL ($E_g^{opt.}$ = 1.70 eV), there is a large difference in the solid-state absorption maxima of 574 nm in BBL versus 474 nm in BBL-P (Table 2.2). The slow rise of absorption from the edge to the absorption maximum in BBL-P is indicative of a more disordered organic semiconductor compared to BBL with a sharp rise in absorption (Figure 2.4b).

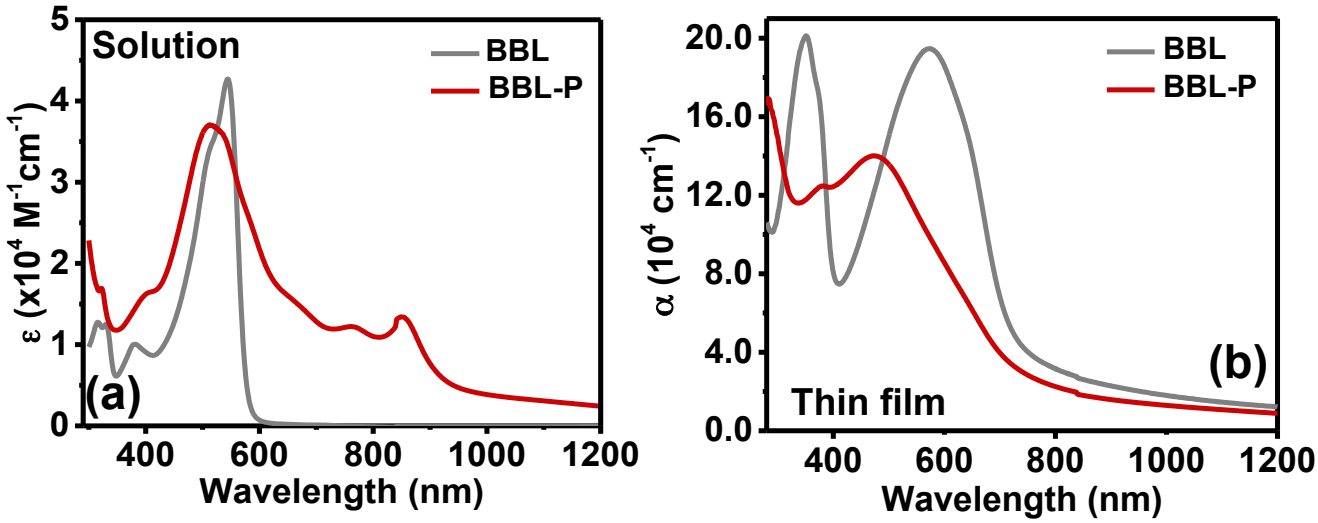

Figure 2.4. Absorption spectrum of BBL-P (red) and BBL (gray) in (a) dilute methanesulfonic acid solution; and (b) thin film on glass substrate.

Table 2.2 Optical Properties and Electronic Structure of BBL-P and BBL.

Polymer	λ_{max}[a] (nm)	ε_{max} (M^{-1} cm^{-1})	λ_{max}[b] (nm)	α (x10^5 cm^{-1})	$E_g^{opt.c}$ (eV)	$E_g^{opt.d}$ (eV)	HOMO (eV)	LUMO (eV)
BBL-P	512	3.7 x 10^4	474	1.4	1.64	1.62	-5.5	-4.0
BBL	545	4.3 x 10^4	574	1.9	1.70	-	-5.9[e]	-4.0[e]

[a]Absorption maximum in MSA solution. [b]Spin-coated thin films from MSA solution. [c]Thin films on glass substrates. [d]Freestanding film. [e]Values taken from Ref. (10).

2.3.3 Thin Film Morphology. Atomic force microscopy (AFM) imaging and two-dimensional grazing-incidence wide-angle X-ray scattering (2D-GIWAXS) are used to respectively characterize the surface morphology and bulk morphology of BBL-P films. AFM height and phase images of BBL-P are shown in Figures A.5a-b whereas the 2D GIWAXS diffraction patterns and 1D line cuts for BBL-P films are presented in Figure 2.5. The peak positions, lamellar spacing, π-π stacking distance, and crystalline coherence length (L_c) are summarized in Table A.1.

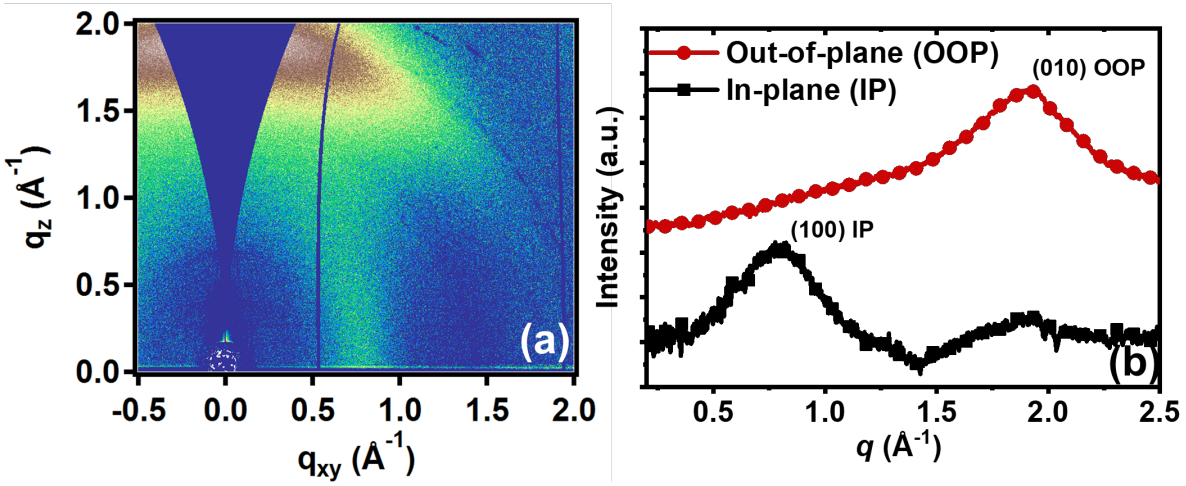

Figure 2.5. (a) 2D-GIWAXS diffraction pattern of BBL-P thin film, and (b) 1D line cuts of GIWAXS patterns in the out-of-plane (OOP) direction and the in-plane (IP) direction.

Films of BBL-P showed a featureless and smooth surface (Figures A.5a-b) with a root-mean-square roughness of 1.6 nm in AFM imaging, suggesting a relatively low degree of polymer crystallinity. BBL-P films exhibited a pronounced (100) diffraction peak in the in-plane (IP) direction at q_{xy} of 0.78 $Å^{-1}$, which corresponds to a lamellar spacing of 8.03 Å (Table A.1). We note that the lamellar packing distance of BBL-P is slightly smaller than that of BBL (8.4 Å),[16] which can be rationalized by the strong intermolecular interactions between the imine nitrogens on the phenazine units. In the out-of-plane (OOP) direction, the BBL-P thin film showed an intense (010) diffraction peak at q_z of 1.90 $Å^{-1}$ resulting in a π-π stacking distance of 3.31 Å, which is comparable to a π-π stacking distance of 3.34 Å for BBL thin films.[16] The presence of the (100) IP diffraction peak and the (010) OOP diffraction peak collectively suggests that most BBL-P crystallites preferentially adopt *face-on* orientations with respect to the substrate. Furthermore, the crystalline coherence length (L_c) of BBL-P in the (100) IP and (010) OOP directions were found to be 1.07 nm and 1.04 nm, respectively, which is significantly lower than those of BBL (~ 12 nm and ~ 25 nm) even at the lowest polymer molecular weight.[16] Thus, substitution of the phenazine moiety for the benzene moiety in the polymer backbone not only renders the BBL-P polymer more amorphous but also changes the molecular orientations from preferentially *edge-on* in BBL[16] to preferentially *face-on* in BBL-P, both of which have implications for *field-effect* electron transport of BBL-P thin films.

2.3.4 Field-Effect Charge Transport Properties. We investigated the electron transport properties of BBL-P ladder polymer by fabricating and characterizing n-channel organic field-effect transistors (OFETs). The transistors were fabricated in a bottom-gate/top-contact device architecture with channel dimensions of 100μm/1000μm (length/width). A thin polystyrene buffer layer was used to passivate silanol charge trapping sites on silicon dioxide surfaces.[19,81]

The presence of a low dielectric constant buffer layer has been previously demonstrated to reduce the number of charge trapping groups and energetic expense from the charge carrier-dipole interactions in BBL OFETs.[19,81] The capacitance per unit area of the gate dielectric was calculated from the dielectric constants and thickness of the layers to be 10.6 nF/cm^2. Representative output and transfer curves are presented in Figure 2.6 and the transistors parameters are summarized in Table A.2.

The n-channel BBL-P OFETs showed reasonable current modulation with good saturation (Figure 2.6a) and minimal hysteresis (Figure A.6). The average saturation region *field-effect* electron mobility (μ_{FET}) of BBL-P in a nitrogen atmosphere was found to be (9.60 ± 1.58) x 10^{-5} cm^2/Vs. The maximum μ_{FET} value of BBL-P on polystyrene buffer layer was 1.21 x 10^{-4} cm^2/Vs (Table A.2), which is about two orders of magnitude lower than that of BBL measured using the same device configuration.[19] The observed lower electron mobility of BBL-P is partly due to the lower polymer molecular weight as exemplified by the low intrinsic viscosity ([η] ~ 0.7 dL/g in MSA at 30.0˚C) compared to that of the previously reported value for BBL ([η] ~ 7.0 dL/g in MSA at 30.0˚C).[16,19] The modest *field-effect* electron mobility of BBL-P can also be attributed to poor polymer crystallinity as well as the predominantly *face-on* molecular orientations observed in the thin film microstructure. The average on/off current ratio was (7.7 ± 3.4) x 10^2 whereas the average threshold voltage was 45.1 ± 1.72 V. We note that improved electron mobility, higher on/off current ratio, and lower threshold voltage can be achieved by further increasing BBL-P molecular weights to not only enhance the polymer crystallinity but also increase the volume fraction of *edge-on* oriented crystallites.[16]

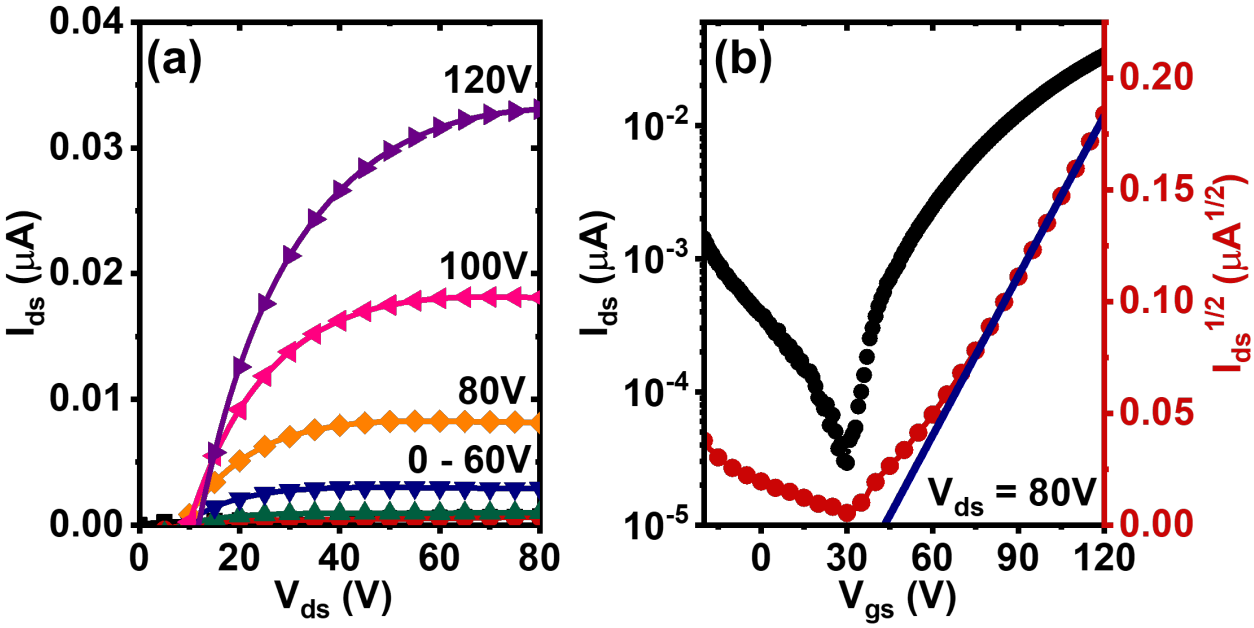

Figure 2.6. (a) Representative output curves of BBL-P n-channel organic field-effect transistor with a channel length/channel width of 100 μm/1000 μm. (b) Representative transfer curve of BBL-P transistor.

2.3.5 Mechanical Properties of BBL-P Thin Films. We also investigated the mechanical properties of BBL-P ladder polymers by using nanoindentation technique. The nanoindentation test enabled local probing of the dynamic mechanical properties of BBL-P films, which could be more sensitive than dynamic mechanical analysis of bulk samples.[82] The nanoindentation measurements were carried out in a constant displacement mode whereby three indents were made across the film surface at each indent depth. The total BBL-P film thickness was determined by profilometer to be around 650 nm, which was sufficiently thick to assume that the measured mechanical properties are intrinsic to BBL-P film without any substrate interference. The load profiles (Figure A.7f) consisted of three processes including 5 seconds of loading, 30 seconds of holding to allow creep effects to settle, and 5 seconds of unloading. The response

load-displacement curve is presented in Figure A.7g. The AFM topography images of the BBL-P film surface collected after each measurement (Figures A.7a-A.7e) showed distinct indent marks.

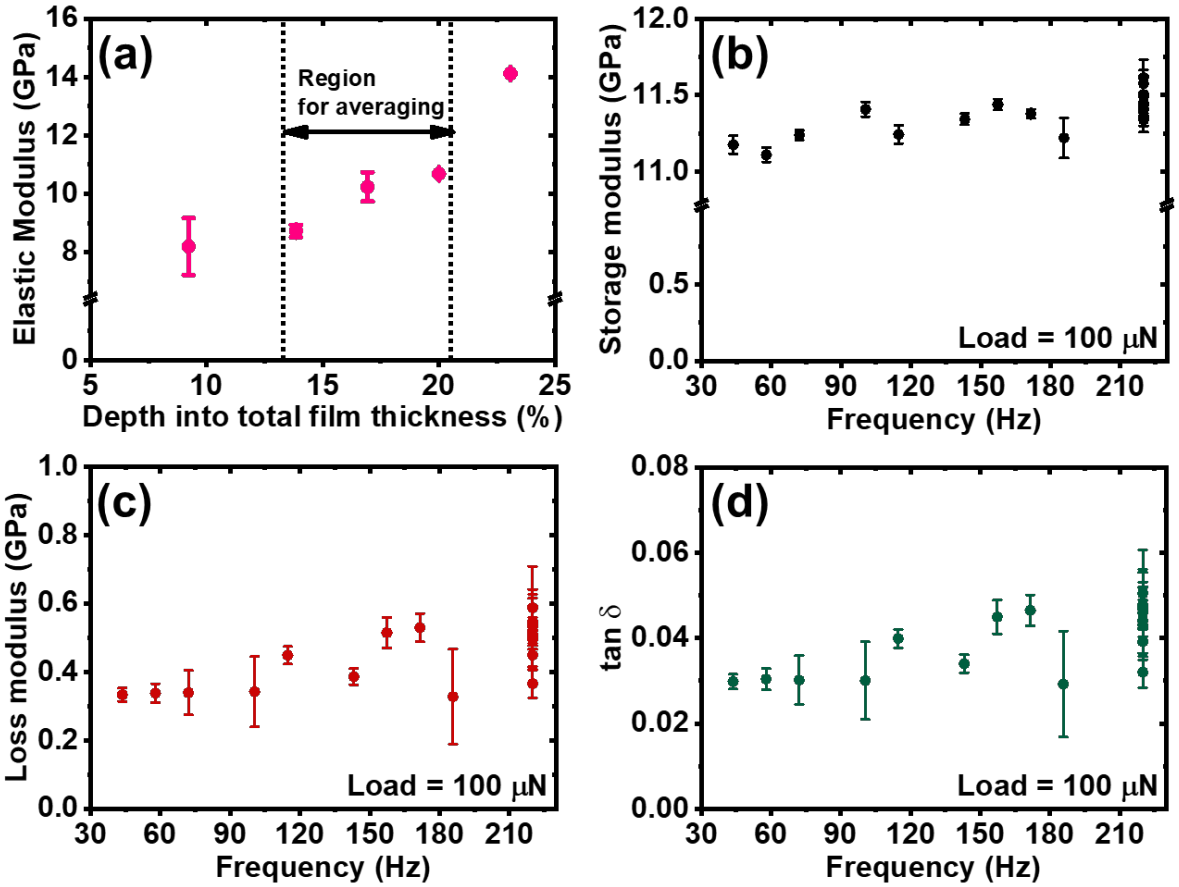

Figure 2.7. (a) Elastic modulus of BBL-P thin films at various indent depths measured by nanoindentation tests. (b-d) Dynamic mechanical properties of BBL-P thin films as a function of frequency measured at room temperature by nano(dynamic mechanical analysis): (b) Storage modulus, (c) Loss modulus, and (d) Loss tangent (tan δ).

As presented in Figure 2.7a, the elastic modulus of BBL-P thin films varied marginally between 13 – 20% indent depth into the total film thickness while values outside this range are likely to be either underestimated (<10%) due to "skin effect"[82] or overestimated due to substrate effects (>20%).[82] Thus, the elastic modulus of BBL-P thin film was found to be 10 GPa which was averaged from the moduli in the range of 13 – 20% into the film thickness.[83,84] The elastic

modulus of BBL-P was a few times higher than that of other non-ladder conjugated polymers (0.7 – 2.7 GPa),[84-88] indicating the superior mechanical properties of rigid-rod ladder polymers.

The dynamic mechanical properties of BBL-P thin films were also investigated by applying a sinusoidal load profile using the nanoindentation probe with an amplitude of 100 μN at varying frequency from 45 Hz to 200 Hz, and the results are shown in Figures 2.7b-d. The storage modulus (*E*') of BBL-P polymers was found to be around 11 GPa and independent of the applied frequency. Similar behavior was also observed for the loss modulus (*E*'') (Figure 2.7c) as a function of the applied frequency. The order of magnitude higher E' value of BBL-P compared to semi-flexible conjugated polymers measured using the same technique accompanied by the relatively constant E' and E'' are indicative of the superior mechanical robustness of the class of rigid-rod ladder polymers. This observation is further confirmed by the small loss tangent (tan $\delta < 0.05$) (Figure 2.7d), which indicates that the BBL-P polymer behaves as a nearly elastic materials in contrast to other non-ladder conjugated polymers.[84] Furthermore, the near-zero tan δ values allow the approximation of the Young's modulus of BBL-P to be ~ 11 GPa.

To place the observed elastic modulus of BBL-P in context, we also performed nanoindentation tests on the parent BBL ladder polymer as a check. The average elastic modulus of BBL film (E_{BBL}) was found to be 7.9 ± 0.4 GPa, which is within a reasonable range of reported values.[89,90] An elastic modulus of about 4 GPa was reported for a BBL filter cake (25*m*m) via dynamic mechanical analysis[89] while that of heat-treated highly oriented BBL fibers was found to be 120 GPa.[90]

2.4 Conclusions

We have synthesized and for the first time investigated the electronic structure, thin film morphology, *field-effect* electron transport, and optical and mechanical properties of phenazine-substituted ladder poly(benzimidazobenzophenanthrolinedione), BBL-P. Although the measured intrinsic viscosity ([h]) of 1.1 dL/g in concentrated H_2SO_4 implies a moderate molecular weight, the BBL-P sample could form strong and flexible freestanding films. In MSA solution, BBL-P absorption spectrum showed an additional long-wavelength peak at 840 nm, which is absent in the spectrum of BBL, and is attributed to an intramolecular charge transfer (ICT) band enabled by protonation of the phenazine moiety in BBL-P. Our characterization of the mechanical properties of BBL-P films by nanoindentation technique gave a high Young's modulus of 11 GPa.

BBL-P thin films have an optical bandgap of 1.6 eV, which is slightly reduced relative to that of BBL (1.7 eV). GIWAXS characterization of the thin film microstructure of BBL-P showed that the degree of crystallinity is reduced and the predominant molecular orientation (*face-on*) is different compared to reported BBL thin films (*edge-on*).[16] We found the LUMO energy level of BBL-P thin films (-4.0 eV) to be identical to that of BBL, however, the measured HOMO energy level of -5.5 eV is significantly elevated compared to BBL (-5.9 eV).[10] BBL-P based n-channel OFETs had an average electron mobility of 1.0×10^{-4} cm^2/Vs, which is about two orders of magnitude less than in BBL[19] likely due to the reduced molecular weight, reduced crystallinity, and unfavorable *face-on* molecular orientations of BBL-P. The present results on BBL-P provide important new insights into how the backbone chain structure of π-conjugated polymers influences the electronic structure, thin film morphology, and optical and charge transport properties. Further investigations of the performance of BBL-P polymer as an n-

channel material of OECTs will be intriguing, as lower crystallinity and the hygroscopic nature of BBL-P may be beneficial to OECT operation.[91,92]

2.5 References

1. Deusen, R. L. V. Benzimidazo-Benzophenanthroline Polymers. *J. Polym. Sci. B Polym. Lett.* **1966**, *4* (3), 211–214, DOI: 10.1002/pol.1966.110040310.

2. Shirakawa, H.; Louis, E. J.; MacDiarmid, A. G.; Chiang, C. K.; Heeger, A. J. Synthesis of Electrically Conducting Organic Polymers: Halogen Derivatives of Polyacetylene, (CH)x. *J. Chem. Soc., Chem. Commun.* **1977**, No. 16, 578–580, DOI: 10.1039/C39770000578.

3. Kim, O.-K. Ladder Polymers as New Polymeric Conductors. *Mol. Cryst.* **1984,** *105* (1), 161–173, DOI: 10.1080/00268948408071650.

4. Wilbourn, K.; Murray, R. W. The Electrochemical Doping Reactions of the Conducting Ladder Polymer Benzimidazobenzophenanthroline (BBL). *Macromolecules* **1988**, *21* (1), 89–96, DOI: 10.1021/ma00179a019.

5. Jenekhe, S. A.; Tibbetts, S. J. Ion Implantation Doping and Electrical Properties of High-Temperature Ladder Polymers. *J. Polym. Sci. B Polym. Phys.* **1988**, *26* (1), 201–209, DOI: 10.1002/polb.1988.090260111.

6. Osaheni, J. A.; Jenekhe, S. A.; Burns, A.; Du, G.; Joo, J. S.; Wang, Z. H.; Epstein, A. J.; Wang, C. S. Spectroscopic and Morphological Studies of Highly Conducting Ion-Implanted Rigid-Rod and Ladder Polymers. *Macromolecules* **1992**, *25* (21), 5828–5835, DOI: 10.1021/ma00047a040.

7. Wang, Z. H.; Du, G.; Joo, J.; Burns, A.; Jasty, S.; Zhou, P.; Epstein, A. J.; Osaheni, J. A.; Jenekhe, S. A.; Wang, C. S. Weak-Localization, Electron-Electron Interaction, and Metal-Insulator-Transition in Ion-Implanted Polymers. *Synth. Met.* **1993**, *57* (2–3), 4829–4835, DOI: 10.1016/0379-6779(93)90824-G.

8. Babel, A.; Jenekhe, S. A. Electron Transport in Thin-Film Transistors From an n-Type Conjugated Polymer. *Adv. Mater.* **2002**, *14* (5), 371–374, DOI: 10.1002/1521-4095(20020304)14:5<371::AID-ADMA371>3.0.CO;2-5.

9. Babel, A.; Jenekhe, S. A. N-Channel Field-Effect Transistors from Blends of Conjugated Polymers. *J. Phys. Chem. B* **2002**, *106* (24), 6129–6132, DOI: 10.1021/jp020695l.

10. Alam, M. M.; Jenekhe, S. A. Conducting Ladder Polymers: Insulator-to-Metal Transition and Evolution of Electronic Structure upon Protonation by Poly(Styrenesulfonic Acid). *J. Phys. Chem. B* **2002,** *106* (43), 11172–11177, DOI: 10.1021/jp021230y.

11. Babel, A.; Jenekhe, S. A. High Electron Mobility in Ladder Polymer Field-Effect Transistors. *J. Am. Chem. Soc.* **2003**, *125* (45), 13656–13657, DOI: 10.1021/ja0371810.

12. Alam, M. M.; Jenekhe, S. A. Efficient Solar Cells from Layered Nanostructures of Donor and Acceptor Conjugated Polymers. *Chem. Mater.* **2004**, *16* (23), 4647–4656, DOI: 10.1021/cm0497069.

13. Jenekhe, S. A.; Yi, S. Efficient Photovoltaic Cells from Semiconducting Polymer Heterojunctions. *Appl. Phys. Lett.* **2000**, *77* (17), 2635–2637, DOI: 10.1063/1.1320022.

14. Sun, H.; Vagin, M.; Wang, S.; Crispin, X.; Forchheimer, R.; Berggren, M.; Fabiano, S. Complementary Logic Circuits Based on High-Performance n-Type Organic Electrochemical Transistors. *Adv. Mater.* **2018**, *30* (9), 1704916, DOI: 10.1002/adma.201704916.

15. Surgailis, J.; Savva, A.; Druet, V.; Paulsen, B. D.; Wu, R.; Hamidi-Sakr, A.; Ohayon, D.; Nikiforidis, G.; Chen, X.; McCulloch, I.; Rivnay, J.; Inal, S. Mixed Conduction in an N-Type Organic Semiconductor in the Absence of Hydrophilic Side-Chains. *Adv. Funct. Mater.* **2021**, *31* (21), 2010165, DOI: 10.1002/adfm.202010165.

16. Wu, H.-Y.; Yang, C.-Y.; Li, Q.; Kolhe, N. B.; Strakosas, X.; Stoeckel, M.-A.; Wu, Z.; Jin, W.; Savvakis, M.; Kroon, R.; Tu, D.; Woo, H. Y.; Berggren, M.; Jenekhe, S. A.; Fabiano, S. Influence of Molecular Weight on the Organic Electrochemical Transistor Performance of Ladder-Type Conjugated Polymers. *Adv. Mater.* **2022**, *34* (4), 2106235, DOI: 10.1002/adma.202106235.

17. Babel, A.; Wind, J. D.; Jenekhe, S. A. Ambipolar Charge Transport in Air-Stable Polymer Blend Thin-Film Transistors. *Adv. Funct. Mater.* **2004**, *14* (9), 891–898, DOI: 10.1002/adfm.200305180.

18. Kim, F. S.; Ahmed, E.; Subramaniyan, S.; Jenekhe, S. A. Air-Stable Ambipolar Field-Effect Transistors and Complementary Logic Circuits from Solution-Processed n/p Polymer Heterojunctions. *ACS Appl. Mater. Interfaces.* **2010**, *2* (11), 2974–2977, DOI: 10.1021/am1006996.

19. Kim, F. S.; Park, C. H.; Na, Y.; Jenekhe, S. A. Effects of Ladder Structure on the Electronic Properties and Field-Effect Transistor Performance of Poly(Benzobisimidazobenzophenanthroline). *Org. Electron.* **2019**, *69*, 301–307, DOI: 10.1016/j.orgel.2019.03.049.

20. Wang, S.; Sun, H.; Ail, U.; Vagin, M.; Persson, P. O. Å.; Andreasen, J. W.; Thiel, W.; Berggren, M.; Crispin, X.; Fazzi, D.; Fabiano, S. Thermoelectric Properties of Solution-Processed n-Doped Ladder-Type Conducting Polymers. *Adv. Mater.* **2016,** *28* (48), 10764–10771, DOI: 10.1002/adma.201603731.

21. Tam, T. L. D.; Lin, M.; Handoko, A. D.; Lin, T. T.; Xu, J. High-Performance & Thermally Stable n-Type Polymer Thermoelectrics Based on a Benzyl Viologen Radical Cation-Doped Ladder-Type Conjugated Polymer. *J. Mater. Chem. A* **2021**, 9, 11787-11793, DOI: 10.1039/D1TA01645H.

22. Yang, C. Y.; Stoeckel, M. A.; Ruoko, T. P.; Wu, H. Y.; Liu, X.; Kolhe, N. B.; Wu, Z.; Puttisong, Y.; Musumeci, C.; Massetti, M.; Sun, H.; Xu, K.; Tu, D.; Chen, W. M.; Woo, H. Y.; Fahlman, M.; Jenekhe, S. A.; Berggren, M.; Fabiano, S. A High-Conductivity n-Type Polymeric

Ink for Printed Electronics. *Nat. Commun.* **2021**, *12* (1), 2345, DOI: 10.1038/s41467-021-22528-y.

23. Volkov, A. V.; Sun, H.; Kroon, R.; Ruoko, T.-P.; Che, C.; Edberg, J.; Muller, C.; Fabiano, S.; Crispin, X. Asymmetric Aqueous Supercapacitor Based on P- and n-Type Conducting Polymers. *ACS Appl. Energy Mater.* **2019**, *2* (8), 5350–5355, DOI: 10.1021/acsaem.9b00853.

24. Xu, K.; Sun, H.; Ruoko, T.-P.; Wang, G.; Kroon, R.; Kolhe, N. B.; Puttisong, Y.; Liu, X.; Fazzi, D.; Shibata, K.; Yang, C.-Y.; Sun, N.; Persson, G.; Yankovich, A. B.; Olsson, E.; Yoshida, H.; Chen, W. M.; Fahlman, M.; Kemerink, M.; Jenekhe, S. A.; Müller, C.; Berggren, M.; Fabiano, S. Ground-State Electron Transfer in All-Polymer Donor–Acceptor Heterojunctions. *Nat. Mater.* **2020**, *19* (7), 738–744, DOI: 10.1038/s41563-020-0618-7.

25. Cheng, P.; Zhao, X.; Zhan, X. Perylene Diimide-Based Oligomers and Polymers for Organic Optoelectronics. *Acc. Mater. Res.* **2022**, *3* (3), 309–318, DOI: 10.1021/accountsmr.1c00191.

26. Li, C.; Wonneberger, H. Perylene Imides for Organic Photovoltaics: Yesterday, Today, and Tomorrow. *Adv. Mater.* **2012**, *24* (5), 613–636, DOI: 10.1002/adma.201104447.

27. Zhou, N.; Facchetti, A. Naphthalenediimide (NDI) Polymers for All-Polymer Photovoltaics. *Mater.* **2018**, *21* (4), 377–390, DOI: 10.1016/j.mattod.2018.02.003.

28. Sommer, M. Conjugated Polymers Based on Naphthalene Diimide for Organic Electronics. *J. Mater. Chem. C* **2014**, *2* (17), 3088–3098, DOI: 10.1039/C3TC31755B.

29. Zhan, X.; Facchetti, A.; Barlow, S.; Marks, T. J.; Ratner, M. A.; Wasielewski, M. R.; Marder, S. R. Rylene and Related Diimides for Organic Electronics. *Adv. Mater.* **2011**, *23* (2), 268–284, DOI: 10.1002/adma.201001402.

30. Kumar, S.; Shukla, J.; Kumar, Y.; Mukhopadhyay, P. Electron-Poor Arylenediimides. *Org. Chem. Front.* **2018**, *5* (14), 2254–2276, DOI: 10.1039/C8QO00256H.

31. Guo, X.; Tu, D.; Liu, X. Recent Advances in Rylene Diimide Polymer Acceptors for All-Polymer Solar Cells. *J. Energy Chem.* **2015**, *24* (6), 675–685, DOI: 10.1016/j.jechem.2015.11.003.

32. Fuktomi, Y.; Nakano, M.; Hu, J. Y.; Osaka, I.; Takimiya, K. Naphthodithiophenediimide (NDTI): Synthesis, Structure, and Applications. *J. Am. Chem. Soc.* **2013**, *135* (31), 11445-11448, DOI: 10.1021/ja404753r.

33. Imai, K.; Kurihara, M.; Mathias, L.; Wittmann, J.; Alston, W. B.; Stille, J. K. Synthesis and Properties of Thermally Stable Ladder Polymers Containing the 1,4-Pyrazine Ring Obtained from Polyheterocyclizations of Tetramines and Tetraketones in Poly(Phosphoric Acid) and m-Cresol. *Macromolecules* **1973**, *6* (2), 158–162, DOI: 10.1021/ma60032a002.

34. Sicree, A. J.; Arnold, F. E.; Deusen, R. L. V. New Imidazoisoquinoline Ladder Polymers. *J. Polym. Sci. Polym. Chem.* **1974**, *12* (2), 265–272, DOI: 10.1002/pol.1974.170120202.

35. Gerber, A. H. Thermally Stable Polymers Derived from 2,3,5,6-Tetraaminopyridine. *J. Polym. Sci. Polym. Chem.* **1973**, *11* (7), 1703–1719, DOI: 10.1002/pol.1973.170110718.

36. Hirvonen, S.; Tenhu, H. Modification of Naphthalenic Unit in BBL Main Chain. *Synth. Met.* **2015**, *207*, 87–95, DOI: 10.1016/j.synthmet.2015.06.013.

37. Arnold, F. E. Ladder Polymers from Tetraaminodiquinoxalpyrene. *J. Polym. Sci. A. Polym. Chem.* **1970**, *8* (8), 2079–2089, DOI: 10.1002/pol.1970.150080816.

38. Tonzola, C. J.; Alam, M. M.; Kaminsky, W.; Jenekhe, S. A. New N-Type Organic Semiconductors: Synthesis, Single Crystal Structures, Cyclic Voltammetry, Photophysics, Electron Transport, and Electroluminescence of a Series of Diphenylanthrazolines. *J. Am. Chem. Soc.* **2003**, *125* (44), 13548–13558,DOI: 10.1021/ja036314e.

39. Mortensen, J.; Heinze, J. The Electrochemical Reduction of Benzene—First Direct Determination of the Reduction Potential. *Angew. Chem. Int. Ed.* **1984**, *23* (1), 84–85, DOI: 10.1002/anie.198400841.

40. Kim, D. H.; Han, Y. W.; Moon, D. K. A Comparative Investigation of Dibenzo[a,c]Phenazine and Quinoxaline Donor–Acceptor Conjugated Polymers: Correlation of Planar Structure and Intramolecular Charge Transfer Properties. *Polymer* **2019**, *185* (17), 121906, DOI: 10.1016/j.polymer.2019.121906.

41. Zhang, Y.; Zou, Y.; Yip, H. L.; Chen, K. S.; Zeigler, D. F.; Sun, Y.; Jen, A. K. Y. Indacenodithiophene and Quinoxaline-Based Conjugated Polymers for Highly Efficient Polymer Solar Cells. *Chem. Mater.* **2011**, *23* (9), 2289–2291, DOI: 10.1021/cm200316s.

42. He, R.; Yu, L.; Cai, P.; Peng, F.; Xu, J.; Ying, L.; Chen, J.; Yang, W.; Cao, Y. Narrow-Band-Gap Conjugated Polymers Based on 2,7-Dioctyl-Substituted Dibenzo[a,c]Phenazine Derivatives for Polymer Solar Cells. *Macromolecules* **2014,** *47* (9), 2921–2928, DOI: 10.1021/ma500333r.

43. Kim, J. H.; Song, C. E.; Kim, H. U.; Kang, I.-N.; Shin, W. S.; Park, M. J.; Hwang, D. H. New Quinoxaline Derivatives as Accepting Units in Donor–Acceptor Type Low-Band Gap Polymers for Organic Photovoltaic Cells. *J. Polym. Sci. A. Polym. Chem.* **2013**, *51* (19), 4136–4149, DOI: 10.1002/pola.26823.

44. Fan, Q.; Liu, Y.; Xiao, M.; Tan, H.; Wang, Y.; Su, W.; Yu, D.; Yang, R.; Zhu, W. Donor–Acceptor Copolymers Based on Benzo[1,2-b:4,5-B′]Dithiophene and Pyrene-Fused Phenazine for High-Performance Polymer Solar Cells. *Org. Electron.* **2014**, *15* (11), 3375–3383, DOI: 10.1016/j.orgel.2014.09.019.

45. Li, Y.; Fu, Y.; Tong, H.; Xie, Z.; Wang, L. Effect of Side-Chain Positions on Morphology and Photovoltaic Properties of Phenazine-Based Donor–Acceptor Copolymers. *J. Polym. Sci. A. Polym. Chem.* **2013**, *51* (13), 2910–2918, DOI: 10.1002/pola.26684.

46. Li, G.; Lu, Z.; Li, C.; Bo, Z. The Side Chain Effect on Difluoro-Substituted Dibenzo[a,c]Phenazine Based Conjugated Polymers as Donor Materials for High Efficiency Polymer Solar Cell. *Polym. Chem.* **2015**, *6* (9), 1613–1618, DOI: 10.1039/C4PY01276C.

47. Wang, K.; Jiang, P.; Zhang, Z. G.; Fu, Q.; Li, Y. Synthesis and Photovoltaic Properties of D–A Copolymers Based on 11,12-Difluorodibenzo[a,c]Phenazine Acceptor Unit. *Macromol. Chem. Phys.* **2013**, *214* (16), 1772–1779, DOI: 10.1002/macp.201300299.

48. Zhu, Y.; Gibbons, K. M.; Kulkarni, A. P.; Jenekhe, S. A. Polyfluorenes Containing Dibenzo[a,c]Phenazine Segments: Synthesis and Efficient Blue Electroluminescence from Intramolecular Charge Transfer States. *Macromolecules* **2007**, *40* (4), 804–813, DOI: 10.1021/ma062445z.

49. Li, Y.; Meng, B.; Tong, H.; Xie, Z.; Wang, L. A Chlorinated Phenazine-Based Donor–Acceptor Copolymer with Enhanced Photovoltaic Performance. *Polym. Chem.* **2014**, *5* (6), 1848–1851, DOI: 10.1039/C3PY01436C.

50. Zhang, J.; Cai, W.; Huang, F.; Wang, E.; Zhong, C.; Liu, S.; Wang, M.; Duan, C.; Yang, T.; Cao, Y. Synthesis of Quinoxaline-Based Donor−Acceptor Narrow-Band-Gap Polymers and Their Cyclized Derivatives for Bulk-Heterojunction Polymer Solar Cell Applications. *Macromolecules* **2011**, *44* (4), 894–901, DOI: 10.1021/ma1027164.

51. Li, S.; He, Z.; Yu, J.; Chen, S.; Zhong, A.; Tang, R.; Wu, H.; Qin, J.; Li, Z. How the Linkage Positions Affect the Performance of Bulk-Heterojunction Polymer Solar Cells. *J. Mater. Chem.* **2012**, *22* (25), 12523–12531, DOI: 10.1039/C2JM32002A.

52. Zhang, X.; Won Shim, J.; Prakash Tiwari, S.; Zhang, Q.; E. Norton, J.; Wu, P.-T.; Barlow, S.; Jenekhe, S. A.; Kippelen, B.; Brédas, J. L.; Marder, S. M. Dithienopyrrole – Quinoxaline / Pyridopyrazine Donor–Acceptor Polymers : Synthesis and Electrochemical, Optical, Charge-Transport, and Photovoltaic Properties. *J. Mater. Chem.* **2011**, *21* (13), 4971–4982,DOI: 10.1039/C0JM04290K.

53. Izumi, A.; Nomura, R.; Masuda, T. Synthesis of A New Class of N-Dopable and Photoluminescent Conjugated Polymers Having Phenazine Units in the Main Chain. *Macromolecules* **2000**, *33* (24), 8918–8920, DOI: 10.1021/ma001282q.

54. Bischak, C. G.; Flagg, L. Q.; Yan, K.; Li, C.-Z.; Ginger, D. S. Fullerene Active Layers for N-Type Organic Electrochemical Transistors. *ACS Appl. Mater. Interfaces* **2019**, *11* (31), 28138–28144, DOI: 10.1021/acsami.9b11370.

55. Savva, A.; Ohayon, D.; Surgailis, J.; Paterson, A. F.; Hidalgo, T. C.; Chen, X.; Maria, I. P.; Paulsen, B. D.; Petty II, A. J.; Rivnay, J.; McCulloch, I.; Inal, S. Solvent Engineering for High-Performance n-Type Organic Electrochemical Transistors. *Adv. Electron. Mater.* **2019**, *5* (8), 1900249, DOI: 10.1002/aelm.201900249.

56. Feng, K.; Shan, W.; Wang, J.; Lee, J.-W.; Yang, W.; Wu, W.; Wang, Y.; Kim, B. J.; Guo, X.; Guo, H. Cyano-Functionalized n-Type Polymer with High Electron Mobility for High-Performance Organic Electrochemical Transistors. *Adv. Mater.* **2022**, *34* (24), 2201340, DOI: 10.1002/adma.202201340.

57. Moser, M.; Hidalgo, T. C.; Surgailis, J.; Gladisch, J.; Ghosh, S.; Sheelamanthula, R.; Thiburce, Q.; Giovannitti, A.; Salleo, A.; Gasparini, N.; Wadsworth, A.; Zozoulenko, I.; Berggren, M.; Stavrinidou, E.; Inal, S.; McCulloch, I. Side Chain Redistribution as a Strategy to

Boost Organic Electrochemical Transistor Performance and Stability. *Adv. Mater.* **2020**, *32* (37), 2002748, DOI: 10.1002/adma.202002748.

58. Chen, S. E.; Flagg, L. Q.; Onorato, J. W.; Richter, L. J.; Guo, J.; Luscombe, C. K.; Ginger, D. S. Impact of Varying Side Chain Structure on Organic Electrochemical Transistor Performance: A Series of Oligoethylene Glycol-Substituted Polythiophenes. *J. Mater. Chem. A* **2022**, *10* (19), 10738–10749, DOI: 10.1039/D2TA00683A.

59. Moser, M.; Savva, A.; Thorley, K.; Paulsen, B. D.; Hidalgo, T. C.; Ohayon, D.; Chen, H.; Giovannitti, A.; Marks, A.; Gasparini, N.; Wadsworth, A.; Rivnay, J.; Inal, S.; McCulloch, I. Polaron Delocalization in Donor–Acceptor Polymers and Its Impact on Organic Electrochemical Transistor Performance. *Angew. Chem., Int. Ed.* **2021**, *60* (14), 7777–7785, DOI: 10.1002/anie.202014078.

60. Deusen, R. L. V.; Goins, O. K.; Sicree, A. J. Thermally Stable Polymers from 1,4,5,8-Naphthalenetetracarboxylic Acid and Aromatic Tetraamines. *J. Polym. Sci., Part A-1: Polym. Chem.* **1968**, *6* (7), 1777–1793, DOI: 10.1002/pol.1968.150060701.

61. Oosterhout, S. D.; Savikhin, V.; Zhang, J.; Zhang, Y.; Burgers, M. A.; Marder, S. R.; Bazan, G. C.; Toney, M. F. Mixing Behavior in Small Molecule:Fullerene Organic Photovoltaics. *Chem. Mater.* **2017**, *29* (7), 3062–3069, DOI: 10.1021/acs.chemmater.7b00067.

62. Hexemer, A.; Bras, W.; Glossinger, J.; Schaible, E.; Gann, E.; Kirian, R.; MacDowell, A.; Church, M.; Rude, B.; Padmore, H. A SAXS/WAXS/GISAXS Beamline with Multilayer Monochromator. *J. Phys.: Conf. Ser.* **2010**, *247*, 012007, DOI: 10.1088/1742-6596/247/1/012007.

63. Frisch, M. J., *et al*., Gaussian 16, Revision C.01, Gaussian, Inc., Wallingford CT, **2016**.

64. Wolfe, J. F.; Loo, B. H.; Arnold, F. E. Rigid-Rod Polymers. 2. Synthesis and Thermal Properties of Para-Aromatic Polymers with 2,6-Benzobisthiazole Units in the Main Chain. *Macromolecules* **1981**, *14* (4), 915–920, DOI: 10.1021/ma50005a005.

65. Roberts, M. F.; Jenekhe, S. A. Lewis-Acid Coordination-Complexes of Polymers .3. Poly(Benzimidazobenzophenanthroline) Ladder and Semiladder Polymers. *Polymer* **1994**, *35* (20), 4313–4325, DOI: 10.1016/0032-3861(94)90088-4.

66. Lee, B. H.; Marvel, C. S. Rigid-Ladder Polymers: Polymers Containing Anthraquinone Recurring Units. *J. Polym. Sci. A. Polym. Chem.* **1983**, *21* (1), 83–87, DOI: 10.1002/pol.1983.170210109.

67. Antonidas, H.; Abkowitz, M. A.; Osaheni, J. A.; Jenekhe, S. A.; Stolka, M. Effects of Humidity on the Dark Conductivity and Dielectric-Properties of Poly(Benzimidazobenzophenanthroline) Thin-Films. *Chem. Mater.* **1994**, *6* (1), 63–66, DOI: 10.1021/cm00037a014.

68. Choudhury, S. D.; Basu, S. Interaction of Phenazine with Water and DNA Bases. *Spectrochim. Acta A Mol. Biomol. Spectrosc.* **2005**, *62* (1–3), 736–739, DOI: 10.1016/j.saa.2005.02.042.

69. Lee, J.; Kalin, A. J.; Yuan, T.; Al-Hashimi, M.; Fang, L. Fully Conjugated Ladder Polymers. *Chem. Sci.* **2017**, *8* (4), 2503–2521, DOI: 10.1039/c7sc00154a.

70. Fazzi, D.; Negri, F. Addressing the Elusive Polaronic Nature of Multiple Redox States in a π-Conjugated Ladder-Type Polymer. *Adv. Electron. Mater.* **2021**, *7* (1), 2000786, DOI: 10.1002/aelm.202000786.

71. Onwubiko, A.; Yue, W.; Jellett, C.; Xiao, M.; Chen, H.-Y.; Ravva, M. K.; Hanifi, D. A.; Knall, A.-C.; Purushothaman, B.; Nikolka, M.; Flores, J.-C.; Salleo, A.; Brédas, J. L.; Sirringhaus, H.; Hayoz, P.; McCulloch, I. Fused Electron Deficient Semiconducting Polymers for Air Stable Electron Transport. *Nat. Commun.* **2018**, *9* (1), 416, DOI: 10.1038/s41467-018-02852-6.

72. Fazzi, D.; Fabiano, S.; Ruoko, T. P.; Meerholz, K.; Negri, F. Polarons in Pi-Conjugated Ladder-Type Polymers: A Broken Symmetry Density Functional Description. *J. Mater. Chem. C* **2019**, *7* (41), 12876–12885, DOI: 10.1039/c9tc03283e.

73. Brédas, J. L.; Beljonne, D.; Coropceanu, V.; Cornil, J. Charge-Transfer and Energy-Transfer Processes in π-Conjugated Oligomers and Polymers: A Molecular Picture. *Chem. Rev.* **2004**, *104* (11), 4971–5004, DOI: 10.1021/cr040084k.

74. Zade, S. S.; Zamoshchik, N.; Bendikov, M. From Short Conjugated Oligomers to Conjugated Polymers. Lessons from Studies on Long Conjugated Oligomers. *Acc. Chem. Res.* **2011**, *44* (1), 14–24, DOI: /10.1021/ar1000555.

75. Quinto, M.; Jenekhe, S. A.; Bard, A. J. Polymer Films on Electrodes. 30. Electrochemistry and Scanning Electrochemical Microscopy Characterization of Benzimidazolebenzophenanthroline-Type Ladder (BBL) and Semiladder (BBB) Polymer Films. *Chem. Mater.* **2001**, *13* (9), 2824–2832, DOI: 10.1021/cm001426f.

76. Jenekhe, S. A.; Lu, L.; Alam, M. M. New Conjugated Polymers with Donor−Acceptor Architectures: Synthesis and Photophysics of Carbazole−Quinoline and Phenothiazine−Quinoline Copolymers and Oligomers Exhibiting Large Intramolecular Charge Transfer. *Macromolecules* **2001**, *34* (21), 7315–7324, DOI: 10.1021/ma0100448.

77. Agrawal, A. K.; Jenekhe, S. A. Synthesis and Processing of Heterocyclic Polymers as Electronic, Optoelectronic, and Nonlinear Optical Materials. 2. New Series of Conjugated Rigid-Rod Polyquinolines and Polyanthrazolines. *Macromolecules* **1993**, *26* (5), 895–905, DOI: 10.1021/ma00057a003.

78. Spano, F. C.; Silva, C. H- and J-Aggregate Behavior in Polymeric Semiconductors. *Annu. Rev. Phys. Chem.* **2014**, *65* (1), 477–500, DOI: 10.1146/annurev-physchem-040513-103639.

79. Más-Montoya, M.; Janssen, R. A. J. The Effect of H- and J-Aggregation on the Photophysical and Photovoltaic Properties of Small Thiophene–Pyridine–DPP Molecules for Bulk-Heterojunction Solar Cells. *Adv. Funct. Mater.* **2017**, *27* (16), 1605779, DOI: 10.1002/adfm.201605779.

80. Pschirer, N. G.; Bunz, U. H. F. Poly(Fluorenyleneethynylene)s by Alkyne Metathesis: Optical Properties and Aggregation. *Macromolecules* **2000**, *33* (11), 3961–3963, DOI: 10.1021/ma0003250.

81. Kim, F. S; Hwang, D. K; Kippelen, B.; Jenekhe, S. A. Enhanced Carrier Mobility and Electrical Stability of N-Channel Polymer Thin Film Transistors by Use of Low-k Dielectric Buffer Layer. *Appl. Phys. Lett.* **2011**, *99* (17), 173303, DOI: 10.1063/1.3655680.

82. An, X.; Wang, K.; Bai, L.; Wei, C.; Xu, M.; Yu, M.; Han, Y.; Sun, N.; Sun, L.; Lin, J.; Ding, X.; Xie, L.; Zhang, Q.; Qin, T.; Huang, W. Intrinsic Mechanical Properties of the Polymeric Semiconductors. *J. Mater. Chem. C* **2020**, *8* (33), 11631–11637, DOI: 10.1039/D0TC02255A.

83. Zheng, Y.; Wang, G. J. N.; Kang, J.; Nikolka, M.; Wu, H. C.; Tran, H.; Zhang, S.; Yan, H.; Chen, H.; Yuen, P. Y.; Mun, J.; Dauskardt, R. H.; McCulloch, I.; Tok, J. B. H.; Gu, X.; Bao, Z. An Intrinsically Stretchable High-Performance Polymer Semiconductor with Low Crystallinity. *Adv. Funct. Mater.* **2019**, *29* (46), 1905340, DOI: 10.1002/adfm.201905340.

84. Root, S. E.; Savagatrup, S.; Printz, A. D.; Rodriquez, D.; Lipomi, D. J. Mechanical Properties of Organic Semiconductors for Stretchable, Highly Flexible, and Mechanically Robust Electronics. *Chem. Rev.* **2017**, *117* (9), 6467–6499, DOI: 10.1021/acs.chemrev.7b00003.

85. Zhang, S.; Galuska, L. A.; Gu, X. Water-Assisted Mechanical Testing of Polymeric Thin-Films. *J. Polym. Sci.* **2021**, *60* (7), 1108–1129, DOI: 10.1002/pol.20210281.

86. Chen, A. X.; Kleinschmidt, A. T.; Choudhary, K.; Lipomi, D. J. Beyond Stretchability: Strength, Toughness, and Elastic Range in Semiconducting Polymers. *Chem. Mater.* **2020**, *32* (18), 7582–7601, DOI: 10.1021/acs.chemmater.0c03019.

87. Xiao, M.; Sadhanala, A.; Abdi-Jalebi, M.; Thomas, T. H.; Ren, X.; Zhang, T.; Chen, H.; Carey, R. L.; Wang, Q.; Senanayak, S. P.; Jellett, C.; Onwubiko, A.; Moser, M.; Liao, H.; Yue, W.; McCulloch, I.; Nikolka, M.; Sirringhaus, H. Linking Glass-Transition Behavior to Photophysical and Charge Transport Properties of High-Mobility Conjugated Polymers. *Adv. Funct. Mater.* **2021**, *31* (7), 2007359, DOI: 10.1002/adfm.202007359.

88. Zhang, Z.; Yu, Y.; Tang, Y.; Guan, Y.; Hu, Y.; Yin, J.; Willets, K.; Ren, S., Kirigami-Inspired Stretchable Conjugated Electronics. *Adv. Electron. Mater.* **2020**, *6*, 1900929, DOI: 10.1002/aelm.201900929

89. Powell, J. W.; Chartoff, R. P.; Viscoelastic properties and stability of BBL ladder polymers. *J. Appl. Polym. Sci.* **1974**, *18*, 83-91, DOI: 10.1002/app.1974.070180107.

90. Wang, C. S.; Lee, C. Y. C.; Arnold, F. E.; Mechanical and Electrical Properties of Heat-Treated Ladder Polymer Fiber. *MRS Proc.,* **1992,** *247*, 747, DOI: 10.1557/PROC-247-747.

91. Giridharagopal, R.; Flagg, L. Q.; Harrison, J. S.; Ziffer, M. E.; Onorato, J. W.; Luscombe, C. K.; Ginger, D. S. Electrochemical Strain Microscopy Probes Morphology-Induced Variations in Ion Uptake and Performance in Organic Electrochemical Transistors. *Nat. Mater.* **2017**, *16* (7), 737–742, DOI: 10.1038/nmat4918.

92. Flagg, L. Q.; Bischak, C. G.; Onorato, J. W.; Rashid, R. B.; Luscombe, C. K.; Ginger, D. S. Polymer Crystallinity Controls Water Uptake in Glycol Side-Chain Polymer Organic Electrochemical Transistors. *J. Am. Chem. Soc.* **2019,** *141* (10), 4345–4354, DOI: 10.1021/jacs.8b12640.

Chapter 3. Random Copolymers of Poly(benzimidazobenzophenanthrolinedione) Featuring Electron-deficient Cyanated Comonomers for Organic Electronics

Chapter 3.1 Cyanated and Noncyanated Conjugated Ladder Copolymers and Model Compound of Poly(benzimidazobenzophenanthroline): Synthesis, Electronic Structure, and n-Doped Electrical Conductivity

3.1.1 Introduction

Fine-tuning the highest occupied molecular orbital (HOMO) and lowest unoccupied molecular orbital (LUMO) energy levels of π-conjugated polymers is of fundamental interest since these parameters largely dictate their performance in organic electronic devices such as organic photovoltaic devices (OPVs),[1–4] organic field-effect transistors (OFETs),[5–9] and organic electrochemical transistors (OECTs).[10,11] By utilizing electron-deficient building blocks that foster low-lying LUMO energy levels that promote operational device stability in air[12–14] and low barriers to charge injection,[15,16] n-Type (electron conducting) π-conjugated polymers can be realized. Another strategy to deepen the LUMO level of n-type π-conjugated polymers is to attach strong electron-withdrawing moieties onto the polymer backbone; typical electron-withdrawing substituents include halogens (fluorine and chlorine),[17–20] boron-nitrogen coordinate bonds,[21,22] or cyano (CN) groups.[10,23–26] Among these, CN functionalization has been particularly effective in creating deep LUMO levels due to its exceptional electron-withdrawing abilities and small steric bulk that allows for planar backbone topologies.[24,26,27] The first examples of CN-functionalized semiconductors were CN-functionalized perylenes, whereby cyanation facilitated

lower-lying HOMO/LUMO levels and a high electron mobility (μ_e) of 0.64 cm^2/Vs.[28,29] Since then, a large number of cyanated n-type polymers have been developed that utilize CN-functionalized building blocks; typical examples such as indenofluorene (IDF),[30,31] rylene diimide (RDI),[32] diarylimide (DAI),[33,34] benzodiazole (BD),[35–37] and dicyanomethylene indanone (ID)[38] are shown in Chart 3.1. Compared to their non-cyanated counterparts, these CN-functionalized polymers showed a 0.15 eV – 0.45 eV decrease in their LUMO energy levels that was usually accompanied by improved electrical conductivity and/or electron mobility.[26] Clearly, CN functionalization is a simple and effective way to deepen the LUMO levels in π-conjugated polymers.

Chart 3.1. Molecular structures of the (a) representative 2CN-functionalized n-type polymeric building blocks, and (b) the new model compound PCN and ladder polymers BBL-2CN and BBL-*x*2CN random copolymers.

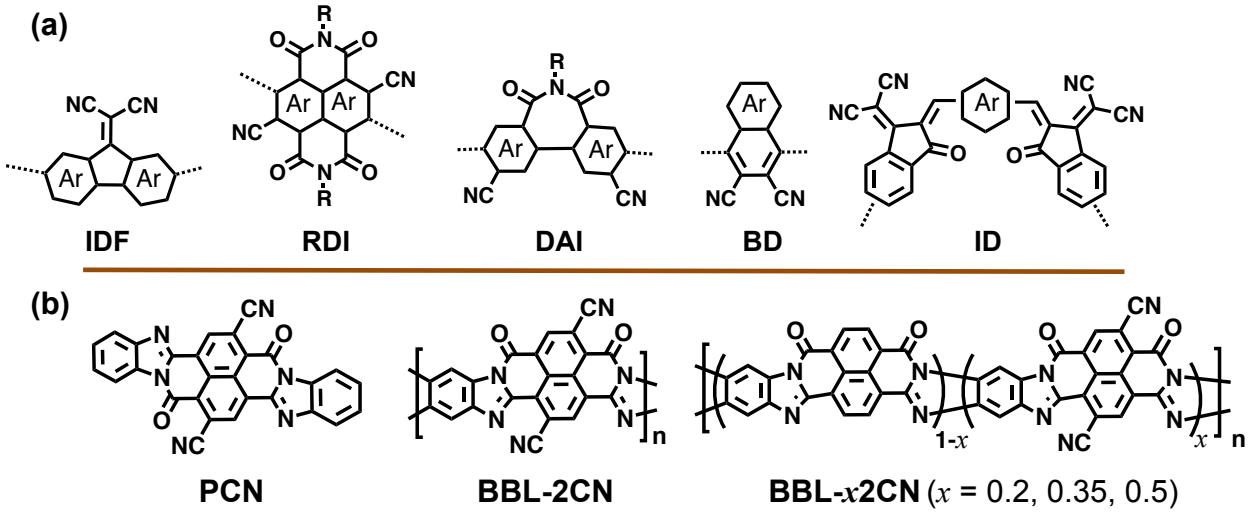

Planarization of the polymeric backbone is another strategy used to fine-tune the energy levels of n-type polymers. One class of polymers that exemplifies this are the π-conjugated rigid-rod ladder polymers that include the well-known prototype n-type ladder poly(benzimidazobenzophenanthroline) (BBL), whose synthesis in 1966 predates that of doped

conducting polymers by over a decade.[39] BBL has seen outstanding success as an n-type semiconducting polymer in OPVs,[40,41] OFETs,[42–44] OECTs,[45–47] and organic thermoelectric devices[48,49] due to its high field-effect electron mobility of ~ 0.1 cm^2/Vs,[50] low LUMO level of -4.16 eV, and extreme chemical and thermal stability. These attributes of BBL are credited to its rigid-rod ladder chain topology that give it a very large persistence length of over 150 nm,[51] tight π-π stacking distances of 3.4 Å,[47] and delocalized molecular orbitals that span several repeat units.[50] Still, only three n-type derivatives of BBL have been reported due to the difficult synthesis of the electron-deficient ladder structure,[19,20,52] and only two of them have shown a deep LUMO level: tetrachlorinated poly(benzimidazoanthradiisoquinolinedione) (Cl_4-BAL) (LUMO = -4.55 eV)[20] and its derivative tetrachlorinated poly(benzimidazoanthradiisoquinolinedione) (Cl_2-BAL) (LUMO = -4.54 eV),[19] both of which show non-planar backbone topologies due to the steric bulk of the chlorine atoms, which is known to disrupt charge transport processes. There are no known examples of n-type derivatives of BBL that are functionalized with electron-deficient moieties and maintain planar backbone topologies.

We report herein the first BBL random copolymer series that features dicyano (2CN) substitution directly on the ladder backbone, BBL-*x*2CN (*x* = 20, 35, 50) (Chart 3.1), which utilizes a novel tetraester monomer, tetraethyl 2,6-cyanonaphthalene-1,4,5,8-tetracarboxylate (NTE-2CN) (3. 1). The model compound 8,17-dioxo-8,17-dihydrobenzo[*lmn*]benzo[4,5]imidazo[2,1-*b*]benzo[4,5]imidazo[2,1-*i*][3,8]phenanthroline-7,16-dicarbonitrile (PCN) (Chart 3.1) was also synthesized in order to aid with structural characterizations of the ladder copolymers. The random copolymer motif was chosen to increase the solubility of the cyanated BBL derivatives in protic acid solutions; we originally synthesized

the novel homopolymer BBL-2CN (Chart 3.1), however we found it to be completely insoluble in acidic solvents, which precluded the study of solution and solid-state properties. The single-crystal structure of NTE-2CN confirms the molecular structure of the monomer. We found that the copolymers and model compound formed high-quality thin films that were used to characterize the molecular structures with Fourier-transform infrared (FTIR), Raman, and X-ray photoelectron (XPS) spectroscopies. The copolymers showed optical bandgaps between 1.60 – 1.65 eV, and cyclic voltammetry measurements revealed that incorporation of 50% NTE-2CN lowers the LUMO level by 0.18 eV compared to BBL. The LUMO level of -4.54 eV of the model compound suggests that the BBL-2CN homopolymer may have a LUMO level beyond -4.34 eV if the solubility issues could be addressed without disrupting planarity. Preliminary results suggest incorporation of 20 – 50 mol% of the 2CN units in the polymer backbone is detrimental to the n-doped conductivities of BBL-*x*2CN polymers.

3.1.2 Experimental Methods.

Materials and Methods. The monomer 1,4,5,8-naphthalenetetracarboxylic acid (NTCA) was purchased from Ambeed and purified according to the procedure.[53] 1,2,4,5-tetraaminobenzene hydrochloride (TABH) was purchased from Ambeed and purified according to a modified published procedure.[54] o-Phenylenediamine, N,N-dimethylformamide (DMF), 1,4,5,8-naphthalenetetracarboxylic anhydride (NTCDA), fuming sulfuric acid (20% free SO_3), dibromohydrantoin (DBH), ethyl iodide (EtI), K_2CO_3, copper (I) cyanide (CuCN), L-proline, conc. hydrochloric acid, polyphosphoric acid (PPA, 84% P_2O_5), toluene, trifluoroacetic acid (TFA), and methanesulfonic acid (MSA) (> 99%) were purchased from Sigma-Aldrich and used as received. Methanol, ethanol, chloroform, dichloromethane, acetone, and hexane were purchased from Fisher Scientific and used as received.

Intrinsic viscosities of the polymers in MSA were measured in an Ubbelohde viscometer suspended in a water bath at 30.0˚C. The concentrations of the polymer solutions were chosen such that the elution time of the polymer solution was 1.1 – 1.8 times that of the pure solvent. The NMR spectra were recorded on a Bruker AV500 (at 500 MHz) using $CDCl_3$ or DMSO-d6 as the solvents. Thermogravimetric analysis (TGA) was conducted on a TA Instrument model Q50 TGA. A heating rate of 10°C /min under a flow of N_2 was used with runs conducted from room temperature to 700°C. Optical absorption spectra were measured on a PerkinElmer model Lambda 900 UV-vis/near-IR spectrophotometer. Solution absorption spectrum was obtained from dilute solutions (10^{-5} M) in MSA or trifluoroacetic acid.

Cyclic voltammetry (CV) experiments were done on an EG&G Princeton Applied Research potentiostat/galvanostat (model 273A). A three-electrode cell was used, using platinum wire as the counter electrode and polymers coated on platinum wires as the working electrode. The reference electrode was $Ag/AgNO_3$ in acetonitrile. The acidic solvent was removed by dipping the substrate in isopropanol (IPA) overnight and was subsequently dried in vacuum oven at 90˚C. The supporting electrolyte solution consists of 0.1 M tetrabutylammonium hexafluorophosphate (Bu_4NPF_6) in anhydrous acetonitrile. The electrolyte was purged with nitrogen for 15 minutes prior to the CV scans to ensure inert and anhydrous conditions. The reduction and oxidation potentials were referenced to the Fc/Fc^+ couple by using ferrocene as an internal standard. The LUMO energy level was estimated using a ferrocene value of -4.8 eV with respect to vacuum level. The LUMO and HOMO levels were determined by using the equations $E_{LUMO} = -(eE_{red}^{onset} + 4.8)$ and $E_{HOMO} = -(eE_{ox}^{onset} + 4.8)$.

Fourier-transform infrared (FTIR) spectroscopy experiments were performed on a Perkin Elmer Frontier spectrometer on the polymer freestanding films and the powdered monomer and

model compound. The resolution was set at 1 cm^{-1} and a set of 16 scans was averaged. Raman spectroscopy of the polymer freestanding films were carried out on a Thermo Scientific DXR2 Raman microscope. A 532-nm laser with a power of 5 mW was focused onto a sample through a 50x objective lens.

Preparation of Thin Films, Doping Method, and Characterization of Electrical Conductivity. Polymer solutions in methanesulfonic acid (MSA) were stirred at elevated temperature (>130^{o}C) for several days to ensure solubilization of the polymer. The polymer solutions were filtered through 1 μm pore size Grade GF/B Glass Microfiber Filters (Whatman GF/B) before use. The filtered polymer solution was then spin-coated onto clean glass substrates (sonicated in acetone, DI water, and isopropanol) at 2000 – 5000 rpm for 30 seconds followed by immersion in isopropanol (IPA) to remove the acidic solvent. The neutral polymer films were dried in a vacuum oven at 60^{o}C overnight.

The undoped neutral polymer films were then moved into a glovebox and annealed at 200^{o}C for 30 minutes prior to doping. 10 mg/mL of N-DMBI in anhydrous chloroform was prepared in the glovebox as the n-type dopant solution. The dopant was deposited onto the neutral polymer film via spin-coating at 1500 rpm for 60 seconds. The doped polymer films were subjected to thermal annealing at 200^{o}C for 20 minutes before being brought to ambient atmosphere for further characterizations.

Electrical conductivity (σ_{dc}) of the doped polymer films were measured by a colinear four-point probe controlled by a Keithley 2400 source-meter unit. For consistency, a 60-second delay between source and measurements was applied. The σ_{dc} value was calculated as follows:

$$\sigma_{dc} = \frac{\pi}{\ln(2)} \frac{1}{R \times t}$$

where σ_{dc} is the room-temperature dc-electrical conductivity (S/cm), R is the measured resistance (Ω), and t is the film thickness (cm).

Synthesis of 4,9-dibromoisochromeno[6,5,4-*def*]isochromene-1,3,6,8-tetraone (NTCDA-2Br). NTCDA (10.0 g, 37.3 mmol) and oleum (93 mL) were combined under nitrogen and stirred. DBH (16.0 g, 55.9 mmol) was added portionwise over 1 hour followed by a temperature increase to 50˚C and the mixture was stirred overnight. The mixture was cooled to room temperature, poured into ice water, and the precipitate was washed with water and methanol and dried under vacuum (18.1 g, > 100% yield). ^{1}H NMR (500 MHz, DMSO-d6, δ): 8.8 ppm (s, 2H).

Synthesis of tetraethyl 2,6-dibromonaphthalene-1,4,5,8-tetracarboxylate (NTE-2Br). NTCDA-2Br (8.0 g, 18.8 mmol), EtI (152.38 g, 977.0 mmol), and K_2CO_3 (15.6 g, 112.8 mmol) were combined under nitrogen and refluxed in EtOH (50 mL) for 15 hours. The ethanol was removed on a rotary evaporator, and DCM was added and washed with water. Purification on a silica gel column with 70% DCM/hexane gave the pure white powder. (5.31 g, 50% yield). ^{1}H NMR (500 MHz, $CDCl_3$, δ): 8.01 ppm (s, 2H), 4.31 (t, 13H, J = 5.3 Hz), 1.35 ppm (m, 15H).

Synthesis of tetraethyl 2,6-cyanonaphthalene-1,4,5,8-tetracarboxylate (NTE-2CN). NTE-2Br (4.0 g, 6.97 mmol), L-proline (1.6 g, 14.0 mmol), CuCN (2.5 g, 27.9 mmol), and anhydrous DMF (320 mL) were combined under nitrogen and heated at 120˚C for 72 hours. The DMF was removed under vacuum and the crude mixture was purified on silica gel column with 80% DCM/hexane followed by trituration from DCM with methanol and recrystallization in EtOH to give the pure product as white needles (1.18 g, 36% yield). ^{1}H NMR (500 MHz, $CDCl_3$, δ): 8.21 ppm (s, 2H), 4.43 ppm (q, 4H, J = 7.05 Hz), 4.35 ppm (q, 4H, J = 7.05 Hz), 1.43 ppm (t, 6H, J = 7.85 Hz), 1.38 ppm (t, 6H, J = 7.85 Hz). ^{13}C NMR (500 MHz, $CDCl_3$, δ): 165.6, 164.5, 138.0, 134.4, 132.0, 130.0, 115.7, 113.8, 63.6, 63.0, 14.1, 13.7 ppm. Anal. calcd for $C_{24}H_{22}N_2O_8$ (%)**:** C, 61.80; H, 4.75; N, 6.01; O, 27.44; found (%):C, 61.55; H, 4.73; N, 5.98.

Synthesis of the Model Compound 8,17-dioxo-8,17-dihydrobenzo[*lmn*]benzo[4,5]imidazo[2,1-*b*]benzo[4,5]imidazo[2,1-*i*][3,8]phenanthroline-7,16-dicarbonitrile (PCN). PPA (10.00 g) was added to a reaction flask equipped with a mechanical stirrer and was purged with nitrogen overnight at 150˚C. The PPA was cooled to room temperature, and NTE-2CN (0.330 g, 0.71 mmol) and o-phenylenediamine (0.191 g, 1.77 mmol) were added. The mixture was stirred for 1 h at room temperature, then the temperature was increased slowly to 150˚C over the course of 2 h. The mixture was stirred overnight and then cooled to room temperature, quenched with EtOH (2 L) and stirred for 1 h before filtering. This was repeated 3 times until the pH of the filtrate was neutral. The crude product was prufied by adding toluene (100 mL) and stirring the slurry for 1 h at 120˚C and filtering three times. This gave the red mixed-isomer product (0.150 g, 50% yield). ^{1}H NMR (500 MHz, DMSO-d6, δ): 9.06 – 8.91 ppm (m, 0.4H), 8.71 – 8.59 ppm (m, 1H), 8.39 – 8.25 ppm (m, 1.3H), 8.10 – 8.08 ppm (m, 0.4H), 7.94 – 7.77 ppm (m, 2H), 7.52 – 7.35 ppm (m, 3H). ^{13}C NMR (500 MHz, DMSO-d6 δ): 169.0, 159.0, 144.0, 143.8, 132.3, 131.7, 132.3, 131.7, 127.1, 127.0, 126.7, 125.4, 121.1, 120.9, 115.9, 115.7, 115.8 ppm. MS (ESI, m/z): $[M + MeOH]^+$ for $C_{29}H_{14}N_6O_3$ calcd: 493.1, found: 493.1.

Synthesis of Polymer BBL-202CN. PPA (35.89 g) was added to a reaction flask equipped with a mechanical stirrer and purged with nitrogen at 150˚C overnight. The PPA was cooled to room temperature and TABH (1.5 g, 5.28 mmol) was added. Dehydrochlorination was allowed to proceed at 75˚C for 24 h. Then, NTE-2CN (0.501 g, 1.08 mmol) and NTCA (1.29 g, 4.23 mmol) were added at the same time. The polymerization mixture was then stirred at 80˚C for 4 hours followed by an incremental temperature increase to 100˚C over 5 hours and then stirred overnight. The temperature of the polymerization mixture was then increased to 150˚C over 8

hours and was stirred overnight to allow the polymer to solidified. The solid polymer dope was cooled to room temperature, quenched with water, and purified via Soxhlet extraction with water for 48 h and methanol for 24 h. The crude product was dried and further purified by reprecipitation from MSA into methanol (yield 1.85 g, 100%). Intrinsic viscosity ([η]): 4.2 dL/g (30.0 °C, MSA).

Synthesis of Polymer BBL-352CN. The polymerization was conducted in the same manner as for BBL-202CN except that 35 mol% of NTE-2CN monomer was used. PPA (30.0 g), TABH (1.27 g, 4.47 mmol), NTE-2CN (0.73 g, 1.57 mmol) and NTCA (0.88 g, 2.91 mmol), (yield 1.63 g, 99%). Intrinsic viscosity ([η]): 1.6 dL/g (30.0 °C, MSA).

Synthesis of Polymer BBL-502CN. The polymerization was conducted in the same manner as for BBL-202CN except that 50 mol% of NTE-2CN monomer was used. PPA (26.0 g), TABH (1.07g, 3.77 mmol), NTE-2CN (0.88 g, 1.89 mmol) and NTCA (0.575 g, 1.89 mmol), (yield 1.39 g, 99%). Intrinsic viscosity ([η]): 1.5 dL/g (30.0 °C, MSA).

3.1.3 Results and Discussion.

3.1.3.1. Synthesis and Characterization. The synthetic details are in the Experimental Methods section, and the reactions are shown in Scheme 3.1. Starting from dibromoisochromeno[6,5,4-*def*]isochromene-1,3,6,8-tetraone (NTCDA, **1**) (Scheme 3.1), the dibromo precursor 4,9-dibromoisochromeno[6,5,4-*def*]isochromene-1,3,6,8-tetraone (NTCDA-2Br, **2**) was synthesized according to the known procedure[55] and was used without further purification. Esterification of **2** using ethyl iodide in ethanol produced the tetraester intermediate, tetraethyl 2,6-dibromonaphthalene-1,4,5,8-tetracarboxylate (NTE-2Br, **3**) which was purified using column chromatography. Finally, **3** was subjected to cyanation in N,N-dimethylformamide (DMF) using an L-proline promoted Rosenmund-von Braun reaction.[56] The novel cyanated monomer NTE-

2CN (**4**) was purified using column chromatography, trituration with methanol in chloroform, and finally recrystallized in ethanol to give **4** as pure white needles in a yield of 36%. The ^{1}H NMR spectra of **2**-**4** are shown in Figures B.1-B.3, and the ^{13}C NMR and Fourier-transform infrared (FTIR) spectra of **4** are in Figure B.4-B.5, respectively.

Scheme 3.1. Synthesis of (a) the new NTE-2CN monomer, (b) PCN model compound, and (c) conjugated random copolymers, BBL-*x*2CN. (DBH = dibromohydrantoin, EtI = ethyl iodide, EtOH = ethanol, DMF = dimethylformamide, PPA = polyphosphoric acid, 84% free P_2O_5).

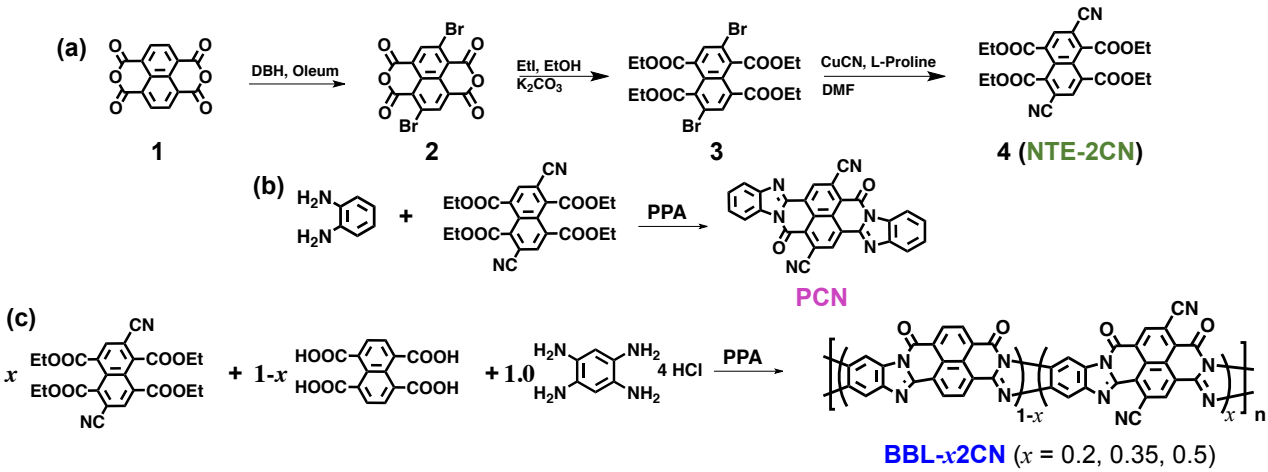

To confirm the isomeric distribution of the cyano groups on the naphthalene backbone, NTE-2CN was subjected to single-crystal X-ray diffraction analysis (Figure 3.1, Tables B.1-B.2). Note that in Figure 3.1, the hydrogen atoms and ester side chain disorder have been omitted for clarity. The NTE-2CN molecules belong to the C2/c space group and are aligned in a monoclinic unit cell with a = 15.2471(10) Å, b = 18.2853(13) Å, c = 8.4312(6) Å, α = 90˚, β = 98.299(4) ˚, γ = 90˚. The NTE-2CN cyanated naphthalene core has a planar geometry and the cyano groups are appended exclusively on the 2,6-positions of the naphthalene ring (Figure 3.1a). The molecules form a face-to-face π-π stacking motif with an intermolecular distance of 3.9 Å (Figure 3.1b-c); the relatively large π-π stacking distance is a result of the steric bulk of the

ester groups that prevent close intermolecular contact. These results demonstrate the molecular structure of the cyanated ester monomer.

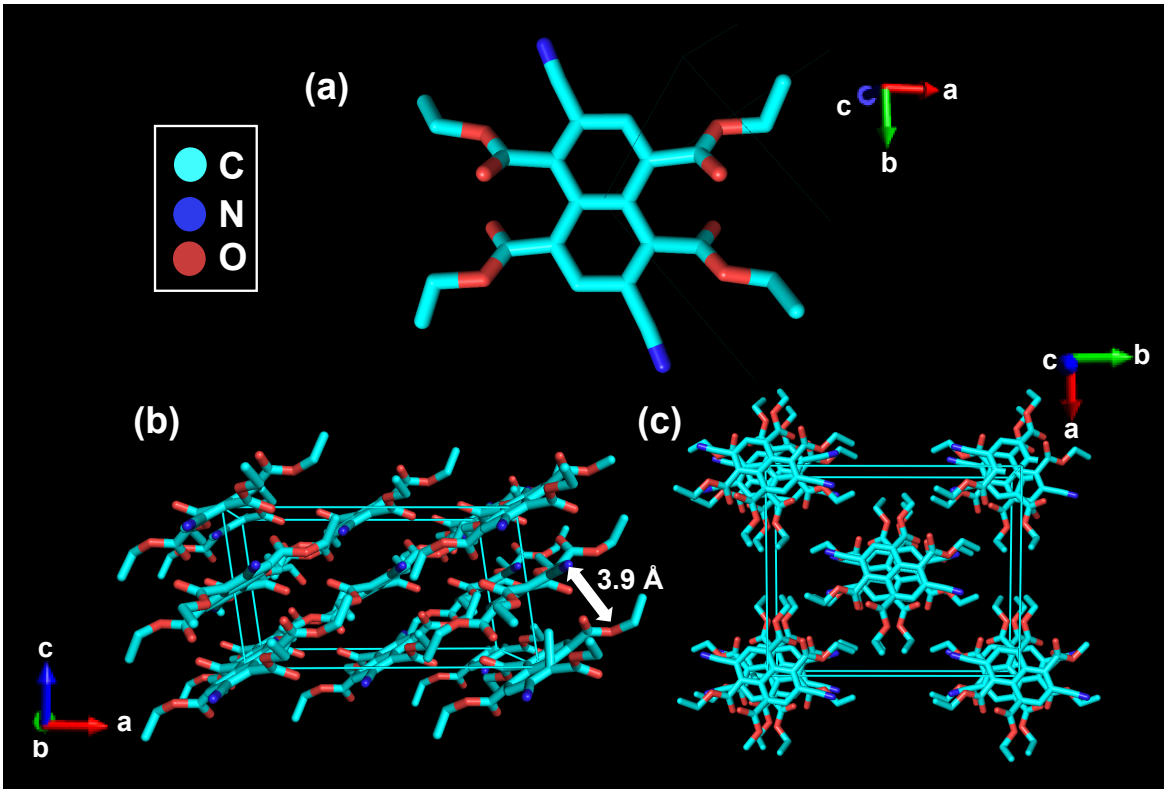

Figure 3.1. Single crystal structure analysis of the monomer NTE-2CN. (a) Skeletal structure with atoms placed at the center of the thermal ellipsoids that were calculated at the 50% probability level. (b) Side view and (c) top view of the unit cell showing face-to-face π-π stacking with an intermolecular distance of 3.9 Å. The hydrogens and ester group disorder have been eliminated for clarity.

The model compound 8,17-dioxo-8,17-dihydrobenzo[*lmn*]benzo[4,5]imidazo[2,1-*b*]benzo[4,5]imidazo[2,1-*i*][3,8]phenanthroline-7,16-dicarbonitrile (PCN) (Scheme 3.1) was synthesized in dilute polyphosphoric acid (PPA) as described in the Experimental Methods section. After 12 h at 150˚C, the mixture was quenched with hot ethanol and filtered three times

to remove the PPA. Since PCN has very limited solubility in highly polar solvents, it was purified by stirring the slurry in hot toluene and filtering three times, which gave the clean product after drying. The structure of PCN was characterized by ^{1}H NMR in DMSO-d6 solution; however due to the isomeric structures of PCN, there are many overlapping peaks in the aromatic region (Figure B.6), which make unambiguous peak assignment difficult. However, based off of the reported ^{1}H NMR spectra of the perinone compound,[57,58] general peak assignments can be made. The broad overlapping resonances at 7.3 ppm, 7.5 ppm, 7.7 – 7.9 ppm, and 8.2 – 8.3 ppm are assigned to the benzene protons, and the overlapping peaks at 8.5 ppm, 8.6 ppm, 8.7 ppm, and 8.9 – 9.0 ppm are due to the naphthalene protons. (Figure B.6). The ^{13}C NMR spectrum shows peaks characteristic of the molecular structure of PCN (Figure B.7). Specifically, the peak at 169.0 ppm is assigned to the carbonyl carbon (C=O), the overlapping peaks at 159.0 ppm are from the imine/amide carbons (C=N/C-N), and the peaks ranging from 115.8– 115.9 ppm are due to nitrile (CN) and C-CN carbons. The broad and overlapping resonances of the peaks are likely from the isomeric structures of PCN (Figure B.7). Finally, electrospray ionization mass spectrometry (ESI mass) was conducted on dilute PCN solutions (10^{-6} M) in MeOH (Figure B.8). The calculated M + MeOH m/z of 493.1 is well matched with the measured m/z of 493.1 in positive ion mode.

The random copolymers were synthesized in pure PPA using 1 equivalent of TABH, and varying equivalents of NTCA and NTE-2CN (Scheme 3.1). For example, BBL-202CN was synthesized from 0.2 equivalents of NTE-2CN and 0.8 equivalents of NTCA, BBL-352CN from 0.35 equivalents of NTE-2CN and 0.65 equivalents of NTCA, and BBL-502CN from 0.5 equivalents of each. The addition of the electron-deficient NTE-2CN monomer dramatically increased the efficiency of the polymerization such that it completed in ~12 hours at 150˚C; this

is in contrast to BBL in which the ring annulation takes place at 180˚C over several days. This result can be attributed to the increased reactivity of the NTE-2CN monomer reduced the thermodynamic and kinetic barrier for the polycondensation. The intrinsic viscosities ([η]) of the polymers measured in methanesulfonic acid (MSA) at 30˚C are 4.2 dL/g, 1.6 dL/g, and 1.5 dL/g for BBL-202CN, BBL-352CN, and BBL-502CN, respectively. The lower [η] values of the BBL-352CN and BBL-502CN polymers stem from the low solubility of these polymers in MSA solutions. Specifically, 30% - 50% of the polymer mass was lost when the MSA solutions were filtered before precipitation, which is likely the insoluble higher molecular weight polymer fractions. Therefore, the purified polymer precipitated from the filtrate contains the lower molecular weight fractions. Thermogravimetric analysis shows that the polymers and model compound are thermally stable with high thermal decomposition temperatures (T_d = 306˚C - 523˚C) and retain more than 70% of their mass at 700˚C (Figure B.9).

The FTIR spectrum of the model compound shown in Figures 3.2a, and the FTIR and Raman spectra of the copolymer freestanding films are shown in Figure 3.2b-c. The peak vibrations and their assignments are in Tables B.3-B.4. We note that the high fluorescence of PCN precluded the acquisition of the Raman spectrum, which is similar to what is reported for perinone.[59] The sharp *v*(C=O) carbonyl stretching mode for the PCN model compound is at 1701 cm^{-1} on the FTIR spectrum (Table B.3). For the polymers, the *v*(C=O) stretches are at 1705 cm^{-1} and 1706 cm^{-1} on the FTIR and Raman spectra, respectively (Table B.4). The intense *v*(C=N) imine stretches can be seen at 1590 cm^{-1} on the FTIR spectrum for PCN (Table B.3), and at 1581 cm^{-1} and 1594 cm^{-1} on the FTIR and Raman spectra, respectively, for the copolymers (Table B.4). Furthermore, single bond *v*(C-N) carbon-nitrogen stretches are seen on the FTIR spectra as medium intensity bands at 1374 cm^{-1} and 1335 cm^{-1} for PCN, and 1373 cm^{-1} and 1304 cm^{-1} for

the copolymers. On the Raman spectra, these peaks appear at 1401 cm^{-1} for the copolymers (Tables B.3 and B.4). We note that the nitrile stretches are absent on all FTIR and Raman spectra, which is in accordance with the FTIR and Raman spectra calculated using density functional theory (DFT) at the ωB97XD 6-31G(d,p) level of theory for the PCN model compound and BBL-502CN oligomer comprised of 6 repeat units (Figure B.10a-c). The combined FTIR and Raman stretches closely match those reported for BBL[60] and provide strong evidence for the molecular structures of the new random copolymers and model compound.

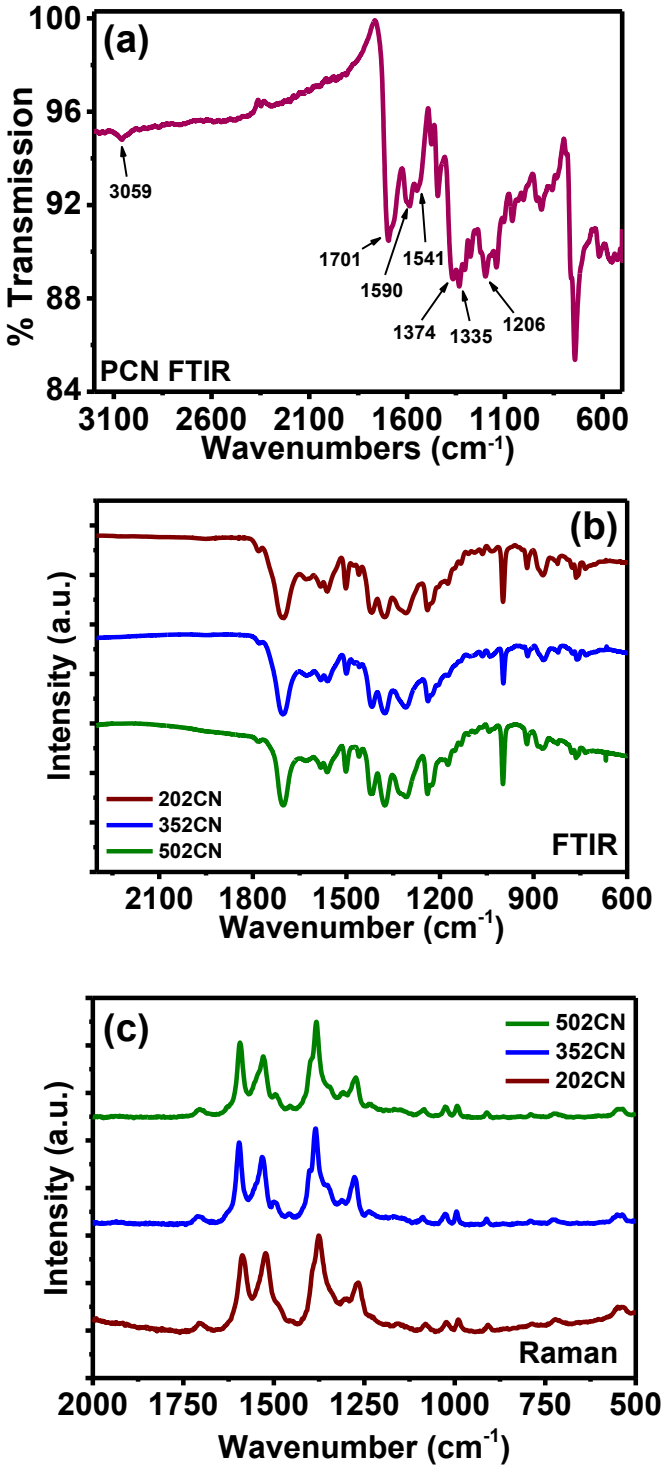

Figure 3.2. (a) The FTIR spectrum of the model compound PCN. (b) The FTIR and (c) Raman spectra of the copolymers.

To further characterize the molecular structures of the novel monomer, model compound, and copolymers, X-ray photoelectron spectroscopy (XPS) was performed on the NTE-2CN needles, and thin films on silicon substrates of PCN and random copolymers. The survey scans are in Figure B.11, the high-resolution scans with optimal peak fitting in Figure 3.3 and B.12, and the tables of C 1s and N 1s binding energies, N 1s Full-Width at Half-Maximum (FWHM), and the residual standard deviations (RSTD) of the N 1s peak fittings are in Tables B.5-B.6. The details of the experimental setup are in the Appendix B. The XPS surveys scans (Figure B.11a-f) shows peaks in the 250 eV – 550 eV regions and are assigned to O 1s, N 1s, and C 1s emissions. The optimal fit of the C 1s spectra (Figure B.12a-f) shows peaks that are similar to what was previously reported for BBL.[61] The peaks at 285.0 eV are associated with C-H/C-C emissions, those typically observed around 285.7 eV are from C=C emissions, and those around 287.0 eV are assigned to C-N emissions (Table B.5). For NTE-2CN, there is a high intensity peak at 286.9 eV that is associated with the C-O emissions of the ester (Table B.5). Finally, the peaks around 288.9 eV and 290.1 eV are assigned to the C=N/C=O and the π-π^* satellite peaks, respectively (Table B.5).

The high-resolution N 1s spectra in Figure 3.3a was best fitted with one peak for NTE-2CN at 399.5 eV from the nitrile group emissions. The N 1s spectra for the model compound and random copolymers show notable differences (Figures 3.3b-f and B.10). First, the binding energies (B.E) vary between 400.6 eV to 401.4 eV for the amide emissions, and between 398.4 eV to 399.3 eV for the combined imine/nitrile emissions (Table B.6) that spectrally broadened as the mol% of CN groups increase. Second, the residual standard deviations (RSTD) are substantially decreased using a 3-peak fit compared to a 2-peak fit (Table B.6). The most likely explanation for these trend is that the nitrile N 1s emissions are overlapping with the imine N 1s

emissions[62,63] such that increasing the mol% of 2CN groups on the backbone is accompanied by a slight variance in B.E. values and decreasing RSTDs using a 3-peak fit (Table B.3). These XPS results give strong evidence for the molecular structures of the cyanated and non-cyanated random copolymers and model compound.

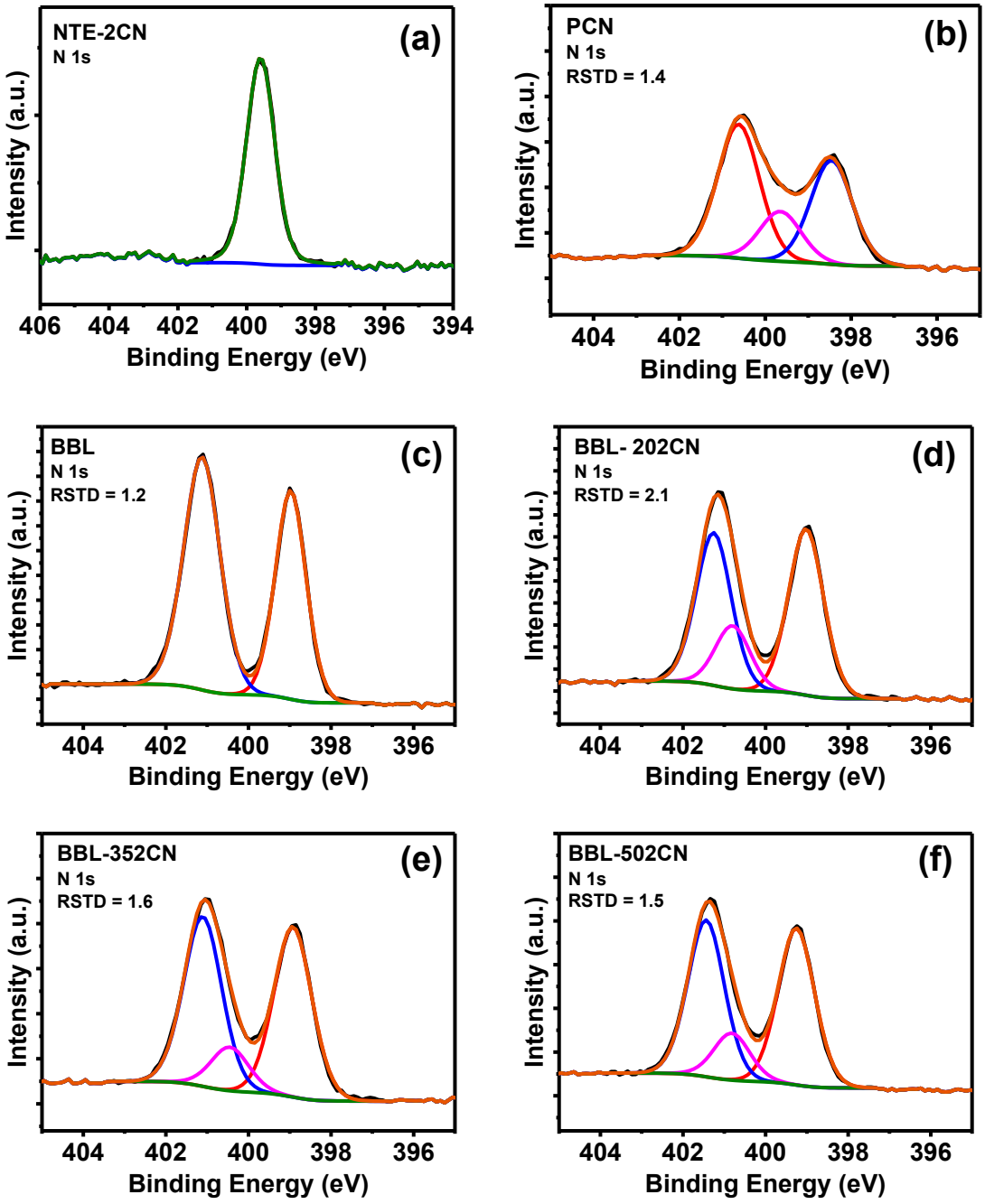

Figure 3.3. High-resolution XPS N 1s spectra for (a) NTE-2CN, (b) PCN, (c) BBL,(e) BBL-202CN, (e) BBL-352CN, and (f) BBL-502CN and their optimal fits.

3.1.3.2. Electronic Structure and Optical Properties. The electronic structure and optical properties of PCN and the random copolymers were investigated using a combination of density functional theory (DFT) calculations and cyclic voltammetry in conjunction with optical absorption spectroscopy. The DFT calculations were performed at the ωB97XD/6-31G(d,p) level of theory on PCN oriented in a *trans* configuration with respect to the imide, and a representative BBL-502CN oligomer comprised of 6 repeat units in a *cis-trans* isomer configuration with the 2CN groups located on the cis moieties. The ground state geometry of PCN (Figure B.13) shows a completely planar molecular structure and fairly well delocalized molecular orbitals where the HOMO is delocalized across the PCN backbone and the LUMO is more localized to the dicyanonaphthalene core. The BBL-502 oligomer also shows a completely coplanar backbone across 6 repeat units (Figure B.14a), however, the HOMO and in particular the and LUMO levels, are extremely localized compared to those in BBL (Figure B.14b).[50,52] While the HOMO extends across 2 repeat units, the LUMO is localized to the central dicyanated repeat unit. This result could indicate that the 2CN moieties in the random copolymer backbone act as a charge trap site that reduces the charge carrier mobility with respect to the parent polymer BBL. [64,65]

We used cyclic voltammetry (CV) to measure the HOMO/LUMO energy levels of PCN and the random copolymers, and the results are summarized in Table 3.1 and Figures 3.4 and B.15. The CVs for the oxidation and reduction processes were collected as thin films coated on platinum wires in acetonitrile with 0.1 M tetrabutylammonium hexafluorophosphate (Bu_4NPF_6) vs. $Ag/AgNO_3$ as the reference electrode. The CVs of the reduction waves of PCN and the BBL-*x*2CN random copolymers are plotted vs. Fc/Fc^+ in Figure 3.4. The PCN model compound shows

3 non-reversible reduction peaks at -0.52 V, -0.86 V, and -1.11 V, which is similar what is reported for the perinone compound and its derivatives.[59] The LUMO level calculated from the onset of reduction at -0.28 V is -4.54 eV (Table 3.1), which is -0.73 eV lower than that reported for perinone (-3.78 eV).[59]

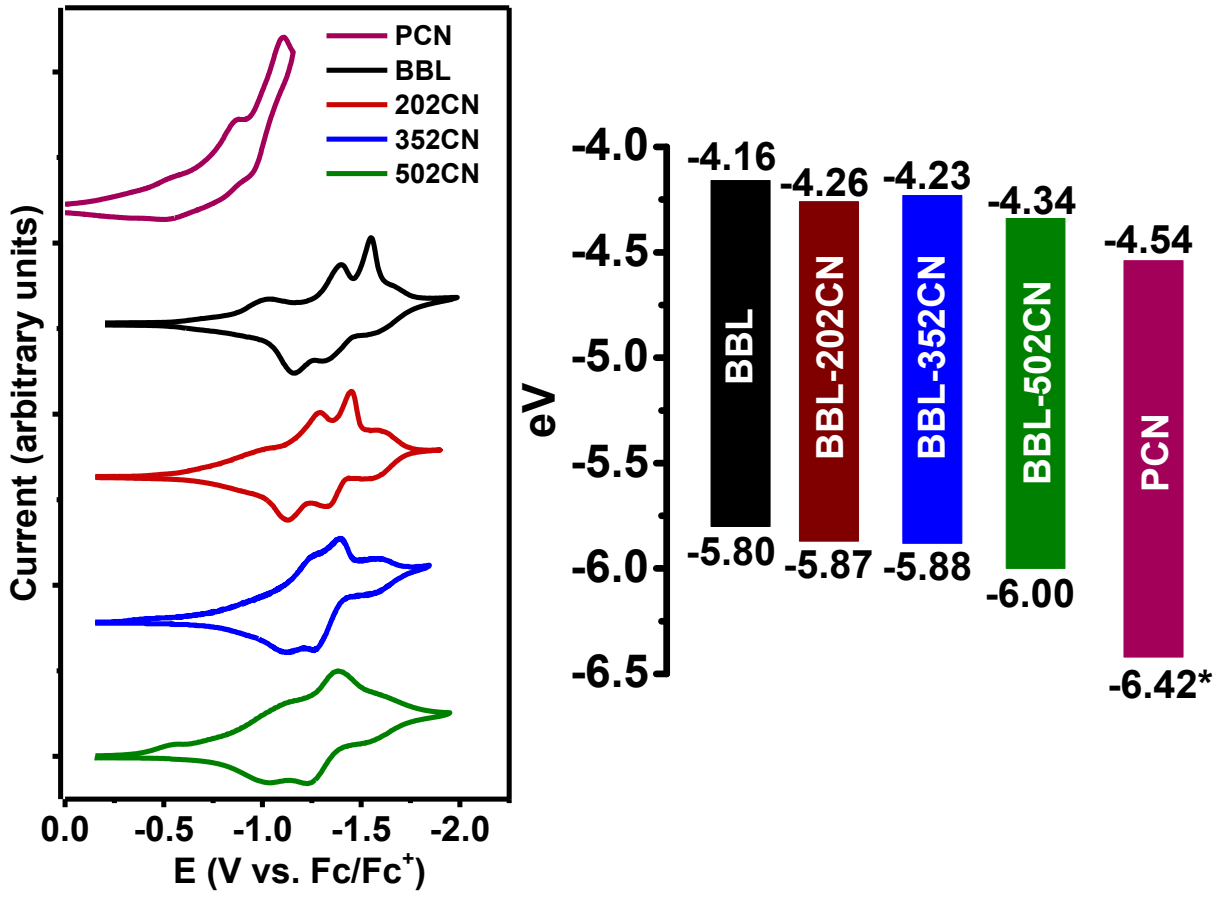

Figure 3.4. The reduction processes and energy levels of PCN and the BBL-*x*2CN random copolymers as thin films in anhydrous acetonitrile with $Ag/AgNO_3$ as the reference electrode and plotted vs. Fc/Fc^+. The scan rate was 15 mV/s. Note that the *HOMO level of PCN was out of range of the CV oxidation scan in acetonitrile and therefore was calculated using HOMO = LUMO – $E_g^{opt.}$

Table 3.1. Electronic and Optical Properties of the model compound PCN and the BBL-*x*2CN Random Copolymers.

Compound	LUMO (eV)	HOMO (eV)	$E_g^{elec.}$ (eV)	$\lambda_{max}^{(a)}$ (nm)	$\varepsilon_{max}^{(a)}$ ($M^{-1}cm^{-1}$)	$\lambda_{max}^{(b)}$ (nm)	$E_g^{opt.\,(b)}$ (eV)
PCN	-4.54	-6.42[(c)]	-	484[(e)]	-	489[(e)]	1.88
BBL	-4.16	-5.80[(d)]	1.70	545	4.2×10^4	576	1.64
BBL-202CN	-4.26	-5.87	1.61	541	4.3×10^4	575	1.60
BBL-352CN	-4.23	-5.88	1.65	535	3.1×10^4	570	1.63
BBL-502CN	-4.34	-6.00	1.66	532	2.9×10^4	557	1.65

[(a)]Absorption maximum in MSA solutions. [(b)]Spin-coated thin films from MSA solution. [(c)]Determined from the equation HOMO = LUMO - $E_g^{opt.}$ [(d)]Taken from reference (50). [(e)]Data collected for TFA solutions.

The copolymers each show 4 quasi-reversible reduction waves (Figure 3.4) accompanied by a notable increase in the reduction potentials moving from BBL to BBL-502CN. For example, the first reduction wave in BBL at -1.02 V shifts to higher potentials with increasing mol% of CN groups: -0.97 V for BBL-202CN and BBL-352CN, and -0.54 V for BBL-502CN. This trend hold for the other 3 reduction peaks (Figure 3.4): -1.29 V/ - 1.45 V/ -1.65 V for BBL-202CN, -1.24 V/ -1.39 V/ -1.59 V for BBL-352CN, and -1.07 V/ -1.38 V/ -1.60 V for BBL-502CN (Figure 3.4). Accordingly, the LUMO energy levels measured from the onset of reduction are also reduced compared to -4.16 eV measured for BBL: -4.26 eV for BBL-202CN, -4.23 eV for BBL-352CN, and -4.34 eV for BBL-502CN (Table 3.1). These results mean that incorporating as little as 20 mol% of the 2CN moieties in backbone of BBL is sufficient to facilitate the reduction process (n-dopability) of the BBL-*x*2CN polymers, and up to 50 mol% of the 2CN

monomer decreases the LUMO energy level by 0.18 eV. The oxidation scans show one non-reversible oxidation peak for each polymer (Figure B.15a-d) from which the HOMO energy levels are derived: -5.87 eV/ -5.88 eV/ -6.00 eV for BBL-202CN/ BBL-352CN/ BBL-502CN. Note that the oxidation peak of PCN was not seen in the oxidation scan ranging from 0 V to 2.0 V, which means the HOMO level is too deep to be measured by cyclic voltammetry in acetonitrile. The electrochemical bandgaps ($E_g^{elec.}$) vary from 1.61 eV to 1.70 eV for the BBL-*x*2CN polymers (Table 3.1).

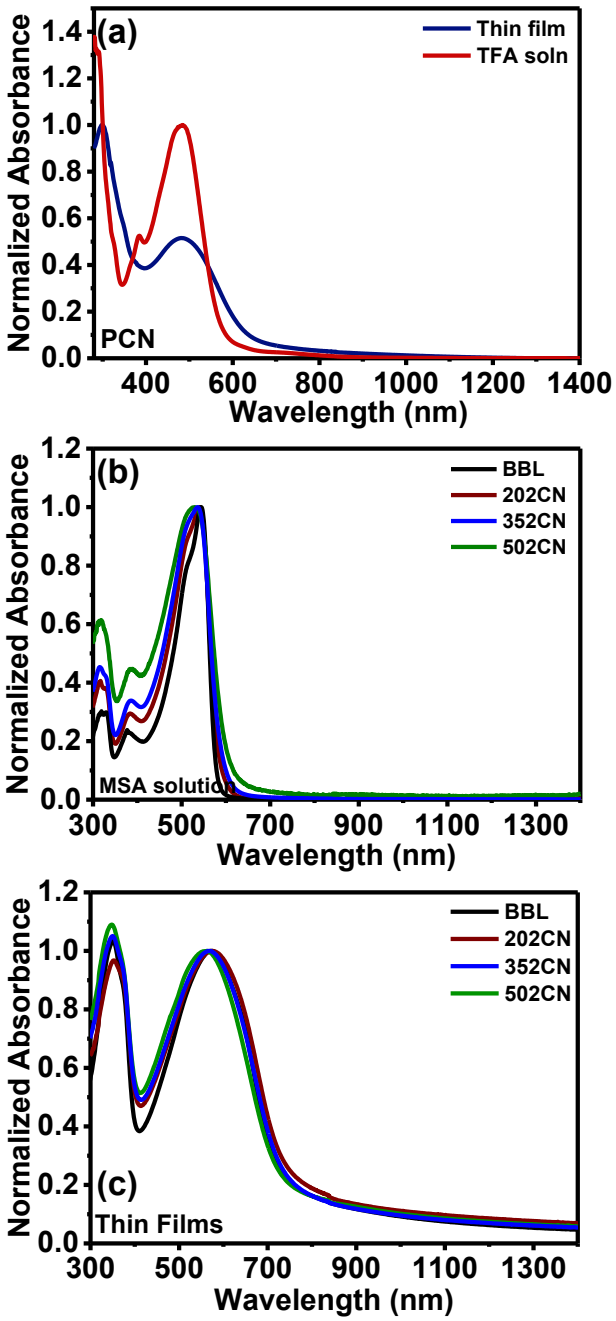

Figure 3.5. Normalized optical absorption spectra of (a) PCN thin film and TFA solution, and BBL-x2CN copolymers as (b) MSA solutions and (c) thin films on glass.

The normalized optical absorption spectra of PCN and the BBL-*x*2CN polymers are shown in Figure 3.5a-c and the absorption maxima in MSA and trifluoroacetic acid solutions and thin film (λ_{max}), molar absorptivity (ε_{max}), and optical bandgaps ($E_g^{opt.}$) are in Table 3.1. The normalized optical absorption spectrum of the PCN model compound in dilute (10^{-5} M) TFA

solution (Figure 3.5a) shows a sharp low-energy peak at 383 nm and an intense lowest-energy peak 484 nm which is assigned the π-π* transition. In thin film, the spectral shape is significantly broadened compared to the solution (Figure 3.5a), and the π-π* peak is *slightly* red-shifted to 489 nm. One interpretation for this trend is that the differences originate from changes in the π-conjugated backbone conformation in solution and solid state. In this case, the protonated molecule in acid solutions would presumably be more planar due to the improved spectral shape.[66] The optical bandgap ($E_g^{opt.}$) calculated from the onset of thin film absorption is 1.88 eV, which is 0.19 eV narrower than the $E_g^{opt.}$ of 2.07 eV reported for perinone.[59] Note that the optical bandgap was used to calculate the HOMO energy level in Figure 3.4.

In solution (Figure 3.5b), the copolymers show similar peaks: two high-energy bands at 321 nm and 382 nm, and a lowest-energy absorption peak ranging from 545 nm – 532 nm (Table 3.1), of which the latter is assigned to the π-π* transition. The molar absorptivites of the π-π* peak in BBL and BBL-202CN are nearly identical (ε_{max} = 4.2 – 4.3 x 10^4 $M^{-1}cm^{-1}$), however they decrease in BBL-352CN and BBL-502CN (ε_{max} = 2.9 – 3.1 x 10^4 $M^{-1}cm^{-1}$). The slightly blue-shifted π-π* peak that is accompanied by decreased absorptivity can be explained to a shortened π-conjugation length of BBL-352CN and BBL-502CN evidenced by the localized molecular orbitals in the DFT calculations previously discussed (Figure B.14). In the thin films (Figure 3.5c), there is one high-energy band at 350 nm and a lowest energy, π-π* transition band that ranges from 576 nm in BBL to 561 nm in BBL-502CN (Table 3.1). The 32 nm – 29 nm red-shifted π-π* peak going from solution to thin film (Table 3.1) indicates increased molecular order in the thin films compared to MSA solutions. The optical bandgaps calculated from the onset of absorption are almost identical; they range between 1.66 eV – 1.70 eV and are slightly smaller than the $E_g^{elec.}$ values measured from cyclic voltammetry (Table 3.1).

3.1.3.3. n-Doped Conductivities of the Random Copolymers. We used 4-(2,3-Dihydro-1,3-dimethyl-1H-benzimidazol-2-yl)-N,N-dimethylbenzenamine (N-DMBI) as a molecular n-dopant to study the effects of cyanation on the electrical conductivity of the series of random copolymers upon doping. Detailed procedure on the doping method is described in the Experimental Methods. Briefly, a 10 mg/mL solution of N-DMBI in chloroform is spin-coated on top of the undoped polymer films at 1500 rpm for 60 seconds followed by thermal annealing at 200˚C for 20 minutes in a Nitrogen-filled glovebox. Afterwards, the doped polymer films were brought to ambient atmosphere for electrical characterization by a colinear four-point probe setup.

The room-temperature dc-electrical conductivity (σ_{dc}) of N-DMBI doped polymer films was found to progressively decrease with increasing composition of cyanated moieties. In particular, the average σ_{dc} of doped BBL films was (6.28 ± 0.51) x 10^{-1} S/cm, which is in agreement with reported values using the same n-dopant.[67] The σ_{dc} was found to decrease by over 20-fold compared to the parent polymer to an average value of (2.47 ± 0.14) x 10^{-2} S/cm in BBL-202CN doped films. Doped films of BBL-352CN and BBL-502CN exhibited extremely high resistance; thus, the films were assumed to remain insulating, and the σ_{dc} values should be around 10^{-12} – 10^{-9} S/cm. These results have suggested that increasing the composition of cyanated moieties up to 50 mol% in the BBL backbone is detrimental to the electrical properties of the doped polymer films.

The incorporation of the 2CN moiety is the downshifting the LUMO energy levels of the BBL-*x*2CN (*x* = 20, 35, and 50) compared to BBL (Figure B.14), which should facilitate facile hydrogen or hydride transfer from the dopant to the polymer backbone.[68,69] We thus rationalized the poor electrical conductivity of this series of random copolymers upon doping partly to the

extreme localization of LUMO orbital distribution that was discussed earlier in the DFT calculations. The localized LUMO on the 2CN unit would severely hamper electron transport leading to marginal electrical conductivity of the doped random copolymer films.

3.1.4 Conclusions

In conclusion, we have synthesized and characterized a new series of n-type BBL random copolymers featuring 2,6-dicyano substitutions on the naphthalene backbone: BBL-*x*2CN (*x* = 20, 35, 50), and the corresponding model compound, PCN. The single-crystal X-ray structure analysis of NTE-2CN confirms the molecular structure of the novel monomer. During the polymerizations, we found that incorporation of NTE-2CN in as little as 20 mol% increased the efficiency of polycondensation such that the polymers were synthesized in under 12 hours using milder conditions compared to that of BBL. The copolymers have excellent film forming properties evidenced by the large-area freestanding films and thin films created from MSA solutions that were used to characterize the molecular structures using FTIR, Raman, and XPS spectroscopies. The BBL-*x*2CN random copolymers combine low LUMO levels (-4.16 eV – 4.34 eV) and attractive optical bandgaps of 1.66 eV – 1.70 eV that vary with the mol% of the 2CN monomer. Specifically, we found that 50 mol% lowered the LUMO level beyond that of BBL by 0.18 eV. Preliminary results show that the n-doped electrical conductivity decreases as the amount of 2CN in the copolymer backbone is increased, which can be explained by the localization of the LUMO energy level that was seen on the DFT calculations. This series of random copolymers provides important insights into the structure-property relationships of solution processable electron-deficient BBL derivatives.

3.1.5 References

1. Fu, H.; Wang, Z.; Sun, Y. Polymer Donors for High-Performance Non-Fullerene Organic Solar Cells. *Angew. Chem. Int. Ed.* **2019**, *58* (14), 4442–4453. DOI: 10.1002/anie.201806291.

2. Long, X.; Dou, C.; Liu, J.; Wang, L. Fine-Tuning LUMO Energy Levels of Conjugated Polymers Containing a B←N Unit. *Macromolecules* **2017**, *50* (21), 8521–8528. DOI: 10.1021/acs.macromol.7b01986.

3. Kleinhenz, N.; Yang, L.; Zhou, H.; Price, S. C.; You, W. Low-Band-Gap Polymers That Utilize Quinoid Resonance Structure Stabilization by Thienothiophene: Fine-Tuning of HOMO Level. *Macromolecules* **2011**, *44* (4), 872–877. DOI: 10.1021/ma1024126.

4. Ye, L.; Zhang, S.; Huo, L.; Zhang, M.; Hou, J. Molecular Design toward Highly Efficient Photovoltaic Polymers Based on Two-Dimensional Conjugated Benzodithiophene. *Acc. Chem. Res.* **2014**, *47* (5), 1595–1603. DOI: 10.1021/ar5000743.

5. Nakano, M.; Osaka, I.; Takimiya, K. Naphthodithiophene Diimide (NDTI)-Based Semiconducting Copolymers: From Ambipolar to Unipolar n-Type Polymers. *Macromolecules* **2015**, *48* (3), 576–584. DOI: 10.1021/ma502306f.

6. Allard, S.; Forster, M.; Souharce, B.; Thiem, H.; Scherf, U. Organic Semiconductors for Solution-Processable Field-Effect Transistors (OFETs). *Angew. Chem. Int. Ed.* **2008**, *47* (22), 4070–4098. DOI: 10.1002/anie.200701920.

7. Lin, Y.; Fan, H.; Li, Y.; Zhan, X. Thiazole-Based Organic Semiconductors for Organic Electronics. *Adv. Mater.* **2012**, *24* (23), 3087–3106. DOI: 10.1002/adma.201200721.

8. Ghosh, S.; Berggren, M.; Zozoulenko, I. Electronic Structures and Optical Properties of P-Type/n-Type Polymer Blends: Density Functional Theory Study. *J. Phys. Chem. C* **2020**, *124* (17), 9203–9214. DOI: 10.1021/acs.jpcc.0c01336.

9. Griggs, S.; Marks, A.; Bristow, H.; McCulloch, I. N-Type Organic Semiconducting Polymers: Stability Limitations, Design Considerations and Applications. *J. Mater. Chem. C* **2021**, *9* (26), 8099–8128. DOI: 10.1039/D1TC02048J.

10. Feng, K.; Shan, W.; Wang, J.; Lee, J.-W.; Yang, W.; Wu, W.; Wang, Y.; Kim, B. J.; Guo, X.; Guo, H. Cyano-Functionalized n-Type Polymer with High Electron Mobility for High-Performance Organic Electrochemical Transistors. *Adv. Mater.* **2022**, *34* (24), 2201340. DOI: 10.1002/adma.202201340.

11. Marks, A.; Chen, X.; Wu, R.; Rashid, R. B.; Jin, W.; Paulsen, B. D.; Moser, M.; Ji, X.; Griggs, S.; Meli, D.; Wu, X.; Bristow, H.; Strzalka, J.; Gasparini, N.; Costantini, G.; Fabiano, S.; Rivnay, J.; McCulloch, I. Synthetic Nuances to Maximize N-Type Organic Electrochemical Transistor and Thermoelectric Performance in Fused Lactam Polymers. *J. Am. Chem. Soc.* **2022**, *144* (10), 4642-4656. DOI: 10.1021/jacs.2c00735.

12. Babel, A.; Wind, J. D.; Jenekhe, S. A. Ambipolar Charge Transport in Air-Stable Polymer Blend Thin-Film Transistors. *Adv. Funct. Mater.* **2004**, *14* (9), 891–898. DOI: 10.1002/adfm.200305180.

13. Hirano, T.; Hanamura, H.; Inoue, M.; Ueda, S.; Watanabe, M.; Tanabiki, M.; Mikami, K. Synthesis of Soluble, Air-Stable Fully Conjugated Ladder Polymers. *Polymer* **2019**, *177*, 282–289. DOI: 10.1016/j.polymer.2019.06.014.

14. Hu, Y.; Gao, X.; Di, C.; Yang, X.; Zhang, F.; Liu, Y.; Li, H.; Zhu, D. Core-Expanded Naphthalene Diimides Fused with Sulfur Heterocycles and End-Capped with Electron-Withdrawing Groups for Air-Stable Solution-Processed n-Channel Organic Thin Film Transistors. *Chem. Mater.* **2011**, *23* (5), 1204–1215. DOI: 10.1021/cm102850j.

15. Fahlman, M.; Fabiano, S.; Gueskine, V.; Simon, D.; Berggren, M.; Crispin, X. Interfaces in Organic Electronics. *Nat. Rev. Mater.* **2019**, *4* (10), 627–650. DOI: 10.1038/s41578-019-0127-y.

16. Zaumseil, J.; Sirringhaus, H. Electron and Ambipolar Transport in Organic Field-Effect Transistors. *Chem. Rev.* **2007**, *107* (4), 1296–1323. DOI: 10.1021/cr0501543.

17. Schmidt, R.; Oh, J. H.; Sun, Y. S.; Deppisch, M.; Krause, A. M.; Radacki, K.; Braunschweig, H.; Könemann, M.; Erk, P.; Bao, Z.; Würthner, F. High-Performance Air-Stable n-Channel Organic Thin Film Transistors Based on Halogenated Perylene Bisimide Semiconductors. *J. Am. Chem. Soc.* **2009**, *131* (17), 6215–6228. DOI: 0.1021/ja901077a.

18. Deshmukh, K. D.; Matsidik, R.; Prasad, S. K. K.; Chandrasekaran, N.; Welford, A.; Connal, L. A.; Liu, A. C. Y.; Gann, E.; Thomsen, L.; Kabra, D.; Hodgkiss, J. M.; Sommer, M.; McNeill, C. R. Impact of Acceptor Fluorination on the Performance of All-Polymer Solar Cells. *ACS Appl. Mater. Interfaces* **2018**, *10* (1), 955–969. DOI: 10.1021/acsami.7b14582.

19. He, Q.; Dexter Tam, T. L.; Lin, T.; Chien, S. W.; Lin, M.; Meng, H.; Huang, W.; Xu, J. π-Extended Poly(Benzimidazoanthradiisoquinolinedione) Ladder-Type Conjugated Polymer. *ACS Macro Lett.* **2022**, *11* (9), 1136–1141. DOI: 10.1021/acsmacrolett.2c00438.

20. He, Q.; Zhang, X.; Tam, T. L. D.; Wang, J.; Chen, H.; Chien, S. W.; Tham, N. N.; Koh, X. Q.; Lee, J. J. C.; Lin, M.; Soh, P. X.; Meng, H.; Huang, W.; Xu, J. Balancing Solubility and Thermoelectric Performance in π-Extended Poly(Benzimidazoanthradiisoquinolinedione) Ladder-Type Conjugated Polymer. *ACS Appl. Electron. Mater.* **2023**. DOI: 10.1021/acsaelm.3c00294.

21. Cao, X.; Min, Y.; Tian, H.; Liu, J. Incorporating Cyano Groups to a Conjugated Polymer Based on Double B←N-Bridged Bipyridine Units for Unipolar n-Type Organic Field-Effect Transistors. *Org. Mater.* **2021**, *3* (04), 469–476. DOI: 10.1055/a-1639-2383.

22. Wang, Y.; Wang, N.; Yang, Q.; Zhang, J.; Liu, J.; Wang, L. A Polymer Acceptor Containing the B←N Unitfor All-Polymer Solar Cells with 14% Efficiency. *J. Mater. Chem. A* **2021**, *9* (37), 21071–21077. DOI: 10.1039/D1TA06041D.

23. Chang, J.; Ye, Q.; Huang, K.-W.; Zhang, J.; Chen, Z.-K.; Wu, J.; Chi, C. Stepwise Cyanation of Naphthalene Diimide for N-Channel Field-Effect Transistors. *Org. Lett.* **2012**, *14* (12), 2964–2967. DOI: 10.1021/ol300914k.

24. Casey, A.; Dimitrov, S. D.; Shakya-Tuladhar, P.; Fei, Z.; Nguyen, M.; Han, Y.; Anthopoulos, T. D.; Durrant, J. R.; Heeney, M. Effect of Systematically Tuning Conjugated Donor Polymer Lowest Unoccupied Molecular Orbital Levels via Cyano Substitution on Organic Photovoltaic Device Performance. *Chem. Mater.* **2016**, *28* (14), 5110–5120. DOI: 10.1021/acs.chemmater.6b02030.

25. Iguchi, K.; Mikie, T.; Saito, M.; Komeyama, K.; Seo, T.; Ie, Y.; Osaka, I. N-Type Semiconducting Polymers Based on Dicyano Naphthobisthiadiazole: High Electron Mobility with Unfavorable Backbone Twist. *Chem. Mater.* **2021**, *33* (6), 2218-2228. DOI: 10.1021/acs.chemmater.1c00204.

26. Li, Y.; Huang, E.; Guo, X.; Feng, K. Cyano-Functionalized Organic and Polymeric Semiconductors for High-Performance n-Type Organic Electronic Devices. *Mat. Chem. Front.* **2023**, *7* (18), 3803–3819. DOI: 10.1039/D3QM00201B.

27. Zhang, Q.; Rech, J. J.; Yan, L.; Liang, Q.; Peng, Z.; Ade, H.; Wu, H.; You, W. Effect of Cyano Substitution on Conjugated Polymers for Bulk Heterojunction Solar Cells. *ACS Appl. Polym. Mater.* **2019**, *1* (12), 3313–3322. https://doi.org/10.1021/acsapm.9b00767.

28. Molinari, A. S.; Alves, H.; Chen, Z.; Facchetti, A.; Morpurgo, A. F. High Electron Mobility in Vacuum and Ambient for PDIF-CN2 Single-Crystal Transistors. *J. Am. Chem. Soc.* **2009**, *131* (7), 2462–2463. DOI: 10.1021/ja809848y.

29. Jones, B. A.; Ahrens, M. J.; Yoon, M.-H.; Facchetti, A.; Marks, T. J.; Wasielewski, M. R. High-Mobility Air-Stable n-Type Semiconductors with Processing Versatility: Dicyanoperylene-3,4:9,10-Bis(Dicarboximides). *Angew. Chem. Int. Ed.* **2004**, *43* (46), 6363–6366. DOI: 10.1002/anie.200461324.

30. Usta, H.; Facchetti, A.; Marks, T. J. Air-Stable, Solution-Processable n-Channel and Ambipolar Semiconductors for Thin-Film Transistors Based on the Indenofluorenebis(Dicyanovinylene) Core. *J. Am. Chem. Soc.* **2008**, *130* (27), 8580–8581. DOI: 10.1021/ja802266u.

31. Song, H.; Deng, Y.; Gao, Y.; Jiang, Y.; Tian, H.; Yan, D.; Geng, Y.; Wang, F. Donor–Acceptor Conjugated Polymers Based on Indacenodithiophene Derivative Bridged Diketopyrrolopyrroles: Synthesis and Semiconducting Properties. *Macromolecules* **2017**, *50* (6), 2344–2353. DOI: 10.1021/acs.macromol.6b02781.

32. Yang, L.; Xiao, C.; Jiang, W.; Wang, Z. Conjugated Donor-Acceptor Copolymers from Dicyanated Naphthalene Diimide. *Tetrahedron* **2014**, *70* (36), 6265–6270. DOI: 10.1016/j.tet.2014.04.002.

33. Feng, K.; Guo, H.; Wang, J.; Shi, Y.; Wu, Z.; Su, M.; Zhang, X.; Son, J. H.; Woo, H. Y.; Guo, X. Cyano-Functionalized Bithiophene Imide-Based n-Type Polymer Semiconductors: Synthesis, Structure–Property Correlations, and Thermoelectric Performance. *J. Am. Chem. Soc.* **2021**, *143* (3), 1539–1552. DOI: 10.1021/jacs.0c11608.

34. Chen, Z.; Li, J.; Wang, J.; Yang, K.; Zhang, J.; Wang, Y.; Feng, K.; Li, B.; Wei, Z.; Guo, X. Imide-Functionalized Fluorenone and Its Cyanated Derivative Based n-Type Polymers: Synthesis, Structure–Property Correlations, and Thin-Film Transistor Performance. *Angew. Chem. Int. Ed.* **2022**, *61* (32), e202205315. DOI: 10.1002/anie.202205315.

35. Shi, S.; Wang, H.; Uddin, M. A.; Yang, K.; Su, M.; Bianchi, L.; Chen, P.; Cheng, X.; Guo, H.; Zhang, S.; Woo, H. Y.; Guo, X. Head-to-Head Linked Dialkylbifuran-Based Polymer Semiconductors for High-Performance Organic Thin-Film Transistors with Tunable Charge Carrier Polarity. *Chem. Mater.* **2019**, *31* (5), 1808–1817. DOI: 10.1021/acs.chemmater.9b00118.

36. You, H.; Kang, H.; Kim, D.; Park, J. S.; Lee, J.-W.; Lee, S.; Kim, F. S.; Kim, B. J. Cyano-Functionalized Quinoxaline-Based Polymer Acceptors for All-Polymer Solar Cells and Organic Transistors. *Chem. Sus. Chem.* **2021**, *14* (17), 3520–3527. DOI: 10.1002/cssc.202100080.

37. You, H.; Lee, S.; Kim, D.; Kang, H.; Lim, C.; Kim, F. S.; Kim, B. J. Effects of the Selective Alkoxy Side Chain Position in Quinoxaline-Based Polymer Acceptors on the Performance of All-Polymer Solar Cells. *ACS Appl. Mater. Interfaces* **2021**, *13* (40), 47817–47825. DOI: 10.1021/acsami.1c12288.

38. Zhang, Z.-G.; Li, Y. Polymerized Small-Molecule Acceptors for High-Performance All-Polymer Solar Cells. *Angew. Chem. Int. Ed.* **2021**, *60* (9), 4422–4433. DOI: 10.1002/anie.202009666.

39. Deusen, R. L. V. Benzimidazo-Benzophenanthroline Polymers. *J. Polym. Sci. B Polym. Lett.* **1966**, *4* (3), 211–214. DOI: 10.1002/pol.1966.110040310.

40. Alam, M. M.; Jenekhe, S. A. Efficient Solar Cells from Layered Nanostructures of Donor and Acceptor Conjugated Polymers. *Chem. Mater.* **2004**, *16* (23), 4647–4656. DOI: 10.1021/cm0497069.

41. Jenekhe, S. A.; Yi, S. Efficient Photovoltaic Cells from Semiconducting Polymer Heterojunctions. *Appl. Phys. Lett.* **2000**, *77* (17), 2635–2637. DOI: 10.1063/1.1320022.

42. Babel, A.; Jenekhe, S. A. High Electron Mobility in Ladder Polymer Field-Effect Transistors. *J. Am. Chem. Soc.* **2003**, *125* (45), 13656–13657. DOI: 10.1021/ja0371810.

43. Babel, A.; Jenekhe, S. A. Electron Transport in Thin-Film Transistors From an n-Type Conjugated Polymer. *Adv. Mater.* **2002**, *14* (5), 371–374. DOI: 10.1002/1521-4095(20020304)14:5<371::AID-ADMA371>3.0.CO;2-5.

44. Babel, A.; Jenekhe, S. N-Channel Field-Effect Transistors from Blends of Conjugated Polymers. *J. Phys. Chem. B* **2002**, *106* (24), 6129–6132. DOI: 10.1021/jp020695l.

45. Wu, X.; Tam, T. L. D.; Chen, S.; Salim, T.; Zhao, X.; Zhou, Z.; Lin, M.; Xu, J.; Loo, Y.-L.; Leong, W. L. All-Polymer Bulk-Heterojunction Organic Electrochemical Transistors with Balanced Ionic and Electronic Transport. *Adv. Mater.* **2022**, *34* (42), 2206118. DOI: 10.1002/adma.202206118.

46. Guo, J.; Flagg, L. Q.; Tran, D. K.; Chen, S. E.; Li, R.; Kolhe, N. B.; Giridharagopal, R.; Jenekhe, S. A.; Richter, L. J.; Ginger, D. S. Hydration of a Side-Chain-Free n-Type Semiconducting Ladder Polymer Driven by Electrochemical Doping. *J. Am. Chem. Soc.* **2023**, *145* (3), 1866–1876. DOI: 10.1021/jacs.2c11468.

47. Wu, H.-Y.; Yang, C.-Y.; Li, Q.; Kolhe, N. B.; Strakosas, X.; Stoeckel, M.-A.; Wu, Z.; Jin, W.; Savvakis, M.; Kroon, R.; Tu, D.; Woo, H. Y.; Berggren, M.; Jenekhe, S. A.; Fabiano, S. Influence of Molecular Weight on the Organic Electrochemical Transistor Performance of Ladder-Type Conjugated Polymers. *Adv. Mater. 34* (4), 2106235. DOI: 10.1002/adma.202106235.

48. Wang, S.; Sun, H.; Ail, U.; Vagin, M.; Persson, P. O. Å.; Andreasen, J. W.; Thiel, W.; Berggren, M.; Crispin, X.; Fazzi, D.; Fabiano, S. Thermoelectric Properties of Solution-Processed n-Doped Ladder-Type Conducting Polymers. *Adv. Mater.* **2016**, *28* (48), 10764–10771. DOI: 10.1002/adma.201603731.

49. Tam, T. L. D.; Lin, M.; Handoko, A. D.; Lin, T. T.; Xu, J. High-Performance & Thermally Stable n-Type Polymer Thermoelectrics Based on a Benzyl Viologen Radical Cation-Doped Ladder-Type Conjugated Polymer. *J. Mater. Chem. A* **2021**. 9, 11787-11793. DOI: 10.1039/D1TA01645H.

50. Kim, F. S.; Park, C. H.; Na, Y.; Jenekhe, S. A. Effects of Ladder Structure on the Electronic Properties and Field-Effect Transistor Performance of Poly(Benzobisimidazobenzophenanthroline). *Org. Electron.* **2019**, *69*, 301–307. DOI: 10.1016/j.orgel.2019.03.049.

51. Berry, G. C. Properties of an Optically Anisotropic Heterocyclic Ladder Polymer (BBL) in Dilute Solution. *J. Polym. Sci.: Polym. Symp.* **1978**, *65* (1), 143–172. DOI: 10.1002/polc.5070650115.

52. West, S. M.; Tran, D. K.; Guo, J.; Chen, S. E.; Ginger, D. S.; Jenekhe, S. A. Phenazine-Substituted Poly(Benzimidazobenzophenanthrolinedione): Electronic Structure, Thin Film Morphology, Electron Transport, and Mechanical Properties of an n-Type Semiconducting Ladder Polymer. *Macromolecules* **2023**, *56* (5), 2081-2091. DOI: 10.1021/acs.macromol.2c01999.

53. Deusen, R. L. V.; Goins, O. K.; Sicree, A. J. Thermally Stable Polymers from 1,4,5,8-Naphthalenetetracarboxylic Acid and Aromatic Tetraamines. *J. Polym. Sci., Part A-1: Polym. Chem.* **1968**, *6* (7), 1777–1793. DOI: 10.1002/pol.1968.150060701.

54. Sicree, A. J.; Arnold, F. E.; Deusen, R. L. V. New Imidazoisoquinoline Ladder Polymers. *J. Polym. Sci. Polym. Chem.* **1974**, *12* (2), 265–272. DOI: 10.1002/pol.1974.170120202.

55. Sasikumar, M.; Suseela, Y. V.; Govindaraju, T. Dibromohydantoin: A Convenient Brominating Reagent for 1,4,5,8-Naphthalenetetracarboxylic Dianhydride. *Asian J. Org. Chem.* **2013**, *2* (9), 779–785. DOI: 10.1002/ajoc.201300088.

56. Wang, D.; Kuang, L.; Li, Z.; Ding, K. L-Proline-Promoted Rosenmund-von Braun Reaction. *Syn. Lett.* **2008**, *2008* (01), 69–72. DOI: 10.1055/s-2007-992409.

57. Taublaender, M. J.; Glöcklhofer, F.; Marchetti-Deschmann, M.; Unterlass, M. M. Green and Rapid Hydrothermal Crystallization and Synthesis of Fully Conjugated Aromatic Compounds. *Angew. Chem. Int. Ed.* **2018**, *57* (38), 12270–12274. DOI: 10.1002/anie.201801277.

58. Loutfy, R. O.; Hor, A. M.; Kazmaier, P. M.; Burt, R. A.; Hamer, G. K. Organic Photoconductive (OPC) Devices Incorporating Bisarylimidazole Perinone Pigments. *Dyes Pigm.* **1991**, *15* (2), 139–156. DOI: /10.1016/0143-7208(91)87013-D.

59. Mamada, M.; Pérez-Bolívar, C.; Kumaki, D.; Esipenko, N. A.; Tokito, S.; Anzenbacher Jr., P. Benzimidazole Derivatives: Synthesis, Physical Properties, and n-Type Semiconducting Properties. *Chem. Eur. J.* **2014**, *20* (37), 11835–11846. DOI: 10.1002/chem.201403058.

60. Roberts, M. F.; Jenekhe, S. A. Lewis-Acid Coordination-Complexes of Polymers .3. Poly(Benzimidazobenzophenanthroline) Ladder and Semiladder Polymers. *Polymer* **1994**, *35* (20), 4313–4325. DOI: 10.1016/0032-3861(94)90088-4.

61. Chen, Y.; Wu, H.-Y.; Yang, C.-Y.; Kolhe, N. B.; Jenekhe, S. A.; Liu, X.; Braun, S.; Fabiano, S.; Fahlman, M. In Situ Spectroscopic and Electrical Investigations of Ladder-Type Conjugated Polymers Doped with Alkali Metals. *Macromolecules* **2022**, *55* (16), 7294–7302. DOI: 10.1021/acs.macromol.2c01190.

62. Jansen, R. J. J.; van Bekkum, H. XPS of Nitrogen-Containing Functional Groups on Activated Carbon. *Carbon* **1995**, *33* (8), 1021–1027. DOI: 10.1016/0008-6223(95)00030-H.

63. A. W. Munz. Structural Precursors and Electronic Structure of the Ladder Type Polymer Poly(bis(benzimidazo)benzophenanthroline) (BBB): A Combined UPS/XPS and STM Study. *Chem. Mater.* **1994**, *6* (12), 2288- 2302. DOI: 10.1021/cm00048a015.

64. Dilmurat, R.; Prodhan, S.; Wang, L.; Beljonne, D. Thermally Activated Intra-Chain Charge Transport in High Charge-Carrier Mobility Copolymers. *J. Chem. Phys.* **2022**, *156* (8), 084115. DOI: 10.1063/5.0082569.

65. Terao, J.; Wadahama, A.; Matono, A.; Tada, T.; Watanabe, S.; Seki, S.; Fujihara, T.; Tsuji, Y. Design Principle for Increasing Charge Mobility of π-Conjugated Polymers Using Regularly Localized Molecular Orbitals. *Nat. Commun.* **2013**, *4* (1), 1691. DOI: 10.1038/ncomms2707.

66. West, S. M.; Tran, D. K.; Guo, J.; Chen, S. E.; Ginger, D. S.; Jenekhe, S. A. P-Type Semiconducting Ladder Poly(Pyrrolobenzothiazine)s: Effects of N-Alkyl Side Chains on the Chain Conformation, Electronic Structure, and Charge Transport Properties. *Macromolecules* **2023**, *56* (24), 10222–10235. DOI: 10.1021/acs.macromol.3c01561.

67. Wang S.; Ruoko, T-P.; Wang, G.; Riera-Galindo, S.; Hultmark, S.; Puttisong, Y.; Moro, F.; Yan, H.; Chen, W. M.; Berggren, M.; Müller, C.; Fabiano, S. Sequential Doping of Ladder-Type Conjugated Polymers for Thermally Stable n-Type Organic Conductors. *ACS Appl. Mater. Interfaces* **2020**, *12* (47), 53003–53011. DOI: 10.1021/acsami.0c16254.

68. Scaccabarozzi, A. D.; Basu, A.; Aniés, F.; Liu, J.; Zapata-Arteaga, O.; Warren, R.; Firdaus, Y.; Nugraha, M. I.; Lin, Y.; Campoy-Quiles, M.; Koch, N.; Müller, C.; Tsetseris, L.; Heeney, M.;Anthopoulos. T. D. Doping Approaches for Organic Semiconductors. *Chem. Rev.* **2022** *122* (4), 4420-4492. DOI: 10.1021/acs.chemrev.1c00581

69. Zeng, Y.; Zheng, W.; Guo, Y.; Han, G,; Yi, Y. Doping Mechanisms of N-DMNI-H for Organic Thermoelectrics: Hydrogen Removal vs. Hydride Transfer. *J. Mater. Chem. A* **2020**, 8, 8323-8328. DOI: 10.1039/D0TA01087A.

Chapter 3.2 Random Copolymers and Model Compound of Ladder Poly(benzimidazobenzophenanthroline) Featuring Dithiinotetracarbonitrile Groups: Synthesis and Electronic Structure

3.2.1 Introduction

π-Conjugated ladder polymers are a class of semiconducting polymers that feature double-stranded ladder architectures that reduce torsional disorder in the backbone. The most widely studied π-conjugated ladder polymer is the prototype n-type semiconducting polymer, ladder poly(benzimidazobenzophenanthroline) (BBL) (Chart 3.2) that was first synthesized in 1966 for aerospace applications more than a decade before the advent of doped conducting polymers in 1977.[1] BBL has been used successfully in a large variety of organic electronic applications over several decades including organic field-effect transistors (OFETs),[2–4] organic photovoltaics (OPVs),[5,6] organic thermoelectrics (OTs),[7–9] and organic electrochemical transistors (OECTs).[10–13] The success of BBL as the prototype n-type semiconducting polymer has been attributed to its rigid-rod planar backbone that enabled a tight π-π stacking distance of 3.4 Å,[13–15] excellent thermal, chemical, and mechanical stability in air, and low lying LUMO energy level of -4.1 eV. Despite the success of BBL, only 3 n-type derivatives have been reported, presumably due to difficult synthesis of tetrafunctionalized electron-deficient moieties.[16–18]

Deepening the LUMO level beyond -4.0 eV is of fundamental interest for n-type semiconductors in order to increase operational stability in air,[19–21] decrease the barrier to charge injection, and improve electron mobility and electrical conductivity.[22–25] Moreover, if the lowest-unoccupied molecular orbital (LUMO) energy level of an acceptor (n-type) polymer is deeper

than the highest-occupied molecular orbital (HOMO) level of a donor (p-type) polymer, then spontaneous ground state electron transfer in the polymer blend could be achieved and thus eliminate the need for external doping or imput of energy.[26,27] By its nature, n- or p-doping creates one type of mobile charge carrier, and the immobile counter charges could disrupt the thin film microstructure, which can negatively impact charge carrier mobility and decrease operational device stabiltiy.[28]

Chart 3.2. Molecular structures of the n-type polymer BBL, the random copolymers featuring dithiinotetracarbonitrile groups BBL-*x*TCN (*x* = 0.2, 0.35, 0.5), and BBL-TCN.

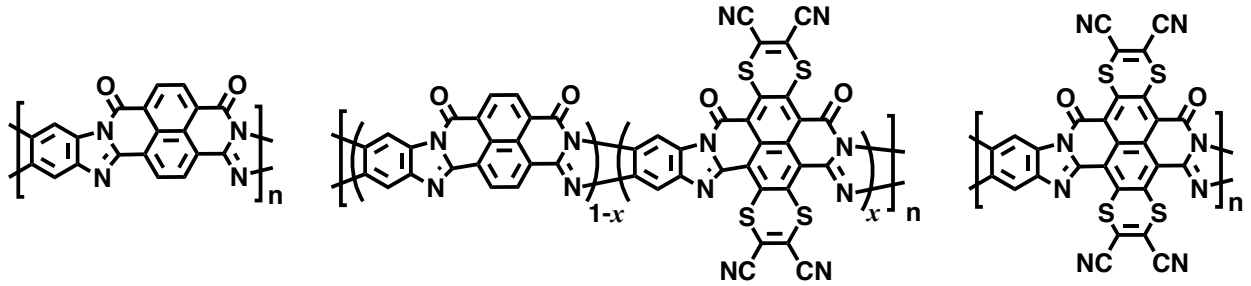

Some effective strategies to synthesize n-type polymers with deep LUMO levels are to functionalize electron-deficient building blocks such as rylene diimides,[20,29,30] isoindigo (IG),[31,32] or diketopyrrolopyrrole (DPP),[33–35] by: (1) introducing heteroatoms into the molecular structure, (2) inducing chain planarization through intra- or inter-molecular covalent or non-covalent interactions, or (3) appending electron-withdrawing substituent onto the backbone. Typical electron-withdrawing moieties include nitro,[36] carboxyl,[37,38] fluorine,[39–41] and cyano groups.[42–45] In one example, naphthalene diimide (NDI) moieties functionalized with electron-deficient dithiinotetracarbonitrile (TCN) groups (NDI-TCN)[46] or simply two cyano groups (NDI-2CN)[47] showed substantially decreased LUMO levels of -4.3 eV and -4.4 eV, respectively, compared to the non-functionalized NDI moiety (LUMO ~ -4.0 eV).[47,48] These representative examples show

that direct 2CN- and TCN-functionalization are effective ways to lower the LUMO levels of n-type π-conjugated systems, though they have not been demonstrated in a π-conjugated ladder polymer architecture.[49]

Here, we report a novel random copolymer series featuring the n-type ladder polymer BBL synthesized with varying mol% of the TCN groups, BBL-*x*TCN (*x* = 0.2, 0.35, and 0.5) (Chart 3.2). The random copolymer architecture was chosen to enhance processability of the copolymers because we discovered that the BBL-TCN homopolymer (Chart 3.2) is insoluble in protic acids. Moreover, functionalization of BBL with TCN allows us to introduce strong electron-withdrawing cyano groups into the backbone of BBL without the use of toxic cyanide salts. The BBL-*x*TCN copolymers were synthesized in pure polyphosphoric acid (PPA) whereby the increased reactivity of the TCN comonomer enabled the polymerizations to complete in 12 hours. The molecular structures of the copolymers were characterized by FTIR, Raman, and X-ray photoelectron (XPS) spectroscopies and were compared those of the model compound, 2,3,14,15-tetramethyl-6,11-dioxo-6,11-dihydro [1,4]dithiino[2',3':5,6]benzo [1,2,3,4*lmn*]benzo[4,5]imidazo[2,1*b*]benzo[4,5]imidazo[1,2-*j*][1,4]dithiino[2,3-*f*][3,8] phenanthroline-8,9,19,20-tetracarbonitrile (PTCNMe). The LUMO energy levels measured using cyclic voltammetry revealed that increasing the TCN moiety up to 50 mol% lowered the LUMO level by 0.20 eV, and the optical bandgaps ($E_{g,}^{opt.}$) of 1.60 – 1.67 eV are relatively unchanged compared to BBL ($E_{g,}^{opt.}$ = 1.64 eV). Our results on this series of BBL-type random copolymers provide important new insights into the structure-property relationships of semiconducting ladder polymers and derivatives of BBL.

3.2.2 Experimental Methods.

Materials and Methods. The monomer 1,4,5,8-naphthalenetetracarboxylic acid (NTCA) was purchased from Ambeed and purified according to the known procedure.[50] 1,2,4,5-tetraaminobenzene hydrochloride was purchased from Ambeed and was purified according to a modified published procedure.[51] The 1,3,8,10-tetraoxo-1,3,8,10-tetrahydro-[1,4]dithiino[2',3':7,8]isochromeno[6,5,4-*def*][1,4]dithiino[2,3-*h*]isochromene-5,6,12,13-tetracarbonitrile (NTA-TCN) monomer was synthesized according to known procedures.[46,52] N,N-dimethylformamide (DMF), disodium dimercaptomaleonitrile, 1,4,5,8-naphthalenetetracarboxylic anhydride (NTCDA), fuming sulfuric acid (20% free SO_3), dibromoisocyanuric acid (DBI), conc. hydrochloric acid, glacial acetic acid, 4,5-dimethylbenzene-1,2-diamine, polyphosphoric acid (PPA, 84% P_2O_5), acetone, toluene, and methanesulfonic acid (MSA) (> 99%) were purchased from Sigma-Aldrich and used as received. Methanol and ethanol were purchased from Fisher Scientific and used as received.

Intrinsic viscosities of the polymers in MSA were measured in an Ubbelohde viscometer suspended in a water bath at 30.0˚C. The concentrations of the polymer solutions were chosen such that the elution time of the polymer solution was 1.1 – 1.8 times that of the pure solvent. The ^{1}H NMR spectrum was recorded on a Bruker AV500 (at 500 MHz) using basic D_2O or DMSO-d6 as the solvents. Thermogravimetric analysis (TGA) was conducted on a TA Instrument model Q50 TGA. A heating rate of 10°C /min under a flow of N_2 was used with runs conducted from room temperature to 880°C. Optical absorption spectra were measured on a PerkinElmer model Lambda 900 UV-vis/near-IR spectrophotometer. Solution absorption spectrum was obtained from dilute solutions (10^{-5} M) in MSA.

Cyclic voltammetry (CV) experiments were performed on an EG&G Princeton Applied Research potentiostat/galvanostat (model 273A). A three-electrode cell was used, using platinum

wire as the counter electrode and polymers coated on platinum wires as the working electrode. The reference electrode was $Ag/AgNO_3$ in acetonitrile. The acidic solvent was removed by dipping the substrate in isopropanol (IPA) overnight and was subsequently dried in vacuum oven at 90˚C. The supporting electrolyte solution consists of 0.1 M tetrabutylammonium hexafluorophosphate (Bu_4NPF_6) in anhydrous acetonitrile. The electrolyte was purged with nitrogen for 15 minutes prior to the CV scans to ensure inert and anhydrous conditions. The reduction and oxidation potentials were referenced to the Fc/Fc^+ couple by using ferrocene as an internal standard. The LUMO energy level was estimated using a ferrocene value of -4.8 eV with respect to vacuum level. The LUMO and HOMO levels were determined by using the equations $E_{LUMO} = -(eE_{red}^{onset} + 4.8)$ and $E_{HOMO} = -(eE_{ox}^{onset} + 4.8)$.

Fourier-transform infrared (FTIR) spectroscopy experiments were performed on a Perkin Elmer Frontier spectrometer by using polymer freestanding films and the thin film of the model compound. The resolution was 1 cm^{-1} and 16 scans were averaged. Raman spectroscopy of the polymer freestanding films and model compound powder were carried out on a Thermo Scientific DXR2 Raman microscope. A 532-nm laser with a power of 5 mW was focused onto a sample through a 50x objective lens.

Gas-phase density functional theory (DFT) and time-dependent DFT (TD-DFT) calculations were performed using the Gaussian 16 suite of programs[53] at the ωB97XD/631-G(d,p) level of theory on the representative model compound, and the polymer comprised of 6 repeat units of alternating NTA-TCN and NTCA monomers oriented in a alternating cis-trans configuration with respect to the imide.

Synthesis of 2,3,14,15-tetramethyl-6,11-dioxo-6,11-dihydro-[1,4]dithiino[2',3':5,6]benzo [1,2,3,4-*lmn*]benzo[4,5]imidazo[2,1-*b*]benzo[4,5]imidazo[1,2-*j*][1,4]dithiino[2,3-*f*][3,8]

phenanthroline-8,9,19,20-tetracarbonitrile (PTCNMe). Polyphosphoric acid (20.0 g) was added to a reaction vessel equipped with a mechanical stirrer and was deoxygenated under nitrogen at 150˚C overnight. NTA-TCN (0.50 g, 0.86 mmol) and 4,5-dimethylbenzene-1,2-diamine (0.25 g, 1.8 mmol) were added at room temperature and stirred at for 1 h before the temperature was increased 150˚C and the reaction was stirred for 4 hours, cooled to room temperature, quenched with ethanol, and the blue precipitate was filtered off and washed with water and ethanol until the pH of the filtrate was neutral. The crude product was dried under vacuum. The product was purified by adding hot toluene at 120˚C (1 L) and was stirred for 1 h before filtering. This was repeated 3 times, and then hot acetone was added and stirred at 50˚C overnight. The black powder was dried under vacuum at 120˚C. (0.24 g, 37% yield). ^{1}H NMR (500 MHz, DMSO-d6, δ): 7.43 ppm (s, 4H), 2.73 ppm (s, 4H), 2.33 ppm (s, 8H).

Synthesis of Polymer BBL-20TCN. PPA (39.88 g) was added to a reaction flask equipped with a mechanical stirrer and was purged with nitrogen at 150˚C overnight. The PPA was cooled to room temperature, and TABH (1.5 g, 5.28 mmol) was added. Dehydrochlorination was conducted at 75˚C for 24 h. Then, NTA-TCN (0.575 g, 1.06 mmol) and NTCA (1.28 g, 4.23 mmol) were added at the same time. The polymerization mixture was stirred at 80˚C for 4 hours followed by an incremental temperature increase to 100˚C over 5 hours and stirred overnight. The temperature of the polymerization mixture was increased to 150˚C over 8 hours and was stirred overnight, during which time the polymer solidified. The solid polymer dope was cooled to room temperature, quenched with water, and purified via Soxhlet extractions with water for 48 h and then methanol for 24 h. The crude product was dried and further purified by precipitation from MSA into methanol (yield 2.05 g, 98%). Intrinsic viscosity ([η]): 1.4 dL/g (30.0 °C, MSA).

Synthesis of Polymer BBL-35TCN. The polymerization was conducted according to the same procedure as the BBL-20TCN polymer, except that 35 mol% of NTA-TCN monomer was used. PPA (44 g), TABH (1.5 g, 5.28 mmol), NTA-TCN (1.00 g, 1.85 mmol) and NTCA (1.04 g, 3.43 mmol), (yield 2.06 g, 90%). Intrinsic viscosity ([η]): 1.3 dL/g (30.0 °C, MSA).

Synthesis of Polymer BBL-50TCN. The polymerization was conducted according to the same procedure as the BBL-20TCN polymer, except that 50 mol% of NTA-TCN monomer was used. PPA (47.9 g), TABH (1.5 g, 5.28 mmol), NTA-TCN (1.44 g, 2.64 mmol) and NTCA (0.803 g, 2.64 mmol), (yield 2.44 g, 97%). Intrinsic viscosity ([η]): 2.5 dL/g (30.0 °C, MSA).

3.2.3 Results and Discussion.

3.2.3.1 Synthesis and Characterization of the Model Compound and Random Copolymers.

The synthetic route to the model compound and random copolymers is shown in Scheme 3.2, and the detailed experimental procedures are in the Experimental Methods section. The 1,3,8,10-tetraoxo-1,3,8,10-tetrahydro-[1,4]dithiino[2',3':7,8]isochromeno[6,5,4-*def*][1,4]dithiino[2,3-*h*]isochromene-5,6,12,13 tetracarbonitrile (NTA-TCN) monomer was synthesized according to known procedures[46,52] in good yields of 94%. The proton NMR and the Fourier-transform infrared (FTIR) spectrum of NTA-TCN are shown in Figure C.1-C.2. In order to help understand the effects of incorporating dithiinotetracarbonitrile (TCN) groups into the backbone of BBL, the model compound, 2,3,14,15-tetramethyl-6,11-dioxo-6,11-dihydro-[1,4]dithiino[2',3':5,6]benzo[1,2,3,4-*lmn*] benzo[4,5]imidazo[2,1*b*] benzo[4,5]imidazo [1,2*j*][1,4]dithiino[2,3-*f*][3,8]phenanthroline-8,9,19,20-tetracarbonitrile (PTCNMe) was synthesized in pure polyphosphoric acid (PPA) identical to that of the random copolymers. The 1,2-diaminobenzene featuring two methyl groups was chosen to help improve the solubility of the model compound in polar aprotic solvents to aid in characterizations while still allowing

solubility in strong acids, such as methanesulfonic acid (MSA). PTCNMe has limited solubility in aprotic solvents such as DMSO, N,N-dimethylformamide (DMF), and trifluoroacetic acid, but has good solubility in strong acids such as MSA. The molecular structure was initially characterized by ^{1}H in DMSO-d6 shown in Figure C.3. The aromatic protons on the benzene ring appear as a 4H singlet at 7.5 ppm, and the methyl group protons appear as 2 singlets at 2.7 ppm and 2.3 ppm, which combined give 12H.

Scheme 3.2. Synthesis of (a) the model compound PTCNMe, and (b) the BBL-*x*TCN random copolymers (PPA= Polyphosphoric acid, 84% free P_2O_5).

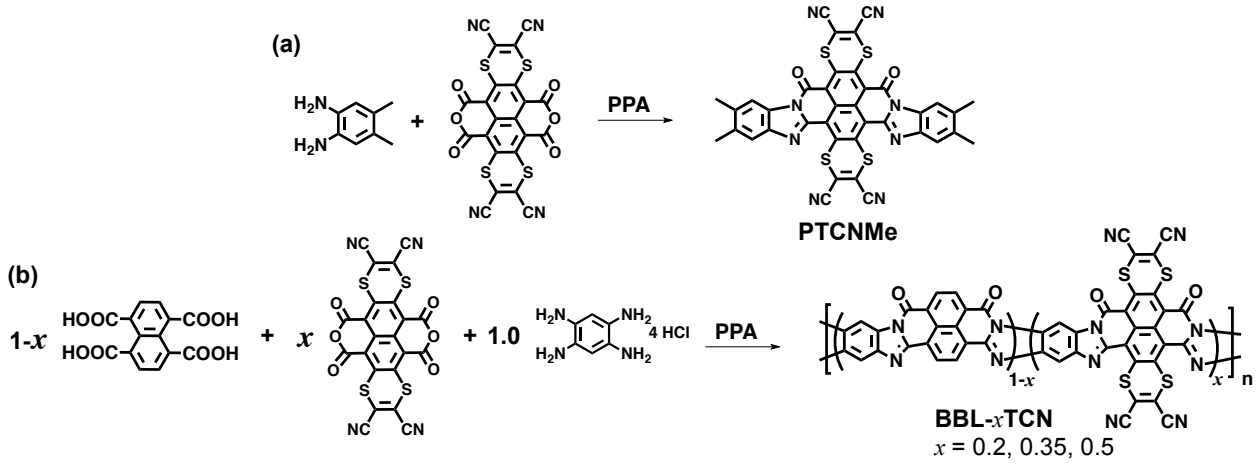

The random copolymers were synthesized with 20 - 50 mol% of the NTA-TCN comonomer (Scheme 3.2). For example, the BBL-20TCN polymer was synthesized from 1.0 equivalent of TABH, 0.2 equivalents of NTA-TCN, and 0.8 equivalents of NTCA. The polycondensation reactions in pure PPA were initiated at 5 wt.% in attempt to induce the liquid-crystalline phase and maximize the molecular weight of each polymer.[54] However, only BBL-20TCN had a noticeable liquid crystalline phase at 150˚C evidenced by shiny green stir opalescence. Notably, after stirring at 150˚C for ~ 12 hours, the copolymers solidified and formed the polymer dopes. In the case of the homopolymer BBL, the polymer dope that is

produced at the end of the reaction forms after stirring at 180˚C for several days at 10 wt.% in PPA. The 12-hour formation of the polymer dope at reduced temperatures results from the enhanced reactivity of the electron-deficient NTA-TCN monomer compared to NTCA, which reduces the thermodynamic and kinetic barriers for polycondensation.

BBL-20TCN and BBL-35TCN have good solubility in strong protic acids and produced red-purple colors in MSA solutions. BBL-50TCN has limited solubility in MSA even at high temperatures (~150˚C) such that during purification, the dilute MSA solution (1 mg/mL) required filtering before precipitation revealing that ~30% of the polymer mass was un-dissolved. This indicates that the filtrate contained the low molecular weight fractions of the copolymer solution. This can be explained by the increased reactivity of the NTA-TCN monomer such that 50 mol% resulted in high molecular weight, insoluble copolymers. The thermal stabilities of the model compound and copolymers were determined by TGA analysis in inert atmosphere and the results are shown in Figure C.5. All three polymers show excellent thermal stability with 5% weight loss ~ 460˚C, which is indicative of their fused ladder architecture.[1,16,51]

The intrinsic viscosities ([η]) of the copolymers in MSA solutions at 30.0˚C are 1.4 dL/g, 1.3 dL/g, and 2.5 dL/g for BBL-20TCN, BBL-35TCN, and BBL-50TCN, respectively. All three polymers have excellent film forming properties such that large area freestanding films could be fabricated. The detailed procedure for the fabrication of the high quality freestanding films is described in Appendix C. Freestanding films were used to characterize the molecular structures of the polymers by FTIR and Raman spectroscopies, and were compared to the FTIR and Raman spectra of the model compound (Figure 3.7a-d). The peak positions are assigned to the various vibrations listed in Table C.1-C.2.

As expected, the BBL-*x*TCN polymers show similar FTIR and Raman stretches that are comparable to those of BBL[16,55] and model compound PTCNMe. On the FTIR spectra (Figure 3.7a,c), the intense carbonyl *ν*(C=O) stretches for the three polymers are at 1705 cm^{-1}, and at 1697 cm^{-1} for the model compound. The medium-intensity *ν*(C=N) imide stretching bands are seen 1632 cm^{-1} for the polymers (Table C.2) and 1654 cm^{-1} for PTCNMe (Table C.1). The medium-intensity stretches at 1503 cm^{-1} and 1466 cm^{-1} are attributed to aromatic carbon-carbon *ν*(C=C) skeletal vibrations (Table C.2), and the single bond carbon-nitrogen stretches appear as sharp peaks around 1380 cm^{-1} and 1305 cm^{-1} for the copolymers. In PTCNMe, these stretches are associated with peaks at 1415 cm^{-1} and 1325 cm^{-1}, respectively (Table C.1). At lower wavenumbers, the polymer mixed skeletal vibrations appear as medium intensity bands at 1239 cm^{-1} and the carbon-sulfur n(C-S) stretching frequency appears as weak bands centered at 949 cm^{-1} (Table C.2).[56] The mixed skeletal vibrations for PTCNMe appear at 1177 cm^{-1}, and the C-S vibrations are at 996 cm^{-1} (Table C.1). We note that the nitrile stretches are absent on the FTIR spectra for the model compound and copolymers, which is in agreement with the DFT-predicted FTIR spectra shown in Figures C.5a,c calculated at the ωB97XD/6-31G(d,p) level of theory. Note that the calculations were performed on the representative BBL-50TCN copolymer with six repeat units arranged in a trans-cis orientation with respect to the imide.[4]

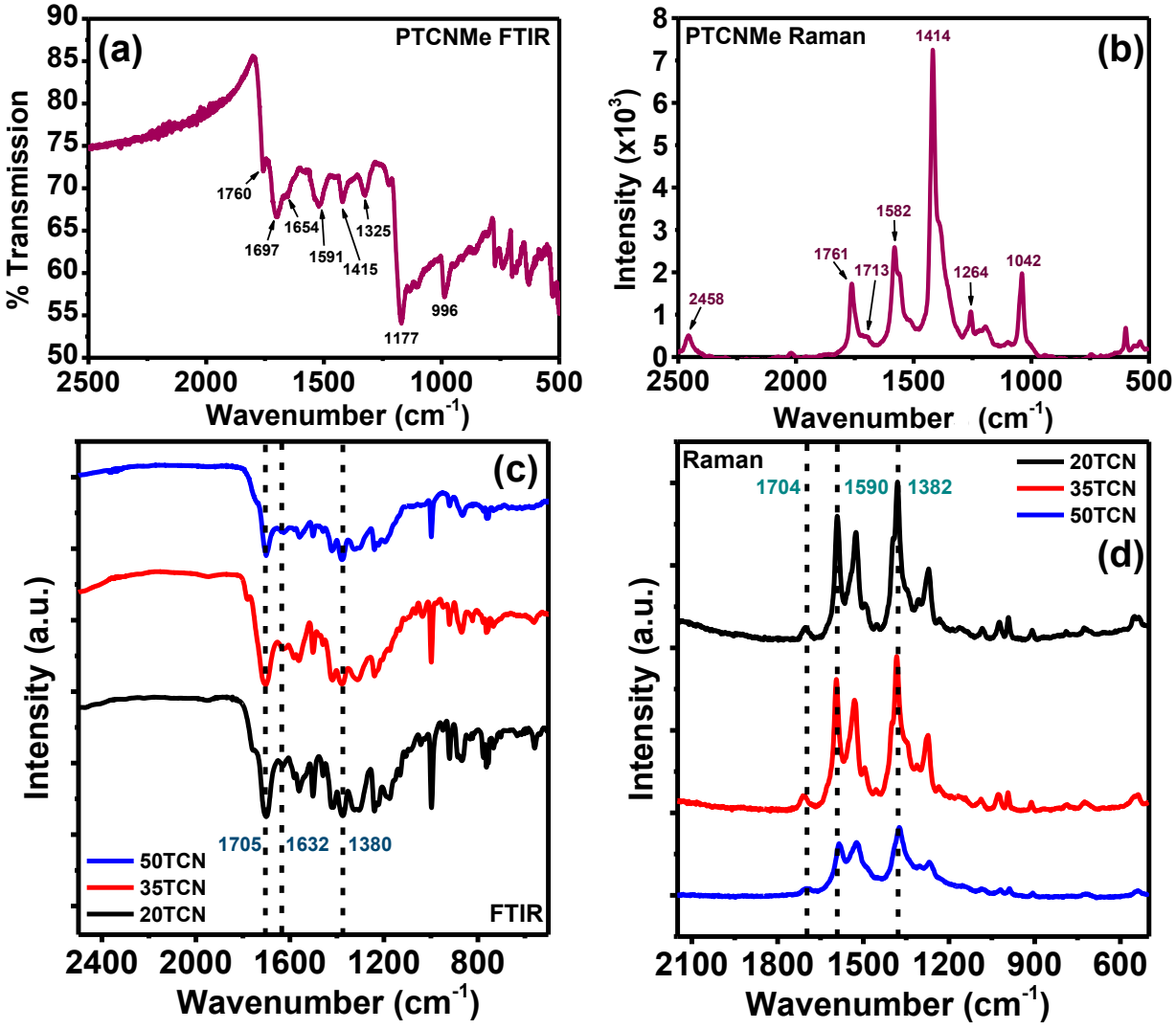

Figure 3.6. FTIR and Raman spectra of (a-b) the PTCNMe model compound and (c-d) the freestanding films of the BBL-*x*TCN random copolymers. The Raman spectra were collected with an excitation laser of 532 nm.

The Raman spectra show similar peaks as the FTIR spectra for the copolymers and model compound (Figure 3.7b,d and Tables C.1-C.2), with the exception of the nitrile stretch seen as a small-intensity peak at 2458 cm^{-1} for PTCNMe (Table C.1) that is absent in the copolymers. This observation is in agreement with the DFT-calculated Raman spectra of the model compound and

copolymers (Figure C.6b) that show no nitrile stretches on the Raman spectra for the copolymers (Figure C.5d). The carbonyl *v* (C=O) stretching frequency appears as low-intensity bands at 1713 cm^{-1} (Table C.1) and 1704 cm^{-1} (Table C.2) for PTCNMe and the BBL-*x*TCN copolymers, respectively. The intense *v* (C=N) imine stretches are at 1582 cm^{-1} for PTCNMe (Table C.1) and 1590 cm^{-1} for the copolymers (Table C.2). The sharp peaks at centered at 1555 cm^{-1} and 1414 cm^{-1} for PTCNMe and 1535 cm^{-1} and 1382 cm^{-1} for the copolymers are assigned to mixed aromatic *v* (C-C/C=C) carbon-carbon stretches (Table C.2). At lower wavenumbers, mixed skeletal vibrations are seen at 1256 cm^{-1}, 1189 cm^{-1}, and at 1267 cm^{-1}, 1020 cm^{-1}, and 990 cm^{-1} for PTCNMe and the copolymers, respectively. Finally, the *v* (C-S) carbon-sulfur stretch is observed as a sharp peak at 1042 cm^{-1} for PTCNMe (Table C.1). The collective FTIR and Raman spectra provide strong evidence for backbone fusion and the molecular structures of the random copolymers.

To further characterize the molecular structures of the model compound and BBL-*x*TCN copolymers, X-ray photoelectron spectroscopy (XPS) analysis was performed on thin films on silicon substrates. The survey scans are shown Figures C.6a-e, the high-resolution scans with optimal peak fitting of the C 1s, N 1s, and S 2p peaks in Figures 3.8 and C.7, and the tables of C 1s and N 1s binging energies, the C 1s and N 1s full-width at half-maximum (FWHM) values, and S 2p binding energies are in Tables C.3-C.4. The survey scans of BBL and the random copolymers (Figure C.6) show three intense peaks in the range of 280 eV - 530 eV that correspond to O 1s, N 1s, and C 1s emissions. Additionally, there are two peaks in the 160 – 230 eV region that correspond to S 2p and S 2s emissions that increase in area with increasing mol% of the TCN moiety. The area of the N 1s and S 2p emission peaks were used to quantify the sulfur/nitrogen ratio in the random copolymers and thus indicate the approximate mol% of NTA-

TCN incorporated into the backbone (Table 3.2). The measured sulfur/nitrogen ratios of 0.18, 0.28, and 0.41 corresponding to BBL-20TCN, BBL-35TCN, and BBL-50TCN, respectively, are closely matched to theoretical values of 0.17 for BBL-20TCN, 0.29 for BBL-35TCN, and 0.33 for BBL-50TCN (Table 3.2). This indicates that the NTA-TCN and NTCA comonomers were successfully incorporated in their approximate expected ratios, with the exception of BBL-50TCN. The 0.08 increase in the measured S/N value indicates an increased amount of NTA-TCN may be incorporated into the copolymer backbone, likely because of the high reactivity of the NTA-TCN monomer combined with the poor solubility of the resultant polymer.

Table 3.2. XPS Parameters Including the Combined Full-width at Half-maximum (FWHM) for N 1s Peaks, and Sulfur/Nitrogen Ratios of the BBL-*x*TCN Random Copolymers.

Compound	N 1s FWHM (eV)	Predicted S/N ratio	Measured S/N ratio
BBL	1.9	N/A	N/A
BBL-20TCN	2.1	0.17	0.18
BBL-35TCN	2.3	0.29	0.28
BBL-50TCN	2.4	0.33	0.41

The high-resolution XPS spectra of the N 1s emissions (Figure 3.8) for the model compound and BBL-*x*TCN copolymers show two separate peaks centered around 399.0 eV and 401.0 eV, which correspond to the imine/nitrile and amide nitrogen emissions, respectively (Table C.4).[57–59] We note that the nitrile nitrogen could not be resolved, which is likely because of the superposition of the nitrile and imine nitrogen peaks (Figure 3.8).[57–59] However, there is a substantial increase in the N 1s FWHM values from 1.9 eV in BBL to 2.4 eV in BBL-50TCN (Table 3.2). One explanation for the peak broadening is increased conformational disorder in the

copolymers as the mol% of the TCN moiety is increased.[60] However, a more likely explanation for the substantial peak broadening given the evidence of the nitrile peak in the previously discussed Raman spectrum (Figure 3.7b), is an increasing amount of underlying nitrile emissions contributing to the N 1s peak area. The presented XPS results provide strong evidence for the molecular structures of the model compound and random copolymers.

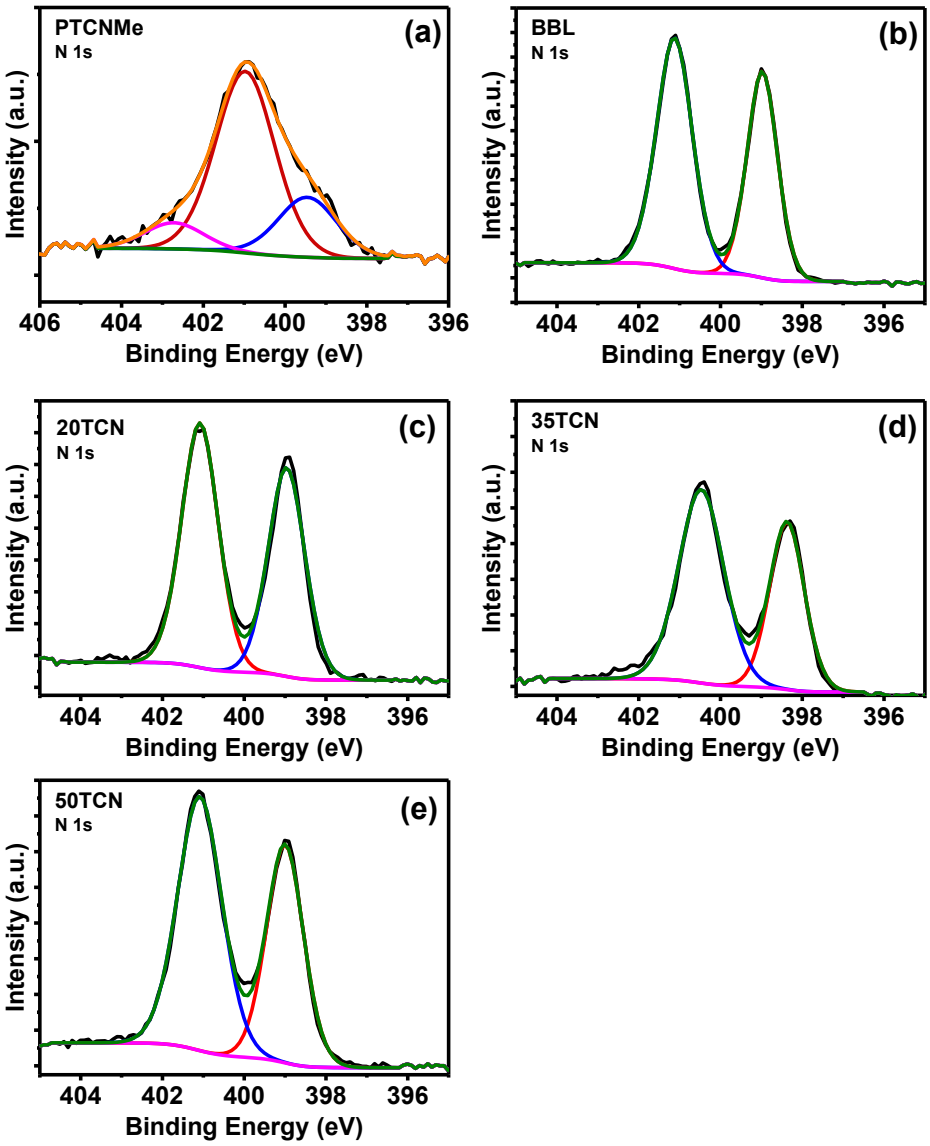

Figure 3.7. XPS spectra of the optimally fit high-resolution N 1s emissions of the PTCNMe model compound and BBL-*x*TCN random copolymers.

3.2.3.2 Electronic Structure. We investigated the electronic structure of the model compound and random copolymers by using a combination of DFT calculations, time-dependent (TD) DFT calculations, and cyclic voltammetry. The DFT and TD-DFT calculations were performed at the ωB97XD/631G(d,p) level of theory on the model compound and representative BBL-50TCN oligomer comprised of 6 repeat units oriented in a *cis-trans* isomeric distribution with respect to the imide, and the TCN moieties are placed on the *cis* repeat units. The ground state geometry of PTCNMe and BBL-50TCN in Figure 3.9 shows severe out-of-plane bending deformations along the π-conjugated backbone as well as through the TCN groups; this result is in contrast to BBL that has a coplanar molecular structure.[4,16] The molecular orbital distributions of PTCNMe are somewhat delocalized across the molecule; specifically, the HOMO is more centered along the benzene-naphthalene moieties, and the LUMO is localized to the naphthalene imide-TCN moieties (Figure 3.9a). The HOMO and in particularly the LUMO of the BBL-50TCN oligomer are extremely localized (Figure 3.9b) compared to the molecular orbital distributions in BBL calculated at the same level of theory.[4,16] The localization of the HOMO and LUMO molecular orbitals implies that charge density may be trapped in the monomeric regions containing the strong electron-withdrawing TCN moiety, which could decrease the electrical conductivity relative to BBL.[24,61]

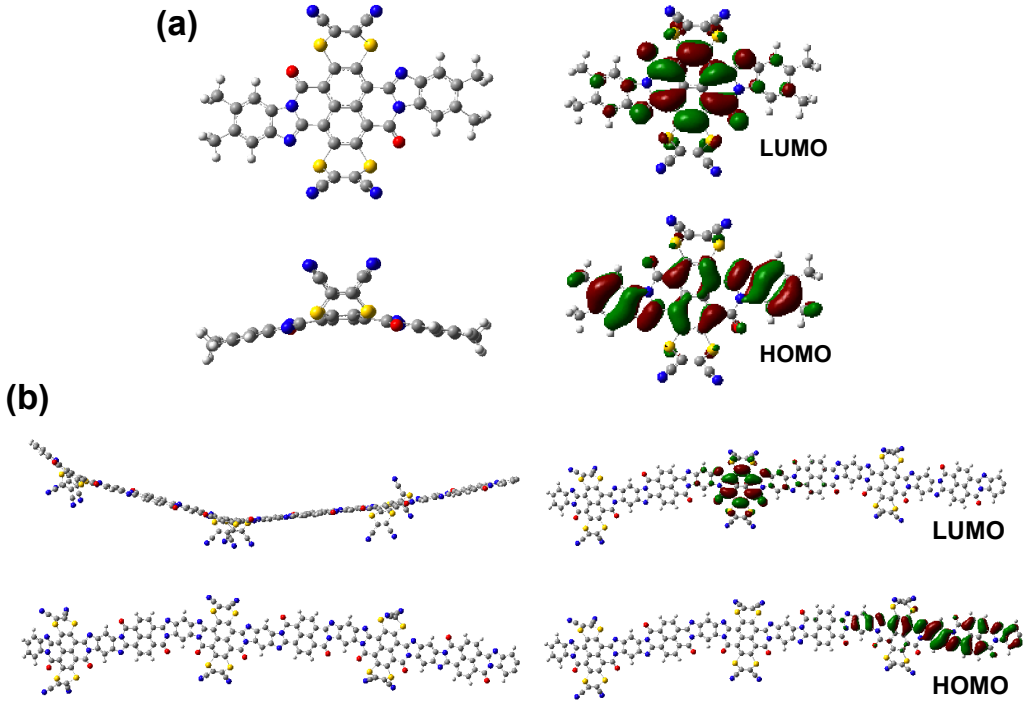

Figure 3.8. DFT calculations of the optimized ground state geometry and frontier molecular orbital distributions of (a) PTCNMe and (b) the representative BBL-50TCN oligomer comprised of 6 repeat units. The calculations were performed at the ωB97XD-631G(d,p) level of theory.

To gain insight into the electron density distributions in the TCN moiety, an electrostatic potential (ESP) map was calculated using the ground state geometry of PTCNMe shown in Figure C.8. Regions of high electron density (negative charges), which are represented as areas of red-orange, are almost exclusively localized on the TCN groups, while areas lacking electron density (positive charges) are shown as the blue-green regions and are accumulated on the central naphthalene core and extending out to the benzene moieties. The localization of the electron density suggests that there may be regions of intramolecular charge transfer (ICT) between the TCN groups and the polyaromatic core. The TD-DFT calculated absorption spectrum for the optimized model compound shown in Figure C.9 closely resembles the experimental thin film absorption spectrum where the π-π* transition is centered at 580 nm. The

pictoral representations of both the electron and hole orbital distributions corresponding to the π-π* transition are shown in Figure C.9c.

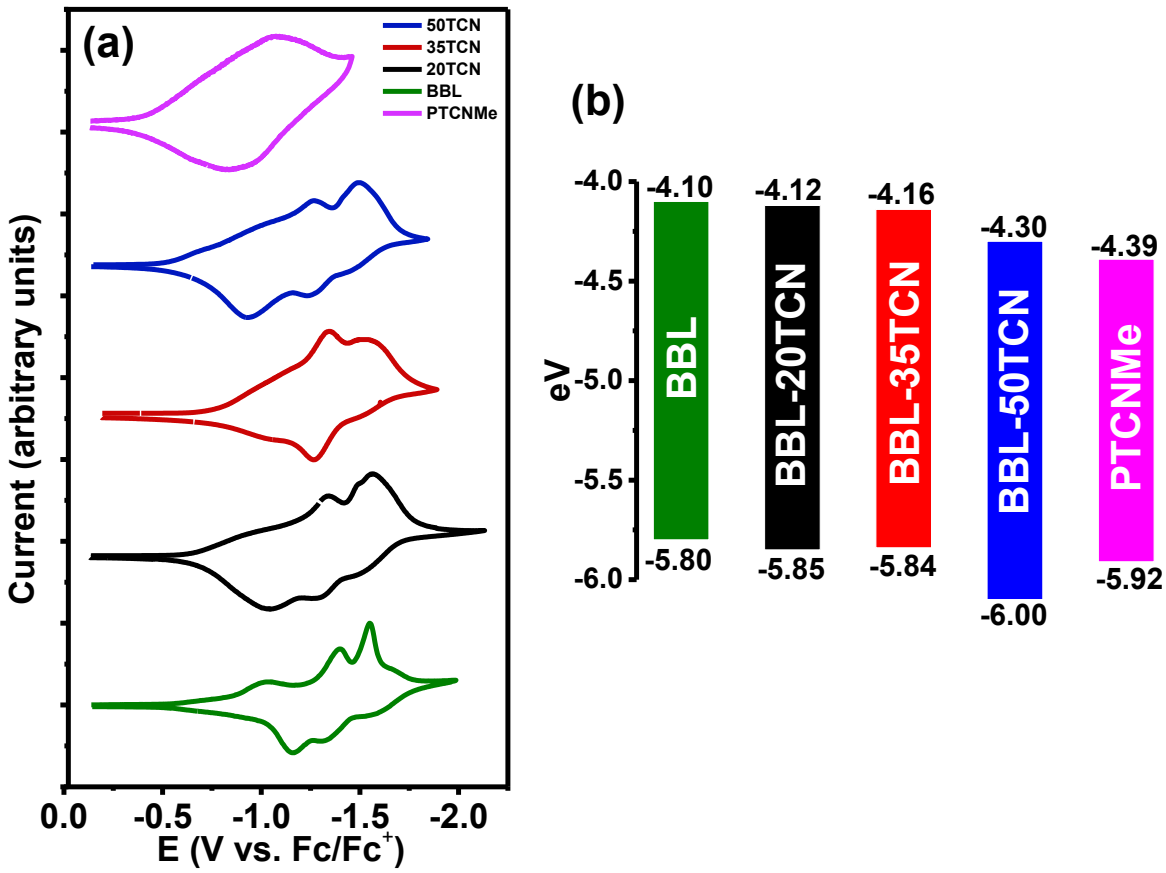

Figure 3.9. (a) Cyclic voltammograms for the reduction processes of PTCNMe and the BBL-*x*TCN random copolymers as thin films measured in 0.1 M Bu_4NPF_6 electrolyte solution using $Ag/AgNO_3$ as the reference electrode and plotted vs. Fc/Fc^+. The scan rate was 15 mV/s. (b) Energy levels of PTCNMe and the BBL-*x*TCN series.

We used cyclic voltammetry (CV) to further investigate the electronic structure of the model compound and random copolymer thin films coated on platinum wires from which the HOMO and LUMO energy levels were derived. The detailed experimental conditions are in the Experimental Methods section, the reduction scans vs. Fc/Fc^+ are shown in Figure 3.10a, and the

HOMO and LUMO energy levels are presented graphically in Figure 3.10b. The energy levels and electrochemical bandgap ($E_g^{elec.}$) are listed in Table 3.3. PTCNMe shows two quasi-reversible reduction peaks at -0.67 V and -1.08 V, and an onset reduction potential at -0.41 V from which a LUMO energy level of -4.39 eV was derived (Table 3.3). We note that the LUMO level of PTCNMe is 0.11 eV lower than that reported for the naphthalene diimide version of –4.28 eV.[46] BBL-20TCN shows four quasi-reversible reduction waves at -0.90 V, -1.35 V, -1.49 V, and -1.56 V (Figure 3.10a), and the LUMO energy level measured from the onset of reduction at -0.68 V was found to be -4.12 eV, which is nearly identical to the LUMO energy level of -4.10 measured for BBL (Figure 3.10b and Table 3.3). Comparing the potentials of all the reduction peaks of the copolymers shows them shifting towards higher potentials with an increasing mol% of the TCN moiety (Figure 3.10a). For example, the first reduction peak in BBL at -1.01 V (Figure 3.10a) is shifted to -0.90 V for BBL-20TCN; this trend continues for all the reduction peaks in BBL-20TCN, BBL-35TCN, and BBL-50TCN (Figure 3.10a). The shift of the reduction peaks towards higher potentials indicates that the reduction process (n-dopability) is facilitated by as little as 20 mol% of the electron-deficient TCN moiety. The reduction scan of BBL-35TCN (Figure 3.10a) shows three quasi-reversible reduction waves at -0.90 V, -1.35 V, and -1.56 V, and the onset of reduction measured at -0.66 V was used to calculate a similar LUMO energy level of -4.16 eV (Figure 3.10b). Increasing the TCN moiety to 50 mol% shifts the quasi-reversible reduction peaks towards even higher potentials: -0.68 V, -0.97 V, -1.26 V, and -1.49 V (Figure 3.10a). Moreover, the measured LUMO energy level of -4.30 eV determined from the onset of reduction at -0.50 V is 0.20 eV lower than for BBL (Table 3.3). This result indicates that at least 50 mol% of the TCN moiety is required to significantly affect the LUMO levels of the random copolymers.

The oxidation scans of the random copolymers and model compound vs. Ag/Ag^+ show one non-reversible oxidation wave each at 1.69 V for BBL-20TCN (Figure C.10a), 1.31 V for BBL-35TCN (Figure C.10b), 1.67 V for BBL-50TCN (Figure C.10c), and 1.59 V for PTCNMe (Figure C.10d). The HOMO energy level of BBL-20TCN was calculated from the onset of oxidation at 1.20 V and found to be -5.85 eV, which is comparable to that reported for BBL (Table 3.3).[4] The onset of oxidation for BBL-35TCN is 1.20 V, which was used to calculate the HOMO energy level of -5.84 eV, and an onset oxidation potential of 1.46 V for BBL-50TCN was used to calculate the HOMO level of -6.00 eV (Table 3.3). Finally, the HOMO level of -5.92 eV was calculated for PTCNMe from the onset of 1.28 V. The electrochemical bandgaps ($E_g^{elec.}$) range from 1.53 eV to 1.80 eV (Table 3.3).

Table 3.3. Electronic Structure Parameters and Optical Properties of the model compound PTCNMe and the BBL-*x*TCN polymers.

Compound	HOMO[(a)] (eV)	LUMO[(a)] (eV)	$E_g^{elec.(a)}$ (eV)	$\lambda_{max}^{(b)}$ (nm)	$\varepsilon_{max}^{(b)}$ (M^{-1} cm^{-1})	$\lambda_{max}^{(c)}$ (nm)	$\alpha_{max}^{(c)}$ (cm^{-1})	$E_g^{opt.(c)}$ (eV)
PTCNMe	-5.92	-4.39	1.53	559	1.9×10^4	580	-	1.52
BBL	-5.80[(d)]	-4.10	1.70	545	4.9×10^4	576	1.9×10^5	1.64
BBL-20TCN	-5.85	-4.12	1.73	542	4.4×10^4	561	1.8×10^5	1.67
BBL-35TCN	-5.84	-4.16	1.70	533	4.4×10^4	561	1.3×10^5	1.63
BBL-50TCN	-6.00	-4.30	1.80	518	1.8×10^4	574	1.4×10^5	1.60

[(a)] Measured from cyclic voltammetry. [(b)] Solution in MSA. [(c)] Spin-coated thin films from MSA solution. [(d)]Value taken from reference (4).

3.2.3.3 Optical Properties. The optical absorption spectra of the model compound and BBL-*x*TCN polymers in MSA solution and as thin films on glass substrates are shown in Figure 3.11, and the normalized optical absorbance spectra of the MSA solutions and thin film on glass are in Figure C.11. The optical properties (molar absorptivity (ε_{max}), absorption coefficient (α), and

optical bandgap ($E_{g,}^{opt.}$)) are summarized in Table 3.3. In MSA solutions, PTCNMe shows two high energy bands at 345 nm (ε_{max} = 1.6 x 10^4 M^{-1} cm^{-1}) and 431 nm (ε_{max} = 1.1 x 10^4 M^{-1} cm^{-1}), and one low energy band at 561 nm (e_{max} = 1.9 x 10^4 M^{-1} cm^{-1}), which can be assigned to the π-π* transition (Figure 3.11a). The copolymers also show two high energy bands centered around 324 nm and 376 nm, and a high intensity, lowest-energy peak ranging from 545 nm in BBL to 518 nm in BBL-50TCN, which can be assigned to the π-π* transition (Figure 3.11b). Going from the 0 – 50 mol% of TCN in the copolymer backbone results in a series of interesting trends in the MSA solution absorption spectrum of the copolymers. First, the π-π* peak is blue-shifted by 27 nm from BBL to BBL-50TCN, which is accompanied by spectral broadening (Figure C.11a). The blue shift can be explained by the increased molecular disorder in the copolymer backbone that was observed on the previously discussed DFT calculations (Figure 3.9). Second, the MSA solution absorption spectra of the random copolymers show a new band appearing around 680 nm that is absent in BBL but present in PTCNMe (Figure 3.11a). We propose this peak is from protonation-enhanced ICT character in the TCN-containing polymers and model compound, whereby protonation of the sulfur groups in the random copolymers enhances the ICT interactions in the polymer backbone.[62–64]

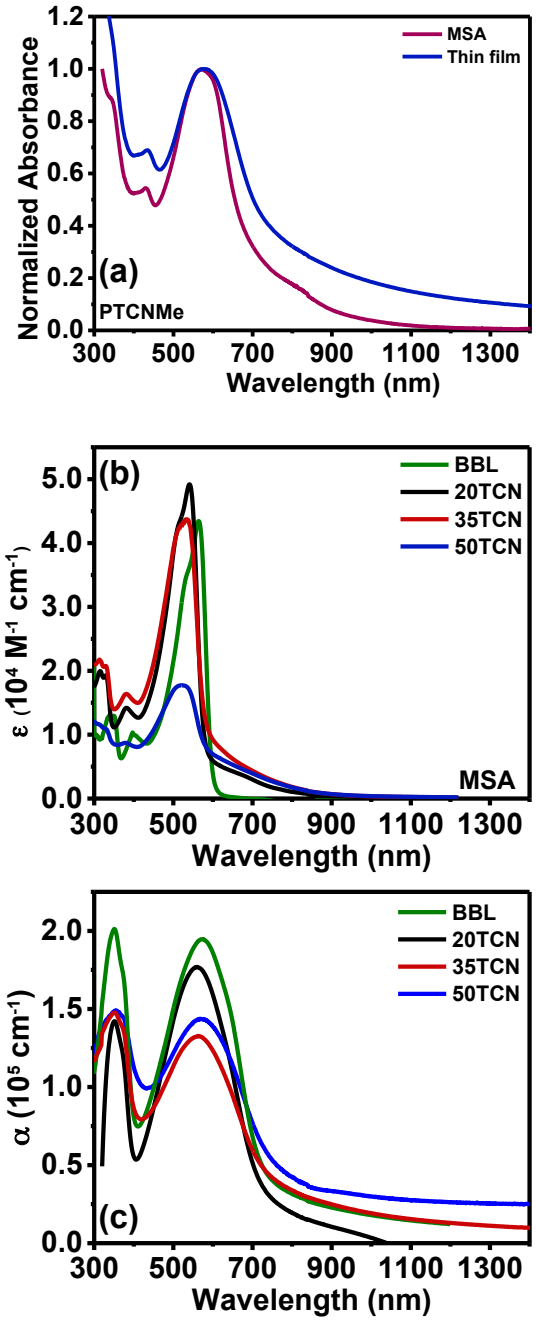

Figure 3.10. (a) Normalized optical absorption spectra of the PTCNMe model compound as a thin film on glass and in MSA solution. Optical absorption spectra of the BBL-*x*TCN copolymers as (b) MSA solutions, and (c) as thin films on glass substrates.

The optical absorption spectrum of PTCNMe thin films on glass show one high energy band at 434 nm and a lowest-energy band, which is assigned to the π-π* transition, at 580 nm. We note that the spectral shape and peak positions of the PTCNMe thin film are closely matched

with the previously discussed simulated absorption spectrum where the π-π* peak is centered at 576 nm (Figure C.9b). The thin film absorption spectra for the copolymers show two broad bands in the 300 – 800 nm region with a high energy peak at 353 nm and the lowest energy peak ranging from 576 - 561 nm for BBL to BBL-50TCN, which can be assigned to the π-π* transition (Table 3.3). The slightly blue-shifted and spectrally broadened 561-nm peak of BBL-35TCN, which is also accompanied by a decreasing α_{max} value (Table 3.3), indicates that the thin films are more disordered compared to BBL thin films. In the case of BBL-50TCN, despite showing the most spectral broadening, the π-π* transition is centered at 574 nm, which is identical to that of BBL, and has a slightly increased α_{max} value relative to BBL-35TCN (Table 3.3). This trend implies that the induction effects of the TCN moiety in the BBL-50TCN backbone are strong enough to slightly increase the effective π-conjugation length relative to BBL-35TCN despite the conformational disorder. The optical bandgaps ($E_g^{opt.}$) calculated from the onset of absorption range between 1.60 eV – 1.67 eV and slightly smaller than the $E_g^{elec.}$ values of 1.70 eV – 1.80 eV measured from the CV scans that were previously discussed (Table 3.3).

Compared to the solution absorption spectra, the thin film spectra have notable differences. In particular, the 680-nm absorption band is absent in the thin film, confirming its protonation-enhanced ICT origins (Figure 3.11a). Additionally, the thin film absorption spectra are red-shifted by 23 nm - 43 nm for the BBL-*x*TCN polymers, and 21 nm for PTCNMe compared to the MSA solution absorption spectra (Table 3.3), which suggests improved molecular ordering of the copolymers and model compound in the solid state compared to the protonated species in MSA solutions.

3.2.4 Conclusions

We have synthesized and investigated the molecular and electronic structure, and optical properties of a series of electron-deficient BBL-based random copolymers featuring dithiinotetracarbonitrile (TCN) moieties, BBL-*x*TCN (*x* = 20, 35, and 50) and the corresponding model compound PTCNMe. We found that the TCN-containing monomer increased the speed of polycondensation such that the copolymers formed in 12 hours and produced copolymers with modest intrinsic viscosity values ranging from 1.3 dL/g - 2.5 dL/g in MSA at 30.0˚C. Additionally, we found that incorporating as little as 20 mol% of the electron-deficient moieties into the backbone decreased the reduction potentials of the polymers, and 50 mol% of the TCN monomer decreased the LUMO energy level by 0.20 eV.

The MSA solution absorption spectra showed the appearance of a small peak at 680 nm, which is absent in the thin film absorption spectra, and is attributed to protonation-enhanced intramolecular charge transfer effects. The thin film absorption spectra of the polymers show similar optical bandgaps ranging from 1.60 eV – 1.67 eV. Notably, we found that incorporation of 35 - 50 mol% of the TCN moiety induced substantial peak broadening in the thin-film optical absorption spectra, which originates from the enhanced structural disorder of the random copolymers that was evidenced by DFT calculations. The present results on the BBL-*x*TCN polymers provide new insights into how functionalization of BBL with electron-deficient moieties influences the synthesis, electronic structure and optical properties of π-conjugated ladder polymers.

3.2.5 References

1. Deusen, R. L. V. Benzimidazo-Benzophenanthroline Polymers. *J. Polym. Sci. B Polym. Lett.* **1966**, *4* (3), 211–214. DOI: 10.1002/pol.1966.110040310.

2. Babel, A.; Jenekhe, S. A. Electron Transport in Thin-Film Transistors From an n-Type Conjugated Polymer. *Adv. Mater.* **2002**, *14* (5), 371–374. DOI: 10.1002/1521-4095(20020304)14:5<371::AID-ADMA371>3.0.CO;2-5.

3. Babel, A.; Jenekhe, S. A. N-Channel Field-Effect Transistors from Blends of Conjugated Polymers. *J. Phys. Chem. B* **2002**, *106* (24), 6129–6132. DOI: 10.1021/jp020695l.

4. Kim, F. S.; Park, C. H.; Na, Y.; Jenekhe, S. A. Effects of Ladder Structure on the Electronic Properties and Field-Effect Transistor Performance of Poly(Benzobisimidazobenzophenanthroline). *Org. Electron.* **2019**, *69*, 301–307. DOI: 10.1016/j.orgel.2019.03.049.

5. Alam, M. M.; Jenekhe, S. A. Efficient Solar Cells from Layered Nanostructures of Donor and Acceptor Conjugated Polymers. *Chem. Mater.* **2004**, *16* (23), 4647–4656. DOI: 10.1021/cm0497069.

6. Jenekhe, S. A.; Yi, S. Efficient Photovoltaic Cells from Semiconducting Polymer Heterojunctions. *Appl. Phys. Lett.* **2000**, *77* (17), 2635–2637. DOI: 10.1063/1.1320022.

7. Wang, S.; Sun, H.; Ail, U.; Vagin, M.; Persson, P. O. Å.; Andreasen, J. W.; Thiel, W.; Berggren, M.; Crispin, X.; Fazzi, D.; Fabiano, S. Thermoelectric Properties of Solution-Processed n-Doped Ladder-Type Conducting Polymers. *Adv. Mater.* **2016**, *28* (48), 10764–10771. DOI: 10.1002/adma.201603731.

8. Tam, T. L. D.; Lin, M.; Handoko, A. D.; Lin, T. T.; Xu, J. High-Performance & Thermally Stable n-Type Polymer Thermoelectrics Based on a Benzyl Viologen Radical Cation-Doped Ladder-Type Conjugated Polymer. *J. Mater. Chem. A* **2021**, 9, 11787-11793. DOI: 10.1039/D1TA01645H.

9. Yang, C.; Stoeckel, M.; Ruoko, T.; Wu, H.; Liu, X.; Kolhe, N.; Wu, Z.; Puttisong, Y.; Musumeci, C.; Massetti, M.; Sun, H.; Xu, K.; Tu, D.; Chen, W.; Woo, H.; Fahlman, M.; Jenekhe, S.; Berggren, M.; Fabiano, S. A High-Conductivity n-Type Polymeric Ink for Printed Electronics. *Nat. Commun.* **2021**, *12* (1). 2354. DOI: 10.1038/s41467-021-22528-y.

10. Sun, H.; Vagin, M.; Wang, S.; Crispin, X.; Forchheimer, R.; Berggren, M.; Fabiano, S. Complementary Logic Circuits Based on High-Performance n-Type Organic Electrochemical Transistors. *Adv. Mater.* **2018**, *30* (9), 1704916. DOI: 10.1002/adma.201704916.

11. Surgailis, J.; Savva, A.; Druet, V.; Paulsen, B. D.; Wu, R.; Hamidi-Sakr, A.; Ohayon, D.; Nikiforidis, G.; Chen, X.; McCulloch, I.; Rivnay, J.; Inal, S. Mixed Conduction in an N-Type Organic Semiconductor in the Absence of Hydrophilic Side-Chains. *Adv. Funct. Mater.* **2021**, *31* (21), 2010165. DOI: 10.1002/adfm.202010165.

12. Guo, J.; Flagg, L. Q.; Tran, D. K.; Chen, S. E.; Li, R.; Kolhe, N. B.; Giridharagopal, R.; Jenekhe, S. A.; Richter, L. J.; Ginger, D. S. Hydration of a Side-Chain-Free n-Type Semiconducting Ladder Polymer Driven by Electrochemical Doping. *J. Am. Chem. Soc.* **2023**, *145* (3), 1866–1876. DOI: 10.1021/jacs.2c11468.

13. Wu, H.-Y.; Yang, C.-Y.; Li, Q.; Kolhe, N. B.; Strakosas, X.; Stoeckel, M.-A.; Wu, Z.; Jin, W.; Savvakis, M.; Kroon, R.; Tu, D.; Woo, H. Y.; Berggren, M.; Jenekhe, S. A.; Fabiano, S. Influence of Molecular Weight on the Organic Electrochemical Transistor Performance of Ladder-Type Conjugated Polymers. *Adv. Mater.* **2022**, *34* (4), 2106235. DOI: 10.1002/adma.202106235.

14. Song, H.; Fratini, A.; Chabinyc, M.; Price, G.; Agrawal, A.; Wand, C.; Brikette, J.; Dudis, D.; Arnold, F. Crystal-structure and Thin-film Morphology of BBL Ladder Polymers. *Synth. Met.* **1995**, *69* (1–3), 533–535. DOI: 10.1016/0379-6779(94)02556-E.

15. Berry, G. C. Properties of an Optically Anisotropic Heterocycle Ladder Polymer (BBL) In Dilute-Solution. *J. Polym. Sci.,C Polym. Symp.* **1978,** 65,143-172. DOI: 10.1002/polc.5070650115.

16. West, S. M.; Tran, D. K.; Guo, J.; Chen, S. E.; Ginger, D. S.; Jenekhe, S. A. Phenazine-Substituted Poly(Benzimidazobenzophenanthrolinedione): Electronic Structure, Thin Film Morphology, Electron Transport, and Mechanical Properties of an n-Type Semiconducting Ladder Polymer. *Macromolecules* **2023**, *56* (5) 2081-2091. DOI: 10.1021/acs.macromol.2c01999.

17. He, Q.; Dexter Tam, T. L.; Lin, T.; Chien, S. W.; Lin, M.; Meng, H.; Huang, W.; Xu, J. π-Extended Poly(Benzimidazoanthradiisoquinolinedione) Ladder-Type Conjugated Polymer. *ACS Macro Lett.* **2022**, *11* (9), 1136–1141. DOI: 10.1021/acsmacrolett.2c00438.

18. He, Q.; Zhang, X.; Tam, T. L. D.; Wang, J.; Chen, H.; Chien, S. W.; Tham, N. N.; Koh, X. Q.; Lee, J. J. C.; Lin, M.; Soh, P. X.; Meng, H.; Huang, W.; Xu, J. Balancing Solubility and Thermoelectric Performance in π-Extended Poly(Benzimidazoanthradiisoquinolinedione) Ladder-Type Conjugated Polymer. *ACS Appl. Electron. Mater.* **2023**. DOI: 10.1021/acsaelm.3c00294.

19. Brixi, S.; Melville, O. A.; Mirka, B.; He, Y.; Hendsbee, A. D.; Meng, H.; Li, Y.; Lessard, B. H. Air and Temperature Sensitivity of N-Type Polymer Materials to Meet and Exceed the Standard of N2200. *Sci. Rep.* **2020**, *10* (1), 4014. DOI: 10.1038/s41598-020-60812-x.

20. Zhan, X.; Facchetti, A.; Barlow, S.; Marks, T. J.; Ratner, M. A.; Wasielewski, M. R.; Marder, S. R. Rylene and Related Diimides for Organic Electronics. *Adv. Mater.* **2011**, *23* (2), 268–284. DOI: 10.1002/adma.201001402.

21. Babel, A.; Wind, J. D.; Jenekhe, S. A. Ambipolar Charge Transport in Air-Stable Polymer Blend Thin-Film Transistors. *Adv. Funct. Mater.* **2004**, *14* (9), 891–898. DOI: 10.1002/adfm.200305180.

22. Griggs, S.; Marks, A.; Bristow, H.; McCulloch, I. N-Type Organic Semiconducting Polymers: Stability Limitations, Design Considerations and Applications. *J. Mater. Chem. C* **2021**, *9* (26), 8099–8128. DOI: 10.1039/D1TC02048J.

23. Anthony, J. E.; Facchetti, A.; Heeney, M.; Marder, S. R.; Zhan, X. N-Type Organic Semiconductors in Organic Electronics. *Adv. Mater.* **2010**, *22* (34), 3876–3892. DOI: 10.1002/adma.200903628.

24. Fratini, S.; Nikolka, M.; Salleo, A.; Schweicher, G.; Sirringhaus, H. Charge Transport in High-Mobility Conjugated Polymers and Molecular Semiconductors. *Nat. Mater.* **2020**, *19* (5), 491–502. DOI: 10.1038/s41563-020-0647-2.

25. Tang, C. G.; Hou, K.; Leong, W. L. The Quest for Air Stability in Organic Semiconductors. *Chem. Mater.* **2024**, *26* (1), 28-53. DOI: 10.1021/acs.chemmater.3c02093.

26. Fahlman, M.; Fabiano, S.; Gueskine, V.; Simon, D.; Berggren, M.; Crispin, X. Interfaces in Organic Electronics. *Nat. Rev. Mater.* **2019**, *4* (10), 627–650. DOI: 10.1038/s41578-019-0127-y.

27. Chen, X.; Jenekhe, S. A. Bipolar Conducting Polymers: Blends of p-Type Polypyrrole and an n-Type Ladder Polymer. *Macromolecules* **1997**, *30* (6), 1728–1733. DOI: 10.1021/ma961121f.

28. Xu, K.; Sun, H.; Ruoko, T.-P.; Wang, G.; Kroon, R.; Kolhe, N. B.; Puttisong, Y.; Liu, X.; Fazzi, D.; Shibata, K.; Yang, C.-Y.; Sun, N.; Persson, G.; Yankovich, A. B.; Olsson, E.; Yoshida, H.; Chen, W. M.; Fahlman, M.; Kemerink, M.; Jenekhe, S. A.; Müller, C.; Berggren, M.; Fabiano, S. Ground-State Electron Transfer in All-Polymer Donor–Acceptor Heterojunctions. *Nat. Mater.* **2020**, *19* (7), 738–744. DOI: 10.1038/s41563-020-0618-7.

29. Cheng, P.; Zhao, X.; Zhan, X. Perylene Diimide-Based Oligomers and Polymers for Organic Optoelectronics. *Acc. Mater. Res.* **2022**, *3* (3), 309–318. DOI: 10.1021/accountsmr.1c00191.

30. Guo, X.; Watson, M. D. Conjugated Polymers from Naphthalene Bisimide. *Org. Lett.* **2008**, *10* (23), 5333–5336. DOI: 10.1021/ol801918y.

31. Randell, N. M.; Boutin, P. C.; Kelly, T. L. Bisisoindigo: Using a Ring-Fusion Approach to Extend the Conjugation Length of Isoindigo. *J. Mater. Chem. A* **2016**, *4* (18), 6940–6945. DOI: 10.1039/C5TA07511D.

32. Yu, Y.; Zhu, D.; Zhu, X.; Ravva, M. K.; Duan, J.; Jiang, L.; Li, Z.; Yue, W. A Novel Class of Rigid-Rod Perylene Diimides and Isoindigo Semiconducting Polymers. *Polym. Chem.* **2022**, 13, 536-544. DOI: 10.1039/D1PY01362A.

33. Ray, S.; Sharma, S.; Salzner, U.; Patil, S. Synthesis and Characterization of Quinoidal Diketopyrrolopyrrole Derivatives with Exceptionally High Electron Affinities. *J. Phys. Chem. C* **2017**, *121* (30), 16088–16097. DOI: 10.1021/acs.jpcc.7b04085.

34. Li, Y.; Sonar, P.; Murphy, L.; Hong, W. High Mobility Diketopyrrolopyrrole (DPP)-Based Organic Semiconductor Materials for Organic Thin Film Transistors and Photovoltaics. *Energy Environ. Sci.* **2013**, *6* (6), 1684–1710. DOI: 10.1039/C3EE00015J.

35. Zhao, X.; Cai, H.; Deng, Y.; Jiang, Y.; Wang, Z.; Shi, Y.; Han, Y.; Geng, Y. Low-Band Gap Conjugated Polymers with Strong Absorption in the Second Near-Infrared Region Based on Diketopyrrolopyrrole-Containing Quinoidal Units. *Macromolecules* **2021**, *54* (7), 3498-3506. DOI: 10.1021/acs.macromol.1c00124.

36. Singh Mehra, K.; Jha, S.; M. Menon, A.; Chopra, D.; Sankar, J. The Deeper It Goes, the Brighter It Glows: NIR Emissive Nitro-Terrylene Diimides with Deep LUMOs. *Chem. Sci.* **2023**, *14* (12), 3147–3153. DOI: 10.1039/D2SC06162G.

37. Lim, D.-H.; Ha, J.-W.; Choi, H.; Cheol Yoon, S.; Ram Lee, B.; Ko, S.-J. Recent Progress of Ultra-Narrow-Bandgap Polymer Donors for NIR-Absorbing Organic Solar Cells. *Nanoscale Adv.* **2021**, *3* (15), 4306–4320. DOI:10.1039/D1NA00245G.

38. Liu, Y.; Zhao, W.; Wu, Y.; Zhang, J.; Li, G.; Li, W.; Ma, W.; Hou, J.; Bo, Z. Enhancing the Power Conversion Efficiency of Polymer Solar Cells to 9.26% by a Synergistic Effect of Fluoro and Carboxylate Substitution. *J. Mater. Chem. A* **2016**, *4* (21), 8097–8104. DOI: 10.1039/C6TA02622B.

39. Zhang, Y.; Kong, L.; Ju, X.; Zhao, J. Effects of Fluoro Substitution on the Electrochromic Performance of Alternating Benzotriazole and Benzothiadiazole-Based Donor–Acceptor Type Copolymers. *Polymers* **2018**, *10* (1), 23. DOI: 10.3390/polym10010023.

40. Bauer, N.; Zhang, Q.; Rech, J. J.; Dai, S.; Peng, Z.; Ade, H.; Wang, J.; Zhan, X.; You, W. The Impact of Fluorination on Both Donor Polymer and Non-Fullerene Acceptor: The More Fluorine, the Merrier. *Nano Res.* **2019**, *12* (9), 2400–2405. DOI: 10.1007/s12274-019-2362-3.

41. Zhang, M.; Guo, X.; Zhang, S.; Hou, J. Synergistic Effect of Fluorination on Molecular Energy Level Modulation in Highly Efficient Photovoltaic Polymers. *Adv. Mater.* **2014**, *26* (7), 1118–1123. DOI: 10.1002/adma.201304427.

42. Casey, A.; Dimitrov, S. D.; Shakya-Tuladhar, P.; Fei, Z.; Nguyen, M.; Han, Y.; Anthopoulos, T. D.; Durrant, J. R.; Heeney, M. Effect of Systematically Tuning Conjugated Donor Polymer Lowest Unoccupied Molecular Orbital Levels via Cyano Substitution on Organic Photovoltaic Device Performance. *Chem. Mater.* **2016**, *28* (14), 5110–5120. DOI: 10.1021/acs.chemmater.6b02030.

43. Feng, K.; Guo, H.; Wang, J.; Shi, Y.; Wu, Z.; Su, M.; Zhang, X.; Son, J. H.; Woo, H. Y.; Guo, X. Cyano-Functionalized Bithiophene Imide-Based n-Type Polymer Semiconductors: Synthesis, Structure–Property Correlations, and Thermoelectric Performance. *J. Am. Chem. Soc.* **2021**, *143* (3), 1539–1552. DOI: 10.1021/jacs.0c11608.

44. Hergué, N.; Mallet, C.; Savitha, G.; Allain, M.; Frère, P.; Roncali, J. Facile Synthesis of 3-Alkoxy-4-Cyanothiophenes As New Building Blocks for Donor−Acceptor Conjugated Systems. *Org. Lett.* **2011**, *13* (7), 1762–1765. DOI: 10.1021/ol200296j.

45. Hirvonen, S.; Tenhu, H. Modification of Naphthalenic Unit in BBL Main Chain. *Synth. Met.* **2015**, *207*, 87–95. DOI: 10.1016/j.synthmet.2015.06.013.

46. Hu, Y.; Gao, X.; Di, C.; Yang, X.; Zhang, F.; Liu, Y.; Li, H.; Zhu, D. Core-Expanded Naphthalene Diimides Fused with Sulfur Heterocycles and End-Capped with Electron-Withdrawing Groups for Air-Stable Solution-Processed n-Channel Organic Thin Film Transistors. *Chem. Mater.* **2011**, *23* (5), 1204–1215. DOI: 10.1021/cm102850j.

47. Chang, J.; Ye, Q.; Huang, K.-W.; Zhang, J.; Chen, Z.-K.; Wu, J.; Chi, C. Stepwise Cyanation of Naphthalene Diimide for N-Channel Field-Effect Transistors. *Org. Lett.* **2012**, *14* (12), 2964–2967. DOI: 10.1021/ol300914k.

48. Guo, X.; Kim, F. S.; Seger, M. J.; Jenekhe, S. A.; Watson, M. D. Naphthalene Diimide-Based Polymer Semiconductors: Synthesis, Structure–Property Correlations, and n-Channel and Ambipolar Field-Effect Transistors. *Chem. Mater.* **2012**, *24* (8), 1434–1442. DOI: 10.1021/cm2034273.

49. Lee, J.; Kalin, A. J.; Yuan, T.; Al-Hashimi, M.; Fang, L. Fully Conjugated Ladder Polymers. *Chem. Sci.* **2017**, *8* (4), 2503–2521. DOI: 10.1039/c7sc00154a.

50. Deusen, R. L. V.; Goins, O. K.; Sicree, A. J. Thermally Stable Polymers from 1,4,5,8-Naphthalenetetracarboxylic Acid and Aromatic Tetraamines. *J. Polym. Sci., Part A-1: Polym. Chem.* **1968**, *6* (7), 1777–1793. DOI: 10.1002/pol.1968.150060701.

51. Arnold, F. E.; Van Deusen, R. L. Preparation and Properties of High Molecular Weight, Soluble Oxobenz[de]Imidazobenzimidazoisoquinoline Ladder Polymer. *Macromolecules* **1969**, *2* (5), 497–502. DOI: 10.1021/ma60011a009.

52. Areephong, J.; Orentas, E.; Sakai, N.; Matile, S. Directional Stack Exchange along Oriented Oligothiophene Stacks. *Chem. Commun.* **2012**, *48* (86), 10618–10620. DOI: 10.1039/C2CC35773A.

53. Frisch, M. J. Frisch, M. J., et al., Gaussian 16, Revision C.01, Gaussian, Inc., Wallingford CT. **2016**.

54. Wolfe, J. F.; Loo, B. H.; Arnold, F. E. Rigid-Rod Polymers. 2. Synthesis and Thermal Properties of Para-Aromatic Polymers with 2,6-Benzobisthiazole Units in the Main Chain. *Macromolecules* **1981**, *14* (4), 915–920. DOI: 10.1021/ma50005a005.

55. Roberts, M. F.; Jenekhe, S. A. Lewis-Acid Coordination-Complexes of Polymers .3. Poly(Benzimidazobenzophenanthroline) Ladder and Semiladder Polymers. *Polymer* **1994**, *35* (20), 4313–4325. DOI: 10.1016/0032-3861(94)90088-4.

56. Liu, G.; Fang, Q.; Xu, W.; Chen, H.; Wang, C. Vibration Assignment of Carbon–Sulfur Bond in 2-Thione-1,3-Dithiole-4,5-Dithiolate Derivatives. *Spectrochim. Acta A Mol. Biomol. Spectrosc.* **2004**, *60* (3), 541–550. DOI: 10.1016/S1386-1425(03)00260-9.

57. Chen, Y.; Wu, H.-Y.; Yang, C.-Y.; Kolhe, N. B.; Jenekhe, S. A.; Liu, X.; Braun, S.; Fabiano, S.; Fahlman, M. In Situ Spectroscopic and Electrical Investigations of Ladder-Type Conjugated Polymers Doped with Alkali Metals. *Macromolecules* **2022**, *55* (16), 7294–7302. DOI: 10.1021/acs.macromol.2c01190.

58. Jansen, R. J. J.; van Bekkum, H. XPS of Nitrogen-Containing Functional Groups on Activated Carbon. *Carbon* **1995**, *33* (8), 1021–1027. DOI: 10.1016/0008-6223(95)00030-H.

59. A. W. Munz. Structural Precursors and Electronic Structure of the Ladder Type Polymer Poly(bis(benzimidazo)benzophenanthroline) (BBB): A Combined UPS/XPS and STM Study. *Chem. Mater*. **1994**, *6* (12), 2288-2302. DOI: 10.1021/cm00048a015.

60. Galeotti, G.; De Marchi, F.; Hamzehpoor, E.; MacLean, O.; Rajeswara Rao, M.; Chen, Y.; Besteiro, L. V.; Dettmann, D.; Ferrari, L.; Frezza, F.; Sheverdyaeva, P. M.; Liu, R.; Kundu, A. K.; Moras, P.; Ebrahimi, M.; Gallagher, M. C.; Rosei, F.; Perepichka, D. F.; Contini, G. Synthesis of Mesoscale Ordered Two-Dimensional π-Conjugated Polymers with Semiconducting Properties. *Nat. Mater.* **2020**, *19* (8), 874–880. DOI: 10.1038/s41563-020-0682-z.

61. Terao, J.; Wadahama, A.; Matono, A.; Tada, T.; Watanabe, S.; Seki, S.; Fujihara, T.; Tsuji, Y. Design Principle for Increasing Charge Mobility of π-Conjugated Polymers Using Regularly Localized Molecular Orbitals. *Nat Commun* **2013**, *4* (1), 1691. DOI: 10.1038/ncomms2707.

62. Farmer, B. L.; Dudis, D. S.; Adams, W. W. Calculation of the Effects of Protonation on Rigid-Rod Polymers. *Polymer* **1994**, *35* (17), 3745–3751. DOI: 10.1016/0032-3861(94)90556-8.

63. Zhu, Y.; Champion, R. D.; Jenekhe, S. A. Conjugated Donor−Acceptor Copolymer Semiconductors with Large Intramolecular Charge Transfer: Synthesis, Optical Properties, Electrochemistry, and Field Effect Carrier Mobility of Thienopyrazine-Based Copolymers. *Macromolecules* **2006**, *39* (25), 8712–8719. DOI: 10.1021/ma061861g.

64. Jenekhe, S. A.; Lu, L.; Alam, M. M. New Conjugated Polymers with Donor−Acceptor Architectures: Synthesis and Photophysics of Carbazole−Quinoline and Phenothiazine−Quinoline Copolymers and Oligomers Exhibiting Large Intramolecular Charge Transfer. *Macromolecules* **2001**, *34* (21), 7315–7324. DOI: 10.1021/ma0100448.

Chapter 4. p-Type Semiconducting Ladder Poly(pyrrolobenzothiazine)s: Effects of N-Alkyl Side Chains on the Chain Conformation, Electronic Structure, and Charge Transport Properties

4.1 Introduction

It is well known that the backbone conformation of π-conjugated polymers directly impacts their electronic structure and properties including molecular orbital distribution, reorganizational energy during charge transfer process, intermolecular transfer integrals,[1,2] and the degree of electronic delocalization. In contrast to *semi-flexible* polymers that show conformational torsions and rotations along the single bonds that link the polymer repeat units, π-conjugated *ladder* polymers feature a double-stranded architecture that is thought to limit conformational distortions and promote backbone rigidity.[1,3–5] The most notable member of the π-conjugated ladder polymers, poly(benzimidazobenzophenanthroline) (BBL) (Chart 4.1), first synthesized in 1966 for aerospace applications due to its extremely high thermal and chemical stability,[6] has been successfully used in a variety of organic electronic and optoelectronic applications over the past 3 decades.[3,7–21] BBL and its derivatives are the only known examples of π-conjugated ladder polymers that have rigid-rod backbones in solution and solid state;[22–25] the scarcity is primarily because of the difficulty in the synthesis of π-conjugated ladder polymers in general.[4,5,25–31] For example, in polymers such as BBL and ladder-type polyaniline derivatives,[32] installing basic sites such as imine nitrogens in the backbone is a key design feature that enables either processing in protic acids or offer unique properties such as acid-doped conductivity. Beyond BBL, there is one other conjugated ladder polymer, called ladder poly(p-phenylene) (LPPP), that has been subjected to rigorous studies of its backbone conformation and persistence length.[34] Interestingly, it was found that LPPP has a *wormlike*

conformation despite its ladder architecture, which means that LPPP showed bending fluctuations in solution.[34] There is a need to further explore the structure-property relationships of π-conjugated ladder polymers since it is evident that they do not exclusively have rigid-rod conformations as widely assumed.

Chart 4.1. Molecular structures of π-conjugated ladder polymers BBL, LPBT and LPBT-Me, and ladder molecule PBBTZ.

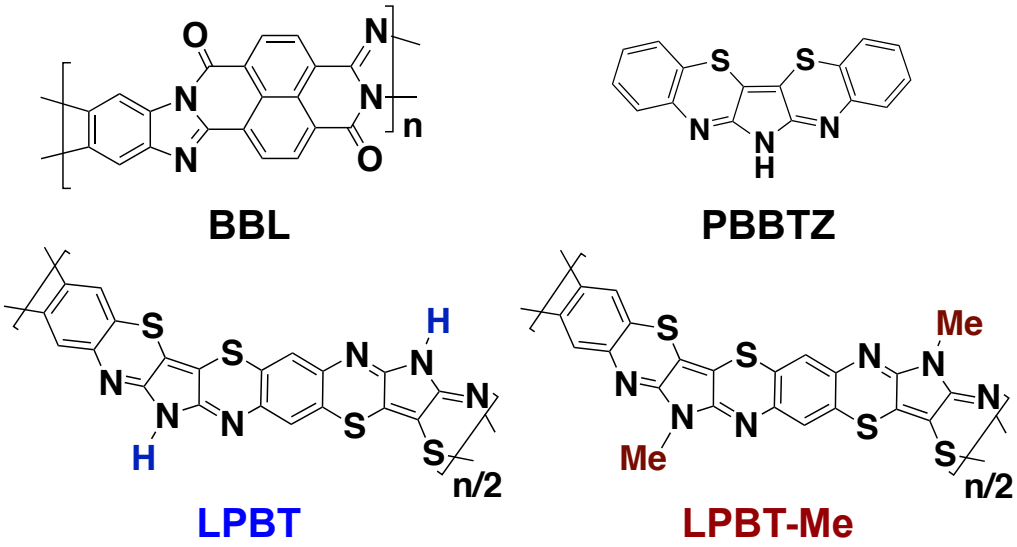

An intriguing ladder small-molecule *p-type* semiconductor, PBBTZ[35] (Chart 4.1), which features an electron rich, co-planar pyrrolobenzothiazine building block, was reported to exhibit high hole mobility (μ_h) values of 0.34 cm^2/Vs in polycrystalline thin film organic field-effect transistors[35] and 3.6 cm^2/Vs in single-crystal field-effect transistors.[36] These results suggested that incorporation of pyrrolobenzothiazine moieties into π-conjugated polymers could enable good charge transport properties. In 2012, a pyrrolobenzothiazine-based π-conjugated ladder polymer featuring 2-octyldodecyl solubilizing groups (PPBBTZ) was reported, although no charge transport properties or molecular geometry studies were reported.[37] Recently, the parent ladder poly(6*H*-pyrrolo[3,2-b:4,5-b']benzothiazine) (LPBT), without solubilizing alkyl chains, was reported; we note that this polymer was named 6*H*-pyrrolo[3,2-*b*:4,5-

b']bis[1,4]benzothiazine ladder (PBBTL), which we believe is incorrectly derived from the model compound PBBTZ.[29] It was shown that LPBT has a HOMO level of -5.0 eV and could be p-type doped with $FeCl_3$ to a moderate electrical conductivity of 1.54 S/cm and moderate thermoelectric properties.[30] Moreover, blends of p-type LPBT and n-type BBL have been used to fabricate p-channel and n-channel organic electrochemical transistors (OECTs), which gave μC^* values of 2.72 and 1.36 F/cmVs,[31] respectively, demonstrating the potential of LPBT in organic electronic devices. However, the intrinsic charge transport properties of LPBT are yet to be investigated, as are the possible effects of N-alkyl substitution to create derivatives of this π-conjugated ladder polymer backbone.

Here, we report the synthesis of new ladder poly(6-methyl-pyrrolo[3,2-b:4,5-b']benzothiazine) (LPBT-Me) along with the parent LPBT (Chart 4.1). We also report detailed investigations of their molecular geometry, electronic structure, thin film microstructure, optical and field-effect charge transport properties. Our choice of the pyrrolobenzothiazine ladder structure as a model system to study the impacts of alkyl side chains on the chain conformation, electronic structure, and charge transport properties is based on the promise of the pyrrolobenzothiazine backbone[32] and ladder polymer[29] as a class of p-type semiconducting materials. Furthermore, the N-H provides a molecular handle for ready attachment of diverse side chains, including solubilizing groups that may enable solution processing in organic solvents.[34] In the present study, a methyl group was chosen because it is the simplest example of an alkylated ladder polymer that still allows good solubility in protic acids. We probed the chain conformation and molecular geometry of LPBT and LPBT-Me in protic acid solutions by doing variable temperature optical absorption spectroscopy and via density functional theory (DFT) and time-dependent DFT calculations on ladder polymer chains of varying degree of protonation.

We show that the π-conjugated backbone of ladder poly(pyrrolobenzothiazine) has a donor-acceptor motif that is very sensitive to protonation in acidic solvents but gives rise to a small bandgap (1.5 eV) that is unaffected by N-methylation. The thin film microstructure of the LPBTs was characterized by grazing-incidence wide-angle X-ray scattering (GIWAXS). We investigated the charge transport properties of the LPBTs by using the organic field-effect transistor (OFET) platform.

4.2 Experimental Methods

Materials and Methods. The 2,5-diamino-1,4-benzenedithiol HCl monomer purchased from Ambeed with 97% purity was recrystallized in 20% HCl solution according to the published procedure before use.[33] 2,3-dibromo-N-methylmaleimide (99%) and 2,3-dibromomaleimide (99%) were purchased from Ambeed and used as received. Polyphosphoric acid (PPA, 84% P_2O_5), phenylphosphonic acid (PhPA), methanesulfonic acid (MSA) (> 99%), formic acid, and triflic acid were purchased from Sigma-Aldrich and used as received. Methanol was purchased from Fisher Scientific and used as received. All reactions were performed under inert atmosphere.

The intrinsic viscosities [η] of the polymers in MSA solutions were measured by an Ubbelohde viscometer which was held at 30˚C using a water bath. The concentrations of the polymer solutions were chosen such that the elution time of the polymer solution was 1.1 – 1.8 times that of the pure solvent.

The ^{1}H NMR spectrum was recorded on a Bruker AV500 (at 500 MHz) using deuterated nitromethane/$GaCl_3$ as the solvent. Thermogravimetric analysis (TGA) was conducted on a TA Instrument model Q50 TGA. A heating rate of 10 °C /min under a flow of N_2 was used with runs conducted from room temperature to 880 °C. Differential scanning calorimetry (DSC) analysis

was performed on a TA Discovery DSC 500 under N_2 by scanning from -10 °C to 350 °C at a heating rate and cooling rate of 10 °C /min. Optical absorption spectra were measured on a PerkinElmer model Lambda 900 UV-vis/near-IR spectrophotometer. Solution absorption spectrum was obtained from dilute (10^{-5} – 10^{-6} M) solutions in methanesulfonic acid, formic acid, and triflic acid.

Cyclic voltammetry (CV) experiments were performed using an EG&G Princeton Applied Research potentiostat/galvanostat (model 273A). A three-electrode cell was used, using a platinum wire as the counter electrodes and the polymers coated onto platinum wires from MSA solution as the working electrodes. The reference electrode was $Ag/AgNO_3$ in acetonitrile. The acidic solvents were removed by dipping the substrates in isopropanol (IPA) overnight and subsequently dried in vacuum oven at 60˚C. The supporting electrolyte solution consisted of 0.1 M tetrabutylammonium hexafluorophosphate (Bu_4NPF_6) in anhydrous acetonitrile. The electrolyte was purged with nitrogen for 15 minutes prior to the scans to ensure inert and anhydrous conditions. The reduction and oxidation potentials were referenced to the Fc/Fc^+ couple by using ferrocene as an internal standard. LUMO energy levels were estimated using the ferrocene value of -4.8 eV with respect to vacuum level.[38,39] The LUMO and HOMO levels were determined by using the equations $E_{LUMO} = -(eE_{red}^{onset} + 4.8)$ and $E_{HOMO} = -(eE_{ox}^{onset} + 4.8)$.

Fourier transform infrared spectroscopy (FTIR) experiments were performed on a Perkin Elmer Frontier spectrometer using free-standing films. The resolution was set at 1 cm^{-1} and a set of 16 scans was averaged. Raman spectroscopy of the free-standing films was carried out on a Thermo Scientific DXR2 Raman microscope. A 532 nm laser with a power of 5mW was focused on a sample through a 50x objective lens.

Grazing incidence wide-angle X-ray scattering (GIWAXS) measurements were conducted at the Advanced Light Source (ALS) at Lawrence Berkley National Laboratory by using the beamlines 7.3.3 and a Pilatus 2M area detector. The images were taken with a beam energy of 10 keV and an incidence angle 0.14˚ with 5 s exposure time. Data were processed using Nika and WAXStools[40] in Igor Pro. Peak positions were determined by Lorentzian peak fittings. The crystal coherence length (L_c) of samples was determined by using the Scherrer equation[41]: $L_c = 2\pi K/\Delta q$, where K is a shape factor (typically 0.9) and Δq is the full width at half-maximum (FWHM) of the diffraction peak. Here, the L_c (100) and L_c (010) were obtained respectively from the FWHM of the (100) diffraction peak in the in-plane (q_{xy}) line-cut and the FWHM of the (010) diffraction peak in the out-of-plane (q_z) line-cut.

Gas-phase molecule density functional theory (DFT) and time-dependent density functional theory (TD-DFT) calculations were performed using the Gaussian 16 suit of programs[42] at the ωB97XD/631-G(d,p) level of theory on the representative oligomers comprising three repeat units. Vertical electronic transitions were calculated for 12 excited states.

Synthesis of LPBT-Me. PPA (42.90 g) was added to a reaction vessel equipped with a mechanical stirrer and heated to 150˚C and purged with nitrogen overnight. The PPA was cooled to 40˚C, and 2,5-diamino-1,4-benzenedithiol HCl (2.73g, 11.2 mmol) was added. The temperature was increased to 70˚C and stirred for 24 hours under nitrogen followed by 3 hours under vacuum to complete the dehydrochlorination. The temperature was then reduced to 65˚C and 2,3-dibromo-N-methylmalemide (3.0 g, 11.2 mmol) was added and stirred overnight. The temperature was increased to 120˚C and stirred for 24 hours. The temperature was then slowly increased to 180˚C and stirred for 72 hours. The reaction mixture was cooled to room temperature, and methanol was added to quench the reaction. The polymer was filtered, washed

with methanol, and dried. The crude polymer was further purified by reprecipitation from MSA into methanol and thoroughly dried at 100˚C under vacuum (2.12 g, 80%). Intrinsic viscosity: 1.7 dL/g (30.0˚C, MSA). Anal. calcd for $C_{11}H_5N_3S_2$ (%): C, 54.30; H, 2.07; N, 17.27; S, 26.36; found (%): C, 50.71; H, 2.15; N, 15.49.

Synthesis of LPBT. The polymerization was carried out according to the same procedure as LPBT-Me, except a binary solvent mixture of PPA:PhPA was used in a 1:1 ratio (28.056 g/28.056 g). 2,5-diamino-1,4-benzenedithiol HCl (2.50 g, 10.20 mmol), 2,3-dibromo-1H-maleimide (2.60 g, 10.20 mmol); (yield, 1.38 g, 60%). Intrinsic viscosity: 2.4 dL/g (30.0˚C, MSA). Anal. calcd for $C_{10}H_3N_3S_2$ (%): C, 52.38; H, 1.32; N, 18.33; S, 27.97; found (%): C, 50.24; H, 1.82; N, 15.69.

4.3 Results and Discussion

4.3.1. Synthesis and Characterization. The synthetic routes to both LPBT and LPBT-Me are shown in Scheme 4.1, and the detailed polymerization procedures are described in Experimental Methods. The parent polymer LPBT was synthesized in a binary acid mixture using polyphosphoric acid (PPA, 84% P_2O_5) and phenylphosphonic acid (PhPA) in a 1:1 wt. ratio according to the published procedure.[30] The addition of PhPA as a co-solvent was to enhance the solubility of the 2,3-dibrmomo-1H-malemide monomer in the PPA reaction medium and thus to prevent sublimation of the monomer at temperatures > 80˚C.[30] Nevertheless, we still observed sublimation of the 2,3-dibromo-1H-malemimide monomer at high temperatures > 80˚C, which means that the stoichiometry of the condensation polymerization is suboptimal. The sublimation of the monomer limited the intrinsic viscosity ([η]) of the LPBT sample to 2.4 dL/g in methanesulfonic acid (MSA) at 30˚C, which is similar to the previously reported polymer ([η] value of 3.7 dL/g in MSA at 25˚C).[30]

Scheme 4.1. Synthesis of LPBT and LPBT-Me (PPA = polyphosphoric acid, 84% free P_2O_5; PhPA = phenylphosphonic acid).

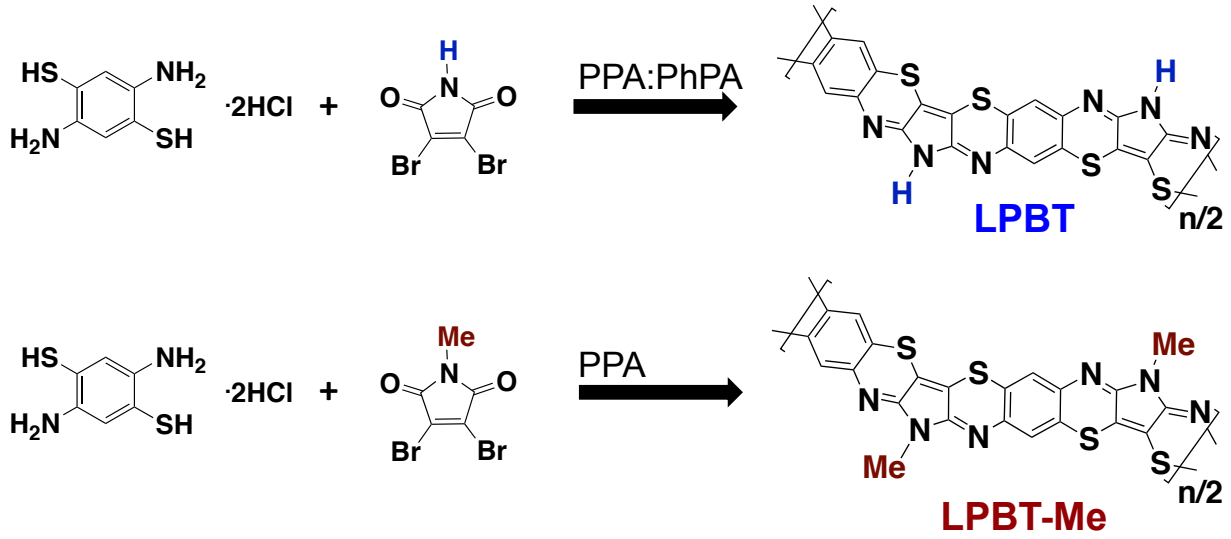

The alkylated polymer LPBT-Me was synthesized in pure PPA since the co-solvent PhPA did not seem to improve the solubility of the maleimide monomer in LPBT synthesis. When the temperature of the polymerization mixture was increased beyond 150˚C, evaporation of 2,3-dibromo-N-methylmaleimide (T_m = 120˚C) was observed. This indicates that the solubility of the methylated monomer in PPA is still too low to afford high molecular weight polymers. Thus, the resulting LPBT-Me sample had a modest intrinsic viscosity [η] value of 1.7 dL/g in MSA at 30˚C. The moderate intrinsic viscosity values of both LPBT and LPBT-Me clearly highlight the limitations of the reaction scheme whereby the poor solubility of 2,3-dibromomaleimide monomers in acid media limits the molecular weight of achieved ladder polymers.

Both polymers were isolated as brown solids and are soluble in strong acids such as MSA and triflic acid. The polymers form good quality thin films when spin-coated from MSA solutions, giving blue-green thin films with shiny lusters. LPBT and LPBT-Me can also be made into high quality free-standing films, which were used to confirm the molecular structures of the

polymers using Fourier-transform infrared spectroscopy (FTIR) and Raman spectroscopy. The detailed procedure for forming the free-standing films is located in the Appendix D. The free-standing films were then used to characterize the molecular structures and thin film microstructures. The FTIR and Raman spectra (Figure 4.1a-d) were analyzed alongside Density Functional Theory (DFT) simulated FTIR and Raman spectra calculated at the ωB97XD/6-31G(d,p) level of theory on oligomers comprising three repeat units each (Figure D.1a-d). The peak positions and assigned vibrational modes are summarized in Tables D.1-D.2 for LPBT and LPBT-Me, respectively.

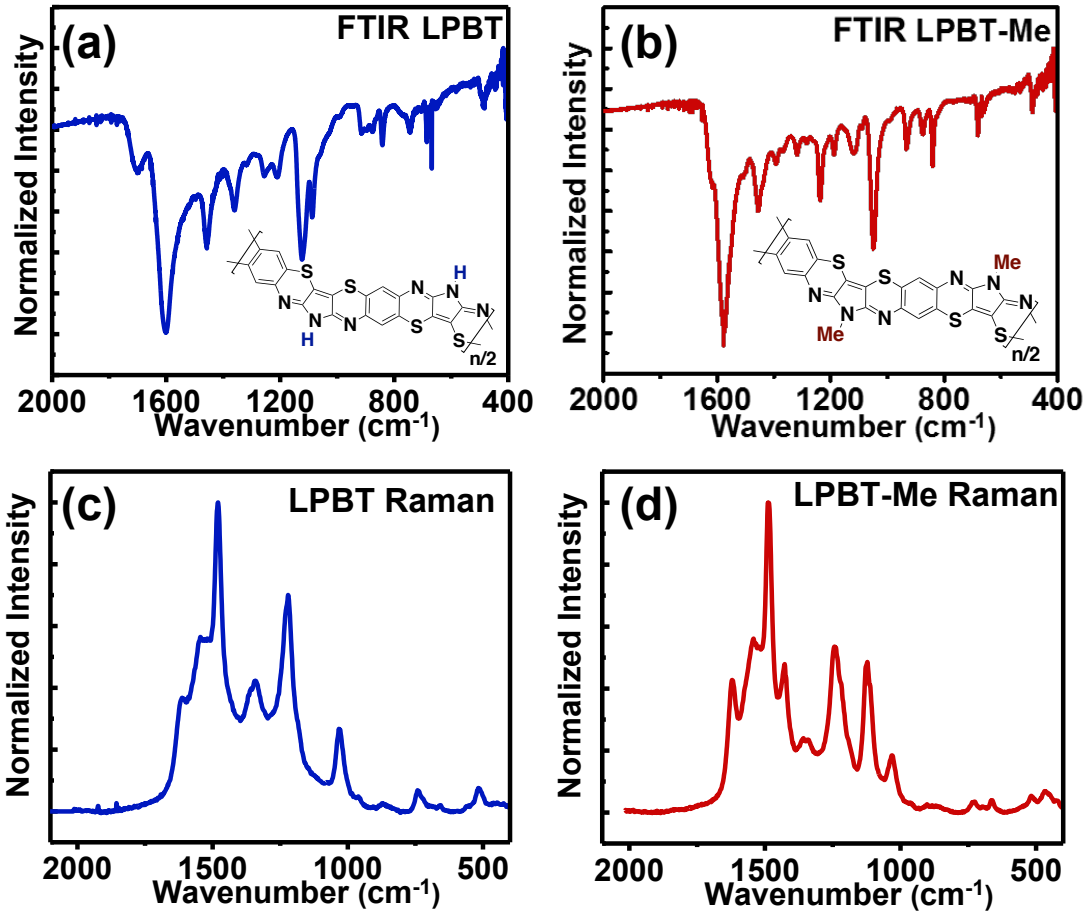

Figure 4.1. Normalized (a) FTIR and (c) Raman spectra for the free-standing films of LPBT, and normalized (b) FTIR and (d) Raman spectra for the free-standing films of LPBT-Me.

The FTIR spectrum of the parent polymer LPBT (Figure 4.1a) has prominent aromatic ν(C=C) stretches at 1698 cm^{-1} and high intensity imine carbon-nitrogen stretches, ν(C=N) and ν(C-N), at 1600 cm^{-1} and 1225 cm^{-1}, respectively. At lower wavenumbers, mixed pyrrole stretches can be seen at 1459 cm^{-1}, 1360 cm^{-1}, and 1124 cm^{-1}. Furthermore, the medium intensity carbon-sulfur ν(C-S) stretch is found at 1085 cm^{-1}.[43] Raman absorption bands for LPBT (Figure 4.1c) show sharp aromatic ν(C=C) stretches at 1611 cm^{-1} and 1482 cm^{-1}, and high intensity imine ν(C=N) stretches at 1545 cm^{-1}. Mixed pyrrole stretches are seen as a high intensity band at 1349 cm^{-1}. The peak at 1235 cm^{-1} can be assigned to mixed skeletal vibrations, and carbon-sulfur ν(C-S) stretches are found at lower wavenumbers at 1032 cm^{-1} and 743 cm^{-1}.[43] We note that the FTIR stretches seen for LPBT are in good agreement with the previously reported infrared spectrum.[30]

LPBT-Me shows similar FTIR stretches compared to the parent polymer (Figure 4.1b). The bands representing the aromatic ν(C=C) stretches are seen at 1613 cm^{-1}. The sharp band at 1577 cm^{-1} originates from imine carbon-nitrogen ν(C=N) stretches and the medium intensity peak at 1239 cm^{-1} is from mixed pyrrole and ν(C-N) vibrations. The ν(C-S) stretching frequency is found at 1046 cm^{-1}.[43] Raman absorption bands for LPBT-Me (Figure 4.1d) show high intensity ν(C=C) stretches at 1619 cm^{-1} and 1488 cm^{-1} and a sharp imine stretching ν(C=N) band at 1542 cm^{-1}. Mixed pyrrole and aromatic vibrations are assigned to the peaks 1428 cm^{-1}, 1362 cm^{-1}, and 1253 cm^{-1}. Finally, the ν(C-S) stretches are seen at 1026 cm^{-1} and 737 cm^{-1}.[43] The observed FTIR and Raman spectra of both LPBT and LPBT-Me are in good agreement with the DFT-calculated spectra (Figure D.1a-d) and provide strong evidence for the molecular structures of both ladder polymers.

We note that the DFT-calculated Raman spectra show higher intensity stretches for LPBT-Me relative to LPBT (Figures D.1c-d); this indicates greater polarizability (α) of the methylated polymer (α = 1946.4 a.u) compared to the parent polymer (α = 1799.6 a.u). The DFT-calculated dipole moment values were found to be 5.64 D and 4.84 D for LPBT-Me and LPBT, respectively. In donor-acceptor π-conjugated systems, the intramolecular charge transfer (ICT) character is partially determined by a combination of polarizability and dipole moment, where larger dipole moments and polarizability typically indicate stronger ICT interactions.[44–46] Therefore, the increased polarizability and dipole moment values for LPBT-Me suggest that methylation enhances ICT character in pyrrolobenzothiazine ladder polymers.

To further characterize the molecular structures of the polymers, we have collected ^{1}H NMR spectra for both LPBT-$GaCl_3$ and LPBT-Me-$GaCl_3$ complexes in deuterated nitromethane[47] and the spectra are shown in Figure D.2. Solutions of both polymers were prepared in deuterated nitromethane containing $GaCl_3$ according to the known procedures.[46] However, we point out the use of the Lewis-acid solutions as NMR solvents is known to produce impurities in the NMR spectra;[25,47] these impurities appear at ~ 5.9 ppm, and ~ 6.3 ppm - 6.5 ppm for both polymers (Figure D.2). The NMR spectra show two main peaks from the benzene protons at 7.2 ppm and 8.1 ppm for LPBT, and a cluster of peaks ~ 7.7 – 8.6 ppm for LPBT-Me. The cluster of peaks for LPBT-Me could be due to the planar/non-planar conformational variations of the LPBT-Me backbone. The methyl peak is seen at 4.1 ppm, which overlaps with the deuterated nitromethane solvent peak at 4.5 ppm.

The thermal stabilities of LPBT and LPBT-Me were probed using thermal gravimetric analysis (TGA) and differential scanning calorimetry (DSC) and the thermograms are shown in Figure D.3a-b in Appendix D. Both polymers show excellent thermal stability measured by TGA

(Figure D.3a) with high thermal decomposition temperatures > 450˚C and retain > 65% of their mass at 800˚C. DSC scans revealed no phase transitions in the range of 25˚C to 350˚C (Figure D.3b), which is typical for ladder polymers to have very high glass transition temperatures over 350˚C.[47]

4.3.2. Electronic Structure of Ladder Poly(pyrrolobenzothiazine)s. We investigated the electronic structures of LPBT and LPBT-Me by density functional theory (DFT) calculations, time-dependent DFT (TD-DFT) calculations, and cyclic voltammetry. The results of the DFT and TD-DFT calculations performed at the ωB97XD/6-31G(d,p) level of theory and are aimed to gain insight into the backbone geometries and frontier molecular orbital distributions and are shown in Figures 4.2a-b. The excited state geometry and vertical electronic excitations for 12 excited states are shown in Figure D.4. The optimized ground state geometry of LPBT-Me (Figure 4.2a) and LPBT (Figure 4.2b) in the gas phase are completely co-planar with both HOMO and LUMO molecular orbitals delocalized across three repeat units. In the excited state, both LPBT and LPBT-Me show planar backbones with electronic transitions between 380 – 1330 nm. The optical bandgaps obtained from the DFT results show the $E_{g.}^{opt} \sim 1.0$ eV for LPBT and 0.9 eV for LPBT-Me. In the visible range, the oscillator strengths for the electronic transitions are more than twice as large for LPBT compared to LPBT-Me (Figure D.4). Oscillator strengths often rise with increasing molecular planarity and rigidity in π-conjugated molecular systems;[48,49] this suggests that LPBT maintains a rigid backbone upon photoexcitation, which is likely due to intramolecular hydrogen bonding.[50] The distance between the pyrrole proton and the imine nitrogen in LPBT was calculated to be 2.70 Å in the ground state and 2.67 Å in the exited state, which are less than the sum of their van der Waals radii (N, 1.55 Å; H, 1.20 Å).[51] In fact, the shorter hydrogen bonding distance in the excited state implies stronger

hydrogen bonds relative to the ground state. Effects of intramolecular hydrogen bonding are also seen in the reorganization energy (λ) calculated for each oligomer upon hole injection. The reorganizational energy is the energy associated with geometry changes when going from a neutral to a charged-state geometry.[52,53] The λ values of 0.77 eV and 1.30 eV calculated for LPBT and LPBT-Me, respectively, show a two-fold decrease for LPBT. This means that intramolecular hydrogen bonding may be crucial in maintaining rigidity upon charge injection for the ladder poly(pyrrolobenzothiazine)s.[48]

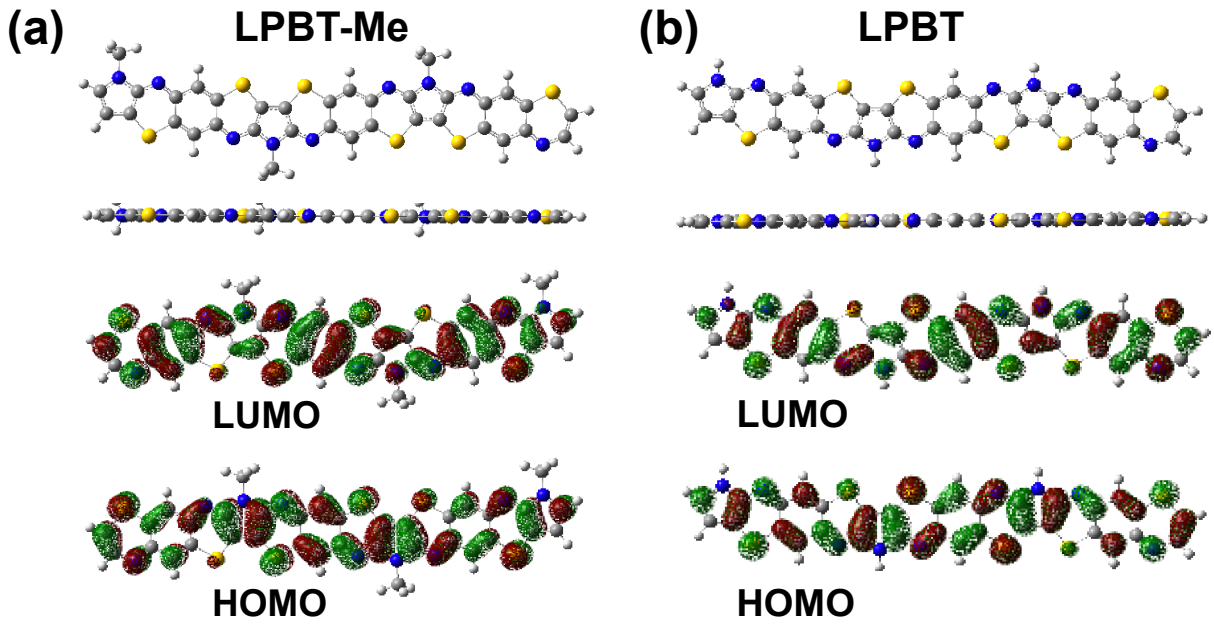

Figure 4.2. DFT calculations using ωB97XD/6-31G(d,p) level of theory for the optimized ground state geometry and molecular orbital distributions for single oligomers comprising 3 repeat units each for (a) LPBT-Me and (b) LPBT. The molecular geometry top and side views are of the same single oligomer.

We used cyclic voltammetry (CV) to measure the oxidation and reduction potentials of the polymers, from which we derived the HOMO and LUMO energies, and the results are summarized in Table 4.1. The oxidation and reduction waves of LPBT and LPBT-Me thin films

coated on platinum wires were measured in 0.1 M tetrabutylammonium hexafluorophosphate (Bu_4NPF_6) in degassed acetonitrile with $Ag/AgNO_3$ as the reference electrode and are shown in Figure 4.3, and additional scans are shown in Figure D.5. LPBT shows two quasi-reversible oxidation waves at 0.97 V and 1.40 V, and one non-reversible reduction wave centered at -1.36 V (Figure 4.3a). The onset oxidation potential of 0.66 V and onset reduction potential of -0.99 V were used to estimate the HOMO and LUMO energy levels of -4.96 eV and -3.27 eV, respectively, for LPBT. The electrochemical bandgap ($E_{g,}^{elec.}$) of LPBT is thus 1.69 eV. The onset oxidation potential of 0.66 V is comparable to the previously reported value of 0.67 V.[30]

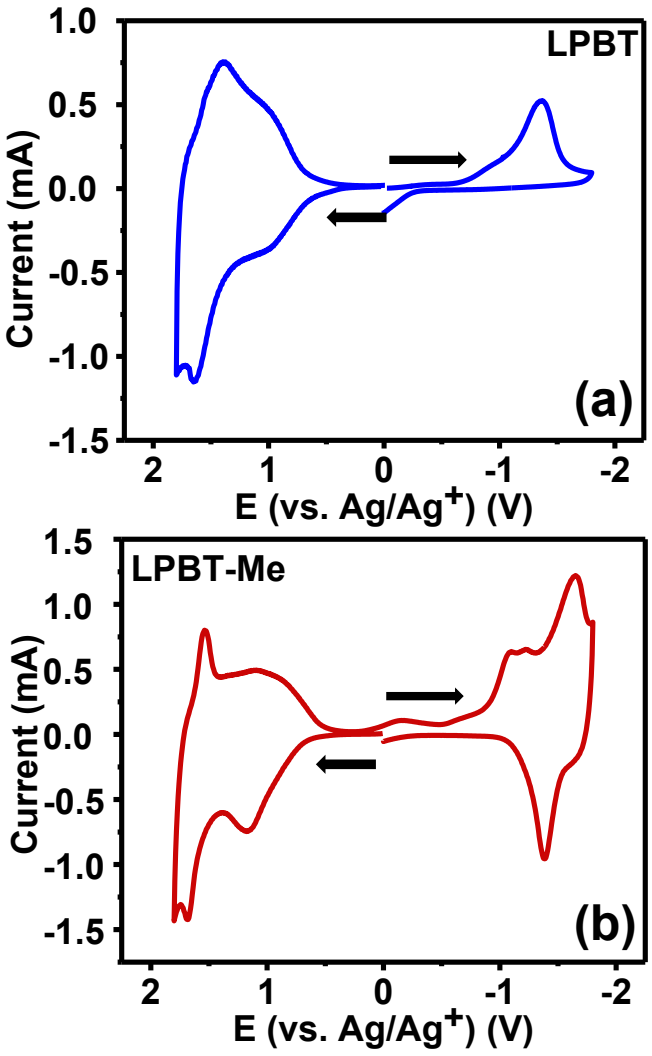

Figure 4.3. Cyclic voltammograms for the oxidation and reduction processes of (a) LPBT and (b) LPBT-Me thin films measured in 0.1 M Bu_4NPF_6 electrolyte solution using $Ag/AgNO_3$ as the reference electrode. The scan rate was 100 mV/s. The arrows indicate the direction of charging.

The methylated polymer, LPBT-Me, also shows two quasi-reversible oxidations waves at 1.06 V and 1.53 V (Figure 4.3b); however, unlike the parent polymer that showed a non-reversible reduction scan, LPBT-Me has a quasi-reversible reduction wave at -1.38 V. The quasi-reversibility of the LPBT-Me reduction wave suggests that the electron transfer process (n-doping) and the resulting radical anion are stabilized due to the methylation of the pyrrole nitrogen. The HOMO and LUMO levels were calculated from the onset oxidation potential and onset reduction potential at 0.59 V and -1.09 V, respectively, and are found to be -5.05 eV for the HOMO and -3.46 eV for the LUMO. Hence, the $E_{g,}^{elec.}$ for LPBT-Me is 1.56 eV; this is 0.13 eV smaller than for LPBT. Additionally, alkylation decreases the HOMO energy level by 0.09 eV, and the LUMO level by 0.19 eV. This reduction in the LUMO level and stabilization of the electron injection and transfer process is explained by changes in electron density in the pyrrolobenzothiazine backbone, which is discussed below.

Table 4.1. Electronic Structure Parameters and Optical Properties of LPBT and LPBT-Me.

Polymer	HOMO (eV)	LUMO (eV)	$E_g^{elec.}$ (eV)	λ_{max} [(a)] (nm)	λ_{max} [(b)] (nm)	λ_{max} [(c)] (nm)	α_{max} [(c)] (cm^{-1})	$E_g^{opt.(c)}$ (eV)
LPBT	-4.96	-3.27	1.69	933	960	676	2.89×10^5	1.49
LPBT-Me	-5.05	-3.46	1.56	936	993	663	2.25×10^5	1.51

[(a)] Solution in MSA. [(b)] Solution in triflic acid. [(c)] Spin-coated thin films from MSA solution.

Electrostatic potential (ESP) maps for each oligomer were calculated using DFT at the ωB97XD/6-31G(d,p) level to visualize the charge distribution with respect to the difference

between positive and negative charges on the oligomer backbones (Figure 4.4).[54–56] A theoretical oligomer bearing a strong electron-donating methoxy group (LPBT-A) was included in the calculation. Increasing the electron-donating ability of the substituent (hydrogen < methyl < methoxy) revealed a trend of increasing electron localization and intramolecular charge transfer (ICT) character in the polymer backbone. In LPBT, slight regions of negative charge (red-orange) are centered on the imine nitrogens and sulfurs of the thiazine moieties, and more positively charged (blue) and neutral (green) regions are found on the pyrrole and benzene moieties (Figure 4.4a). This spatial localization of the electron density on thiazine implies intramolecular charge transfer (ICT) interactions[55,56] between the electronically coupled thiazine and pyrrole/benzene moieties whereby positive charges (holes) are transferred from the benzene and pyrrole moieties to the thiazine moieties. The effect is enhanced in LPBT-Me; methylation of the pyrrole nitrogen increases the electron density around thiazine, which explains the lower LUMO energy level and stabilization of the electron injection and transfer process.[57] The more negative ESP value of the imine nitrogen indicates its increased basicity (Figure 4.4b). The effect is more pronounced in the theoretical oligomer LPBT-A, which has the largest electron cloud on the thiazine nitrogens and has the most ICT character of the series (Figure 4.4c). The alkylation-induced enhancement in electron density of the imine nitrogens also means that LPBT-Me has improved solubility in protic acids, which is consistent with our experimental observations that LPBT-Me has improved solubility in acids.

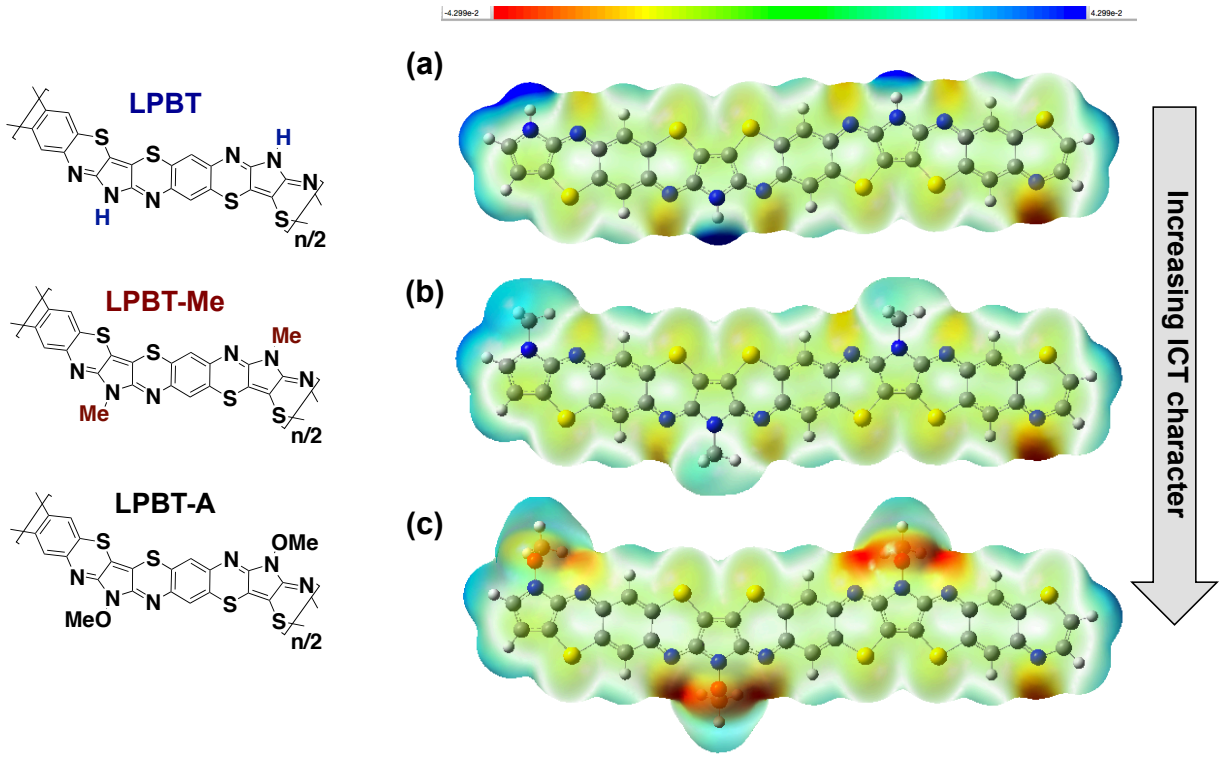

Figure 4.4. Electrostatic potential (ESP) map calculated using DFT ωB97XD/6-31G(d,p) level of theory for (a) LPBT, (b) LPBT-Me, and (c) a theoretical oligomer with a methoxy group, LPBT-A.

4.3.3. Optical Absorption Spectra and Molecular Geometry in Protic Acid Solutions. The optical absorption spectra of the ladder polymers in MSA solutions are shown in Figure 4.5 and the lowest energy peak positions are summarized in Table 4.1. To corroborate our spectroscopic results and gain a deeper understanding of the optical features seen in both polymers, DFT calculations were run at the ωB97XD/6-31G(d,p) level of theory on oligomers bearing +1, +2, and +6 protonation states with the corresponding positive charge on the imine nitrogens (Figures 4.6 and D.6). We note that it is more energetically favorable to protonate the imine nitrogens compared to the sulfur sites,[58] and thus imine protonation was chosen for the calculations.

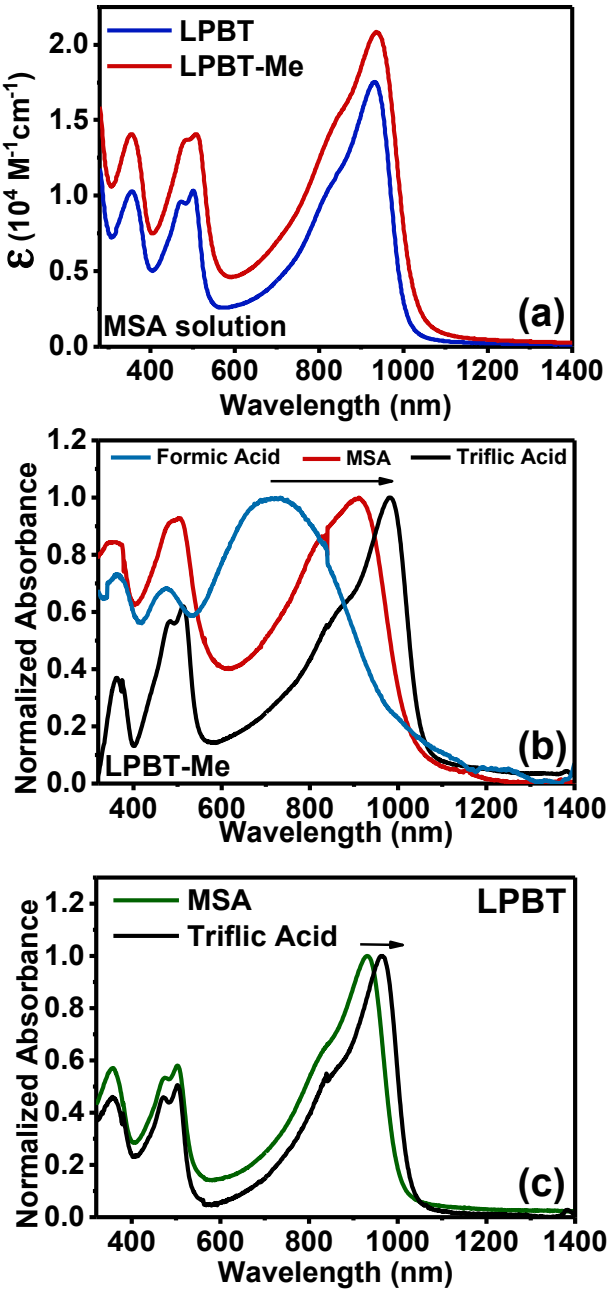

Figure 4.5. Optical absorption spectra of the ladder polymers (a) in MSA solution. Normalized absorption spectra in dilute (10^{-6} M) protic acid solutions of varying pKa values: (b) LPBT-Me and (c) LPBT.

In MSA solution (Figure 4.5a), LPBT has two well-resolved high-energy bands at 354 nm (ε_{max} = 1.05 x 10^4 $M^{-1}cm^{-1}$) and 502 nm (ε_{max} = 1.06 x 10^4 $M^{-1}cm^{-1}$), of which the latter can be assigned to the π-π^* transition. The intense lowest-energy absorption band centered at 933 nm

originates from protonation-enhanced intramolecular charge transfer.[59,60] This phenomenon is seen in many imine nitrogen-containing π-conjugated polymers in protic acid solutions where the ICT band is significantly red-shifted relative to the π-π* band.[25,59–61] The effects of protonation on the ICT band are corroborated with DFT calculations shown in Figure D.6a, which show protonation (+1 and +6 protonation states) induces spatial localization of the HOMO and LUMO molecular orbitals that correspond to the ICT character seen in the optical absorption spectra.[57,62,63]

The optical absorption spectrum of LPBT-Me in MSA solution in Figure 4.5a shows similar features as the parent LPBT. The spectrum shows two high-energy peaks at 352 nm (ε_{max} = 1.51 x 10^4 $M^{-1}cm^{-1}$) and 508 nm (ε_{max} = 1.38 x 10^4 $M^{-1}cm^{-1}$), and a lowest energy peak at 936 nm. Similar to LPBT, the peaks at 508 nm and 936 nm represent the π-π* transition and ICT band, respectively. The ICT band has the same origins as the parent LPBT, which was seen on the DFT calculations of the protonated oligomers (Figure D.6b).

To understand the effects of the protonation on the ICT bands, optical absorption spectra were collected in dilute protic acid solutions of varying pKa values shown in Figure 4.5b-c.[47,58,64] The optical absorption spectra of LPBT-Me show that as the pKa of the acid solvent decreases (formic acid, 3.75 > MSA, -1.9 > triflic acid, -14.7), the ICT band (Figure 4.5b) red shifts from formic acid ($\lambda_{formic\ acid}$ = 721 nm) to triflic acid ($\lambda_{triflic\ acid}$ = 993 nm), with increasing vibronic features and spectral narrowing. LPBT has a similar trend from MSA (λ_{MSA} = 933 nm) to triflic acid ($\lambda_{triflic\ acid}$ = 960 nm) (Figure 4.5c), except that LPBT is insoluble in formic acid. This means that the imine nitrogens are apparently not basic enough to abstract hydrogen from formic acid, which is in agreement with the DFT calculations (see ESP map, Figure 4.4) that showed decreased electron density around the imine nitrogens. We propose that these trends are caused

by (1) protonation-enhanced differences in electron density distributions on the π-conjugated backbones, resulting in variable stiffness of the polymer chain, and (2) intra- and inter-molecular hydrogen-bonding interactions (or lack thereof in the case of LPBT-Me). When partially protonated in formic acid (pKa = 3.75) or MSA (pKa = -1.9), the polymer chains preferentially adopt non-planar backbone conformations. This was observed in DFT calculations on optimized oligomers protonated at the imine nitrogens bearing +1, +2, or +6 charges that resulted in out-of-plane bending deformations between the thiazine and pyrrole moieties that decreased as the protonation state increased (Figure 4.6a-b). Similar phenomena have been seen for other protonated rigid-chain polymers such as poly(p-phenylenebenzobis(oxazole)) (PBO) and poly(p-phenylenebenzobis(thiazole)) (PBTZ) in *ab initio* calculations[58] and molecular dynamics studies.[65] However, LPBT shows a smaller degree of bending deformations (+1 protonation state, 156˚) relative to LPBT-Me (+1 pronation state, 150˚), which implies that LPBT is more rigid than LPBT-Me. Both intra- and inter-molecular H-bonding interactions likely contribute to the improved rigidity of LPBT. In triflic acid (pKa = -14.7), both polymers are almost fully protonated and preferentially adopt more planar backbone conformations, although they still retain strong ICT interactions (Figure D.6). The optical absorption spectra of LPBT-Me compared to those of LPBT exhibits a 3-nm and 20-nm red shift in MSA and triflic acid, respectively (Figure 4.5b-c), which corroborates the enhanced protonation-enhanced ICT character observed in the DFT calculations (Figure D.6). The results are also in agreement with the CV measurements, which showed that LPBT-Me has a lowered LUMO energy level.

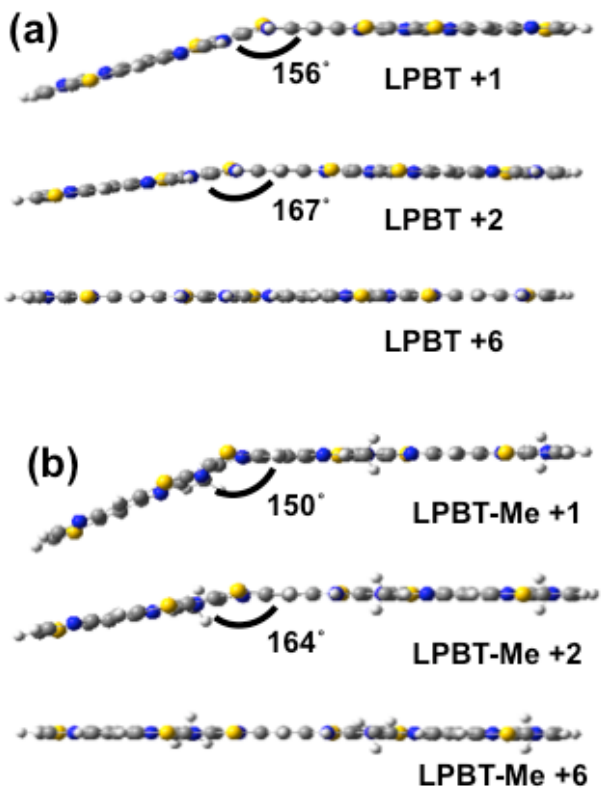

Figure 4.6. DFT-calculated optimized geometries of oligomers bearing +1, +2, and +6 protonation states for (a) LPBT and (b) LPBT-Me, where both oligomers were protonated on the imine nitrogens. Calculations performed at the ωB97XD/6-31G(d,p) level of theory.

Variable temperature absorption spectra in dilute (10^{-5} M) triflic acid and MSA solutions (Figure 4.7a-e) were collected for temperatures between 20˚C – 100˚C to gauge the rigidity of the protonated ladder polymer backbones. As the temperature increases, the ICT band of the LPBT absorption spectrum in MSA solutions blue shifts from 933 nm to 920 nm with accompanying spectral broadening and decreased absorbance (Figure 4.7a,f). In triflic acid, a blue shift is not observed, however, the absorption band weakens with increasing temperature (Figure 4.7b,f). The absorption spectrum of MSA solutions of LPBT-Me show that the ICT band undergoes a large decrease in absorbance with spectral broadening accompanied by a sizeable blue shift from 936 nm to 898 nm upon heating (Figure 4.7c,f). In contrast, triflic acid solutions

of LPBT-Me undergo a small blue shift from 993 nm to 991 nm and a small decrease in molar absorptivity (Figure 4.7d,f). The observed changes in position, intensity, and structure of the ICT bands of both polymers can be understood to arise from thermally accessible conformation distributions.[62] These changes are particularly evident in the MSA solutions; at higher temperatures, the ensembles of the polymer chains on average will be more distorted and non-planar. The non-planar chain geometries will decrease the average degree of conjugation as reflected in the blue-shifted, spectrally broadened, and weakened ICT bands.

BBL shows no thermochromism or conformational disorder (Figure 4.7e,f) due the rigidity of the protonated ladder poly(benzimidazobenzophenanthroline)s backbone,[13] which is in contrast to the ladder polymers studied here that both show thermochromic responses (Figure 4.7). The effects of protonation state on the polymers' molecular geometry are apparent in optical absorption spectra in triflic acid (Figures 4.7b,d,f) that show the geometry of the near fully protonated polymers are not sensitive to temperature changes, such that there are no accompanying blue-shifts for LPBT, and minimal blue-shifts for LPBT-Me (2 nm) which is what is observed in the BBL spectrum in MSA solution (Figure 4.7e,f). Also, it is evident that alkylation causes increased conformational disorder (Figure 4.7a,c). The differences in conformational disorder can be explained in terms of π-electron delocalization and hydrogen bonding interactions. The protonation-enhanced spatial separation of the HOMO and LUMO molecular orbitals (i.e., the ICT interactions) (Figure D.6) help explain the conformational disorder in the polymers[62,66,67] owing to the well-known fact that charge delocalization increases π-bond character across the polymer backbone and strengthens the bonds within π-systems.[68] In triflic acid, in which the polymer chains are more fully protonation, the electron density is more delocalized thereby increasing the rigidity of the π-conjugated backbone. Therefore, increased

electron delocalization in LPBT (Figure 4.4) in combination with the hydrogen bonding interactions increases the stiffness of the polymer backbone.

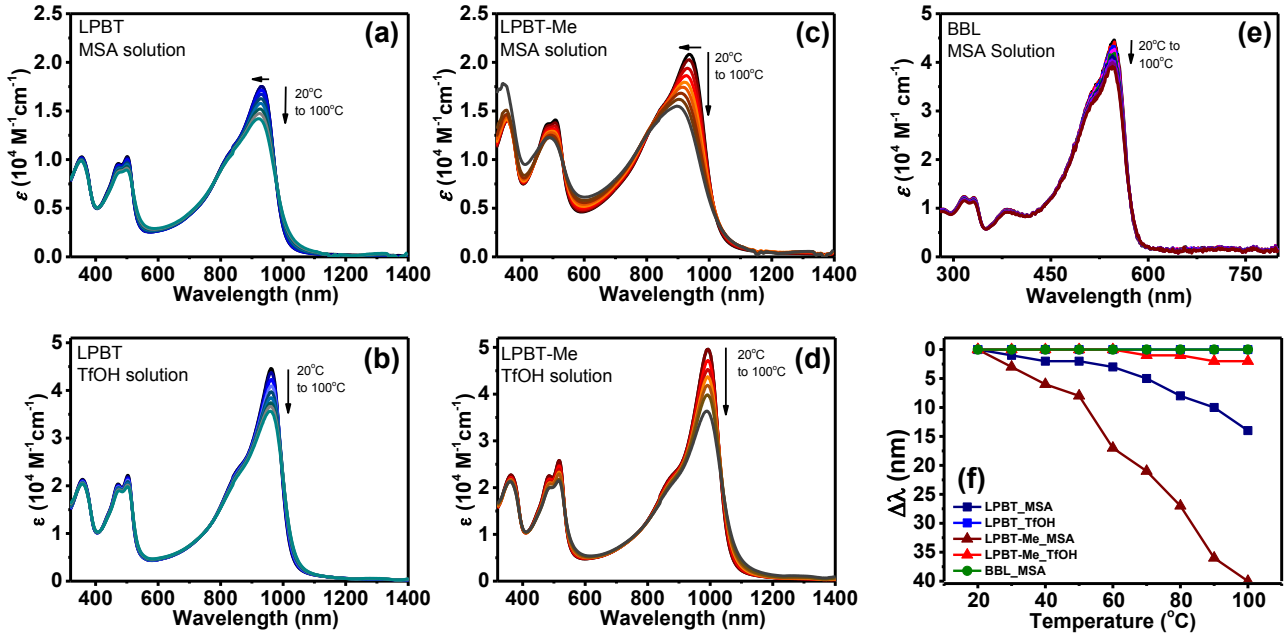

Figure 4.7. Variable temperature optical absorption spectra of LPBT in (a) MSA and (b) triflic acid solutions (10^{-5} M), LPBT-Me in (c) MSA and (d) triflic acid solutions (10^{-5} M), (e) BBL in MSA solution (10^{-5} M), (f) the blue-shifts of the maximum wavelengths with increasing temperature for LPBT, LPBT-Me, and BBL in MSA solutions and LPBT and LPBT-Me in triflic acid solutions.

Although both LPBT and LPBT-Me exhibit thermochromism in solutions whereas BBL does not, they are to a much lesser degree than many other semi-flexible polymers including alkylated polythiophenes,[68,69] polyphenylene derivatives,[69] poly(phenylene vinylene),[70] and others.[1] Thus we can conclude that while the double-stranded ladder architecture explored here has not eliminated structural fluctuations, it has suppressed them compared to single-stranded polymer architecture. It is likely that the complete electron delocalization and lack of ICT character in BBL previously shown by DFT calculations[25] enhances its rigidity in protic acids.

Indeed, the protonation-enhanced flexibility of the ladder backbone does impact the solid-state morphology and charge transport properties, which are discussed below.

4.3.4. Solid-State Optical Properties. The thin film absorption spectra of LPBT and LPBT-Me were collected from thin films spin-coated onto glass substrates from MSA solutions. The detailed procedure is described in the Appendix D. The thin film absorption spectra are shown in Figure 4.8 and the optical parameters (absorption coefficient (a), absorption maximum (λ_{max}), and optical bandgaps ($E_g^{opt.}$)) are summarized in Table 4.1.

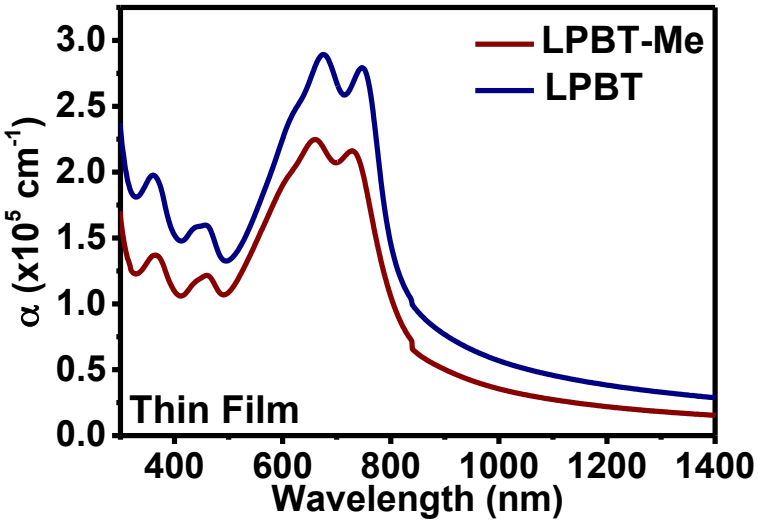

Figure 4.8. Optical absorption spectrum of the ladder polymers spin-coated from MSA solutions onto glass substrates.

The thin film absorption spectrum of LPBT (Figure 4.8) has bands in the 300 - 850 nm range with an absorption coefficient (α) of 2.78 x10^5 cm^{-1} at the lowest energy absorption band maximum (λ_{max}) of 749 nm. At the λ_{max} value of 676 nm, the α_{max} value is 2.89 x10^5 cm^{-1}. The intense absorption band has vibronic peaks at 676 nm and 749 nm. The optical bandgap ($E_g^{opt.}$) of LPBT measured from the onset of thin film absorption is 1.49 eV, which is identical to the previously reported bandgap of 1.51 eV for LPBT.[30] Compared to the absorption spectrum of

LPBT in MSA solution (Figure 4.5a), the solid-state absorption spectrum is distinctly different. First, the MSA solution spectrum with the lowest-energy peak at 933 nm is substantially red shifted from the thin film absorption spectrum (with the lowest-energy peak at 749 nm). This 174-nm red-shift of the absorption spectrum due to protonation confirms the enhancement of the ICT character of the LPBT backbone in MSA solution. Second, the vibronic structure of the main absorption band in the solid state is significantly enhanced compared to what is observed in the MSA solution absorption; this difference can be understood by the much more rigid chains in the solid state.

The thin film absorption spectrum of LPBT-Me (Figure 4.8) is very similar to that of the parent LPBT; it spans the 300 - 840 nm region with the main absorption band centered at 731 nm ($\alpha = 2.16 \times 10^5$ cm^{-1}) (Table 4.1); the lowest energy absorption λ_{max} at 663 nm has an α_{max} value of 2.25×10^5 cm^{-1}. The absorption edge optical bandgap of LPBT-Me is 1.51 eV, which is similar to that of the parent LPBT. The DFT-calculated optical bandgaps of LPBT and LPBT-Me ($E_{g,}^{opt.}$ ~ 0.9 - 1.0 eV) are significantly smaller compared to those obtained experimentally, which is a commonly seen phenomenon in the bandgaps calculated for extended π-systems and are typically attributed to deficiencies of many density-functional methods.[70–72] We note that while the electrochemical bandgap ($E_{g,}^{elec.}$ = 1.56 eV) of LPBT-Me derived from cyclic voltammetry measurements discussed above is 0.13 eV smaller than that of LPBT ($E_{g,}^{elec.}$ = 1.69 eV), the optical bandgaps of LPBT and LPBT-Me are nearly identical. The larger difference between the electrochemical bandgap and optical bandgap in LPBT (0.2 eV) compared to LPBT-Me (0.06 eV) indicates that LPBT has a greater effective exciton binding energy (E_b). A decreased E_b value in the methylated polymer likely arises in part from the previously discussed stronger ICT effect and a larger calculated dipole moment in LPBT-Me (μ = 5.64 D) compared to LPBT (μ =

4.84 D). [73–75] However, the main difference in the thin film absorption spectrum of the N-methyl polymer, LPBT-Me, compared to that of LPBT is that the lowest-energy absorption band is broadened (full-width at the half-maximum [FWHM] = 297 nm) compared to the FWHM = 289 nm in LPBT. This is an indication of increased disorder in the LPBT-Me thin film relative to that of LPBT. These results corroborate the previously discussed DFT calculations that show that the parent polymer has larger oscillator strengths in the simulated absorption spectra (Figure D.4) and a nearly two-fold decrease in the reorganizational energies (λ_{LPBT} = 0.77 eV and $\lambda_{LPBT\text{-}Me}$ = 1.3 eV).

4.3.5. Thin Film Microstructures of LPBT and LPBT-Me. Two-dimensional grazing incidence wide-angle X-ray scattering (2D-GIWAXS) was employed to examine the thin film microstructures of LPBT and LPBT-Me ladder polymers. The 2D-GIWAXS diffraction patterns along with the corresponding 1D-linecuts in both the out-of-plane (OOP) and in-plane (IP) directions are shown in Figure 4.9. The diffraction peak position (q), interplanar spacings (d), crystalline coherence length (L_c), and the paracrystallinity disorder (g) are summarized in Table 4.2.

LPBT thin films exhibited a pronounced (010) diffraction peak centered at q_z = 1.86 Å^{-1} in the out of plane (OOP) direction, corresponding to a π-π packing distance of 3.38 Å (Table 4.2), which is identical to the previously reported π-π packing distance of ~ 3.4 Å.[30] The L_c values and the g parameter of LPBT in the π-stacking direction were found to be 1.39 nm and 18.6%, respectively (Table 4.2). In the case of LPBT-Me, a distinct (010) diffraction peak at q_z = 1.83 Å^{-1} was accompanied by a (100) diffraction peak at q_z = 0.74 Å^{-1} in the OOP direction. As a result, the π-π packing distance and the lamellar distance of LPBT-Me chains were calculated to be 3.43 Å and 8.46 Å, respectively (Table 4.2). The slightly large $d_{\pi\text{-}\pi}$ of LPBT-Me relative to

LPBT can be attributed to the more disordered LPBT-Me backbone, which would prevent the polymer chains from approaching each other and stacking tightly. The $L_{c,(010)}$ value of LPBT-Me was 1.20 nm, which corresponds to about 4 layers of chains stacked along the π-direction within one crystallite, which is slightly smaller than that of LPBT, which features up to 5 consecutive layers of chains per crystallite (Table 4.2). Furthermore, LPBT-Me was found to exhibit a slightly higher degree of lattice disorder, g_{π} = 20.2%, relative to the parent LPBT. These subtle differences in the microstructures of LPBT and LPBT-Me suggest a more disordered nature in the methylated polymer, which collectively has implications for charge transport properties as discussed below.

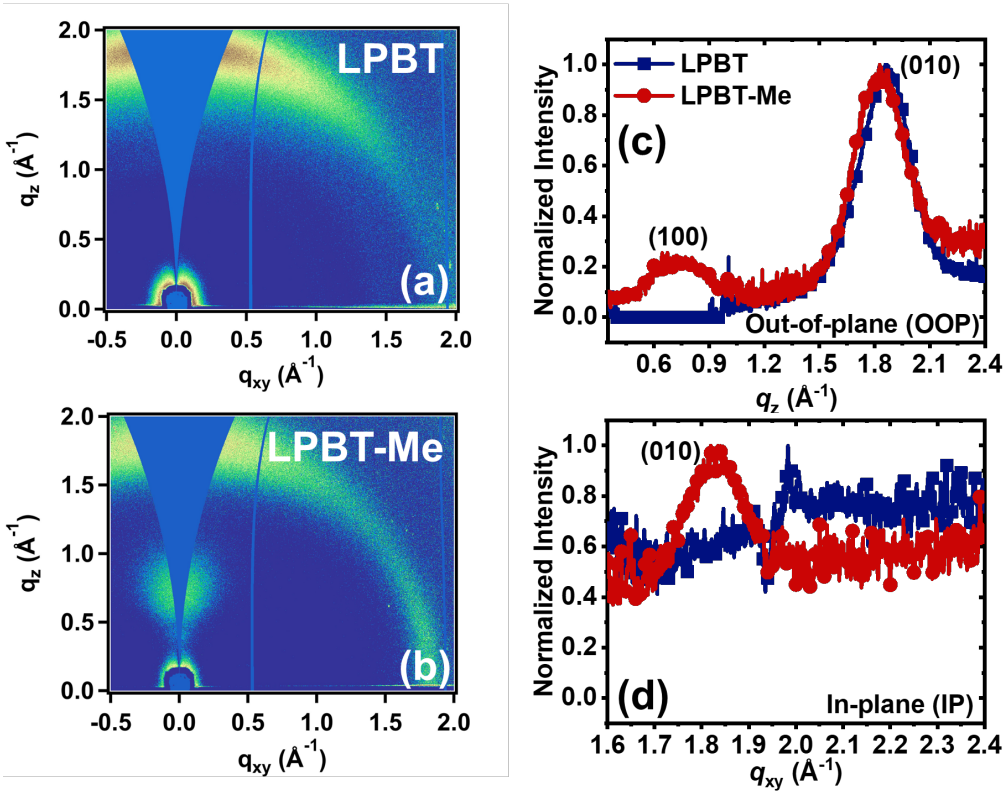

Figure 4.9. 2D-GIWAXS diffraction patterns of LPBT (a) and LPBT-Me (b) thin films; 1D line cuts of GIWAXS patterns in the out-of-plane (OOP) direction (c) and the in-plane (IP) direction (d).

Table 4.2. Summary of Diffraction Peak Position (q), Interplanar Spacing (d), Crystalline Coherence Length (L_c), Number of Stacked Layers Within a Crystallite (N), and Paracrystallinity Disorder (g) of LPBT and LPBT-Me Thin Films.

Polymer	$q_{z,(010)\ OOP}$ (Å^{-1})	$d_{\pi\text{-}\pi}$ (Å)	$L_{c,(010)\ OOP}$ (nm)	Number of layers ($N_{\pi\text{-}\pi}$)	g_{π} (%)	$q_{z,(100)\ OOP}$ (Å^{-1})	d_{lam} (Å)
LPBT	1.860	3.38	1.39	5.1	18.6	-	-
LPBT-Me	1.834	3.43	1.20	4.5	20.2	0.742	8.46

4.3.6. Field-Effect Charge Transport Properties of LPBT and LPBT-Me. We investigated the charge transport properties of LPBT and LPBT-Me by using bottom-gate/top-contact organic field-effect transistors (OFETs) devices and the output and transfer curves are shown in Figure 4.10, whereas the numerical hole transport properties are summarized in Table 4.3.

The average saturation region hole mobility (μ_h) of LPBT was found to be (3.10 ± 0.39) x 10^{-3} cm^2/Vs, and the average threshold voltage (V_T) was calculated to be -44.6 ± 3.1 V (Table 4.3). The maximum μ_h of LPBT was 3.74 x 10^{-3} cm^2/Vs, which is about an order of magnitude lower than that extracted from previously reported OECT measurements.[31] The hole mobility of the methylated counterpart, LPBT-Me, was decreased by over two-fold to an average value of (1.30 ± 0.21) x 10^{-3} cm^2/Vs and a maximum value of 1.64 x 10^{-3} cm^2/Vs (Table 4.3). The average V_T value of LPBT-Me was -42.9 ± 3.4 V and comparable to that of LPBT. Moreover, the on/off current ratio (I_{on}/I_{off}) of LPBT ($I_{on}/I_{off} \sim 10^3$) was about an order of magnitude higher than that of LPBT-Me ($I_{on}/I_{off} \sim 10^2$). These results indicate that methylation has negative effects on the macroscopic charge transport properties of the class of conjugated ladder poly(pyrrolobenzothiazine)s.

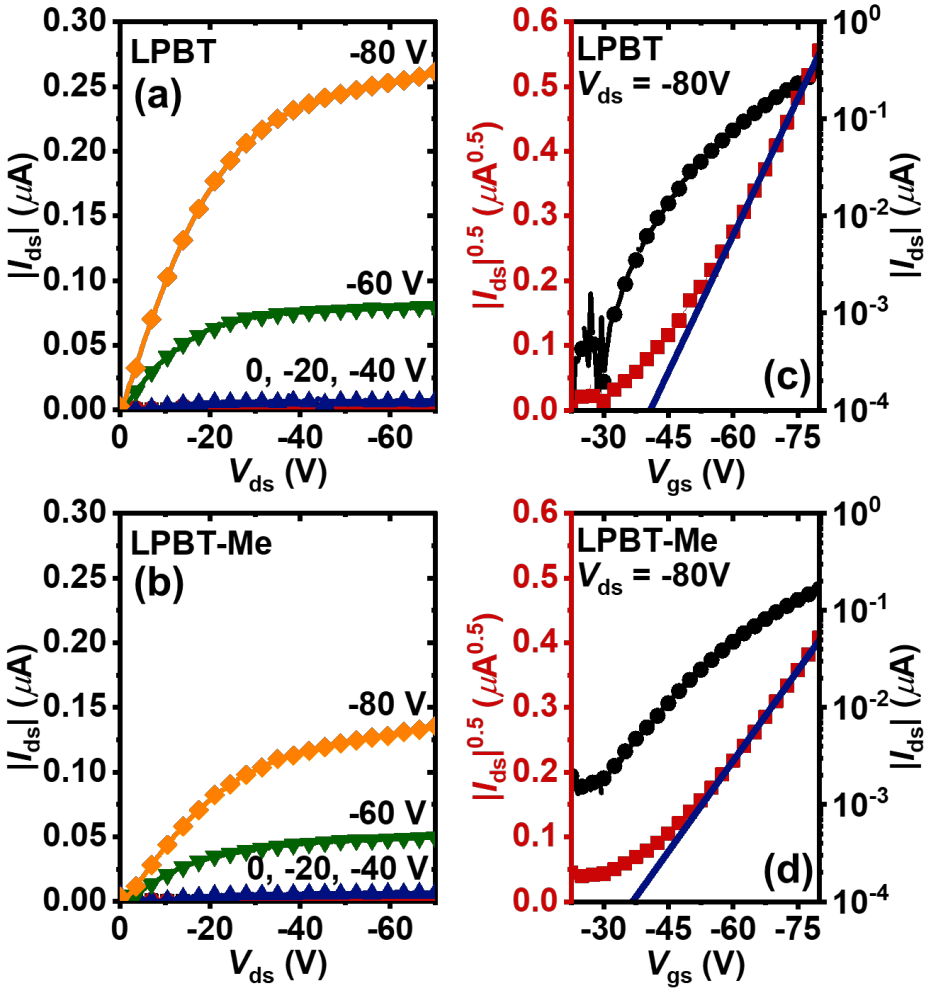

Figure 4.10. (a, b) Output curves of p-channel organic field-effect transistor (OFET) devices of LPBT (a) and LPBT-Me (b) ladder polymers; (c, d) Transfer curves of p-channel OFET devices of LPBT (c) and LPBT-Me (d) ladder polymers measured in saturated regimes (V_{ds} = -80V).

Table 4.3. Hole Transport Properties of LPBT and LPBT-Me Conjugated p-Type Ladder Polymers Measured by Organic Field-Effect Transistors.

Polymer	μ_{ave} [a] (10^{-3} cm^2/Vs)	μ_{max} (10^{-3} cm^2/Vs)	V_T [b] (V)	I_{on}/I_{off} [c]
LPBT	3.10 ± 0.39	3.74	-44.6 ± 3.1	(1.4 ± 0.9) x 10^3
LPBT-Me	1.30 ± 0.21	1.64	-42.9 ± 3.4	(6.1 ± 2.7) x 10^2

[a] μ_{ave}, average *field-effect* hole mobility (+/- one standard deviation); [b] V_τ, average threshold voltage (+/- one standard deviation); [c] I_{on}/I_{off}, on/off current ratio. Average values and standard deviations were calculated from at least 15 different devices.

Given the similar polymer molecular weights, comparable HOMO energy levels, and semiconductor bandgaps of LPBT and LPBT-Me, the two-fold mobility gap could be attributed to the more disordered nature of LPBT-Me. We propose that the increased conformational disorder in LPBT-Me compared to LPBT might not only disrupt intrachain hole delocalization as evidenced by the more localized HOMO orbital distributions seen in LPBT-Me (Figure D.6) but also interfere with tight interchain packing as discussed earlier, both of which resulted in the observed poor hole mobility of LPBT-Me. We note that the hole mobility of both LPBT and LPBT-Me remain relatively modest compared to several state-of-the-art p-type semiconducting polymers.[76–79] The inferior hole transport properties can be rationalized by the low polymer molecular weights and the flexible polymer backbone. Nevertheless, the LPBT and LPBT-Me backbone holds tremendous potential to become the prototypical p-type semiconducting ladder polymer if the polymer synthesis protocol could be improved to suppress monomer sublimation by solvent engineering such that higher polymer molecular weights can be obtained. Incorporating much longer side chains to potentially induce liquid crystalline ordering of the poly(pyrrolobenzothiazine) backbone is another approach that could improve charge transport properties of this class of ladder polymers.[80]

4.4. Conclusions

We have synthesized the new *p-type* semiconducting LPBT-Me and the known LPBT and used them to investigate the effects of N-alkyl substitution on the chain conformation, electronic structure, and charge transport properties of ladder poly(pyrrolobenzothiazine)s. The LPBTs were found to be a class of small-bandgap polymer semiconductors, whose optical bandgap of 1.5 eV is unchanged by N-alkyl side chain substitution. The π-conjugated backbone of the ladder LPBTs was found to exhibit a donor-acceptor architecture, which facilitates

enhanced intramolecular charge transfer (ICT) upon protonation in acid solutions. Partial protonation of either LPBT or LPBT-Me gives rise to a more flexible backbone evidenced by thermochromism and confirmed by planar/non-planar chain conformation variation with degree of protonation seen in DFT calculations.

Our GIWAXS characterization of the thin film microstructures of LPBT and LPBT-Me shows that N-methyl substitution results in an increased π-π stacking distance, reduced crystallinity, and increased lattice disorder. The average field-effect hole mobility decreased from 3.1×10^{-3} cm^2/Vs in LPBT to 1.3×10^{-3} cm^2/Vs in LPBT-Me, which is likely limited by the relatively low molecular weights of these ladder polymers. The observed factor of 2.4 difference in carrier mobility between LPBT and LPBT-Me could be explained by the differences in their thin film microstructures and DFT-predicted reorganization energies.

4.5. References

1. Cao, Z.; Leng, M.; Cao, Y.; Gu, X.; Fang, L. How Rigid Are Conjugated Non-Ladder and Ladder Polymers? *J. Polym. Sci.* **2022**, *60* (3), 298-310: DOI: 10.1002/pol.20210550.

2. Griggs, S.; Marks, A.; Bristow, H.; McCulloch, I. N-Type Organic Semiconducting Polymers: Stability Limitations, Design Considerations and Applications. *J. Mater. Chem. C* **2021**, *9* (26), 8099–8128. DOI: 10.1039/D1TC02048J.

3. Kim, F. S.; Park, C. H.; Na, Y.; Jenekhe, S. A. Effects of Ladder Structure on the Electronic Properties and Field-Effect Transistor Performance of Poly(Benzobisimidazobenzophenanthroline). *Org. Electron.* **2019**, *69*, 301–307. DOI: 10.1016/j.orgel.2019.03.049.

4. Lee, J.; Kalin, A. J.; Yuan, T.; Al-Hashimi, M.; Fang, L. Fully Conjugated Ladder Polymers. *Chem. Sci.* **2017**, *8* (4), 2503–2521. DOI: 10.1039/c7sc00154a.

5. Teo, Y. C.; Lai, H. W. H.; Xia, Y. Synthesis of Ladder Polymers: Developments, Challenges, and Opportunities. *Eur. J. Chem.* **2017**, *23* (57), 14101–14112. DOI: 10.1002/chem.201702219.

6. Deusen, R. L. V. Benzimidazo-Benzophenanthroline Polymers. *J. Polym. Sci. B Polym. Lett.* **1966**, *4* (3), 211–214. DOI: 10.1002/pol.1966.110040310.

7. Babel, A.; Jenekhe, S. A. Electron Transport in Thin-Film Transistors From an n-Type Conjugated Polymer. *Adv. Mater.* **2002**, *14* (5), 371–374. DOI: 10.1002/1521-4095(20020304)14:5<371::AID-ADMA371>3.0.CO;2-5.

8. Babel, A.; Jenekhe, S. A. n-Channel Field-Effect Transistors from Blends of Conjugated Polymers. *J. Phys. Chem. B* **2002**, *106* (24), 6129–6132. DOI: 10.1021/jp020695l.

9. Alam, M. M.; Jenekhe, S. A. Efficient Solar Cells from Layered Nanostructures of Donor and Acceptor Conjugated Polymers. *Chem. Mater.* **2004**, *16* (23), 4647–4656. DOI: 10.1021/cm0497069.

10. Jenekhe, S. A.; Yi, S. Efficient Photovoltaic Cells from Semiconducting Polymer Heterojunctions. *Appl. Phys. Lett.* **2000**, *77* (17), 2635–2637. DOI: 10.1063/1.1320022.

11. Sun, H.; Vagin, M.; Wang, S.; Crispin, X.; Forchheimer, R.; Berggren, M.; Fabiano, S. Complementary Logic Circuits Based on High-Performance n-Type Organic Electrochemical Transistors. *Adv. Mater.* **2018**, *30* (9), 1704916. DOI: 10.1002/adma.201704916.

12. Surgailis, J.; Savva, A.; Druet, V.; Paulsen, B.; Wu, R.; Hamidi-Sakr, A.; Ohayon, D.; Nikiforidis, G.; Chen, X.; McCulloch, I.; Rivnay, J.; Inal, S. Mixed Conduction in an N-Type Organic Semiconductor in the Absence of Hydrophilic Side-Chains. *Adv. Funct. Mater.* **2021**, *31* (21), 2010165. DOI: 10.1002/adfm.202010165.

13. Wu, H.-Y.; Yang, C.-Y.; Li, Q.; Kolhe, N. B.; Strakosas, X.; Stoeckel, M.-A.; Wu, Z.; Jin, W.; Savvakis, M.; Kroon, R.; Tu, D.; Woo, H. Y.; Berggren, M.; Jenekhe, S. A.; Fabiano, S. Influence of Molecular Weight on the Organic Electrochemical Transistor Performance of Ladder-Type Conjugated Polymers. *Adv. Mater.* **2022**, *34* (4), 2106235. DOI: 10.1002/adma.202106235.

14. Babel, A.; Wind, J. D.; Jenekhe, S. A. Ambipolar Charge Transport in Air-Stable Polymer Blend Thin-Film Transistors. *Adv. Funct. Mater.* **2004**, *14* (9), 891–898. DOI: 10.1002/adfm.200305180.

15. Kim, F. S.; Ahmed, E.; Subramaniyan, S.; Jenekhe, S. A. Air-Stable Ambipolar Field-Effect Transistors and Complementary Logic Circuits from Solution-Processed n/p Polymer Heterojunctions. *ACS Appl. Mater. Interfaces.* **2010**, *2* (11), 2974–2977. DOI: 10.1021/am1006996.

16. Alam, M. M.; Jenekhe, S. A. Conducting Ladder Polymers: Insulator-to-Metal Transition and Evolution of Electronic Structure upon Protonation by Poly(Styrenesulfonic Acid). *J. Phys. Chem. B* **2002**, *106* (43), 11172–11177. DOI: 10.1021/jp021230y.

17. Tam, T. L. D.; Lin, M.; Handoko, A. D.; Xu, J. Thermoelectric Performances of N-Doped Ladder-Type Conjugated Polymers Using Various Viologen Radical Cations. *ACS Appl. Polym. Mater.* **2021**, *3* (11), 5596–5603. DOI: 10.1021/acsapm.1c00920.

18. Wang, S.; Sun, H.; Ail, U.; Vagin, M.; Persson, P. O. Å.; Andreasen, J. W.; Thiel, W.; Berggren, M.; Crispin, X.; Fazzi, D.; Fabiano, S. Thermoelectric Properties of Solution-Processed n-Doped Ladder-Type Conducting Polymers. *Adv. Mater.* **2016**, *28* (48), 10764–10771. DOI: 10.1002/adma.201603731.

19. Yang, C.-Y.; Stoeckel, M.-A.; Ruoko, T.-P; Wu, H.-Y; Liu, X.; Kolhe, N. B.; Wu, Z.; Puttisong, Y.; Musumeci, C.; Massetti, M.; Sun, H.; Xu, K.; Tu, D.; Chen, W. M.; Woo, H. Y.; Fahlman, M.; Jenekhe, S. A.; Berggren, M.; Fabiano, S. A High-Conductivity n-Type Polymeric Ink for Printed Electronics. *Nat. Commun.* **2022**, *13* (1), 1792. DOI: 10.1038/s41467-021-22528-y.

20. Volkov, A.; Sun, H.; Kroon, R.; Ruoko, T.; Che, C.; Edberg, J.; Muller, C.; Fabiano, S.; Crispin, X. Asymmetric Aqueous Supercapacitor Based on P- and n-Type Conducting Polymers. *ACS Appl. Energy Mater.* **2019**, *2* (8), 5350–5355. DOI: 10.1021/acsaem.9b00853.

21. Guo, J.; Flagg, L. Q.; Tran, D. K.; Chen, S. E.; Li, R.; Kolhe, N. B.; Giridharagopal, R.; Jenekhe, S. A.; Richter, L. J.; Ginger, D. S. Hydration of a Side-Chain-Free n-Type Semiconducting Ladder Polymer Driven by Electrochemical Doping. *J. Am. Chem. Soc.* **2023**, *145* (3), 1866–1876. DOI: 10.1021/jacs.2c11468.

22. Briseno, A. L.; Mannsfeld, S. C. B.; Shamberger, J. P.; Ohuchi, F. S.; Bao, Z.; Jenekhe, S. A.; Xia, Y. Self-Assembly, Molecular Packing, and Electron Transport in n-Type Polymer Semiconductor Nanobelts. *Chem. Mater.* **2008**, *20* (14), 4712–4719. DOI: 10.1021/cm8010265.

23. Nayak, K.; Mark, J. E. Chain Packing in Two Aromatic Heterocyclic Polymers, One of Which Has a Ladder Structure. *Makromol. Chem.* **1986**, *187* (6), 1547–1550. DOI: 10.1002/macp.1986.021870623.

24. Song, H. H.; Fratini, A. V.; Chabinyc, M.; Price, G. E.; Agrawal, A. K.; Wand, C.-S.; Burkette, J.; Dudis, D. S.; Arnold, F. E. Crystal Structure and Thin Film Morphology of BBL Ladder Polymer. *Synth. Met.* **1995**, 69 (1–3), 533–535. DOI: 10.1016/0379-6779(94)02556-E.

25. West, S. M.; Tran, D. K.; Guo, J.; Chen, S. E.; Ginger, D. S.; Jenekhe, S. A. Phenazine-Substituted Poly(Benzimidazobenzophenanthrolinedione): Electronic Structure, Thin Film Morphology, Electron Transport, and Mechanical Properties of an n-Type Semiconducting Ladder Polymer. *Macromolecules* **2023**, *56* (5) 2081-2091. DOI: 10.1021/acs.macromol.2c01999.

26. Imai, K.; Kurihara, M.; Mathias, L.; Wittmann, J.; Alston, W. B.; Stille, J. K. Synthesis and Properties of Thermally Stable Ladder Polymers Containing the 1,4-Pyrazine Ring Obtained from Polyheterocyclizations of Tetramines and Tetraketones in Poly(Phosphoric Acid) and m-Cresol. *Macromolecules* **1973**, *6* (2), 158–162. DOI: 10.1021/ma60032a002.

27. Sicree, A. J.; Arnold, F. E.; Deusen, R. L. V. New Imidazoisoquinoline Ladder Polymers. *J. Polym. Sci. Polym. Chem.* **1974**, *12* (2), 265–272. DOI: 10.1002/pol.1974.170120202.

28. Gerber, A. H. Thermally Stable Polymers Derived from 2,3,5,6-Tetraaminopyridine. *J. Polym. Sci. Polym. Chem.* **1973**, *11* (7), 1703–1719. DOI: 10.1002/pol.1973.170110718.

29. Arnold, F. E. Ladder Polymers from Tetraaminodiquinoxalpyrene. *J. Polym. Sci. A. Polym. Chem.* **1970**, *8* (8), 2079–2089. DOI: 10.1002/pol.1970.150080816.

30. Tam, T. L. D.; Lin, M.; Chien, S. W.; Xu, J. Facile Synthesis of Solubilizing a Group-Free, Solution-Processable p-Type Ladder Conjugated Polymer and Its Thermoelectric Properties. *ACS Macro. Lett.* **2022**, *11* (1), 110–115. DOI: 10.1021/acsmacrolett.1c00696.

31. Wu, X.; Tam, T. L. D.; Chen, S.; Salim, T.; Zhao, X.; Zhou, Z.; Lin, M.; Xu, J.; Loo, Y.-L.; Leong, W. L. All-Polymer Bulk-Heterojunction Organic Electrochemical Transistors with Balanced Ionic and Electronic Transport. *Adv. Mater.* **2022**, *34* (42), 2206118. DOI: 10.1002/adma.202206118.

32. Leng, M.; Koripally, N.; Huang, J.; Vriza, A.; Lee, K. Y.; Ji, X.; Li, C.; Hays, M.; Tu, Q.; Dunbar, K.; Xu, J.; Ng, T. N.; Fang, L. Synthesis and Exceptional Operational Durability of Polyaniline-Inspired Conductive Ladder Polymers. *Mater. Horiz.* **2023**, *10* (10), 4354–4364. DOI: 10.1039/D3MH00883E.

33. Wolfe, J. F.; Loo, B. H.; Arnold, F. E. Rigid-Rod Polymers. 2. Synthesis and Thermal Properties of Para-Aromatic Polymers with 2,6-Benzobisthiazole Units in the Main Chain. *Macromolecules* **1981**, *14* (4), 915–920. DOI: 10.1021/ma50005a005.

34. Hickl, P.; Ballauff, M.; Scherf, U.; Müllen, K.; Lindner, P. Characterization of a Ladder Polymer by Small-Angle X-Ray and Neutron Scattering. *Macromolecules* **1997**, *30* (2), 273–279. DOI: 10.1021/ma961038s.

35. Hong, W.; Wei, Z.; Xi, H.; Xu, W.; Hu, W.; Wang, Q.; Zhu, D. 6H-Pyrrolo[3,2-b:4,5-B′]Bis[1,4]Benzothiazines: Facilely Synthesized Semiconductors for Organic Field-Effect Transistors. *J. Mater. Chem.* **2008**, *18* (40), 4814–4820. DOI: 10.1039/B809486A.

36. Wei, Z.; Hong, W.; Geng, H.; Wang, C.; Liu, Y.; Li, R.; Xu, W.; Shuai, Z.; Hu, W.; Wang, Q.; Zhu, D. Organic Single Crystal Field-Effect Transistors Based on 6H-Pyrrolo[3,2–b:4,5–B´]Bis[1,4]Benzothiazine and Its Derivatives. *Adv. Mater.* **2010**, *22* (22), 2458–2462. DOI: 10.1002/adma.201000088.

37. Wang, S.; Hong, W.; Ren, S.; Li, J.; Wang, M.; Gao, X.; Li, H. New Ladder-Type Conjugated Polymer with Broad Absorption, High Thermal Durability, and Low Band Gap. *J. Polym. Sci. A. Polym. Chem.* **2012**, *50* (20), 4272–4276. DOI: 10.1002/pola.26234.

38. Trasatti, S. The Absolute Electrode Potential: An Explanatory Note (Recommendations 1986). *Pure Appl. Chem.* **1986**, *58* (7), 955–966. DOI: 10.1351/pac198658070955.

39. Pommerehne, J.; Vestweber, H.; Guss, W.; Mahrt, R. F.; Bässler, H.; Porsch, M.; Daub, J. Efficient Two Layer Leds on a Polymer Blend Basis. *Adv. Mater.* **1995**, *7* (6), 551–554. DOI: 10.1002/adma.19950070608.

40. Oosterhout, S. D.; Savikhin, V.; Zhang, J.; Zhang, Y.; Burgers, M. A.; Marder, S. R.; Bazan, G. C.; Toney, M. F. Mixing Behavior in Small Molecule:Fullerene Organic Photovoltaics. *Chem. Mater.* **2017**, *29* (7), 3062–3069. DOI: 10.1021/acs.chemmater.7b00067.

41. Hexemer, A.; Bras, W.; Glossinger, J.; Schaible, E.; Gann, E.; Kirian, R.; MacDowell, A.; Church, M.; Rude, B.; Padmore, H. A SAXS/WAXS/GISAXS Beamline with Multilayer Monochromator. *J. Phys.: Conf. Ser.* **2010**, *247*, 012007. DOI: 10.1088/1742-6596/247/1/012007.

42. Frisch, M. J. Frisch, M. J., et al., Gaussian 16, Revision C.01, Gaussian, Inc., Wallingford CT. **2016**.

43. Liu, G.; Fang, Q.; Xu, W.; Chen, H.; Wang, C. Vibration Assignment of Carbon–Sulfur Bond in 2-Thione-1,3-Dithiole-4,5-Dithiolate Derivatives. *Spectrochim. Acta A Mol. Biomol. Spectrosc.* **2004**, *60* (3), 541–550. DOI: 10.1016/S1386-1425(03)00260-9.

44. Yang, H.; Fan, H.; Wang, Z.; Yan, H.; Dong, Y.; Cui, C.; Ade, H.; Li, Y. Impact of Isomer Design on Physicochemical Properties and Performance in High-Efficiency All-Polymer Solar Cells. *Macromolecules* **2020**, *53* (20), 9026–9033. DOI: 10.1021/acs.macromol.0c01405.

45. Cui, Y.; Yao, H.; Gao, B.; Qin, Y.; Zhang, S.; Yang, B.; He, C.; Xu, B.; Hou, J. Fine-Tuned Photoactive and Interconnection Layers for Achieving over 13% Efficiency in a Fullerene-Free Tandem Organic Solar Cell. *J. Am. Chem. Soc.* **2017**, *139* (21), 7302–7309. DOI: 10.1021/jacs.7b01493.

46. Yong Lee, J.; Kim, K. S.; Jin Mhin, B. Intramolecular Charge Transfer of π-Conjugated Push–Pull Systems in Terms of Polarizability and Electronegativity. *J. Chem. Phys.* **2001**, *115* (20), 9484–9489. DOI: 10.1063/1.1413986.

47. Roberts, M. F.; Jenekhe, S. A. Lewis-Acid Coordination-Complexes of Polymers .3. Poly(Benzimidazobenzophenanthroline) Ladder and Semiladder Polymers. *Polymer* **1994**, *35* (20), 4313–4325. DOI: 10.1016/0032-3861(94)90088-4.

48. Mahmood, A.; Tang, A.; Wang, X.; Zhou, E. First-Principles Theoretical Designing of Planar Non-Fullerene Small Molecular Acceptors for Organic Solar Cells: Manipulation of Noncovalent Interactions. *Phys. Chem. Chem. Phys.* **2019**, *21* (4), 2128–2139. DOI: 10.1039/C8CP05763J.

49. Duan, R.; Han, G.; Qu, L. B.; Yi, Y. Importance of Molecular Rigidity on Reducing the Energy Losses in Organic Solar Cells: Implication from Geometric Relaxations of A–D–A Electron Acceptors. *Mater. Chem. Front.* **2021**, *5* (10), 3903–3910. DOI: 10.1039/D1QM00026H.

50. Vezie, M. S.; Few, S.; Meager, I.; Pieridou, G.; Dörling, B.; Ashraf, R. S.; Goñi, A. R.; Bronstein, H.; McCulloch, I.; Hayes, S. C.; Campoy-Quiles, M.; Nelson, J. Exploring the Origin of High Optical Absorption in Conjugated Polymers. *Nat. Mater.* **2016**, *15* (7), 746–753. DOI: 10.1038/nmat4645.

51. Batsanov, S. S. Van Der Waals Radii of Elements. *Inorg.* **2001**, *37* (9), 15. DOI: 10.1023/A:1011625728803.

52. Brédas, J. L.; Beljonne, D.; Coropceanu, V.; Cornil, J. Charge-Transfer and Energy-Transfer Processes in π-Conjugated Oligomers and Polymers: A Molecular Picture. *Chem. Rev.* **2004**, *104* (11), 4971–5004. DOI: 10.1021/cr040084k.

53. Zade, S. S.; Zamoshchik, N.; Bendikov, M. From Short Conjugated Oligomers to Conjugated Polymers. Lessons from Studies on Long Conjugated Oligomers. *Acc. Chem. Res.* **2011**, *44* (1), 14–24. DOI: 10.1021/ar1000555.

54. Murray, J. S.; Politzer, P. The Electrostatic Potential: An Overview. *WIREs Comput. Mol. Sci.* **2011**, *1* (2), 153–163. DOI: 10.1002/wcms.19.

55. Yao, H.; Cui, Y.; Qian, D.; Ponseca, C. S.; Honarfar, A.; Xu, Y.; Xin, J.; Chen, Z.; Hong, L.; Gao, B.; Yu, R.; Zu, Y.; Ma, W.; Chabera, P.; Pullerits, T.; Yartsev, A.; Gao, F.; Hou, J. 14.7% Efficiency Organic Photovoltaic Cells Enabled by Active Materials with a Large Electrostatic Potential Difference. *J. Am. Chem. Soc.* **2019**, *141* (19), 7743–7750. DOI: 10.1021/jacs.8b12937.

56. Xia, H.; Xu, X.; Qian, C.; Guo, J.; Zhao, J.; Zhang, K.; Tan, H.; Peng, Q.; Zhu, Q. A–D–A–D–A-Type Oligomer versus A–D–A-Type Small Molecule: Synthesis and Advanced Effect of the D–A Repeat Unit on Morphology and Photovoltaic Properties. *ACS Appl. Energy Mater.* **2022**, *5* (3), 3146-3155. DOI: 10.1021/acsaem.1c03759.

57. Kim, B.-G.; Ma, X.; Chen, C.; Ie, Y.; Coir, E. W.; Hashemi, H.; Aso, Y.; Green, P. F.; Kieffer, J.; Kim, J. Energy Level Modulation of HOMO, LUMO, and Band-Gap in Conjugated Polymers for Organic Photovoltaic Applications. *Adv. Funct.l Mater.* **2013**, *23* (4), 439–445. DOI: 10.1002/adfm.201201385.

58. Farmer, B. L.; Dudis, D. S.; Adams, W. W. Calculation of the Effects of Protonation on Rigid-Rod Polymers. *Polymer* **1994**, *35* (17), 3745–3751. DOI: 10.1016/0032-3861(94)90556-8.

59. Jenekhe, S. A.; Lu, L.; Alam, M. M. New Conjugated Polymers with Donor−Acceptor Architectures: Synthesis and Photophysics of Carbazole−Quinoline and Phenothiazine−Quinoline Copolymers and Oligomers Exhibiting Large Intramolecular Charge Transfer. *Macromolecules* **2001**, *34* (21), 7315–7324. DOI: 10.1021/ma0100448.

60. Agrawal, A. K.; Jenekhe, S. A. Synthesis and Processing of Heterocyclic Polymers as Electronic, Optoelectronic, and Nonlinear Optical Materials. 2. New Series of Conjugated Rigid-Rod Polyquinolines and Polyanthrazolines. *Macromolecules* **1993**, *26* (5), 895–905. DOI: 10.1021/ma00057a003.

61. Zhang, Q. T.; Tour, J. M. Imine-Bridged Planar Poly(Phenylenethiophene)s and Polythiophenes. *J. Am. Chem. Soc.* **1997**, *119* (41), 9624–9631. DOI: 10.1021/ja964223u.

62. Hedström, S.; Henriksson, P.; Wang, E.; Andersson, M. R.; Persson, P. Temperature-Dependent Optical Properties of Flexible Donor–Acceptor Polymers. *J. Phys. Chem. C* **2015**, *119* (12), 6453–6463.DOI: 10.1021/jp511246n.

63. Onwubiko, A.; Yue, W.; Jellett, C.; Xiao, M.; Chen, H.-Y.; Ravva, M. K.; Hanifi, D. A.; Knall, A.-C.; Purushothaman, B.; Nikolka, M.; Flores, J.-C.; Salleo, A.; Bredas, J.-L.; Sirringhaus, H.; Hayoz, P.; McCulloch, I. Fused Electron Deficient Semiconducting Polymers for Air Stable Electron Transport. *Nat. Commun.* **2018**, *9* (1), 416. DOI: 10.1038/s41467-018-02852-6.

64. Yang, C. J.; Jenekhe, S. A. Conjugated Aromatic Polyimines. 2. Synthesis, Structure, and Properties of New Aromatic Polyazomethines. *Macromolecules* **1995**, *28* (4), 1180–1196. DOI: 10.1021/ma00108a054.

65. Farmer, B. L.; Chapman, B. R.; Dudis, D. S.; Adams, W. W. Molecular Dynamics of Rigid Rod Polymers. *Polymer* **1993**, *34* (8), 1588–1601. DOI: 10.1016/0032-3861(93)90314-Z.

66. Salaneck, W. R.; Inganäs, O.; Thémans, B.; Nilsson, J. O.; Sjögren, B.; Österholm, J. -E.; Brédas, J. L.; Svensson, S. Thermochromism in Poly(3-hexylthiophene) in the Solid State: A Spectroscopic Study of Temperature-dependent Conformational Defects. *J. Chem. Phys.* **1988**, *89* (8), 4613–4619. DOI: 10.1063/1.454802.

67. Roux, C.; Leclerc, M. Thermochromic Properties of Polythiophene Derivatives: Formation of Localized and Delocalized Conformational Defects. *Chem. Mater.* **1994**, *6* (5), 620–624. DOI: 10.1021/cm00041a011.

68. Danielsen, S. P. O.; Davidson, E. C.; Fredrickson, G. H.; Segalman, R. A. Absence of Electrostatic Rigidity in Conjugated Polyelectrolytes with Pendant Charges. *ACS Macro. Lett.* **2019**, *8* (9), 1147–1152. DOI: 10.1021/acsmacrolett.9b00551.

69. Roux, C.; Bergeron, J.-Y.; Leclerc, M. Thermochromic Properties of Polythiophenes: Structural Aspects. *Makromol. Chem.* **1993**, *194* (3), 869–877. DOI: 10.1002/macp.1993.021940311.

70. Hutchison, G. R.; Zhao, Y.-J.; Delley, B.; Freeman, A. J.; Ratner, M. A.; Marks, T. J. Electronic Structure of Conducting Polymers: Limitations of Oligomer Extrapolation Approximations and Effects of Heteroatoms. *Phys. Rev. B* **2003**, *68* (3), 035204. DOI: 10.1103/PhysRevB.68.035204.

71. Sun, H.; Autschbach, J. Electronic Energy Gaps for π-Conjugated Oligomers and Polymers Calculated with Density Functional Theory. *J. Chem. Theory Comput.* **2014**, *10* (3), 1035–1047. DOI: 10.1021/ct4009975.

72. Jain, M.; Chelikowsky, J. R.; Louie, S. G. Reliability of Hybrid Functionals in Predicting Band Gaps. *Phys. Rev. Lett.* **2011**, *107* (21), 216806. DOI: 10.1103/PhysRevLett.107.216806.

73. Wu, P.-T.; Kim, F. S.; Champion, R. D.; Jenekhe, S. A. Conjugated Donor−Acceptor Copolymer Semiconductors. Synthesis, Optical Properties, Electrochemistry, and Field-Effect Carrier Mobility of Pyridopyrazine-Based Copolymers. *Macromolecules* **2008**, *41* (19), 7021–7028. DOI: 10.1021/ma801348b.

74. Leenaers, P. J.; Maufort, A. J. L. A.; Wienk, M. M.; Janssen, R. A. J. Impact of π-Conjugated Linkers on the Effective Exciton Binding Energy of Diketopyrrolopyrrole–Dithienopyrrole Copolymers. *J. Phys. Chem. C* **2020**, *124* (50), 27403–27412. DOI: 10.1021/acs.jpcc.0c08768.

75. Izquierdo, M. A.; Broer, R.; Havenith, R. W. A. Theoretical Study of the Charge Transfer Exciton Binding Energy in Semiconductor Materials for Polymer:Fullerene-Based Bulk Heterojunction Solar Cells. *J. Phys. Chem. A* **2019**, *123* (6), 1233–1242. DOI: 10.1021/acs.jpca.8b12292.

76. Chen, Z.; Cai, P.; Chen, J.; Liu, X.; Zhang, L.; Lan, L.; Peng, J.; Ma, Y.; Cao, Y. Low Band-Gap Conjugated Polymers with Strong Interchain Aggregation and Very High Hole Mobility Towards Highly Efficient Thick-Film Polymer Solar Cells. *Adv. Mater.* **2014**, *26* (16), 2586–2591. DOI: 10.1002/adma.201305092.

77. Park, S.; Lim, B. T.; Kim, B.; Son, H. J.; Chung, D. S. High Mobility Polymer Based on a π-Extended Benzodithiophene and Its Application for Fast Switching Transistor and High Gain Photoconductor. *Sci. Rep.* **2014**, *4* (1), 5482. DOI: 10.1038/srep05482.

78. Kang, I.; Yun, H.-J.; Chung, D. S.; Kwon, S.-K.; Kim, Y.-H. Record High Hole Mobility in Polymer Semiconductors via Side-Chain Engineering. *J. Am. Chem. Soc.* **2013**, *135* (40), 14896–14899. DOI: 10.1021/ja405112s.

79. Luo, L.; Huang, W.; Yang, C.; Zhang, J.; Zhang, Q. Recent Advances on π-Conjugated Polymers as Active Elements in High Performance Organic Field-Effect Transistors. *Front. Phys.* **2021**, *16* (3), 33500. DOI: 10.1007/s11467-020-1045-6.

80. McCulloch, I.; Heeney, M.; Bailey, C.; Genevicius, K.; MacDonald, I.; Shkunov, M.; Sparrowe, D.; Tierney, S.; Wagner, R.; Zhang, W.; Chabinyc, M. L.; Kline, R. J.; McGehee, M. D.; Toney, M. F. Liquid-Crystalline Semiconducting Polymers with High Charge-Carrier Mobility. *Nat. Mater.* **2006**, *5* (4), 328–333. DOI: 10.1038/nmat1612.

Chapter 5. Ladder Poly(Thienobenzothiazine): Synthesis, Electronic Structure, Optical Properties, and p-Doped Electrical Conductivity of a Narrow Bandgap p-Type Ladder Polymer

5.1. Introduction

In the past few decades, there has been the been great interest in lowering the bandgap of π-conjugated polymers to improve near infrared (NIR) absorption, electrical conductivity and ambipolar charge transport properties.[1–4] A common approach to reduce the bandgap of semiconducting polymers is to utilize an electron donor-acceptor (D-A) motif that features electronically coupled electron-rich and electron-deficient moieties. Careful selection of donor and acceptor building blocks has allowed the synthesis finely-tuned semiconducting polymers with strong intramolecular charge transfer (ICT) character and narrow bandgaps that can produce systems with efficient photoinduced charge transfer and separation for applications in organic photovoltaics (OPVs),[5–8] transparent electrodes,[1,9,10] and photodetectors.[11,12] Another strategy to reduce the bandgap of π-conjugated polymers is to enhance the co-planarity between adjacent aromatic rings.[13,14] Double-stranded ladder polymers are a class of π-conjugated polymers that exemplifies this approach. Their ladder architecture and an ideal persistent ribbon-like conformations limit torsional disorder.[15,16] However, the members of this class are rare due to difficulties associated with synthesis and processing.[17–19] Recent examples of π-conjugated ladder polymers that feature pronounced D-A character are the ladder poly(pyrrolobenzothiazine)s.[20,21] We previously showed that their small optical bandgap of ~ 1.5 eV are unchanged by N-alkylation, and that this class of ladder polymers posses strong protonation-enhanced ICT effects which is attributed to their D-A architecture.[21]

Compared to other heteroatomic polycyclic polymers, those incorporating thiophene building blocks have garnered the most attention due to their chemical and environmental stability in the undoped state, straightforward structural modifications, and intrinsically small bandgaps.[22–26] Thiophene-based molecules and polymers first became popular in the 1980s when soluble, alkylated polythiophenes were synthesized.[27,28] Since then, the rapid progress of thiophene-based electronic and optoelectronic devices have resulted in a huge number of publications.[29–34] Thiophene-based semiconductors have large structural diversities that have enabled the understanding of detailed structure-property relationships that allows the synthesis of finely tuned polymers to suit the specific application;[35,36] this has enabled state-of-the-art organic electronic devices to be developed. For example, the most recently reported high-performance active layers in OPVs contain thiophene fragments or fused-ring thiophene systems such as dithieno[3',2':3,4;2",3":5,6]benzo[1,2-*c*][1,2,5]thiadiazole,[37,38] 12,13-alkyl-12,13-dihydro-[1,2,5] thiadiazolo[3,4-*e*]thieno[2",3":4',5']thieno[2',3':4,5]pyrrolo[3,2-*g*]thieno[2',3':4,5]thieno[3,2-*b*] indole,[39,40] and 4,8-bis(5-(2-ethylhexyl)-4-fluorothiophen-2-yl)benzo[1,2-*b*:4,5-*b'*] dithiophene,[41,42] among others.

The success of thiophene semiconductors originates from the unique properties of the sulfur heteroatom. The sulfur atom in thiophene fosters strong electronic coupling though noncovalent interactions such as π-π, S-H, and S-N in the solid state which can lead to planar geometries.[43–46] Moreover, the larger atomic radius of the sulfur atom and aromaticity of the thiophene ring leads to improved orbital overlap between the highest-occupied molecular orbital (HOMO) energy level of the adjacent atoms in the solid state, which can lower the HOMO energy level of the polymer.[47] This is in contrast to the smaller atomic radius and increased electronegativity of the nitrogen and oxygen atoms in pyrrole and furan, respectively, that

decreases the aromaticity across the π-conjugated system and give rise to higher lying HOMO energy levels that can widen the bandgap and decrease air stability of the π-conjugated semiconductor.[48,49]

Chart 5.1. Molecular structures of model compound TBBT and conjugated p-type ladder polymer LTBT.

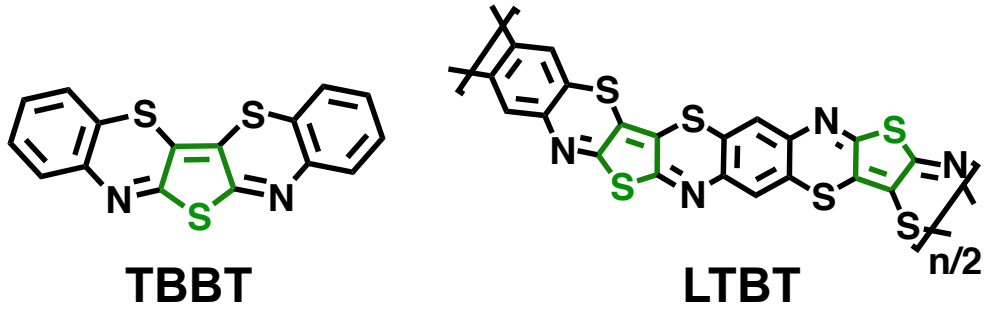

Despite the overwhelming success of thiophene-containing polymers, only one solution-processable polymer p-type ladder polymer has been synthesized.[50] Here, we report the synthesis of a new thiophene-based π-conjugated ladder polymer, ladder poly(thieno[3,2-b:4,5-b']benzothiazine) (LTBT), and its model compound thieno[3,2-b:4,5-b']bis[1,4]benzothiazine (TBBT) (Chart 5.1). We also report detailed investigations of the molecular structure, electronic structure, thin-film microstructure, optical properties, and electrical conductivity of p-doped LTBT. The new polymer LTBT was synthesized using a unique solvent system that resulted in excellent film forming properties as evidenced by large area freestanding films that were used to characterize the molecular structure using Fourier-transform infrared (FTIR) and Raman spectroscopies. The highly crystalline nature of TBBT enabled solution phase growth of single crystals that were subjected to X-ray diffraction that verified the molecular structure. We found that LTBT has a donor-acceptor motif with respect to the thiophene-benzothiazine, strong protonation-enhanced intramolecular charge transfer (ICT) that extends into the infrared region,

and a narrow thin-film optical bandgap of 1.28 eV. We measured the average electrical conductivity of LTBT doped with $FeCl_3$ and found it to be 3.3 x 10^{-1} S/cm.

5.2. Experimental Methods

Materials and Methods. 2,5-diamino-1,4-benzenedithiol HCl (97%) was purchased from Ambeed and recrystallized in 20% HCl before use. Perbromothiophene (98%) was purchased from Ambeed and used as received. Polyphosphoric acid (PPA, 84% P_2O_5), sulfolane, methanesulfonic acid (MSA) (> 99%), trifluoroacetic acid (TFA), triflic acid, fuming nitric acid (red, 90% > HNO_3), dichloromethane (DCM), acetone, dimethylformamide (DMF), deuterated dimethylsulfoxide (DMSO-d6), deuterated TFA (TFA-d), $FeCl_3$, and 2-aminobenzenethiol were purchased from Sigma-Aldrich and used as received. Methanol, acetic acid and acetonitrile were purchased from Fisher Scientific and used as received. All reactions were performed under inert atmosphere unless otherwise stated.

The intrinsic viscosity [η] of the polymer was measured on the MSA solution in an Ubbelohde viscometer suspended in a water bath at 30.0˚C. The concentrations of the polymer solution was chosen such that the elution time of the polymer solution was 1.1 – 1.8 times that of the pure solvent.

Thermogravimetric analysis (TGA) was conducted on a TA Instrument model Q50 TGA. A heating rate of 10 °C /min under a flow of N_2 was used with runs conducted from room temperature to 880 °C. Differential scanning calorimetry (DSC) analysis was performed on a TA Discovery DSC 500 under N_2 by scanning from -10 °C to 400 °C at a heating rate and cooling rate of 10 °C /min. Optical absorption spectra were measured on a PerkinElmer model Lambda 900 UV-vis/near-IR spectrophotometer. Solution absorption spectrum was obtained from dilute

solutions (10^{-5} M) in methanesulfonic acid and triflic acid. The ^{1}H and ^{13}C NMR spectra were recorded on a Bruker AV500 (at 500 MHz) using deuterated DMSO or TFA as the solvent.

Cyclic voltammetry (CV) experiments were performed on an EG&G Princeton Applied Research potentiostat/galvanostat (model 273A). A three-electrode cell was used, using platinum wire as the counter electrodes and the polymer coated onto a platinum wire from MSA solution as the working electrodes. Solution phase cyclic voltammetry was performed at a concentration of 3 mg/mL. The reference electrode was $Ag/AgNO_3$ in acetonitrile. The acidic solvents were removed by dipping the substrates in isopropanol (IPA) overnight and subsequently dried in vacuum oven at 60˚C. The supporting electrolyte solution consists of 0.1M tetrabutylammonium hexafluorophosphate (Bu_4NPF_6) in anhydrous acetonitrile. The electrolyte was purged with nitrogen for 15 minutes prior to the scans to ensure inert and anhydrous conditions. The reduction and oxidation potentials were referenced to the Fc/Fc^{+} couple by using ferrocene as an internal standard. LUMO energy levels were estimated using ferrocene value of -4.8 eV with respect to vacuum level. The LUMO and HOMO levels were determined by using the equations $E_{LUMO} = -(eE_{red}^{onset} + 4.8)$ and $E_{HOMO} = -(eE_{ox}^{onset} + 4.8)$.

Fourier-transform infrared spectroscopy (FTIR) experiments were performed on a Perkin Elmer Frontier spectrometer using freestanding films of LTBT and needles of TBBT. The resolution was set at 1 cm^{-1} and a set of 16 scans was averaged. Raman spectroscopy of the freestanding films was carried out on a Thermo Scientific DXR2 Raman microscope. A 532 nm laser with a power of 5mW was focused on a sample through a 50x objective lens.

Gas-phase density functional theory (DFT) and time-dependent density functional theory (TD-DFT) calculations were performed using the Gaussian 16 suit of programs[51] at the

ωB97XD/631-G(d,p) level of theory on the representative oligomers comprising three repeat units. Vertical electronic transitions were calculated for 12 excited states.

Preparation of Thin Film, Doping Method, and Characterization of Electrical Conductivity. Solutions of LTBT in methanesulfonic acid (MSA) at 15 mg/mL were stirred at elevated temperature (>130˚C) for at least a day to ensure solubilization of the polymer. The LTBT/MSA polymer solution was filtered through 1 μm pore size Grade GF/B Glass Microfiber Filters (Whatman GF/B) before use. The filtered polymer solution was then spin-coated onto clean glass substrates (sonicated in acetone, DI water, and isopropanol) at 5000 rpm for 30 seconds followed by immediate immersion in isopropanol (IPA) for deprotonation. The pH of the deprotonation solvent (IPA) was checked to ensure complete acid removal. The neutral polymer films were dried in a vacuum oven at 60˚C overnight.

The undoped neutral polymer films were then moved into a nitrogen-filled glovebox for doping study. A stock solution of 100 mM $FeCl_3$ in anhydrous acetonitrile was made, stored in the glovebox, and diluted to the desired concentration immediately before use. 200 μL of dopant solution (20 mM $FeCl_3$ in acetonitrile) was deposited onto the polymer film (1.5 x 1.5 cm^2) followed by a 90 s delay before spinning off the excess solution at 7000 rpm for 10 s. The doped polymer films were subjected to thermal annealing at different temperatures. The doped films were brought to ambient atmosphere for further characterizations.

Electrical conductivity (σ_{dc}) of doped LTBT films were measured by a colinear four-point probe controlled by a Keithley 2400 source-meter unit. For consistency, a 60-second delay between source and measurements was applied due to the rapid de-doping of the polymer films in ambient environment. The σ_{dc} value was calculated as follows:

$$\sigma_{dc} = \frac{\pi}{\ln(2)} \frac{1}{R \times t}$$

where σ_{dc} is the room-temperature dc-electrical conductivity (S/cm), R is the measured resistance (Ω), and t is the film thickness (cm).

Synthesis of 3,4-dibromothiophene-2,5-dione. Fuming nitric acid (35 mL) was added to a reaction vessel and chilled to 0˚C. Then, a mixture of perbromothiophene (5.0 g, 12.5 mmol) in DCM (13.5 mL) was added over 20 minutes. The reaction mixture was then stirred for 1 hour at 0˚C, poured into ice water, extracted with DCM, and washed with water. The solvent was removed on a rotary evaporator and the crude solid obtained was dried at 50˚C in a vacuum oven. The final product was purified using vacuum sublimation at 100˚C where a yellow, crystalline solid was collected (yield 2.5 g, 74%). ^{1}H NMR (500 MHz, DMSO-d6, δ): no peaks observed. ^{13}C NMR (500 MHz, DMSO-d6, δ): 183.38, 141.03 Anal. calcd for $C_4Br_2O_2S$ (%)**:** C, 17.67; H, 0.00; O, 11.77; found (%): C, 17.83; H, 0.0; O, 12.51.

Synthesis of 6H-thieno[3,2-b:4,5-b]bis[1,4]benzothiazine (TBBT). Glacial acetic acid (24 mL) was added to a reaction vessel equipped with a reflux condenser and purged with nitrogen for 15 minutes. 2-aminothiophenol (1.0 g, 7.99 mmol) and 3,4-dibromothiophene-2,5-dione (1.09 g, 4.00 mmol) were added, and the mixture was refluxed for 6 hours. The reaction mixture was then cooled to room temperature, filtered, and washed with methanol and acetone. The crude solid was then recrystallized in DMF to give red needles (yield, 0.830 g, 64%). ^{1}H NMR (500 MHz, TFA-d, δ): 7.68 (d, J = 6.4 Hz, 2H), 7.56 (m, 6H). Anal. calcd for $C_{16}H_8N_2S_3$ (%)**:** C, 59.23; H, 2.49; N, 8.63; found (%): C, 59.31; H, 2.16; N, 8.63.

Synthesis of Ladder Poly(thienobenzothiazine) (LTBT). PPA (16.78 g) was added to a reaction flask equipped with a mechanical stirrer and purged with nitrogen at 150˚C overnight. The PPA was cooled to room temperature and 2,5-diamino-1,4-benzenedithiol HCl (1.78 g, 7.17 mmol) was added. Dehydrochlorination was conducted at room temperature for 24 h followed by

70˚C for 24 h. Then, 3,4-dibromothiophene-2,5-dione (1.95 g, 7.17 mmol) dissolved in deoxygenated sulfolane (16.78 g) was added. The polymerization mixture was stirred at 80˚C overnight followed by an incremental temperature increase to 150˚C over 8 hours. The temperature of the polymerization mixture was increased to 180˚C over 4 hours and was stir for 40 hours. The polymer dope was cooled to room temperature, quenched with methanol, and purified under Soxhlet extraction with water for 24 h followed by methanol for 24 h. The crude product was dried and further purified by reprecipitation from MSA into methanol (yield 1.67 g, 95%). Intrinsic viscosity ([η]): 2.0 dL/g (30.0 °C, MSA) Anal. calcd for $C_{10}H_2N_2S_3$ (%)**:** C, 48.76; H, 0.82; N, 11.37; S, 39.05; found (%): C, 48.48; H, 1.28; N, 11.18.

5.3. Results and Discussion

5.3.1. Synthesis and Characterization of LTBT and TBBT.

Scheme 5.1. Synthesis of TBBT and LTBT (HNO_3 = fuming nitric acid, DCM = dichloromethane, AcOH = glacial acetic acid, PPA = polyphosphoric acid (84% free P_2O_5), and PPA/Sulfolane 1:1 w/w).

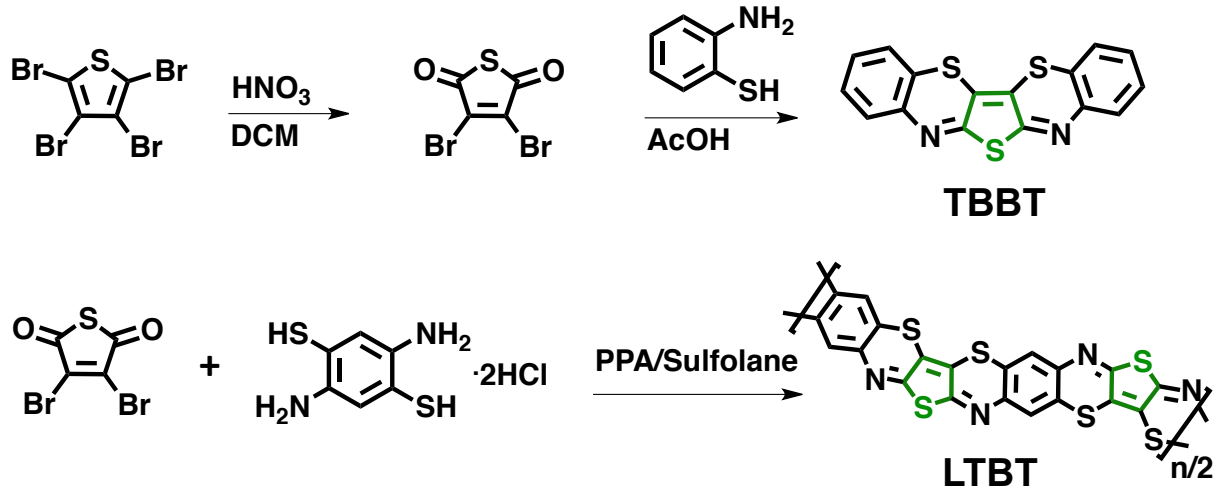

The synthetic routes to the model compound and ladder polymer are shown in Scheme 5.1 and the detailed synthetic procedures are described in the Experimental Methods section. The

2,5-diamino-1,4-benzenedithiol HCl monomer was purchased with 97% purity and purified according to the published procedure before use.[52] The 3,4-dibromothiophene-2,5-dione monomer was synthesized according to a modified procedure[53] where the perbromothiophene starting material is subjected to oxidation with fuming, red nitric acid. The 2,5-aromatic positions are the most reactive towards oxidation and therefore no side products were isolated. Purification by vacuum sublimation at 100˚C produced pure yellow crystals in 74% yield that were characterized by ^{1}H NMR (Figure E.1), ^{13}C NMR (Figure E.2), Fourier-transform infrared (FTIR) spectroscopy (Figure E.3), and elemental analysis (Experimental Methods). The model compound 6H-thieno[3,2-b:4,5-b]bis[1,4]benzothiazine (TBBT) was prepared through condensation of 3,4-dibromothiophene-2,5-dione and 2-aminothiophenol in refluxing acetic acid (Scheme 5.1). The crude product was recrystallized from N,N-dimethylformamide (DMF), which gave red needles in 64% yield. TBBT is completely soluble in trifluoroacetic acid (TFA) and methanesulfonic acid (MSA) at room temperature and partially soluble in polar aprotic solvents such as DMF and dimethyl sulfoxide (DMSO). Solutions of TBBT form thin films when spin-coated from TFA onto glass substrates. However, the thin films became highly opaque when submerged in methanol or water to remove the acidic solvent, which is indicative of its highly crystalline nature. The molecular structure of TBBT was characterized by ^{1}H NMR (Figure E.4) and FTIR spectroscopy (Figure E.5).

The polymer ladder poly(thienobenzothiazine) (LTBT) was prepared through the polycondensation of 2,5-diamino-1,4-benzenedithiol HCl monomer and 3,4-dibromothiophene-2,5-dione monomer in a solvent mixture of polyphosphoric acid (PPA) and sulfolane. Sulfolane was chosen as the co-solvent for several reasons: (1) our previous work on the synthesis of pyrrolobenzothiazine ladder polymers showed that the 2,3-dibromomalemide monomers had

limited solubility in pure acid solvents,[21] (2) the 3,4-dibromothiophene-2,5-dione monomer has excellent solubility in sulfolane, (3) and PPA and sulfolane are miscible and stable at high temperatures (> 180˚C).[52] Sulfolane and PPA were used in a 1:1 w/w ratio whereby 3,4-dibromothiophene-2,5-dione was dissolved in sulfolane prior to addition to the dehydrochlorinated 2,5-diamino-1,4-benzenedithiol in PPA. An immediate color change from pale yellow to red was seen, indicating good reactivity of the monomers in the PPA/sulfolane solvent system. No sublimation or evaporation of the monomers was observed, and a very high polymer yield of 95% indicates excellent incorporation of the monomers into the polymer backbone. We note that the polymerization time was restricted to 40 hours at 180˚C to limit the polymer molecular weight due to solubility issues we observed of higher molecular weight LTBT polymers that were originally synthesized.

LTBT was isolated as a brown solid and forms purple-red solutions in acid. The intrinsic viscosity ([η]) was measured to be 2.0 dL/g at 30.0 °C in MSA. Even with [η] limited to 2.0 dL/g, MSA solutions require high temperatures (~ 140˚C for 24 h) to ensure complete solubilization at concentrations of 7 mg/mL or higher. Solutions of LTBT in MSA can be spin-coated into thin films or drop cast into freestanding films (Figure 5.1a). The detailed fabrication procedures to form the thin films and freestanding films are in the Appendix E. The freestanding films were used to confirm the molecular structure though Fourier-transform infrared (FTIR) and Raman spectroscopies.

The FTIR and Raman spectra of the LTBT freestanding film (Figure 5.1) and the FTIR spectrum of the TBBT needles (Figure E.5) were collected in ambient atmosphere and the peak positions assigned to the vibrational modes listed in Tables E.1 and E.2. The FTIR spectrum of LTBT in Figure 5.1b shows prominent ν(C=C) stretching modes at 1601 cm^{-1}, and at 1589 cm^{-1}

and 1564 cm^{-1} for TBBT (Figure E.5). Aromatic imine ν(C=N) stretches are seen at 1534 cm^{-1} for LTBT (Figure 5.1b), and 1539 cm^{-1} for TBBT (Figure E.5a). At lower wavenumbers, single bond carbon-nitrogen ν(C-N) stretches and carbon-sulfur stretches ν(C-S) can be found at 1226 cm^{-1} and 1150 cm^{-1} for LTBT (Figure 5.1b), and 1238 cm^{-1} and 1150 cm^{-1} for TBBT, respectively (Figure E.5a). The Raman spectra of LTBT in Figure 5.1c show similar features as the FTIR. The carbon-carbon ν(C=C/C-C) stretch (known as the *Я* band, or "effective coordinate")[54–57] is observed at 1462 cm^{-1} (Figure 5.1c). Carbon-nitrogen imine ν(C=N) stretches are seen at 1592 cm^{-1} and 1530 cm^{-1}, (Figure 5.1c), and mixed aromatic thiophene/benzene vibrations can be assigned to the high intensity peak at 1487 cm^{-1}. Mixed aromatic intraring modes are seen at 1268 and 1155 cm^{-1}, and the carbon-sulfur stretches ν(C-S) present as a small peak at 1073 cm^{-1} (Figure 5.1c). The observed FTIR and Raman data collectively provide strong evidence for the backbone fusion and molecular structures of the polymer LTBT and molecule TBBT.

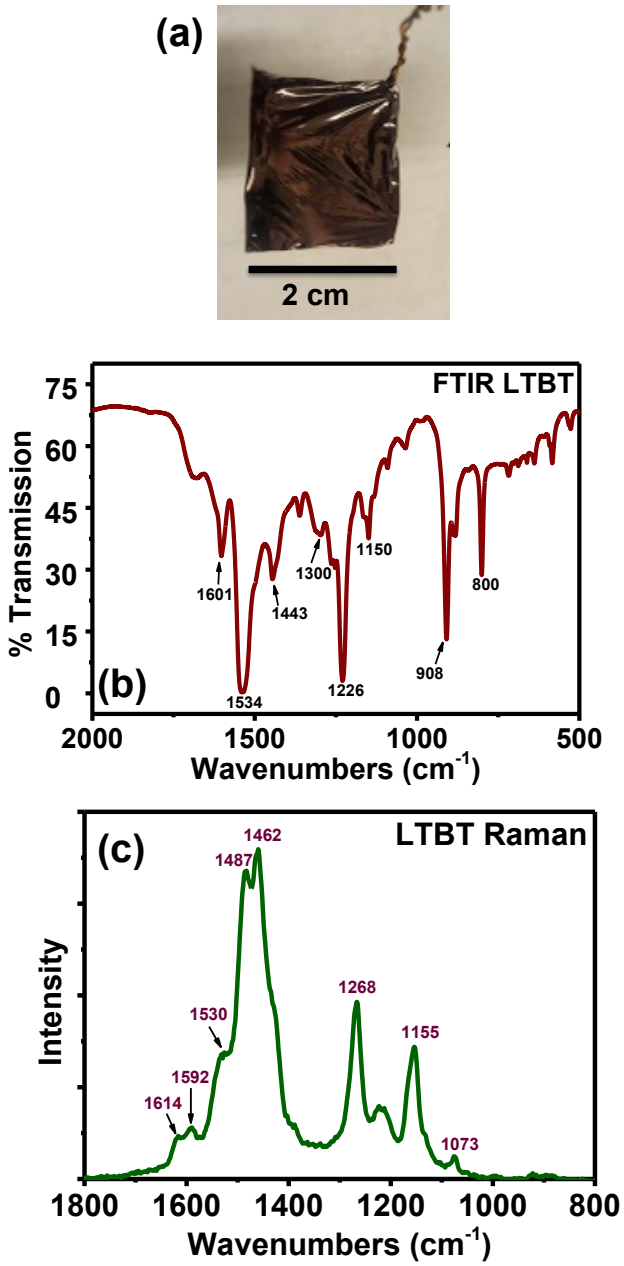

Figure 5.1. (a) LTBT freestanding film with an edge of 2 cm. (b) Fourier-transform infrared (FTIR) spectrum of the LTBT freestanding film and (c) Raman spectrum of the LTBT freestanding film with an excitation laser of 532 nm.

The thermal stabilities of LTBT and TBBT were probed using thermal gravimetric analysis (TGA) and differential scanning calorimetry (DSC), and the spectra are shown in Figure E.6. Both TBBT and LTBT have high thermal stability, showing 5% weight losses at 324˚C and 538˚C, respectively, which is indicative of their fused backbone architecture. Additionally, no phase transitions are seen between 0˚C - 300˚C for TBBT, or between 0˚C - 400˚C for LTBT, which agrees with other literature reports of conjugated ladder polymers having glass transition temperatures (T_g) over 400˚C.[58]

5.3.2. X-ray Crystal Structure of TBBT. Single crystals of TBBT suitable for x-ray structural determinations were grown via diffusion of ethanol into dilute (~ 1 mg/mL) DMF solutions and the experimental details for x-ray crystallography and a table of crystallographic data and atomic coordinates are given in Appendix E (Tables E.3 and E.4). Single-crystal x-ray diffraction analysis of TBBT (Figure 5.2) show that the molecules are aligned in an orthorhombic unit cell with a = 17.198(9) Å, b = 20.222(12) Å, c = 3.782(2) Å. The crystals of TBBT have a planar geometry across the central thiophene and benzothiazine moieties (Figure 5.2a) and form a face-to-face π-π stacking motif with minimal geometric displacement between neighbors in the π-π stacking direction (Figure 5.2b-c). The vertical distance between TBBT molecules is 3.80 Å (Figure 5.2c). We note that the measured π-π stacking distance of TBBT is 0.40 Å greater than that reported for the pyrrole-based small molecule PBBTZ (3.40 Å),[59] which is likely due to Pauli repulsion between adjacent sulfur atoms in the TBBT molecules.[45,46] The van der Waals radii of two sulfur atoms is 3.60 Å,[60] which is the theoretical minimum distance between two π-stacked TBBT molecules. The single-crystal structural data of TBBT demonstrates the crystalline nature of the thienobenzothiazine moiety and confirms the molecular structure.

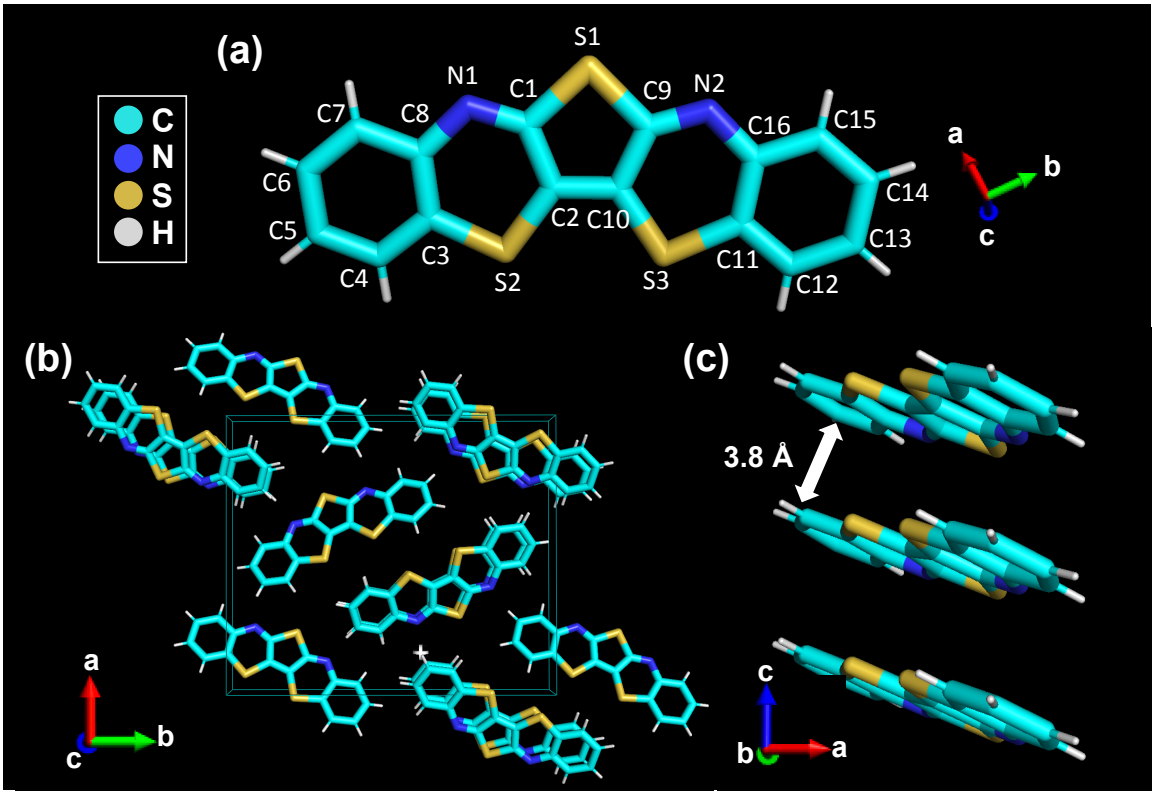

Figure 5.2. (a) Skeletal structure with atoms placed at the center of the thermal ellipsoids that were calculated at the 50% probability level with atom numbering scheme. (b) Organization of the molecules in a single unit cell. (c) Packing of the molecules along the *c*-axis with an intermolecular distance of 3.8 Å.

5.3.3. Theoretical Calculations and Electronic Structure of LTBT and TBBT. We performed density functional theory (DFT) and time-dependent density functional theory (TD-DFT) calculations at the ωB97XD/6-31G(d,p) level of theory to further our understanding of the ground state and excited state molecular geometry and frontier molecular orbital distributions of LTBT and TBBT. The optimized ground state geometry of LTBT is planar (Figure 5.3a) with HOMO and LUMO molecular orbitals delocalized across the backbone. In order to gain insight into the effects of protonation, calculations were performed on imine-protonated oligomers bearing a +1 charge (Figure 5.3b). We note that it is energetically favorable to protonate imine

nitrogens over sulfur moieties.[61] The ground state geometry of LTBT remains planar upon protonation (Figure 5.3b), possibly due to the S-H non-covalent interaction created upon protonation. The calculated distance between the imine hydrogen and thiophene sulfur is 2.83 Å, which is less than the sum of their van der Waals radii (S+H = 2.89 Å),[60] which means that S-H interaction likely contributes to the observed planarity of the protonated polymer chain. Inducing non-covalent interactions is a widely exploited strategy used to reduced the conformational distortions in many π-conjugated polymers, such as those containing diketopyrroles,[62,63] functionalized thiophenes,[64] and pyrazines. The pictoral representation of the HOMO and LUMO orbital distributions of the protonated oligomer bearing a +1 charge is shown in Figure 5.3b; clearly, protonation induces strong spatial localization of the molecular orbitals, suggesting that LTBT will have strong protonation-enhanced ICT character in acidic solvents. [65] TBBT also has a planar ground-state geometry and delocalized HOMO and LUMO orbital distributions as shown in Figure E.7.

The TD-DFT calculated excited-state geometry, optical absorption spectrum, and the corresponding pictorial representations of the molecular orbitals associated with the lowest-energy transition for LTBT is shown in Figure E.8. The excited state geometry is coplanar with delocalized HOMO and LUMO energy levels distributed across the ladder backbone, and the π-π* transition is centered at 1170 nm, which indicates this polymer may have a narrow optical bandgap.

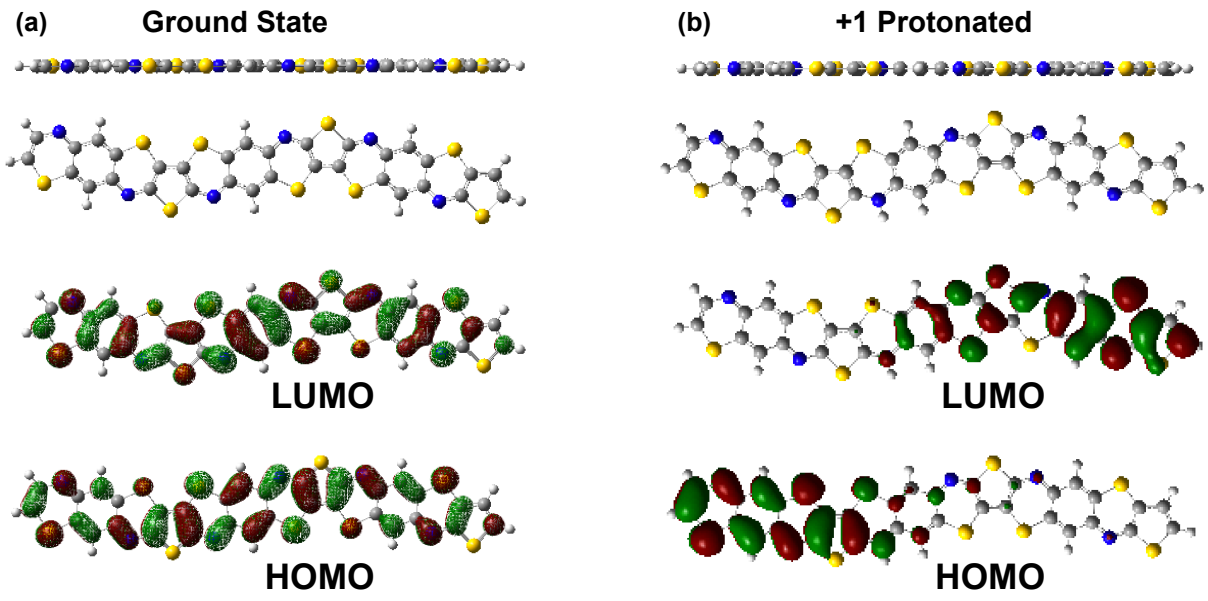

Figure 5.3. DFT calculated optimized ground-state geometry and the pictoral representation of the frontier molecular orbital distributions of (a) the neutral oligomer and (b) the protonated (+1) oligomer. Calculations performed at the ωB97XD/6-31G(d,p) level of theory.

The reorganizational energy (λ) of LTBT was calculated from the sum of relaxation energies in the neutral and cationic state to gain insight into the energy associated with geometry changes upon with charge injection.[66,67] Figure E.9 shows the cationic geometry and the polaron orbital distribution of the oligomer. A fairly large reorganizational energy of 1.39 eV was calculated for LTBT, which could suggest that LTBT undergoes geometry changes upon charge injection and may not have a rigid-rod chain topology like BBL.[68,69] Note that calculated λ values decrease with polymer chain length and more accurate reorganizational energy calculations require more than 12 repeat units.[67]

We further investigated the electronic structures of LTBT and TBBT by using cyclic voltammetry (CV) measurements. The HOMO and LUMO energy levels of TBBT and LTBT are summarized in Table 5.1, and the oxidation waves of LTBT thin films coated on platinum wires

and of TBBT needles dissolved in acetonitrile at 10^{-5} M in 0.1 M tetrabutylammonium hexafluorophosphate (Bu_4NPF_6) with $Ag/AgNO_3$ as the reference electrode are shown in Figure 5.4a-b. The reduction waves are shown in Figure E.10. LTBT shows two quasi-reversible oxidation waves at 1.29 V and 1.85 V (Figure 5.4a), and one non-reversible reduction wave (Figure E.10a) at -0.87 V. The onset oxidation potential of 0.90 V and onset reduction potential of -0.59 V were used to estimate the HOMO and LUMO energy levels of -5.17 eV and -3.75 eV, respectively (Table 5.1). The model compound TBBT shows two non-reversible oxidation waves, which are centered at 1.45 V and 1.85 V (Figure 5.4b), and one non-reversible reduction wave at -1.22 V (Figure E.10b). The TBBT onset oxidation and reduction potentials of 1.48 V and -0.66 V, respectively, were used to measure the HOMO / LUMO energy levels of -6.37 eV / -3.59 eV, which are similar those of the polymer LTBT (Table 5.1). The electrochemical bandgaps ($E_g^{elec.}$) are 1.42 eV and 2.78 eV for LTBT and TBBT, respectively (Table 5.1).

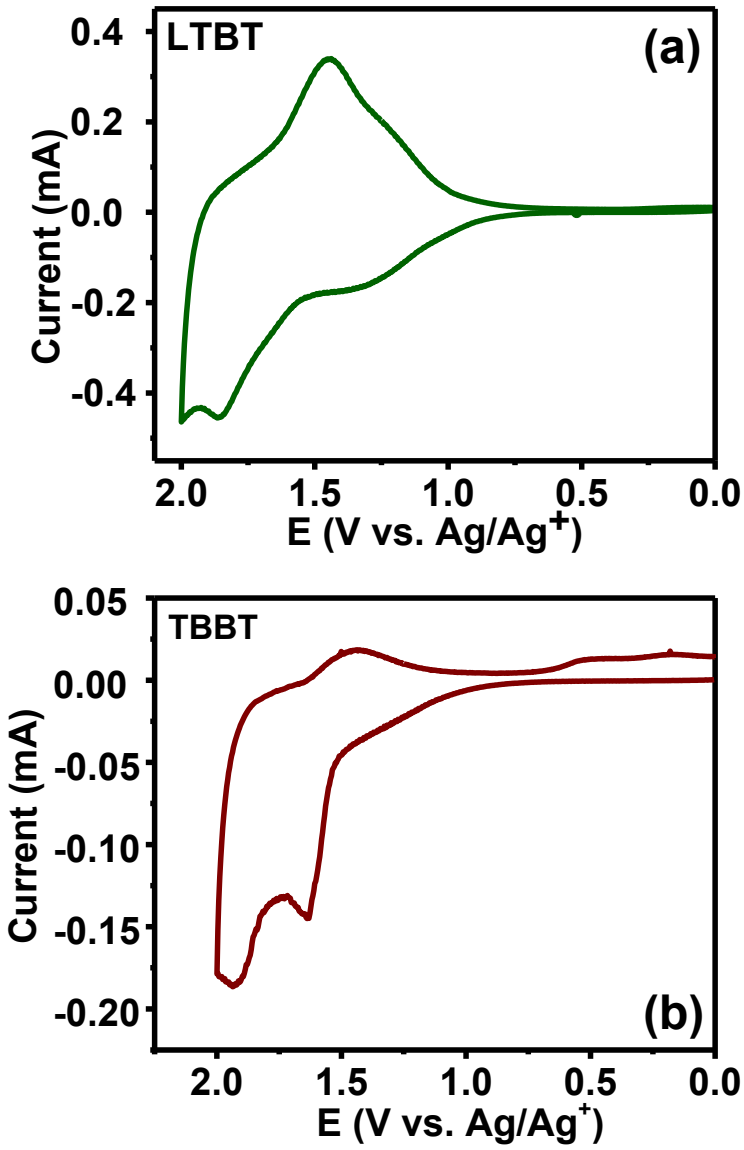

Figure 5.4. Cyclic voltammograms measured in 0.1 M Bu_4NPF_6 electrolyte solution using $Ag/AgNO_3$ as the reference electrode of the oxidation processes of (a) LTBT thin films coated on platinum wires, and (b) TBBT needles in solution. The scan rate was 100 mV/s.

Table 5.1. Electronic Structure Parameters and Optical Properties of LTBT and TBBT.

Compound	HOMO (eV)	LUMO (eV)	$E_g^{elec.}$ (eV)	$\lambda_{max}^{(a)}$ (nm)	$\varepsilon_{max}^{(a)}$ ($M^{-1}cm^{-1}$)	$\lambda_{max}^{(b)}$ (nm)	$\alpha_{max}^{(b)}$ (cm^{-1})	$E_g^{opt.(b)}$ (eV)	$\lambda_{max}^{(c)}$ (nm)
LTBT	-5.17	-3.75	1.42	1151	2.4×10^4	825	9.9×10^4	1.28	1192
TBBT	-6.37	-3.59	2.78	693	1.9×10^4	525	4.4×10^4	2.05	---

[(a)] Solution in MSA. [(b)] Thin film on glass. [(c)] Solution in TfOH.

5.3.4. Optical Properties of LTBT and TBBT. The optical absorption spectra of LTBT and TBBT in MSA solution and in thin film are shown in Figures 5.5 and the lowest energy peak positions (λ_{max}), optical band gap ($E_g^{opt.}$), molar absorptivity (ε_{max}), and absorption coefficient (α_{max}) are summarized in Table 5.1. The MSA-solution optical absorption spectrum of TBBT (Figure 5.5a) shows peaks in the 300 nm – 700 nm region with the π-π* transition assigned to the peak at 455 nm (ε_{max} = 1.5 x 10^4 M^{-1} cm^{-1}) and a lowest energy peak at 693 nm (ε_{max} = 1.9 x 10^4 M^{-1} cm^{-1}) which can be attributed to protonation-enhanced intramolecular charge transfer (ICT), a phenomenon which is seen in many imine-bearing π-conjugated systems.[70] For LTBT, the MSA-solution absorption spectrum (Figure 5.5a) shows three high-energy bands at 302 nm (ε_{max} = 1.6 x 10^4 M^{-1} cm^{-1}), 362 nm (ε_{max} = 1.2 x 10^4 M^{-1} cm^{-1}), and 532 nm (ε_{max} = 1.2 x 10^4 M^{-1} cm^{-1}), of which the latter can be assigned to the π-π* transition. The intense lowest-energy band at 1151 nm (ε_{max} = 2.4 x 10^4 M^{-1} cm^{-1}) originates from protonation-enhanced intramolecular charge transfer. The effects of protonation on the ICT band are corroborated by the previously discussed DFT calculations (Figure 5.3b) whereby protonation induces spatial localization of the HOMO and LUMO molecular orbitals that correspond to the observed ICT character in MSA solution (Figure 5.3b).

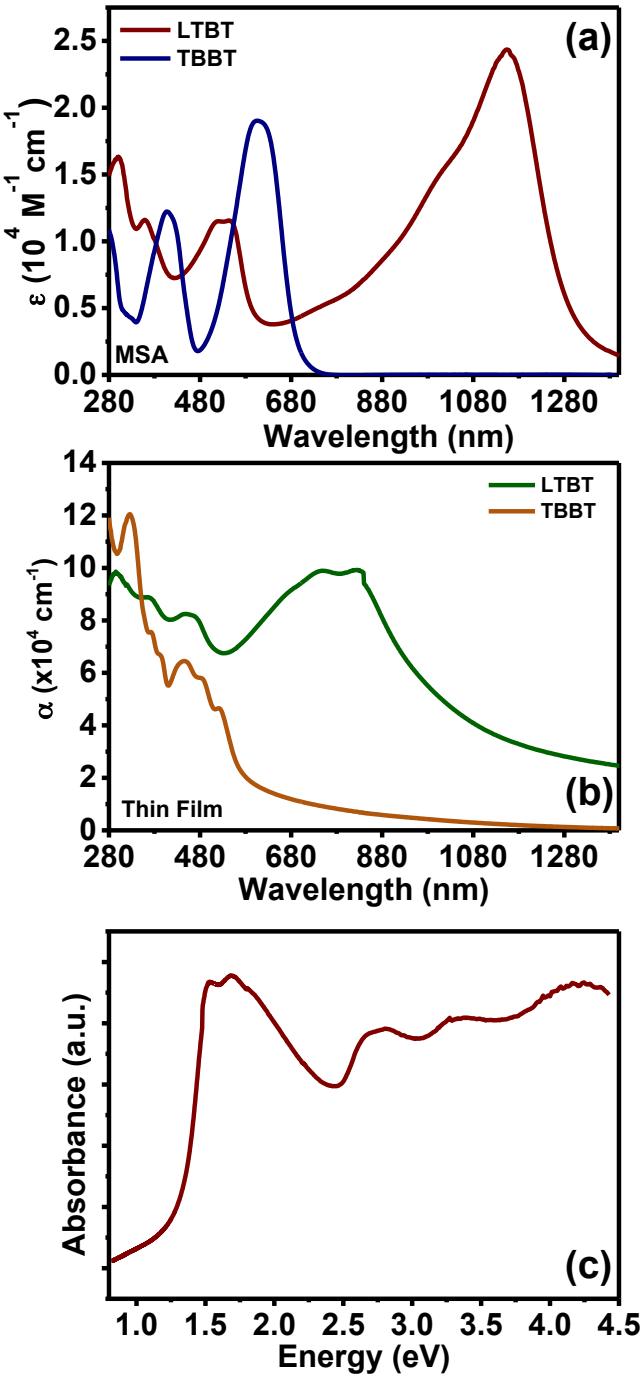

Figure 5.5. Optical absorption spectra of TBBT and LTBT in (a) dilute MSA solution (10^{-5} M), and (b) as thin films on glass substrates. (c) The thin film absorption spectrum of LTBT plotted vs. electron volts to determine the optical bandgap.

The thin-film absorption spectrum of TBBT (Figure 5.5b) has multiple peaks in the 300 – 525 nm region, and the lowest-energy peak (π-π* transition) is centered at 525 nm (α_{max} = 4.4 x10^4 cm^{-1}). The optical bandgap calculated from the onset of absorption in Figure E.11 is 2.05 eV, which is 0.73 eV smaller than the electrochemical bandgap ($E_g^{elec.}$) of 2.78 eV, which suggests that TBBT may have a large effective exciton binding energy (E_b).[71–73] Compared to the thin film absorption spectra, in MSA solutions the lowest energy peak is red-shifted by 168 nm (Table 5.1), which demonstrates that the ICT character of TBBT is enhanced by protonation.

The thin-film absorption spectrum of LTBT (Figure 5.5b) shows peaks between 300 nm – 900 nm with the π-π* peak centered at 825 nm (α_{max} = 9.9 x10^4 cm^{-1}). The optical bandgap ($E_g^{opt.}$) measured from the onset of the thin film absorption is 1.28 eV (Figure 5.5c), which is 0.14 eV smaller than the $E_g^{elec.}$ of 1.42 eV, indicating a reduced E_b of 0.14 eV compared to model compound (Table 5.1). In contrast to the optical absorption spectrum in MSA, the thin film absorption spectrum is markedly different. In particular, the MSA solution absorption spectrum with the lowest-energy absorption peak at 1151 nm is red-shifted by 326 nm from that of the thin film (λ_{max} = 825 nm). This large 326-nm difference in lowest energy peak positions confirms protonation enhancement of the ICT character as previously discussed.

In order to gauge the polymer chain topology in protic acid solutions, variable-temperature optical absorption spectra were collected in both MSA and triflic acid solutions ranging from 20˚C – 100˚C (Figure E.12). In the MSA solution absorption spectrum, increasing the temperature is associated with the ICT band blue shifting from 1151 nm to 1107 nm accompanied by decreasing molar absorptivity and vibronic structures (Figure E.12a). In contrast to the MSA solution, the variable-temperature absorption spectrum in triflic acid does not show any changes of the λ_{max} (Figure E.12b). The observed thermochromism in MSA solution means

that the polymer chain topology is semi-flexible when partially protonated in weaker acids like MSA (pKa ~ -2).[74] However, when fully protonated in triflic acid (pKa ~ -14) the LTBT polymer chain is more rigid. Clearly, LTBT is not a rigid-rod polymer unlike the ladder polymer BBL that shows no thermochromism in MSA solutions in the same temperature range.[21]

5.3.6 Electrical Conductivity of Doped LTBT Thin Films. We used ferric chloride ($FeCl_3$) as a p-type dopant to study the electrical conductivity of doped LTBT thin films, since it has been demonstrated to have a low electron affinity (EA ~ 5.5 eV)[20] and capable of effectively oxidizing various p-type conjugated polymers.[20,75-80] Detailed doping procedure is described in the Experimental Method section whereby solution-sequential processing was used to dope LTBT thin films. This strategy has been showed to be a highly effective technique to produce highly conducting polymer films by means of fine-tuning dopant diffusion into the polymer film without compromising film quality, creating large dopant aggregates, or disrupting the polymer crystal structures.[81-85] In short, the dopant solution (20 mM $FeCl_3$ in acetonitrile) was deposited onto the neat LTBT thin films followed by a 90-second delay before spinning off the excess solution. The doped polymer films were then thermally annealed at various temperatures prior to characterizing the room-temperature dc-electrical conductivity (σ_{dc}) via colinear four-point probe technique in ambient environment. The numerical values of σ_{dc} as a function of annealing temperatures and its room-temperature stability are summarized in Table 5.2.

Upon deposition of $FeCl_3$, the forest-green colored undoped LTBT films turned brown indicating successful doping reactions and the formation of polaronic charge carriers. However, the brown-colored doped films quickly turned to green-colored films within seconds of exposing to air indicating rapid de-doping and quenching of polarons/bipolarons due to side reactions with either oxygen or moisture.[86]

Table 5.2. Dc-Electrical Conductivity (σ_{dc}) of $FeCl_3$-Doped LTBT Thin Films as a Function of Annealing Temperature and Storage Duration.

Variable	Condition	$\sigma_{dc,\ average}$ (S/cm)[(a)]
Annealing Temperature	80°C – 10 min	$(1.06 \pm 0.26) \times 10^{-1}$
	100°C – 10 min	$(3.31 \pm 0.31) \times 10^{-1}$
	120°C – 10 min	$(2.67 \pm 1.07) \times 10^{-1}$
	140°C – 10 min	$(1.35 \pm 0.99) \times 10^{-1}$
Stability	Day 0	$(3.31 \pm 0.31) \times 10^{-1}$
	Day 1	$(4.48 \pm 0.78) \times 10^{-2}$
	Day 2	$(1.26 \pm 0.53) \times 10^{-3}$
	Day 3	$(1.13 \pm 0.57) \times 10^{-3}$
	Day 4	$(7.11 \pm 4.37) \times 10^{-4}$

[(a)]Average values are obtained from three different samples.

Undoped LTBT films were insulating with extremely high resistance ($>>10^6$ Ω). Upon doping with $FeCl_3$ and annealed at 100°C for 10 min, LTBT films exhibited an average σ_{dc} of $(3.31 \pm 0.31) \times 10^{-1}$ S/cm (Table 5.2) where a maximum value of 3.78×10^{-1} S/cm was observed. Higher annealing temperatures resulted in a rapid decrease in electrical conductivity (Figure 5.6a). We note that the σ_{dc} of doped LTBT films are rather modest compared to state-of-the-art p-type conducting polymers considering that the thermodynamic requirements for efficient doping are sufficiently achieved ($HOMO_{LTBT} < LUMO_{FeCl3}$). Atomic force microscopy (AFM) imaging showed that the surfaces of LTBT neat films were rather rough with large aggregates (RMS roughness ~ 5 – 7 nm), especially when probed over large dimensions (1 – 2 μm) (Figure E.13). Such suboptimal surface morphology could hinder diffusion of $FeCl_3$ molecules into the polymer films; thus, limiting the electrical conductivity. Furthermore, the rapid de-doping in ambient conditions partly contributed to the low σ_{dc} of doped LTBT films. As a result of the observed air instability of LTBT doped film, we monitored the room-temperature electrical conductivity over

several days. The σ_{dc} values decreased by over two orders of magnitude within the first two days before leveling off at around 10^{-3} S/cm. Despite its relatively poor ambient stability, LTBT still showed at least several orders of magnitude enhancement of conductivity upon doping; thus, suggesting its potential for future device applications.

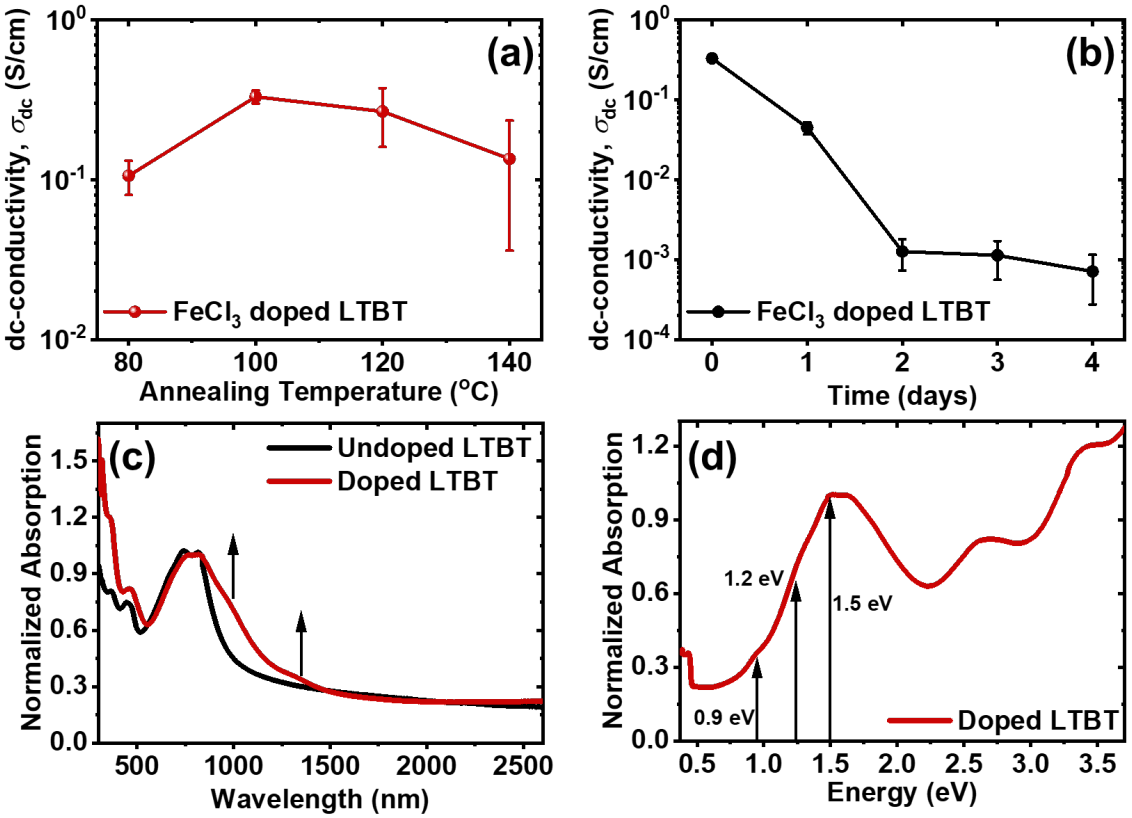

Figure 5.6. (a) Dc-electrical conductivity (σ_{dc}) of $FeCl_3$ doped LTBT thin films at various annealing temperatures; (b) Stability of electrical conductivity of LTBT doped films in ambient air; (c) Thin film optical absorption spectra of undoped and $FeCl_3$ doped LTBT thin films; (d) Optical absorption spectra of LTBT doped films in energy space.

UV-Vis-NIR optical absorption spectra were used to further confirm the formation of polaronic species and rationalize the modest electrical conductivity of $FeCl_3$ doped LTBT films. Upon doping, the vibronic features of the π-π* transition band were diminished accompanied by two new broad absorption bands centered at around 1000 nm (1.2 eV) and 1345 nm (0.9 eV)

(Figures 5.6c and 5.6d) indicating the generation of polaronic charge carriers. However, the lack of absorption extending to further NIR region (> 1500 nm) suggests that charge carriers in $FeCl_3$ doped LTBT are rather localized,[20] which further explains the observed modest electrical conductivity.

5.4. Conclusions

In this study, we report the synthesis and detailed characterization of the electronic structure, optical properties, electrical conductivity and thin film morphology of the new p-type ladder polymer ladder poly(thienobenzothiazine) (LTBT). The single-crystal structure of the model compound thienobis(benzothiazine) (TBBT) was also reported. LTBT has excellent film-forming properties as evidenced by the large area freestanding films, and a combination of DFT calculations and optical absorption measurements revealed that LTBT has a strong donor-acceptor character that enabled a narrow optical bandgap of 1.28 eV. Moreover, protonation-enhanced intramolecular charge transfer (ICT) character was observed in the infrared region in MSA-solution absorption spectra, evidenced by a 326-nm red shift of the lowest energy peak compared to the thin film absorption spectrum.

The average electrical conductivity was measured to be $(3.31 \pm 0.31) \times 10^{-1}$ S/cm when p-doped with $FeCl_3$. The modest p-doped electrical conductivity of LTBT is attributed to the combination poor air stability of the doped polymer films and the rough film surface that was seen in the AMF images. The results presented demonstrate the potential of the new thiophene-based p-type polymer LTBT in organic electronics and provide important insights into the structure-property relationships of semiconducting ladder polymers.

5.5. References

1. Dou, L.; Liu, Y.; Hong, Z.; Li, G.; Yang, Y. Low-Bandgap Near-IR Conjugated Polymers/Molecules for Organic Electronics. *Chem. Rev.* **2015**, *115* (23), 12633–12665. DOI: 10.1021/acs.chemrev.5b00165.

2. Scharber, M. C.; Sariciftci, N. S. Low Band Gap Conjugated Semiconducting Polymers. *Adv. Mater. Tech.s* **2021**, *6* (4), 2000857. DOI: 10.1002/admt.202000857.

3. Kawabata, K.; Saito, M.; Osaka, I.; Takimiya, K. Very Small Bandgap π-Conjugated Polymers with Extended Thienoquinoids. *J. Am. Chem. Soc.* **2016**, *138* (24), 7725–7732. DOI: 10.1021/jacs.6b03688.

4. Mikie, T.; Osaka, I. Small-Bandgap Quinoid-Based π-Conjugated Polymers. *J. Mater. Chem. C* **2020**, *8* (41), 14262–14288. DOI: 10.1039/D0TC01041C.

5. Jenekhe, S. A.; Yi, S. Efficient Photovoltaic Cells from Semiconducting Polymer Heterojunctions. *Appl. Phys. Lett.* **2000**, *77* (17), 2635–2637. DOI: 10.1063/1.1320022.

6. Bundgaard, E.; Krebs, F. C. Low Band Gap Polymers for Organic Photovoltaics. *Sol. Energy Mater. Sol. Cells* **2007**, *91* (11), 954–985. DOI: 10.1016/j.solmat.2007.01.015.

7. Chochos, C. L.; Choulis, S. A. How the Structural Deviations on the Backbone of Conjugated Polymers Influence Their Optoelectronic Properties and Photovoltaic Performance. *Prog. Polym. Sci.* **2011**, *36* (10), 1326–1414. DOI: 10.1016/j.progpolymsci.2011.04.003.

8. Li, Y.; Xu, G.; Cui, C.; Li, Y. Flexible and Semitransparent Organic Solar Cells. *Adv. Energy Mater.* **2018**, *8* (7), 1701791. DOI: 10.1002/aenm.201701791.

9. Shrotriya, V.; Wu, E. H.-E.; Li, G.; Yao, Y.; Yang, Y. Efficient Light Harvesting in Multiple-Device Stacked Structure for Polymer Solar Cells. *Appl. Phys. Lett.* **2006**, *88* (6), 064104. DOI: 10.1063/1.2172741.

10. Chueh, C.-C.; Chien, S.-C.; Yip, H.-L.; Salinas, J. F.; Li, C.-Z.; Chen, K.-S.; Chen, F.-C.; Chen, W.-C.; Jen, A. K.-Y. Toward High-Performance Semi-Transparent Polymer Solar Cells: Optimization of Ultra-Thin Light Absorbing Layer and Transparent Cathode Architecture. *Adv. Energy Mater.* **2013**, *3* (4), 417–423. DOI: 10.1002/aenm.201200679.

11. Vella, J. H.; Huang, L.; Eedugurala, N.; Mayer, K. S.; Ng, T. N.; Azoulay, J. D. Broadband Infrared Photodetection Using a Narrow Bandgap Conjugated Polymer. *Sci. Adv.* **2021**, *7* (24), eabg2418. DOI: 10.1126/sciadv.abg2418.

12. Lim, D.-H.; Ha, J.-W.; Choi, H.; Cheol Yoon, S.; Ram Lee, B.; Ko, S.-J. Recent Progress of Ultra-Narrow-Bandgap Polymer Donors for NIR-Absorbing Organic Solar Cells. *Nanoscale Adv.* **2021**, *3* (15), 4306–4320. DOI: 10.1039/D1NA00245G.

13. Salzner, U.; Lagowski, J. B.; Pickup, P. G.; Poirier, R. A. Comparison of Geometries and Electronic Structures of Polyacetylene, Polyborole, Polycyclopentadiene, Polypyrrole,

Polyfuran, Polysilole, Polyphosphole, Polythiophene, Polyselenophene and Polytellurophene. *Synth. Met.* **1998**, *96* (3), 177–189. DOI: 10.1016/S0379-6779(98)00084-8.

14. Gierschner, J.; Cornil, J.; Egelhaaf, H.-J. Optical Bandgaps of π-Conjugated Organic Materials at the Polymer Limit: Experiment and Theory. *Adv. Mater.* **2007**, *19* (2), 173–191. DOI: 10.1002/adma.200600277.

15. Tran, D. K.; West, S. M.; Guo, J.; Chen, S. E.; Ginger, D. S.; Jenekhe, S. A. Chain Length Dependence of Electron Transport in an N-Type Conjugated Polymer with a Rigid-Rod Chain Topology. *J. Am. Chem. Soc.* **2024**, *146* (2), 1435-1446. DOI: 10.1021/jacs.3c10650.

16. Wu, H.-Y.; Yang, C.-Y.; Li, Q.; Kolhe, N. B.; Strakosas, X.; Stoeckel, M.-A.; Wu, Z.; Jin, W.; Savvakis, M.; Kroon, R.; Tu, D.; Woo, H. Y.; Berggren, M.; Jenekhe, S. A.; Fabiano, S. Influence of Molecular Weight on the Organic Electrochemical Transistor Performance of Ladder-Type Conjugated Polymers. *Adv. Mater.* **2022**, *34* (4), 2106235. DOI: 10.1002/adma.202106235.

17. Teo, Y. C.; Lai, H. W. H.; Xia, Y. Synthesis of Ladder Polymers: Developments, Challenges, and Opportunities. *Eur. J. Chem.* **2017**, *23* (57), 14101–14112. DOI: 10.1002/chem.201702219.

18. Lee, J.; Kalin, A. J.; Yuan, T.; Al-Hashimi, M.; Fang, L. Fully Conjugated Ladder Polymers. *Chem. Sci.* **2017**, *8* (4), 2503–2521. DOI: 10.1039/c7sc00154a.

19. Cao, Z.; Leng, M.; Cao, Y.; Gu, X.; Fang, L. How Rigid Are Conjugated Non-Ladder and Ladder Polymers? *J. Polym. Sci.* **2022**, *60* (3), 298. DOI: 10.1002/pol.20210550.

20. Tam, T. L. D.; Lin, M.; Chien, S. W.; Xu, J. Facile Synthesis of Solubilizing a Group-Free, Solution-Processable p-Type Ladder Conjugated Polymer and Its Thermoelectric Properties. *ACS Macro. Lett.* **2022**, *11* (1), 110–115. DOI: 10.1021/acsmacrolett.1c00696.

21. West, S. M.; Tran, D. K.; Guo, J.; Chen, S. E.; Ginger, D. S.; Jenekhe, S. A. P-Type Semiconducting Ladder Poly(Pyrrolobenzothiazine)s: Effects of N-Alkyl Side Chains on the Chain Conformation, Electronic Structure, and Charge Transport Properties. *Macromolecules* **2023**, *56* (24), 10222–10235. DOI: 10.1021/acs.macromol.3c01561.

22. Kaloni, T. P.; Giesbrecht, P. K.; Schreckenbach, G.; Freund, M. S. Polythiophene: From Fundamental Perspectives to Applications. *Chem. Mater.* **2017**, *29* (24), 10248–10283. DOI: 10.1021/acs.chemmater.7b03035.

23. Ferraris, J. P.; Andrus, R. G.; Hrncir, D. C. Steric Effects on the Optical and Electrochemical Properties of N-Substituted Pyrrole–Thiophene Monomers and Polymers. *J. Chem. Soc., Chem. Commun.* **1989**, No. 18, 1318–1320. DOI: 10.1039/C39890001318.

24. Zhang, S.; Ocheje, M. U.; Huang, L.; Galuska, L.; Cao, Z.; Luo, S.; Cheng, Y.-H.; Ehlenberg, D.; Goodman, R. B.; Zhou, D.; Liu, Y.; Chiu, Y.-C.; Azoulay, J. D.; Rondeau-

Gagné, S.; Gu, X. The Critical Role of Electron-Donating Thiophene Groups on the Mechanical and Thermal Properties of Donor–Acceptor Semiconducting Polymers. *Adv. Electron. Mater.* **2019**, *5* (5), 1800899. DOI: 10.1002/aelm.201800899.

25. Pathiranage, T. M. S. K.; Dissanayake, D. S.; Niermann, C. N.; Ren, Y.; Biewer, M. C.; Stefan, M. C. Role of Polythiophenes as Electroactive Materials. *J. Polym. Sci. A: Polym. Chem.* **2017**, *55* (20), 3327–3346. DOI: 10.1002/pola.28726.

26. Hong, S. Y.; Marynick, D. S. Understanding the Conformational Stability and Electronic Structures of Modified Polymers Based on Polythiophene. *Macromolecules* **1992**, *25* (18), 4652–4657. DOI: 10.1021/ma00044a029.

27. Sugimoto, R.; Takeda, S.; Gu, H. B.; Yoshino, K. Preparation of Soluble Polythiophene Derivatives Utilizing Transition Metal Halides as Catalysts and Their Property. *Chem. Express* **1986**, *1*, 635–638.

28. Jen, K.-Y.; G. Miller, G.; L. Elsenbaumer, R. Highly Conducting, Soluble, and Environmentally-Stable Poly(3-Alkylthiophenes). *J. Chem. Soc., Chem. Commun.* **1986**, (17), 1346–1347. DOI: 10.1039/C39860001346.

29. Cinar, M. E.; Ozturk, T. Thienothiophenes, Dithienothiophenes, and Thienoacenes: Syntheses, Oligomers, Polymers, and Properties. *Chem. Rev.* **2015**, *115* (9), 3036–3140. DOI: 10.1021/cr500271a.

30. Chan, H. S. O.; Ng, S. C. Synthesis, Characterization and Applications of Thiophene-Based Functional Polymers. *Prog. Polym. Sci.* **1998**, *23* (7), 1167–1231. DOI: 10.1016/S0079-6700(97)00032-4.

31. Mehmood, U.; Al-Ahmed, A.; Hussein, I. A. Review on Recent Advances in Polythiophene Based Photovoltaic Devices. *Renewable and Sustainable Energy Rev.* **2016**, *57*, 550–561. DOI: 10.1016/j.rser.2015.12.177.

32. K, N.; Rout, C. S. Conducting Polymers: A Comprehensive Review on Recent Advances in Synthesis, Properties and Applications. *RSC Adv.* **2021**, *11* (10), 5659–5697. DOI: 10.1039/D0RA07800J.

33. Vallan, L.; Istif, E.; Gómez, I. J.; Alegret, N.; Mantione, D. Thiophene-Based Trimers and Their Bioapplications: An Overview. *Polymers* **2021**, *13* (12), 1977. DOI: 10.3390/polym13121977.

34. Turkoglu, G.; Cinar, M. E.; Ozturk, T. Thiophene-Based Organic Semiconductors. In Jiang, X. (eds) *Sulfur Chemistry*. Topics in Current Chemistry Collections; Springer International Publishing. **2019**, 79–123. DOI: 10.1007/978-3-030-25598-5_3.

35. Fichou, D. Handbook of Oligo- and Polythiophenes. In *Handbook of Oligo- and Polythiophenes*; John Wiley & Sons, Ltd, **1998**. DOI: 10.1002/9783527611713.fmatter.

36. Barbarella, G.; Zangoli, M.; Di Maria, F. Chapter Three - Synthesis and Applications of Thiophene Derivatives as Organic Materials. In Scriven, E. F. V. (eds) *Adv. Heterocycl. Chem.* Academic Press, **2017**, 123, 105–167. DOI: 10.1016/bs.aihch.2017.01.001.

37. Jin, K.; Xiao, Z.; Ding, L. D18, an Eximious Solar Polymer! *J. Semicond.* **2021**, *42* (1), 010502. DOI: 10.1088/1674-4926/42/1/010502.

38. Li, Y.; Huang, W.; Zhao, D.; Wang, L.; Jiao, Z.; Huang, Q.; Wang, P.; Sun, M.; Yuan, G. Recent Progress in Organic Solar Cells: A Review on Materials from Acceptor to Donor. *Molecules* **2022**, *27* (6), 1800. DOI: 0.3390/molecules27061800.

39. Liu, F.; Jiang, Y.; Xu, R.; Su, W.; Wang, S.; Zhang, Y.; Liu, K.; Xu, S.; Zhang, W.; Yi, Y.; Ma, W.; Zhu, X. Nonfullerene Acceptor Featuring Unique Self-Regulation Effect for Organic Solar Cells with 19 % Efficiency. *Angew. Chem.* **2024**, *136* (3), e202313791. DOI: 10.1002/ange.202313791.

40. Li, C.; Zhou, J.; Song, J.; Xu, J.; Zhang, H.; Zhang, X.; Guo, J.; Zhu, L.; Wei, D.; Han, G.; Min, J.; Zhang, Y.; Xie, Z.; Yi, Y.; Yan, H.; Gao, F.; Liu, F.; Sun, Y. Non-Fullerene Acceptors with Branched Side Chains and Improved Molecular Packing to Exceed 18% Efficiency in Organic Solar Cells. *Nat. Energy* **2021**, *6* (6), 605–613. DOI: 10.1038/s41560-021-00820-x.

41. Tang, X.; Chen, Y.; Liao, H.; Zheng, T.; Weng, C.; Zhang, X.; Shen, P. Improving the Photovoltaic Performance of PBDB-T:PC71BM-Based Ternary Solar Cells by Employing Arylmethylene-Substituted Small Molecules as the Guest Acceptor. *ACS Appl. Energy Mater.* **2024**. DOI: 10.1021/acsaem.3c03094.

42. Zheng, Z.; Wang, J.; Bi, P.; Ren, J.; Wang, Y.; Yang, Y.; Liu, X.; Zhang, S.; Hou, J. Tandem Organic Solar Cell with 20.2% Efficiency. *Joule* **2022**, *6* (1), 171–184. DOI: 10.1016/j.joule.2021.12.017.

43. Minemawari, H.; Yamada, T.; Matsui, H.; Tsutsumi, J.; Haas, S.; Chiba, R.; Kumai, R.; Hasegawa, T. Inkjet Printing of Single-Crystal Films. *Nature* **2011**, *475* (7356), 364–367. DOI: 10.1038/nature10313.

44. Izawa, T.; Miyazaki, E.; Takimiya, K. Molecular Ordering of High-Performance Soluble Molecular Semiconductors and Re-Evaluation of Their Field-Effect Transistor Characteristics. *Adv. Mater.* **2008**, *20* (18), 3388–3392. DOI: 10.1002/adma.200800799.

45. Liu, B.; Rocca, D.; Yan, H.; Pan, D. Beyond Conformational Control: Effects of Noncovalent Interactions on Molecular Electronic Properties of Conjugated Polymers. *JACS Au* **2021**, *1* (12), 2182–2187. DOI: 10.1021/jacsau.1c00284.

46. Huang, H.; Yang, L.; Facchetti, A.; Marks, T. J. Organic and Polymeric Semiconductors Enhanced by Noncovalent Conformational Locks. *Chem. Rev.* **2017**, *117* (15), 10291–10318. DOI: 10.1021/acs.chemrev.7b00084.

47. Zhang, W.; Liu, Y.; Yu, G. Heteroatom Substituted Organic/Polymeric Semiconductors and Their Applications in Field-Effect Transistors. *Adv. Mater.* **2014**, *26* (40), 6898–6904. DOI: 10.1002/adma.201305297.

48. Mintmire, J. W.; White, C. T.; Elert, M. L. Conformation and Electronic Structure of Heterocyclic Ring Chain Polymers. *Synth. Met.* **1988**, *25* (2), 109–119. DOI: 10.1016/0379-6779(88)90347-5.

49. Tang, C. G.; Hou, K.; Leong, W. L. The Quest for Air Stability in Organic Semiconductors. *Chem. Mater.* **2024**, *36* (1), 28-53. DOI: 10.1021/acs.chemmater.3c02093.

50. Yin, Y.; Zhang, S.; Chen, D.; Guo, F.; Yu, G.; Zhao, L.; Zhang, Y. Synthesis of an Indacenodithiophene-Based Fully Conjugated Ladder Polymer and Its Optical and Electronic Properties. *Polym. Chem.* **2018**, *9* (17), 2227–2231. DOI: 10.1039/C8PY00351C.

51. Frisch, M. J. Frisch, M. J., et al., Gaussian 16, Revision C.01, Gaussian, Inc., Wallingford CT. **2016**.

52. Wolfe, J. F.; Loo, B. H.; Arnold, F. E. Rigid-Rod Polymers. 2. Synthesis and Thermal Properties of Para-Aromatic Polymers with 2,6-Benzobisthiazole Units in the Main Chain. *Macromolecules* **1981**, *14* (4), 915–920. DOI: 10.1021/ma50005a005.

53. Wang, S.; Hong, W.; Ren, S.; Li, J.; Wang, M.; Gao, X.; Li, H. New Ladder-Type Conjugated Polymer with Broad Absorption, High Thermal Dtability, and Low Band Gap. *J. Polym. Sci. A. Polym. Chem.* **2012**, *50* (20), 4272–4276. DOI: 10.1002/pola.26234.

54. Mosca, S.; Milani, A.; Castiglioni, C.; Hernández Jolín, V.; Meseguer, C.; López Navarrete, J. T.; Zhao, C.; Sugiyasu, K.; Ruiz Delgado, M. C. Raman Fingerprints of π-Electron Delocalization in Polythiophene-Based Insulated Molecular Wires. *Macromolecules* **2022**, *55* (9), 3458–3468. DOI: 10.1021/acs.macromol.1c02458.

55. Tian, B.; Zerbi, G. Lattice Dynamics and Vibrational Spectra of Pristine and Doped Polypyrrole: Effective Conjugation Coordinate. *J. Chem. Phys.* **1990**, *92* (6), 3892–3898. DOI: 10.1063/1.457795.

56. Zerbi, G. Vibrational Spectroscopy of Conducting Polymers: Theory and Perspective. In *Handbook of Vibrational Spectroscopy*; John Wiley & Sons, Ltd, **2007**. DOI: 10.1002/9780470027325.s8920.

57. Hernandez, V.; Castiglioni, C.; Del Zoppo, M.; Zerbi, G. Confinement Potential and π-Electron Delocalization in Polyconjugated Organic Materials. *Phys. Rev. B* **1994**, *50* (14), 9815–9823. DOI: 10.1103/PhysRevB.50.9815.

58. Roberts, M. F.; Jenekhe, S. A. Lewis-Acid Coordination-Complexes of Polymers .3. Poly(Benzimidazobenzophenanthroline) Ladder and Semiladder Polymers. *Polymer* **1994**, *35* (20), 4313–4325. DOI: 10.1016/0032-3861(94)90088-4.

59. Hong, W.; Wei, Z.; Xi, H.; Xu, W.; Hu, W.; Wang, Q.; Zhu, D. 6H-Pyrrolo[3,2-b:4,5-B′]Bis[1,4]Benzothiazines: Facilely Synthesized Semiconductors for Organic Field-Effect Transistors. *J. Mater. Chem.* **2008**, *18* (40), 4814–4820. DOI: 10.1039/B809486A.

60. Batsanov, S. S. Van Der Waals Radii of Elements. *Inorg.* **2001**, *37* (9), 15. DOI: 10.1023/A:1011625728803.

61. Farmer, B. L.; Dudis, D. S.; Adams, W. W. Calculation of the Effects of Protonation on Rigid-Rod Polymers. *Polymer* **1994**, *35* (17), 3745–3751.DOI: 10.1016/0032-3861(94)90556-8.

62. Kim, H. G.; Kang, B.; Ko, H.; Lee, J.; Shin, J.; Cho, K. Synthetic Tailoring of Solid-State Order in Diketopyrrolopyrrole-Based Copolymers via Intramolecular Noncovalent Interactions. *Chem. Mater.* **2015**, *27* (3), 829–838. DOI: 10.1021/cm503864u.

63. Li, Y.; Sonar, P.; Murphy, L.; Hong, W. High Mobility Diketopyrrolopyrrole (DPP)-Based Organic Semiconductor Materials for Organic Thin Film Transistors and Photovoltaics. *Energy Environ. Sci.* **2013**, *6* (6), 1684–1710. DOI: 10.1039/C3EE00015J.

64. Guo, X.; Liao, Q.; Manley, E. F.; Wu, Z.; Wang, Y.; Wang, W.; Yang, T.; Shin, Y.-E.; Cheng, X.; Liang, Y.; Chen, L. X.; Baeg, K.-J.; Marks, T. J.; Guo, X. Materials Design via Optimized Intramolecular Noncovalent Interactions for High-Performance Organic Semiconductors. *Chem. Mater.* **2016**, *28* (7), 2449–2460. DOI: 10.1021/acs.chemmater.6b00850.

65. Tian, Y.-H.; Kertesz, M. Low-Bandgap Pyrazine Polymers: Ladder-Type Connectivity by Intramolecular S···N(Sp2) Interactions and Hydrogen Bonds. *Macromolecules* **2009**, *42* (7), 2309–2312. DOI: 10.1021/ma900082w.

66. Brédas, J. L.; Beljonne, D.; Coropceanu, V.; Cornil, J. Charge-Transfer and Energy-Transfer Processes in π-Conjugated Oligomers and Polymers: A Molecular Picture. *Chem. Rev.* **2004**, *104* (11), 4971–5004. DOI: 10.1021/cr040084k.

67. Zade, S. S.; Zamoshchik, N.; Bendikov, M. From Short Conjugated Oligomers to Conjugated Polymers. Lessons from Studies on Long Conjugated Oligomers. *Acc. Chem. Res.* **2011**, *44* (1), 14–24. DOI: 10.1021/ar1000555.

68. Berry, G. C. Properties of an Optically Anisotropic Heterocyclic Ladder Polymer (BBL) in Dilute Solution. *J. Polym. Sci.: Polym. Symp.* **1978**, *65* (1), 143–172. DOI: 10.1002/polc.5070650115.

69. Berry, G. C.; Yen, S. P. Structure and Properties of a Heterocyclic Polymer. *Addition and Condensation Polymerization Processes*, **1969**, 734–756. DOI: 10.1021/ba-1969-0091.ch048.

70. Yang, C. J.; Jenekhe, S. A. Conjugated Aromatic Polyimines. 2. Synthesis, Structure, and Properties of New Aromatic Polyazomethines. *Macromolecules* **1995**, *28* (4), 1180–1196. DOI: 10.1021/ma00108a054.

71. Wu, P.-T.; Kim, F. S.; Champion, R. D.; Jenekhe, S. A. Conjugated Donor−Acceptor Copolymer Semiconductors. Synthesis, Optical Properties, Electrochemistry, and Field-Effect Carrier Mobility of Pyridopyrazine-Based Copolymers. *Macromolecules* **2008**, *41* (19), 7021–7028. DOI: 10.1021/ma801348b.

72. Leenaers, P. J.; Maufort, A. J. L. A.; Wienk, M. M.; Janssen, R. A. J. Impact of π-Conjugated Linkers on the Effective Exciton Binding Energy of Diketopyrrolopyrrole–Dithienopyrrole Copolymers. *J. Phys. Chem. C* **2020**, *124* (50), 27403–27412. DOI: 10.1021/acs.jpcc.0c08768.

73. Izquierdo, M. A.; Broer, R.; Havenith, R. W. A. Theoretical Study of the Charge Transfer Exciton Binding Energy in Semiconductor Materials for Polymer:Fullerene-Based Bulk Heterojunction Solar Cells. *J. Phys. Chem. A* **2019**, *123* (6), 1233–1242. DOI: 10.1021/acs.jpca.8b12292.

74. Hedström, S.; Henriksson, P.; Wang, E.; Andersson, M. R.; Persson, P. Temperature-Dependent Optical Properties of Flexible Donor–Acceptor Polymers. *J. Phys. Chem. C* **2015**, *119* (12), 6453–6463. DOI: 10.1021/jp511246n.

75. Zeng, H.; Mohammed, M.; Untilova, V.; Boyron, O.; Berton, N.; Limelette, P.; Schmaltz, B.; Brinkmann. M. Fabrication of Oriented n-Type Thermoelectric Polymers by Polarity Switching in a DPP-Based Donor–Acceptor Copolymer Doped with $FeCl_3$. *Adv. Electron. Mater.* **2021**, 7, 2000880. DOI: 10.1002/aelm.202000880.

76. Liang, Z.; Zhang, Y.; Souri, M; Luo, X.; Boehm, M. A.; Li, R.; Zhang, Y.; Wang, T.; Kim. D-Y.; Mei, J.; Marder, S. M.; Graham, K. R. Influence of Dopant Size and Electron Affinity on the Electrical Conductivity and Thermoelectric Properties of a Series of Conjugated Polymers. *J. Mater. Chem. A*. **2018**, 6, 16495-16505. DOI: 10.1039/C8TA05922E.

77. Wu, L.; Li, H.; Chai, H.; Xu, Q.; Chen, Y.; Chen, L. Anion-Dependant Molecular Doping and Charge Transport in Ferric Salt-Doped P3HT for Thermoelectric Application. *CS Appl. Electron. Mater.* **2021**, *3* (3), 1252–1259. DOI: 10.1021/acsaelm.0c01067.

78. Kim, N. Y.; Lee, T. S.; Lee, D. Y.; Oh, J. G.; Lee, K.; Kim, J. Y.; An, T. K.; Jeong, Y. J.; Jang, J.; Kim, Y-H. Enhanced Doping Efficiency and Thermoelectric Performance of Diketopyrrolopyrrole-based Conjugated Polymers with Extended Thiophene Donors. *J. Mater. Chem. C*. **2021**,9 , 340-347. DOI:10.1039/D0TC04094k.

79. Geon, X.; Du, T.; Xu, C.; Liu, Y.; Deng, Y.; Geng, Y. Realizing *p*-Type and *n*-Type Doping of a Single Conjugated Polymer via Incorporation of a Thienoisatin-Terminated Quinoidal Unit. *Adv. Funct. Mater.* **2023**, 33, 2300809. DOI: 10.1002/adfm.202300809.

80. Gregory, S. A.; Hanus, R.; Atassi, A.; Rinehart, J. M.; Wooding, J. P.; Menon, A. K.; Losego, M. D.; Snyder, G. J.; Yee, S. K. Quantifying Charge Carrier Localization in Chemically Doped Semiconducting Polymers. *Nat. Mater.* **2021**, 20 (10), 1414-1421. DOI: 10.1038/s41563-021-01008-0.

81. Scholes, D. T.; Hawks, S. A.; Yee, Y. P.; Wu, H.; Lindemuth, J. R.; Tolbert, S. H.; Schwartz, B. J. Overcoming Film Quality Issues for Conjugated Polymers Doped with F_4TCNQ by Solution Sequential Processing: Hall Effect, Structural, and Optical Measurements. *J. Phys. Chem. Lett.* **2015**, *6* (23), 4786–4793. DOI: 10.1021/acs.jpclett.5b02232.

82. Fontana, M. T.; Stanfield, D. A.; Scholes, D. T.; Winchell, K. J.; Tolbert, S. H.; Schwartz, B. J. Evaporation vs. Solution Sequential Doping of Conjugated Polymers: F_4TCNQ Doping of Micrometer-Thick P3HT Films for Thermoelectrics. *J. Phys. Chem. C.* **2019**, *123* (37), 22711–22724. DOI: 10.1021/acs.jpcc.9b05069.

83. Wang S.; Ruoko, T-P.; Wang, G.; Riera-Galindo, S.; Hultmark, S.; Puttisong, Y.; Moro, F.; Yan, H.; Chen, W. M.; Berggren, M.; Müller, C.; Fabiano, S. Sequential Doping of Ladder-Type Conjugated Polymers for Thermally Stable n-Type Organic Conductors. *ACS Appl. Mater. Interfaces* **2020**, *12* (47), 53003–53011. DOI: 10.1021/acsami.0c16254.

84. Scholes, D. T.;. Yee, P. Y.; McKeown, G. R.; Li, S.; Kang, H.; Lindemuth, J. R.; Xia, X.; King, S. C.; Seferos, D. S.; Tolbert, S. H.; Schwartz, B. J. Designing Conjugated Polymers for Molecular Doping: The Roles of Crystallinity, Swelling, and Conductivity in Sequentially-Doped Selenophene-Based Copolymers. *Chem. Mater.* **2019** *31* (1), 73-82. DOI: 10.1021/acs.chemmater.8b02648

85. Jacobs, I. E.; Aasen, E. W.; Oliveira, J. L.; Fonseca, T. N.; Roehling, J. D.; Li, J.; Zhang, G.; Augustine, M. P.; Mascal, M.; Moulé, A. J. Comparison of Solution-mixed and Sequentially Processed P3HT:F_4TCNQ Films: Effect of Doping-induced Aggregation on Film Morphology. *J. Mater. Chem. C.* **2016**, 4, 3454-3466. DOI: 10.1039/C5TC04207K.

86. Jha, M.; Santiana, J. M.; Jacob, A. A.; Light, K.; Hong, M. L.; Lau, M. R.; Filardi, L. R.; Miao, H.; Gurses, S. M.; Kronawitter, C. X.; Mascal, M.; Moulé, A. J. Stability Study of Molecularly Doped Semiconducting Polymers, *J. Phys. Chem. C.* **2024**, *128* (3), 1258-1266. DOI: 10.1021/acs.jpcc.3c06044.

Chapter 6. Conclusions and Outlook

6.1. Conclusions

Organic semiconducting polymers are of broad and fundamental interest for applications in organic photovoltaics, organic field-effect transistors, organic electrochemical transistors, and organic thermoelectric devices. One of the most attractive features of semiconducting polymers is their synthetic tunability that allows the synthesis of polymers with properties that suit the specific application. π-Conjugated ladder polymers are of particular interest due to their ideal ribbon-like conformations that limits conformational disorder and endows them with large persistence lengths that are known to benefit charge transport. The projects present in this dissertation focused on the synthesis and studies of both known and new p-/n-type π-conjugated ladder polymers and addressed some challenges in the field by elucidating structure-property relationships that govern their performance in organic electronics.

In Chapter 2, I discussed the synthesis and properties of the phenazine-substituted BBL derivative BBL-P, whose initial synthesis was reported several years before the discovery of the semiconducting properties of π-conjugated polymers in 1977. The elemental analysis and thermal gravimetric analysis revealed that BBL-P is intrinsically hygroscopic and retains ~ 8-11% water even after rigorous drying under vacuum at temperatures > 100˚C. The optical absorption spectrum in protic acid solutions showed a lowest-energy peak at 840 nm, which is attributed to protonation-enhanced intramolecular charge transfer (ICT) character. Additionally, I found that extending the π-conjugation length by phenazine substitution has minimal impact on the LUMO energy level, which was measured to be identical to BBL at -4.0 eV. I also discovered that BBL-P thin films have reduced crystallinity and preferential *face-on* molecular

orientations, both of which contributed to a comparatively decreased field-effect electron mobility (μ_e) of 1.2 x10^{-4} cm^2/Vs. I demonstrated that BBL-P has excellent film-forming properties such that large area freestanding films with areas 1-2 cm^2 can be created. These freestanding films have robust mechanical properties in the out-of-plane direction exemplified by a large Young modulus of 11 GPa.

Chapter 3 focuses on the design, synthesis, and properties of two series of BBL-based random copolymers featuring cyanated electron-withdrawing moieties: BBL-*x*2CN and BBL-*x*TCN (*x* = 20, 35, and 50). The random copolymer architecture was chosen for these studies in order to balance the solubility and processability of the ladder polymers, which allowed me to study the effects of appending strong electron-withdrawing moieties onto the backbone of BBL. I originally synthesized the homopolymers BBL-2CN and BBL-2TCN and found them to be insoluble in protic acids.

In Section 3.1, synthesized a series of random copolymers BBL-*x*2CN featuring two cyano groups appended directly to the naphthalene core. I accomplished this by designing and synthesizing a new dicyano-tetraester monomer, NTE-2CN; single-crystal X-ray analysis of NTE-2CN confirmed the successful isolation of the 2,6-dicyano isomer. I found that the incorporation of 20 mol% of NTE-2CN increased the speed of the polycondensations such that they completed in less than 12 hours at 150˚C compared to BBL (*x* = 0). I discovered that the BBL-*x*2CN series and the accompanying model compound are predicted to show no conformational distortions according to DFT calculations. The thin film absorption measurements showed optical bandgaps of 1.60 eV – 1.65 eV, and low LUMO levels of -4.16 eV to -4.34 eV were measured on cyclic voltammetry. Specifically, 50 mol% of the NTE-2CN monomer lowered the LUMO level by 0.18 eV compared to BBL. The effects of cyanation on

the electrical conductivities were studied by n-doping the polymer thin films and preliminary results indicate that incorporation of 20 – 50 mol% of 2CN in the backbone is detrimental to the electrical conductivities, which can partly be explained by the extreme localization of the LUMO energy level shown on the DFT calculations.

In Section 3.2, I extend my cyanation strategy to synthesize a second random copolymer series featuring dithiinotetracarbonitrile (TCN) groups: BBL-*x*TCN (*x* = 0.2, 0.35, 0.5). Similar to the BBL-*x*2CN polymers, I found that incorporation of as little as 20 mol% of the TCN-based monomer into the BBL backbone increased the speed of the polymerizations and resulted in polymers with modest intrinsic viscosities ranging from 1.3 dL/g – 2.5 dL/g in MSA at 30˚C. The molecular structures of the polymers were characterized by FTIR, Raman and X-ray photoelectron spectroscopy and were comparable to those of the model compound PTCNMe. I showed that 50 mol% of the TCN moiety is required to lower the LUMO level by 0.2 eV compared to BBL, which demonstrates the efficacy of TCN-backbone functionalization as an approach to lower the LUMO level of n-type semiconducting ladder polymers. Unlike the BBL-2CN series, DFT calculations revealed that increasing the mol% of the TCN moiety also increased the structural disorder, which was also implied on the optical absorption spectroscopy.

Chapter 4 describes the synthesis and properties of two p-type π-conjugated ladder polymers, the known polymer LPBT and the new alkylated polymer, LPBT-Me. Here, I studied the effects of N-alkylation on the polymer chain conformation, electronic structure and charge transport properties of p-type ladder polymers and found that both polymers have donor-acceptor motifs and strong intramolecular charge transfer character when protonated. Additionally, both polymers have small optical bandgaps of 1.5 eV that was unchanged by N-alkylation. I discovered that both polymers show substantial thermochromism when protonated

in acid solutions, which is in contrast to BBL that shows no thermochromism in protic acid solutions. This means that ladder poly(pyrrolobenzothiazine)s are not rigid-rod ladder polymers like BBL, but rather undergo planar/non-planar conformational changes that vary with the degree of protonation, which I corroborated with DFT calculations. The field-effect hole mobility of the parent polymer LPBT was increased at 3.1 x 10^{-3} cm^2/Vs compared to 1.3 x 10^{-3} cm^2/Vs measured for LPBT-Me. This difference is understood by the increased crystallinity and decreased lattice disorder in the thin films of LPBT that was evidenced in 2D X-ray diffraction experiments.

Continuing my studies of p-type ladder polymers in Chapter 5, I discussed the synthesis and characterization of a new thiophene-based p-type ladder polymer LTBT, and its model compound TBBT. I synthesized LTBT using a binary solvent system of PPA and sulfolane to improve the solubility of my new 2,5-dione thiophene monomer in the polymerization medium. I limited the polymerization reaction time to 40 h in order to enhance the processability of the polymer, which resulted in a polymer with [η] = 2.0 dL/g in MSA at 30˚C. Single-crystal X-ray analysis of TBBT showed that the molecule has a coplanar backbone and a π-π stacking distance of 3.8 Å. LTBT exhibited a narrowed optical bandgap of 1.28 eV and strong protonation-enhanced intramolecular charge transfer character that extends in the infrared region. I also found that LTBT shows thermochromism in MSA (pKa ~ -1.9) solutions, but not in triflic acid solutions (pKa ~ -14.7), which implies that it undergoes conformational distortions when partially protonated. A moderate average electrical conductivity of (3.31 ± 0.31) x 10^{-1} S/cm was found when p-doped with $FeCl_3$, which demonstrate the potential of LTBT in organic electronics.

Overall, the studies presented in this dissertation have provided new knowledge to the field of semiconducting polymers and have presented newfound insights into the fundamental structure-property relationship of both n-type and p-type π-conjugated ladder polymers for organic electronics. Moving forward, new studies of π-conjugated polymers should continue to push the boundaries of knowledge of π-conjugated ladder polymers in order to design new state-of-the-art semiconductors for technological innovations.

6.2. Outlook

Rigid-rod π-conjugated ladder polymers are a promising class of semiconducting polymers with utility in organic electronic devices. Defect-free π-conjugated ladder polymers are exceedingly rare due to the difficult synthesis of tetrafunctionalized monomers and/or inefficient post-annulations of prepolymers. Thusly, a good first approach to develop new ladder polymers is to functionalize and derivatize known ladder polymers such as BBL in order to study the structure-property relationships that govern performance in electronic devices. This strategy was used in Chapters 2 and 3 where I synthesized and characterized n-type derivatives of BBL featuring electron-deficient monomers. Due to the insolubility of the homopolymers BBL-TCN and BBL-2CN, I utilized the random copolymer motif to enable solution processing, which highlights the main challenge in the field of semiconducting ladder polymers: insolubility of the ladder backbone. Going forward, the solubility of BBL-derivatives could be improved to afford the study of the solution and solid-state properties though side-chain engineering. For example, an alkyl chain could be attached to the naphthalene backbone on the NTE-2CN monomer. An alternative approach would be to attach the alkyl chains to the tetraamine monomer. Increasing the molecular diversity of semiconducting ladder polymers is the first step

towards enabling rational design of new ladder polymers for organic electronic device applications.

It is clear that the limited solubility of ladder polymers is the major roadblock to fully realize their potential as semiconductors in organic electronics. For example, a key design criterion to maximize charge transport is to increase the molecular weight of the ladder polymer, which I highlighted in Chapters 2 and 4. To establish accurate structure-property relationships, high molecular weight ladder polymers must be synthesized reproducibly. For example, the highest recorded [η] value for the prototype ladder polymer BBL is limited to 32.0 dL/g, and this result has never been reproduced. The next best BBL polymer has [η] = 21.0 dL/g, which represents a significant decrease in the molecular weight. In another example, the insolubility of the BBL-502CN and BBL-50TCN copolymers discussed in Chapter 3 limited the molecular weights such that only the low molecular weight fractions were isolated. Since many properties, including charge transport properties and electrical conductivities, depend directly on the molecular weight, future studies should focus on establishing polymerization routes that synthesize well-defined, soluble ladder polymers that approach a target molecular weight.

Solubilizing the ladder backbone though side-chain engineering would address another key challenge in the field: processing the polymers into thin films for electronic devices. Currently, ladder polymers without solubilizing groups are processed exclusively using protic acid solutions, such as MSA or conc. H_2SO_4, or in air-sensitive Lewis-acid complexes. To bring π-conjugated ladder polymers to market, moving away from these processing methods is of critical importance since using strong acids on an industrial scale is a safety issue and processing in inert conditions is impractical.

Processing ladder polymers in non-acid solvents is also of critical importance in the context of characterization. Currently, the structural characterization of BBL and other ladder polymers is extremely limited because many modern techniques, like size-exclusion chromatography, are not compatible with the strong acids used to solubilize ladder polymers. A few example polymers that could be synthesized with solubilizing alkyl chains, possibly using the sulfolane/PPA solvent system that I described in Chapter 5, include ladder pyrazinoquinoxalines (LPPQ-R), ladder pyrrolobenzothiazine (LPBT-R), and perylene-substituted BBL derivatives (PBL-R) (Figure 6.1).

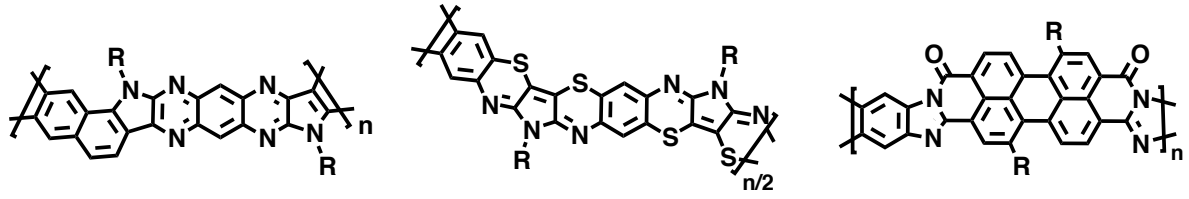

Figure 6.1. Examples of potential ladder polymers featuring alkyl chains. R = long alkyl chain.

Understanding the structure-property relationships of π-conjugated ladder polymers must be extended to the polymer chain topology. In Chapters 4 and 5 I showed that ladder architecture does not exclusively lead to the rigid-rod chain topology. I showed that the ladder pyrrolobenzothiazine and ladder thienobenzothiazine polymers have planar/non-planar conformational variations when protonated and do not have a rigid-rod ladder topology. Beyond temperature-dependent optical absorption measurements, light scattering, neutron scattering, and temperature-dependent Raman spectroscopy experiments could be used to not only elucidate conformational disorder in the polymer chain, but also to measure other fundamental parameters such as persistence lengths.

Appendix A

Appendix A presents supplementary information to accompany Chapter 2: Phenazine-Substituted Poly(benzimidazobenzophenanthrolinedione): Electronic Structure, Thin Film Morphology, Electron Transport, and Mechanical Properties of an n-Type Semiconducting Ladder Polymer

A.1 Additional Experimental Methods

Preparation of BBL-P Thin Films on Glass Substrates.

BBL-P was dissolved in methanesulfonic acid (MSA) at a concentration of 20 – 25 mg/mL and stirred at 125˚C for at least a week to ensure complete dissolution. Soda lime glass substrates or indium tin oxide (ITO) substrates were cleaned sequentially in detergent, DI water, acetone, and isopropyl alcohol. The cleaned substrates were treated with air plasma for 10 mins. The BBL-P polymer solution was spun on substrates at 1000 rpm for 30 seconds, and the wet films were baked at 120˚C for 12 hours. At this stage, the BBL-P thin films were sufficiently dried and showed a shiny gold surface. The temperature was gradually increase to 200˚C with a ramping rate of 20˚C/hour to remove any residual acidic solvents ($T_{b,\,MSA}$ = 167˚C). The resulting BBL-P films showed dark brown color with a shiny gold surface and was used for further characterizations (UV-Vis, CV, and nanoindentation tests).

Fabrication of Freestanding Films.

Films of BBL-P were prepared on initial supporting glass substrates using a similar procedure as described above where the BBL-P solution (25 mg/mL) was spun at 700 rpm for 45 seconds, and the films were baked overnight at 120˚C. Instead of additional annealing at higher temperature, the BBL-P thin films were slowly cooled down to room temperature and submerged in DI water. Upon exposure to water, BBL-P films swelled significantly due to its intrinsic hygroscopic

nature; thus, films can be peeled from the supporting substrate, floated on water surface, lifted off, and dried to form freestanding films. These freestanding films were used for further characterizations (UV-Vis, FTIR, and Raman spectroscopy).

Fabrication and Characterization of OFETs. n-Channel organic field-effect transistors (OFETs) were fabricated in a bottom-gate/top-contact device architecture with a polymer buffer layer. The substrate is comprised of heavily n-doped silicon (< 0.005 S/cm; 500 μm) with a 300 nm-thick silicon oxide layer. The substrates were cleaned by sequentially sonicating in DI water, acetone, and isopropyl alcohol. The cleaned substrates were then treated with air plasma for 10 mins. Insulating polystyrene (PS) was dissolved in anhydrous toluene (5 mg/mL) and stirred at room temperature overnight. The PS solution was spin-coated onto the substrates at 3000 rpm for 60 seconds followed by drying in vacuum oven at 60˚C overnight to produce a 17.0 nm (± 0.12 nm) thick layer. On top of the PS-coated substrates, the BBL-P thin films were deposited by spin-coating a BBL-P solution in MSA (25 mg/mL) at 5000 rpm for 30 seconds. The acidic solvent was removed by dipping the films in a mixture of isopropanol (IPA) and ethylene glycol (EG) (1:1, v:v) several times for 12 hours. Afterwards, the BBL-P films were submerged in 100% IPA for at least 5 hours to wash away excess ethylene glycol. Finally, the BBL-P films were dried in vacuum oven at 100˚C overnight and then annealed at 170˚C on a hot plate for 10 min in a nitrogen-filled glovebox. Source and drain electrodes were defined by thermal evaporation of gold electrodes (60 nm). Channel width (W) and length (L) were 1000 μm and 100 μm, respectively. The transistors were tested by using a Keithley 4200 semiconductor characterization system inside a nitrogen atmosphere. The field-effect electron mobility (μ) was extracted by analyzing the current – voltage data with the saturation-region equation:

$$I_{ds} = \frac{\mu W C_i}{2L}\left(V_{gs} - V_t\right)^2$$

where I_{ds} is the source-drain current, μ is field-effect mobility, C_i is the capacitance of gate insulator (10.6 nF/cm^2), V_{gs} is source-gate voltage bias, and V_t is threshold voltage.

Characterization of Mechanical Properties by Nanoindentation Test. The elastic modulus was measured using Hysitron TI 980 TriboIndenter. The nanoindentation test required a Berkovich tip compressing into the sample while measuring the force and displacement. The tests were carried out in both constant displacement and constant load mode. Three indents were made across the film surface at each displacement and load value. The reported elastic modulus was the average of the moduli in the range of 10 – 20% depth into the total film thickness to minimize any substrate effects. Dynamic mechanical analysis (DMA) was done by applying an oscillating load with maximum amplitude of 100 μN at varying frequency from 45Hz to 200 Hz. Samples were made by spin-coating BBL-P onto a glass substrate using procedure described earlier. The total thickness of the BBL-P sample was determined to be 650 nm using a profilometer.

A.2 Supplementary Figures

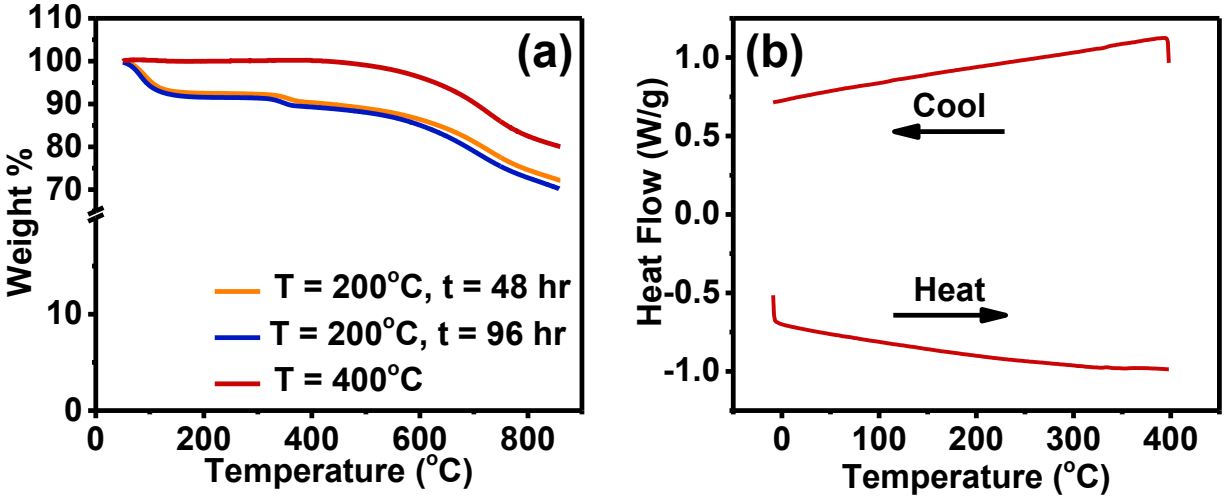

Figure A.1. (a) TGA of BBL-P (at 10˚C/min under N_2) taken after 48 hours drying (orange), 96 hours drying (blue) at 200˚C under vacuum, and drying to 400˚C in the TGA, cooling to 50˚C, and ramping up to 880˚C (red). (b) DSC heating and cooling scans of BBL-P with a heating and cooling rate of 10˚C/min under N_2 gas flow.

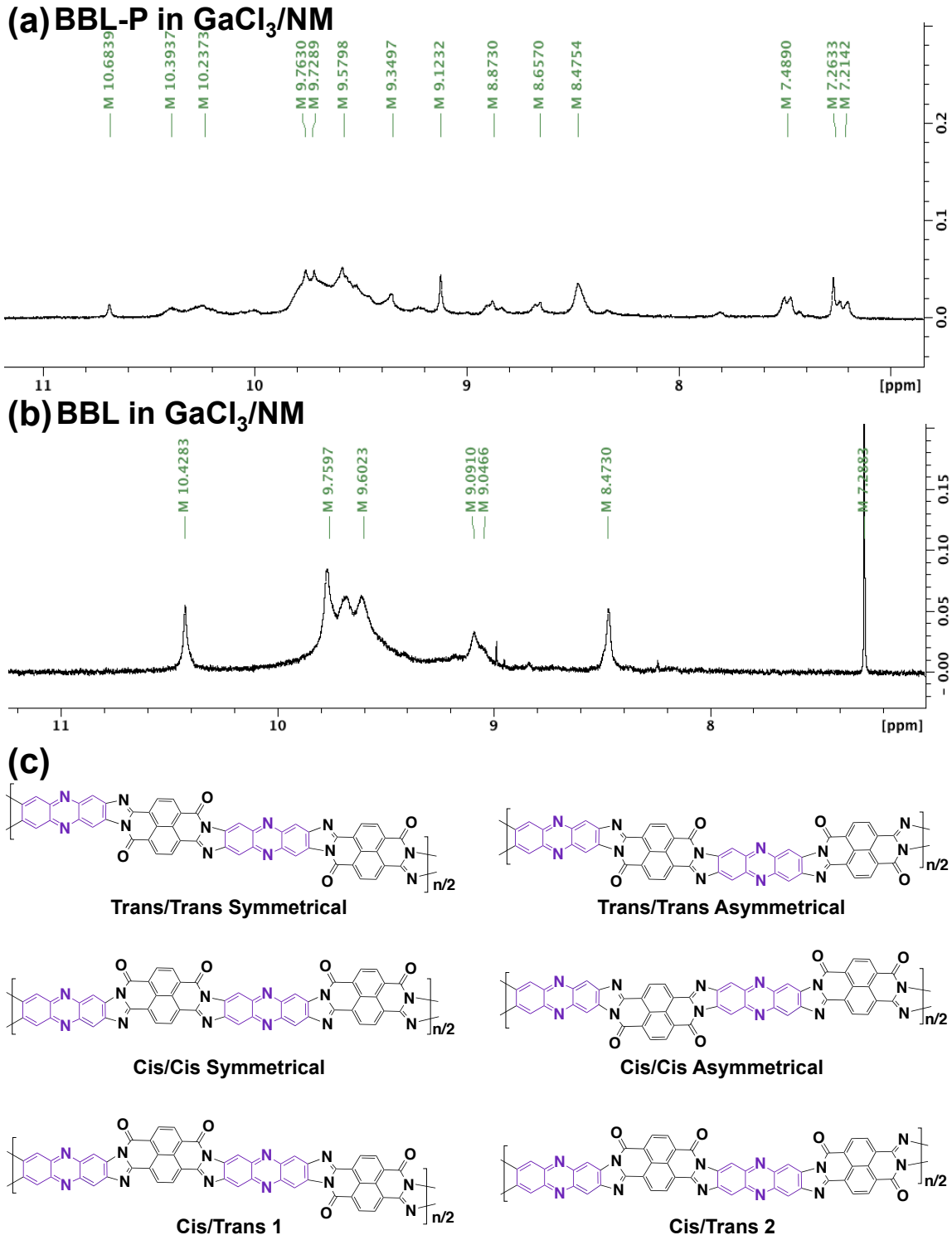

Figure A.2. Proton NMR spectrum of (a) BBL-P and (b) BBL in $GaCl_3$/nitromethane-d3, and (c) possible structural isomers of the BBL-P monomeric repeat unit.

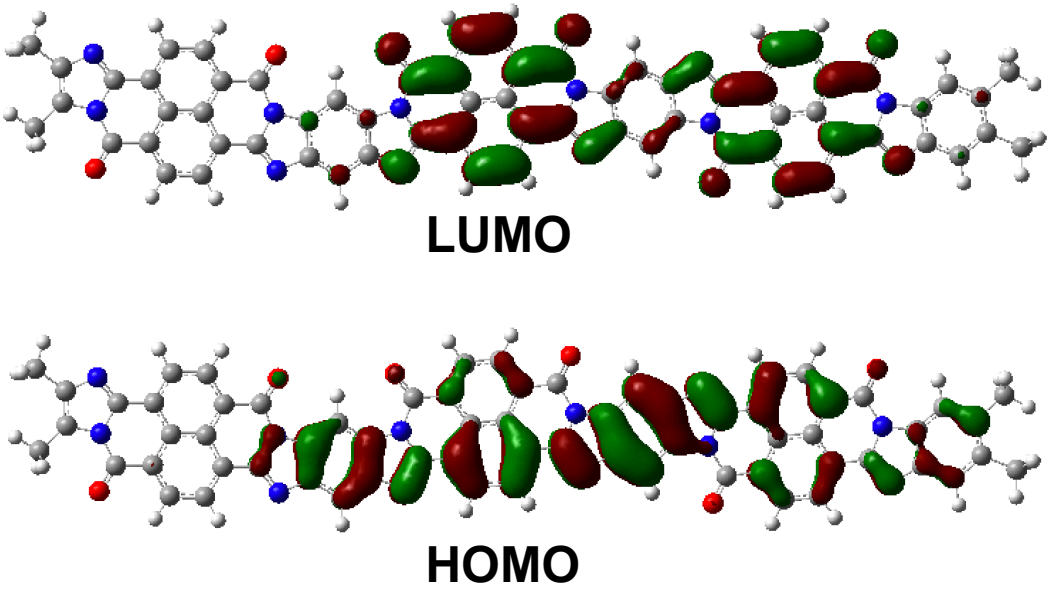

Figure A.3. Pictorial representation of the DFT-calculated ground state frontier molecular orbitals of BBL oriented in a trans-cis-trans geometry. Calculations were performed at the ωB97XD/6-31G(d,p) level of theory.

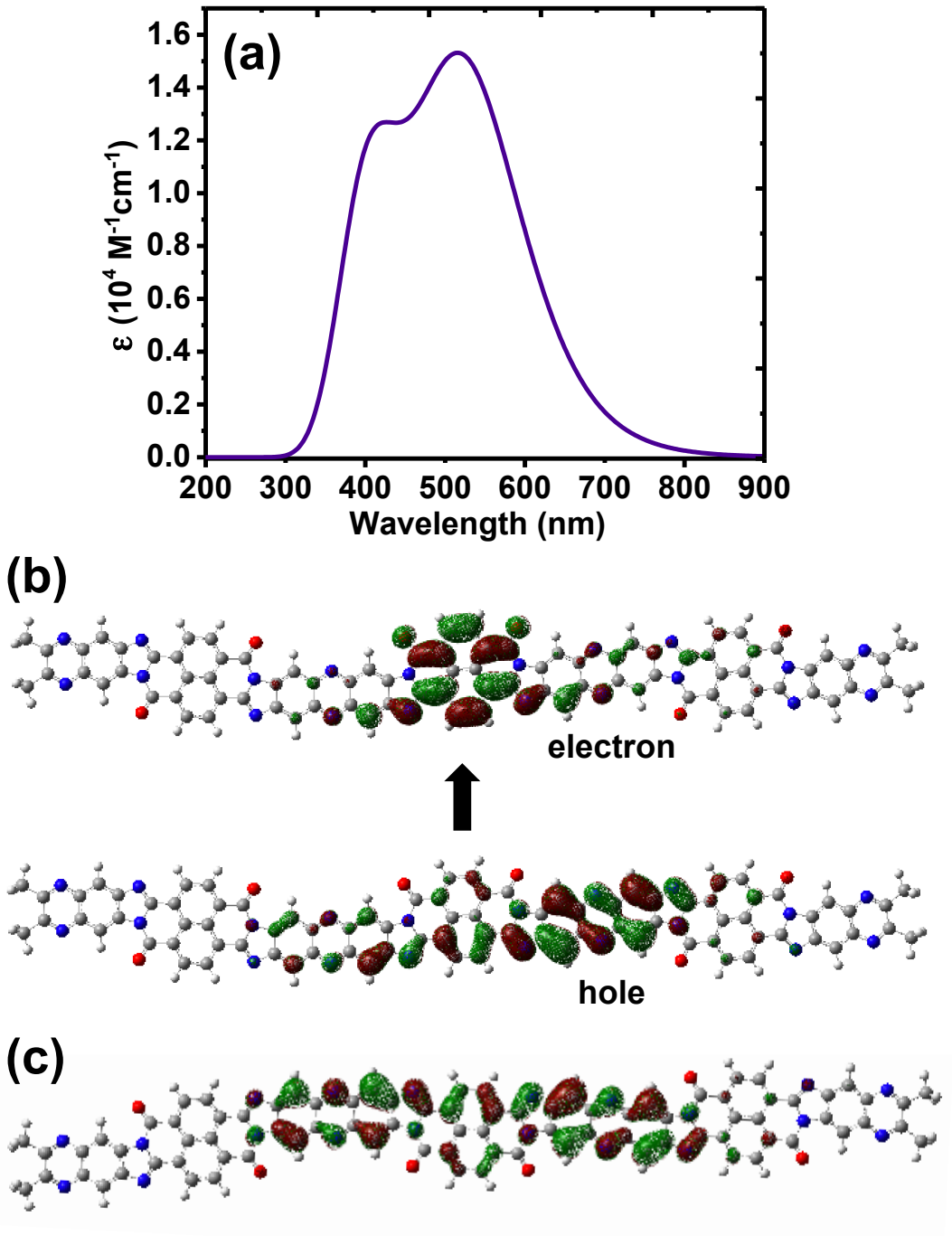

Figure A.4. (a) Simulated absorption spectrum of the gas phase BBL-P oligomer calculated at the time-dependent (TD) ωB97XD/6-31G(d,p) level of theory calculated with 12 excited states (λ_{max} = 527 nm), (b) The pictorial representation of hole and electron orbital distributions for the lowest energy transition (π-π^*) at 527 nm, and (c) The anionic BBL-P oligomer showing polaron orbital distribution calculated at the same ωB97XD/6-31G(d,p) level of theory.

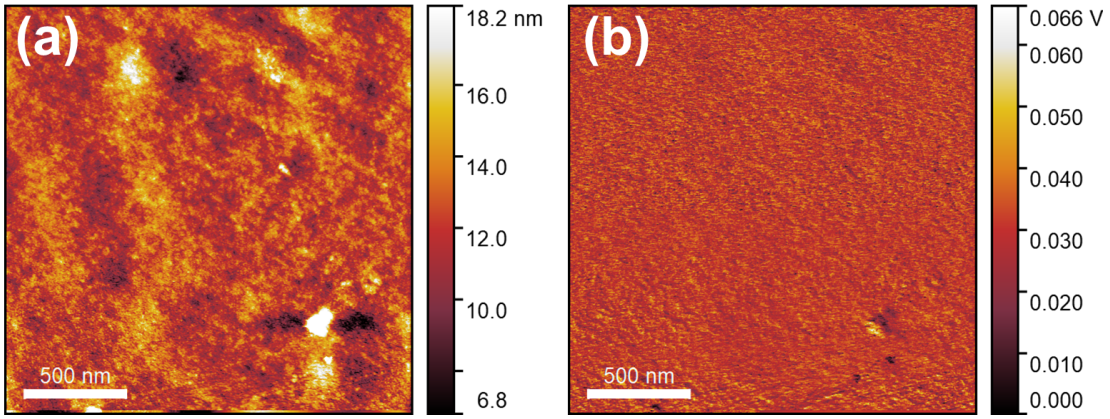

Figure A.5. (a) AFM height image of BBL-P thin film (2 µm x 2 µm) and (b) AFM phase image of BBL-P thin film (2 µm x 2 µm).

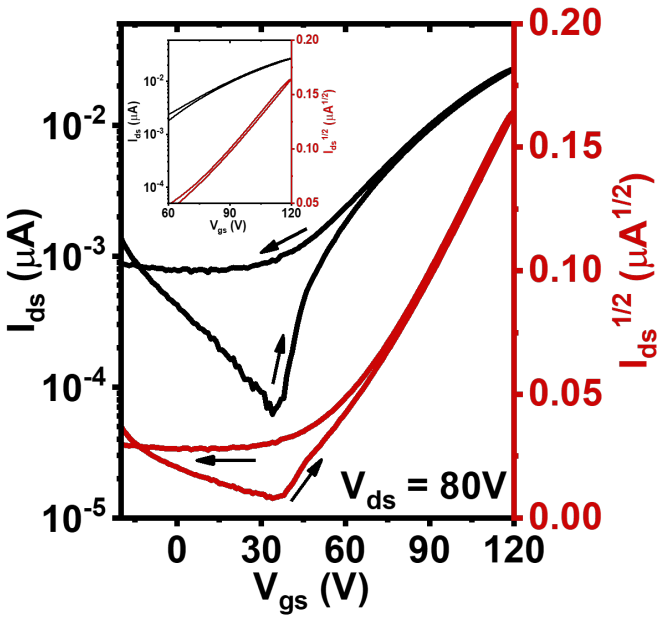

Figure A.6. Transfer curve of BBL-P transistors with reverse and forward scans. The inset shows a zoomed-in region with gate voltage varying between 60 V and 120 V.

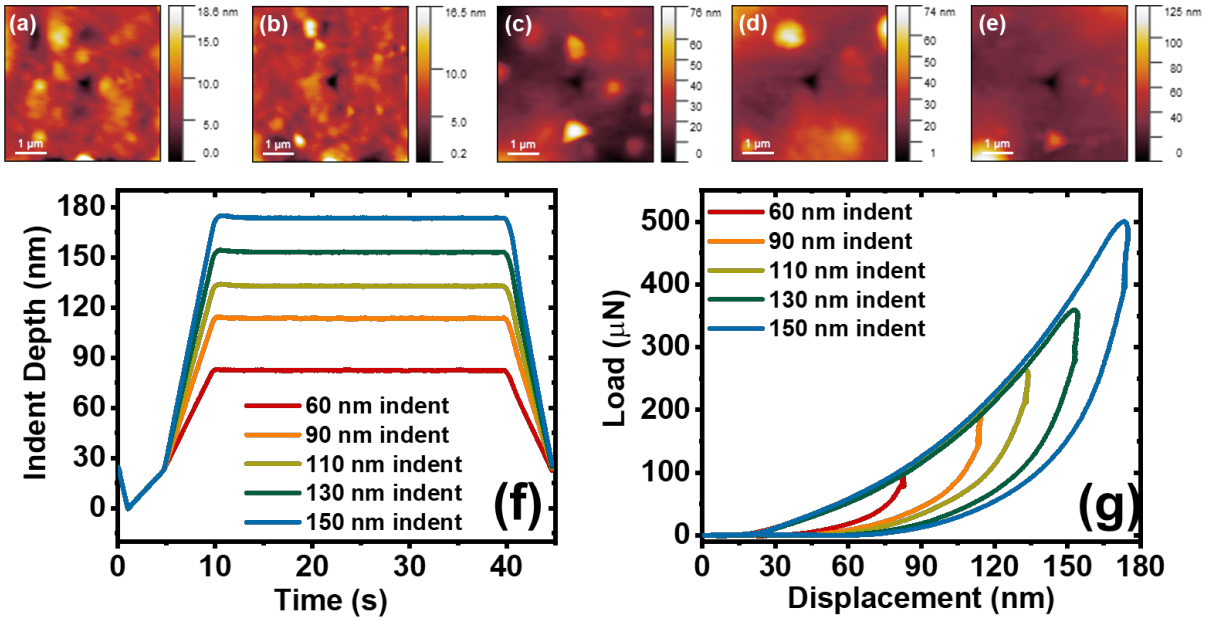

Figure A.7. (a-e) AFM topography images of BBL-P films after nanoindentation tests at various indent depths (60 nm (a), 90 nm (b), 110 nm (c), 130 nm (d), and 150 nm (e)), (f) Indent depth as a function of time, and (g) Load-displacement response curve of BBL-P films (thickness = 650 nm) at various indent depths.

A.3 Supplementary Tables

Table A.1. Summary of Diffraction Peak Positions (q), d-Spacings, and Crystalline Coherence Length (L_c) in the In-Plane (IP) and Out-of-Plane (OOP) Directions of BBL-P.

Parameter	Value
q_{xy} (Å^{-1})	0.78
q_z (Å^{-1})	1.90
d_{100} (Å)	8.03
d_{010} (Å)	3.31
L_c (100) IP (nm)	1.07
L_c (010) OOP (nm)	1.04

Table A.2. Charge Transport Properties of BBL-P Ladder Polymer Characterized by Organic Field-Effect Transistor (OFET) with Channel Length/Channel Width of 100 μm/1000 μm.

Parameter	Value
$\mu_{FET,ave}$ (cm^2/Vs)[(a)]	(9.60 ± 1.58) x 10^{-5}
$\mu_{FET,max}$ (cm^2/Vs)	1.21 x 10^{-4}
I_{on}/I_{off}[(a)]	(7.7 ± 3.4) x 10^2
V_t (V)[(a)]	45.1 ± 1.72

[(a)] Average values are obtained from 17 individual devices.

Appendix B

Appendix B presents supplementary Information to Chapter 3.1: Cyanated and Noncyanated Conjugated Ladder Copolymers and Model Compound of Poly(benzimidazobenzophenanthroline): Synthesis, Electronic Structure, and Thin Film Morphology.

B.1 Additional Experimental Methods

Single Crystal X-Ray Analysis.

Single crystals of NTE-2CN were grown from slow diffusion of ethanol into chloroform, which produced colorless needles. A colorless needle, measuring 0.26 x 0.05 x 0.05 mm^3 was mounted on a loop with oil. Data was collected at -173°C on a Bruker APEX II single crystal X-ray diffractometer, Mo-radiation, equipped with a Miracol X-ray optical collimator. Crystal-to-detector distance was 40 mm and exposure time was 15 seconds per frame for all sets. The scan width was 0.5°. Data collection was 96.7% complete to 25° in ϑ. A total of 36582 reflections were collected covering the indices, -18<=h<=18, -21<=k<=21, -10<=l<=10. 2018 reflections were symmetry independent and the R_{int} = 0.0342 indicated that the data was excellent. Indexing and unit cell refinement indicated a C-centered monoclinic lattice. The space group was found to be C 2/c (No. 15). The data was integrated and scaled using SAINT, SADABS within the APEX2 software package by Bruker.[1] Solution by direct methods (SHELXT[2-3] or SIR97[4-5]) produced a complete heavy atom phasing model consistent with the proposed structure. The structure was completed by difference Fourier synthesis with SHELXL.[6-7] Scattering factors are from Waasmair and Kirfel.[8] Hydrogen atoms were placed in geometrically idealised positions and constrained to ride on their parent atoms with C---H distances in the range 0.95-1.00

Angstrom. Isotropic thermal parameters U_{eq} were fixed such that they were $1.2U_{eq}$ of their parent atom Ueq for CH's and $1.5U_{eq}$ of their parent atom U_{eq} in case of methyl groups. All non-hydrogen atoms were refined anisotropically by full-matrix least-square. Within the solvent free structure, half of molecule is related to the other by an inversion center in the center of the molecule. The side chains are disordered to avoid overlapping.

X-Ray Photoelectron Spectroscopy.

All XPS spectra were taken on a Kratos Axis-Ultra DLD spectrometer. This instrument has a monochromatized Al Kα X-ray and a low energy electron flood gun for charge neutralization. X-ray spot size for these acquisitions was on the order of 700 x 300 μm. Pressure in the analytical chamber during spectral acquisition was less than $5x10^{-9}$ Torr. Pass energy for survey and detailed spectra (composition) was 80 eV. Pass energy for the high-resolution spectra was 20 eV. The take-off angle (the angle between the sample normal and the input axis of the energy analyzer) was 0˚(0 degree take-off angle ~ 100 Å sampling depth). The Kratos Vision2 software program was used to determine peak areas and to calculate the elemental compositions from peak areas. CasaXPS was used to peak fit the high-resolution spectra. For the high-resolution spectra, a Shirley background was used and all binding energies were referenced to the C ls C-C bonds at 285.0 eV.

Preparation of Polymer Thin Films on Glass Substrates.

The polymers was dissolved in methanesulfonic acid (MSA) at a concentration of 10 – 15 mg/mL and stirred at 125˚C for several days to ensure complete dissolution. Soda lime glass substrates or indium tin oxide (ITO) substrates were cleaned sequentially in detergent, DI water, acetone, and isopropyl alcohol (IPA). The polymer solutions were spun on substrates at 1000 rpm for 30 seconds, and the wet films were submerged in ethylene glycol (EG) for one hour,

followed by EG:IPA 80:20 for one hour, EG:IPA 50:50 for one hour, then finally IPA for 12 hours. The polymer films were then dried at 90˚C for 12 hours, which exhibited a shiny copper colored surface.

Fabrication of Freestanding Films.

Films of the polymers were prepared on initial supporting glass substrates where the polymer solutions (25 mg/mL) were drop-cast onto glass substrates, and the films were baked overnight at 120˚C. The polymer thin films were slowly cooled down to room temperature and submerged in DI water. Upon exposure to water, the polymer films can be peeled from the supporting substrate, floated on water surface, lifted off, and dried to form freestanding films. These freestanding films were used for further characterizations (FTIR and Raman spectroscopy).

B.2 Supplementary Figures

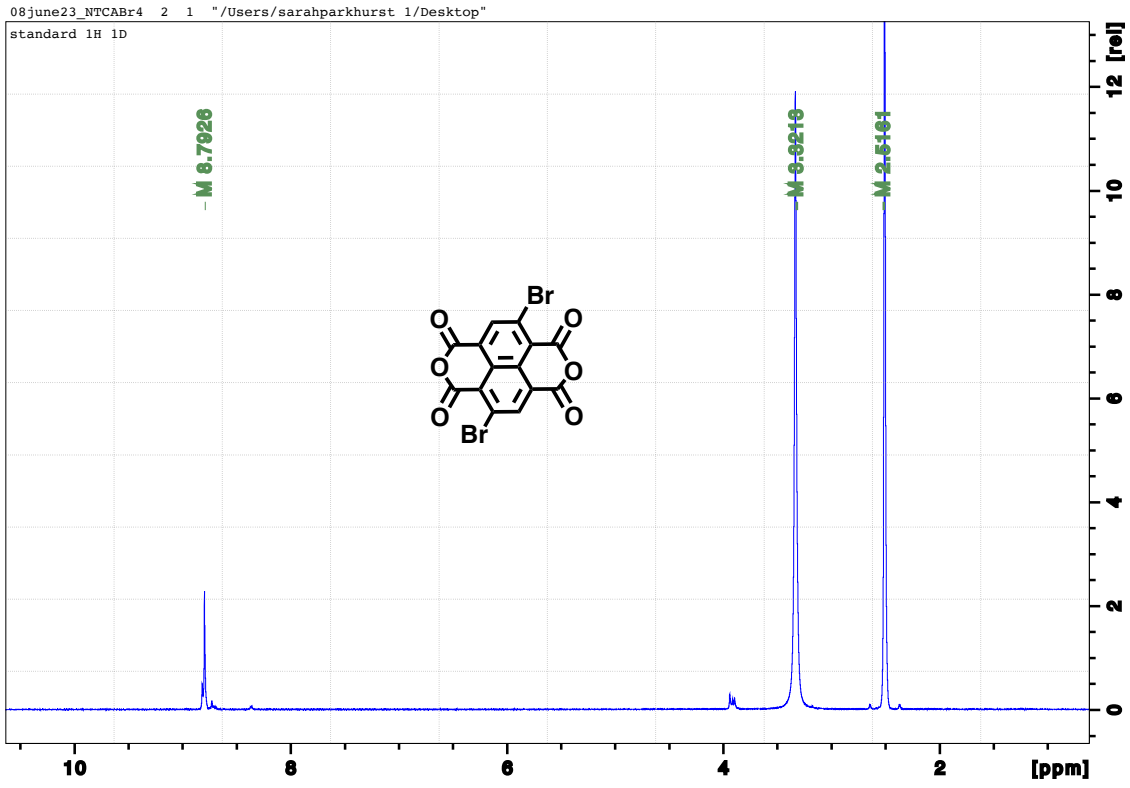

Figure B.1. Proton NMR of NTCDA-2Br (**2**) in DMSO-d6.

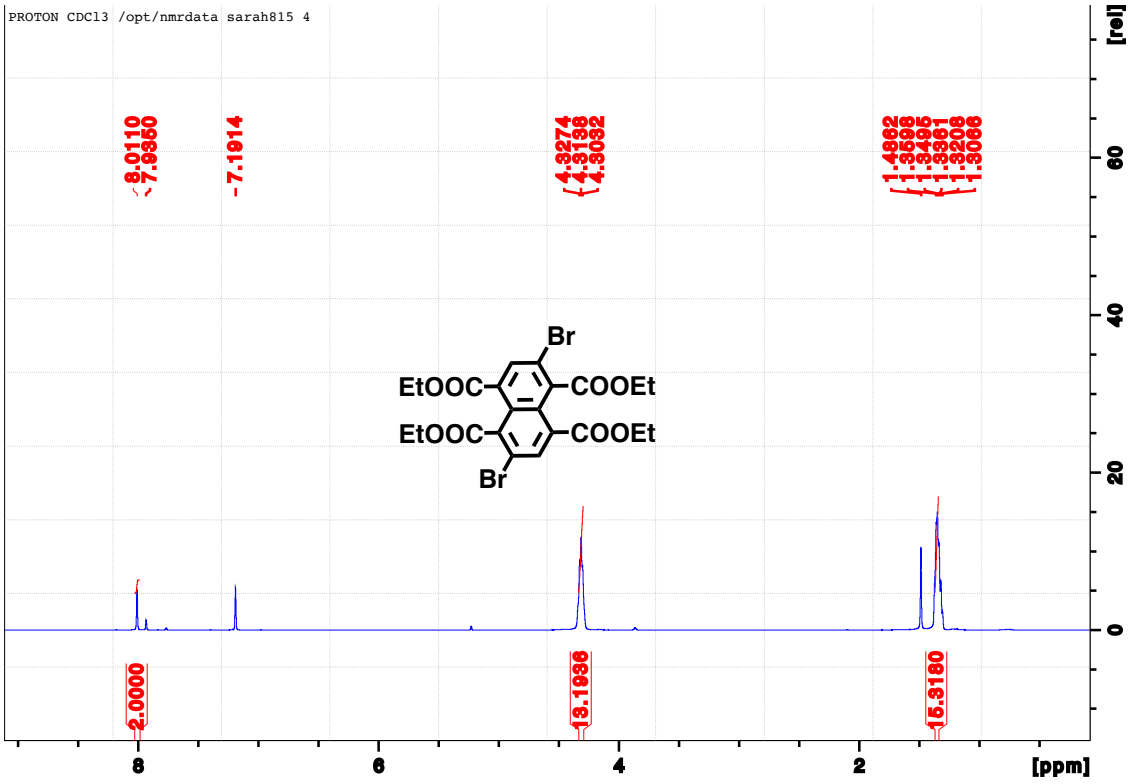

Figure B.2. Proton NMR of NTE-2Br (**3**) in $CDCl_3$.

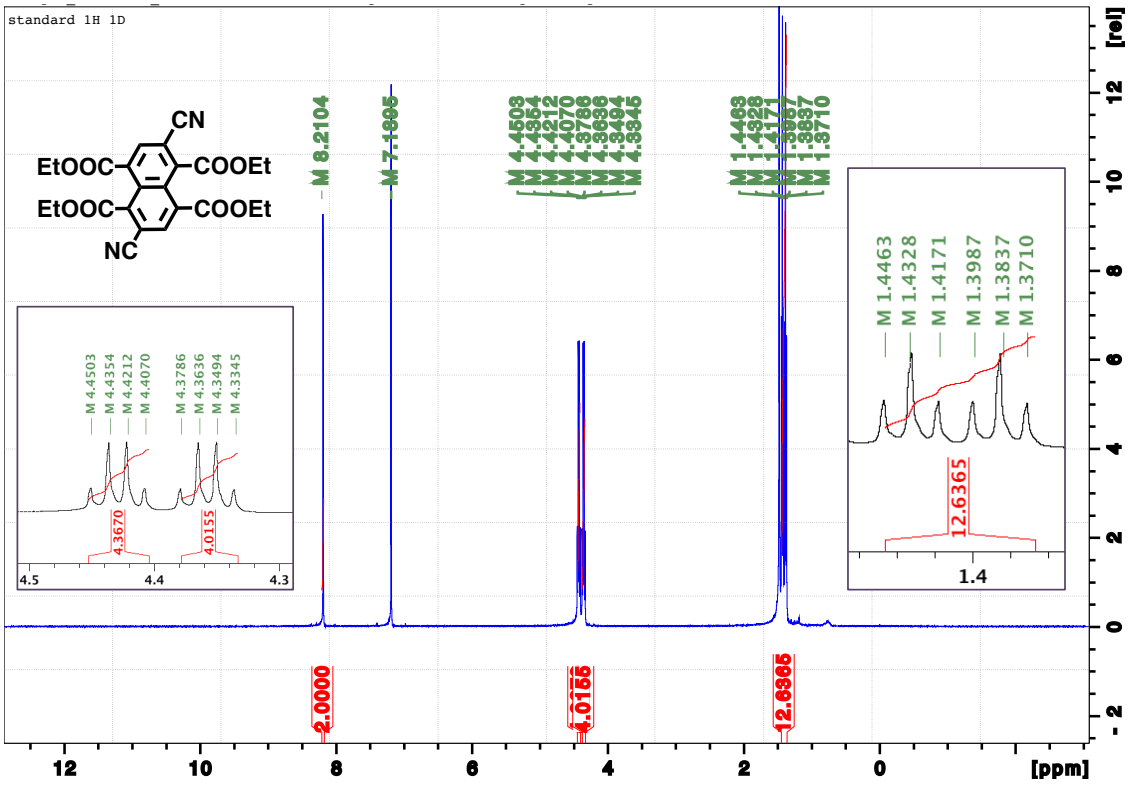

Figure B.3. Proton NMR of NTE-2CN (**4**) in $CDCl_3$. The inserts show the peak splitting.

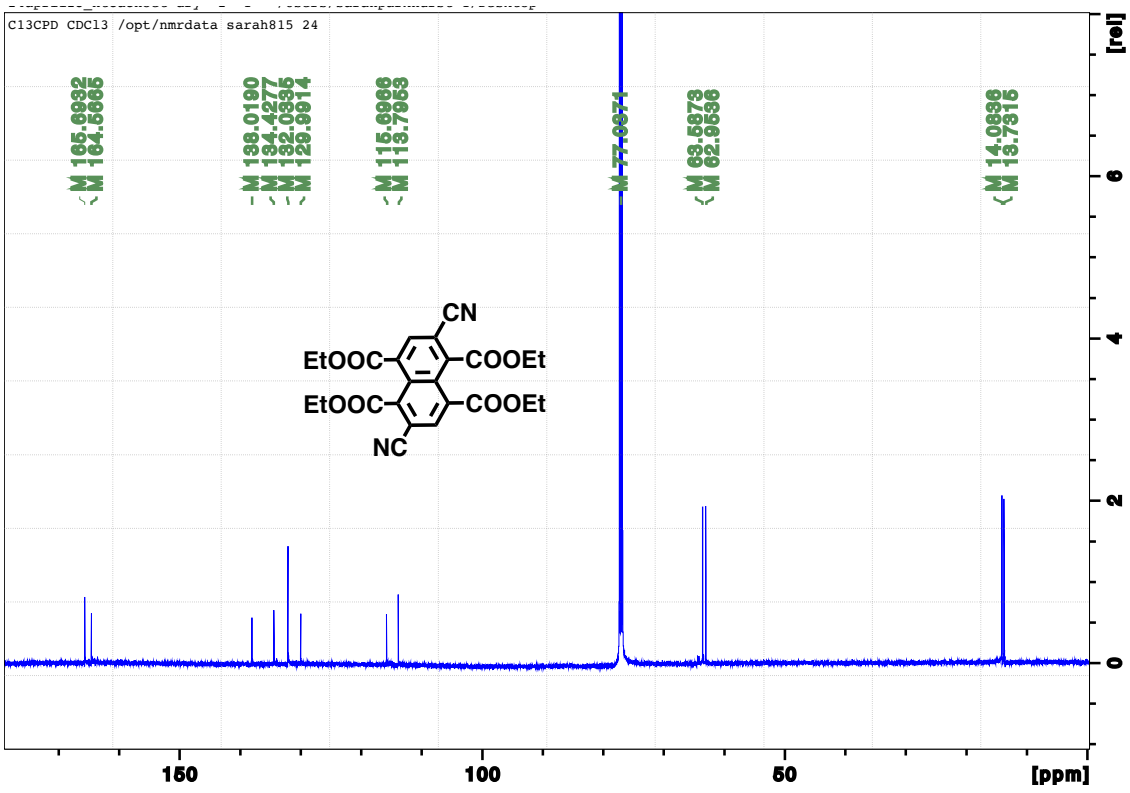

Figure B.4. Carbon NMR of NTE-2CN (**4**) in $CDCl_3$.

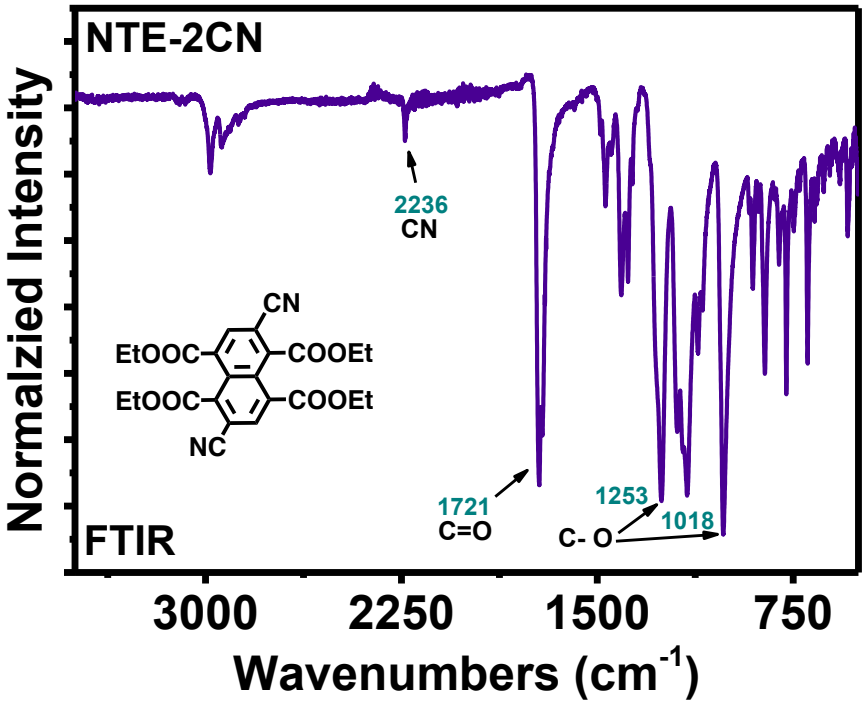

Figure B.5. FTIR spectrum of the NTE-2CN (**4**) crystals.

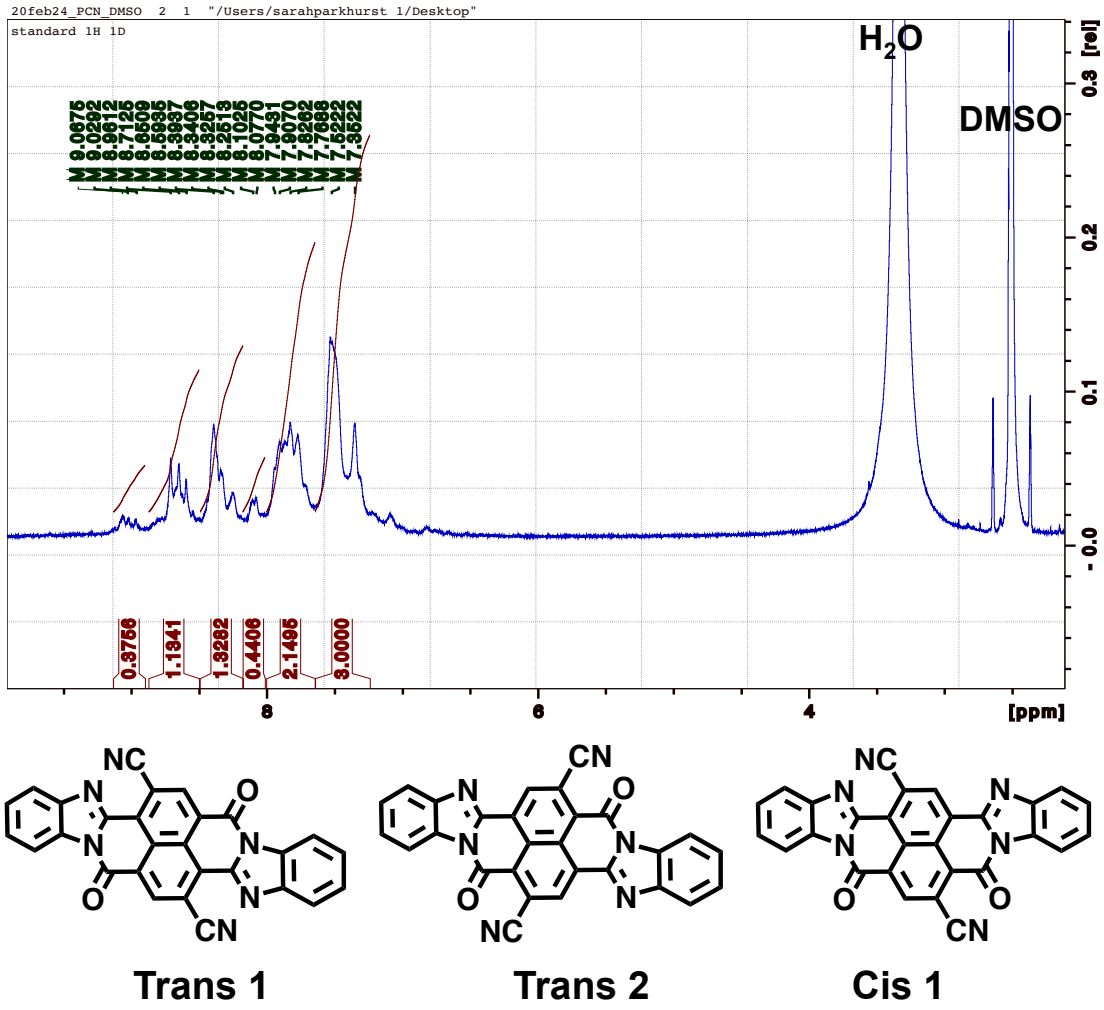

Figure B.6. Proton NMR of PCN in DMSO-d6 and the possible isomers of PCN, which contribute to the overlapping resonances in the aromatic region.

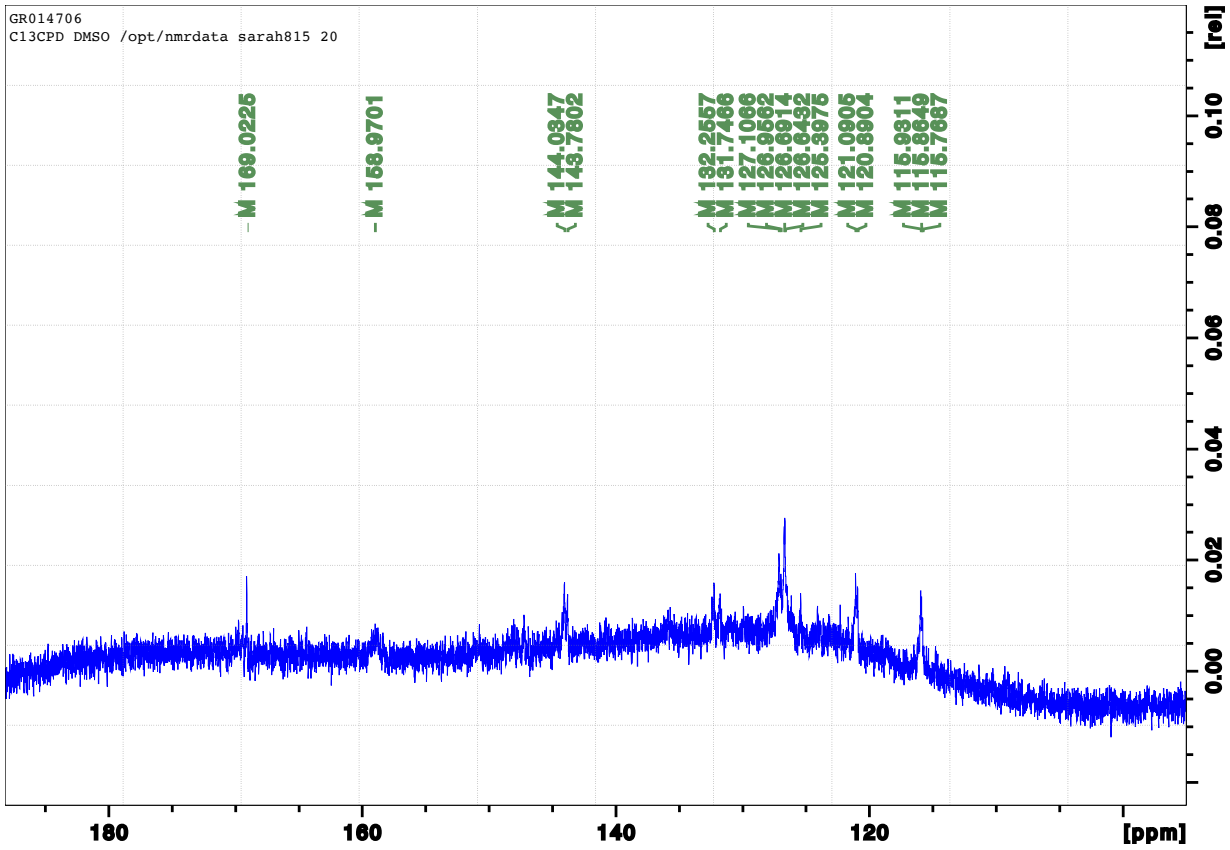

Figure B.7. Carbon NMR of PCN in DMSO-d6.

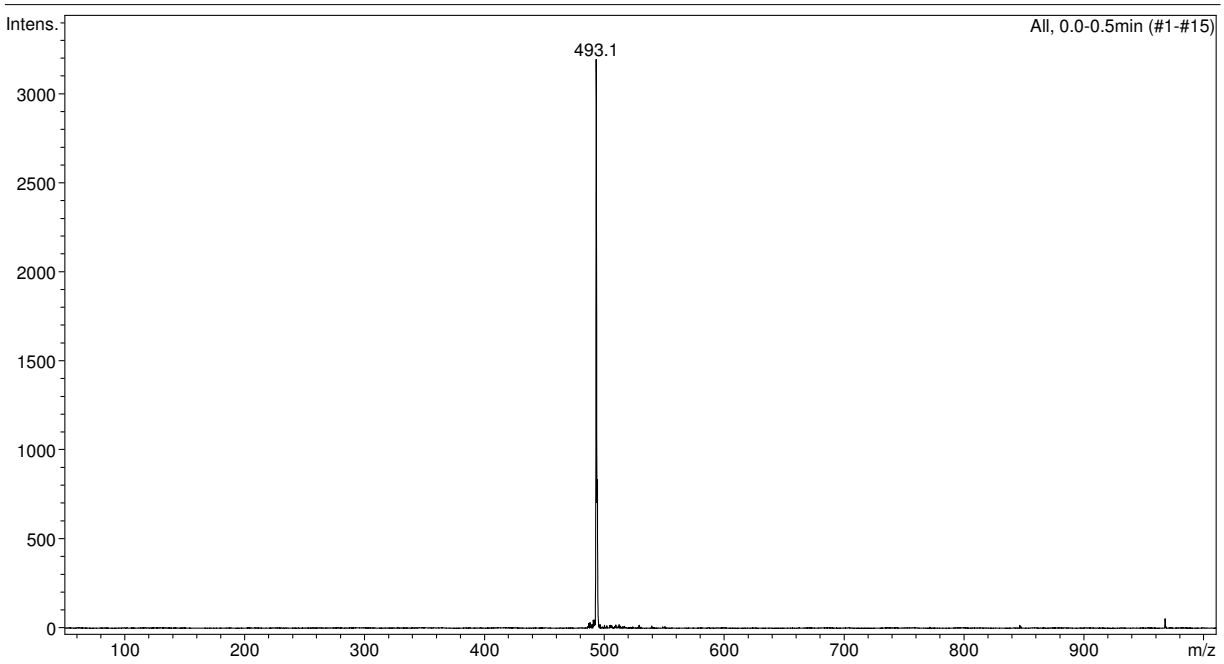

Figure B.8. ESI mass spectrum of PCN in dilute methanol (10^{-6} M).

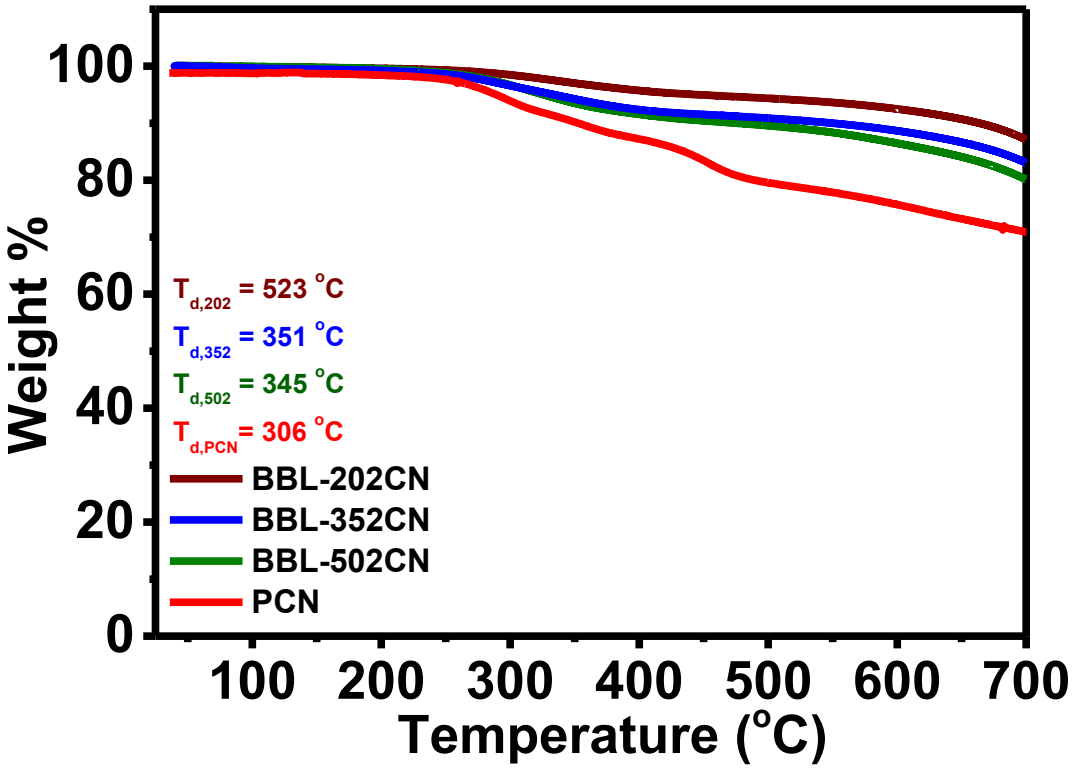

Figure B.9. TGA scans of the BBL-*x*2CN random copolymers under N_2 with a scan rate of 10˚C/min.

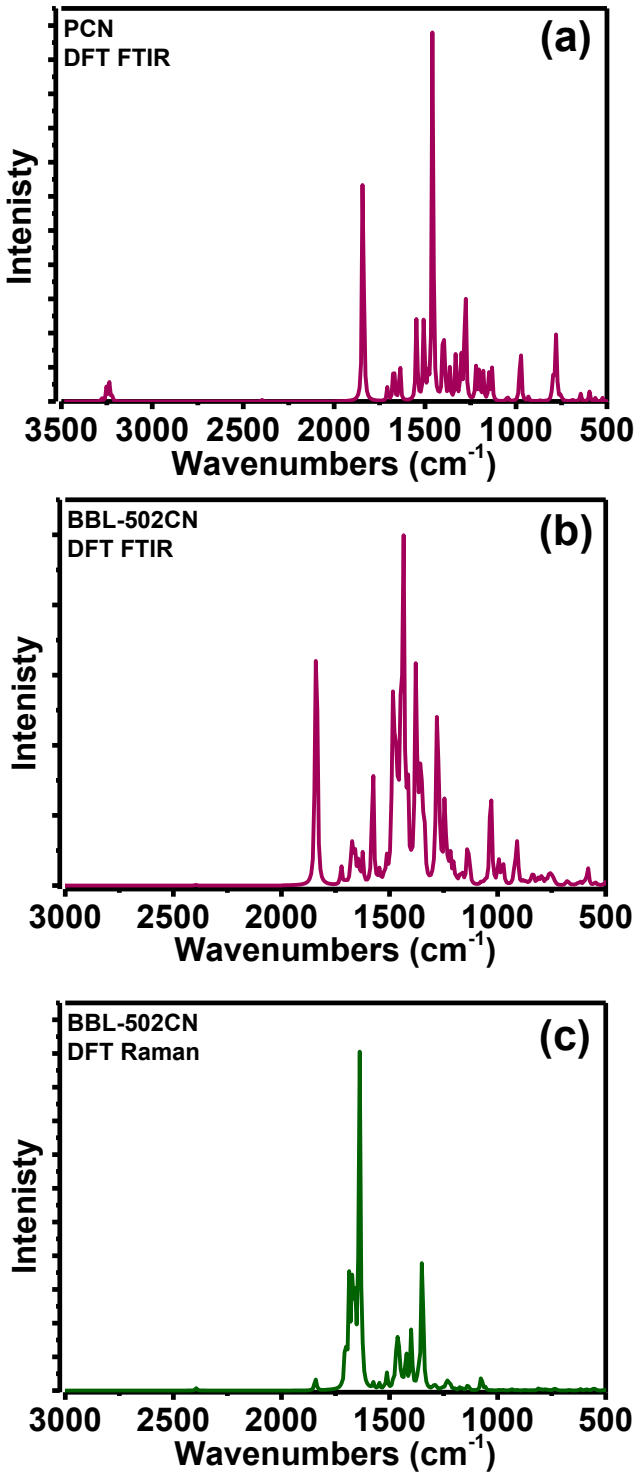

Figure B.10. DFT-calculated (a) FTIR spectrum of PCN, and the (b) FTIR and (c) Raman spectra of the BBL-502CN oligomer. Calculations were performed at the ωB97XD 6-31G(d,p) level of theory.

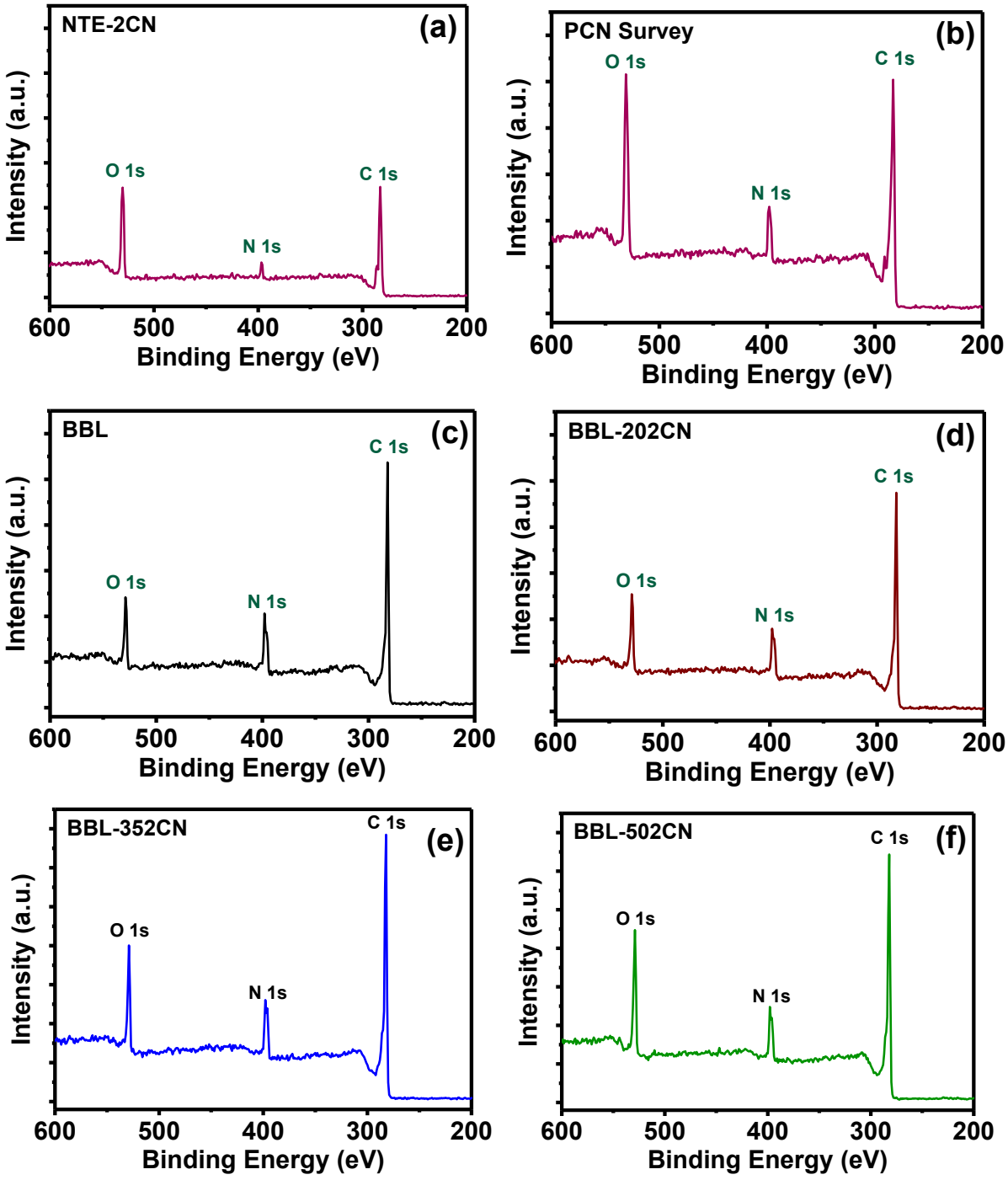

Figure B.11. Survey scans of the (a) NTE-2CN crystals on silicon substrates, and thin films on silicon substrates of (b) PCN, (c) BBL, (d) BBL-202CN, (e) BBL-352CN, and (f) BBL-502CN.

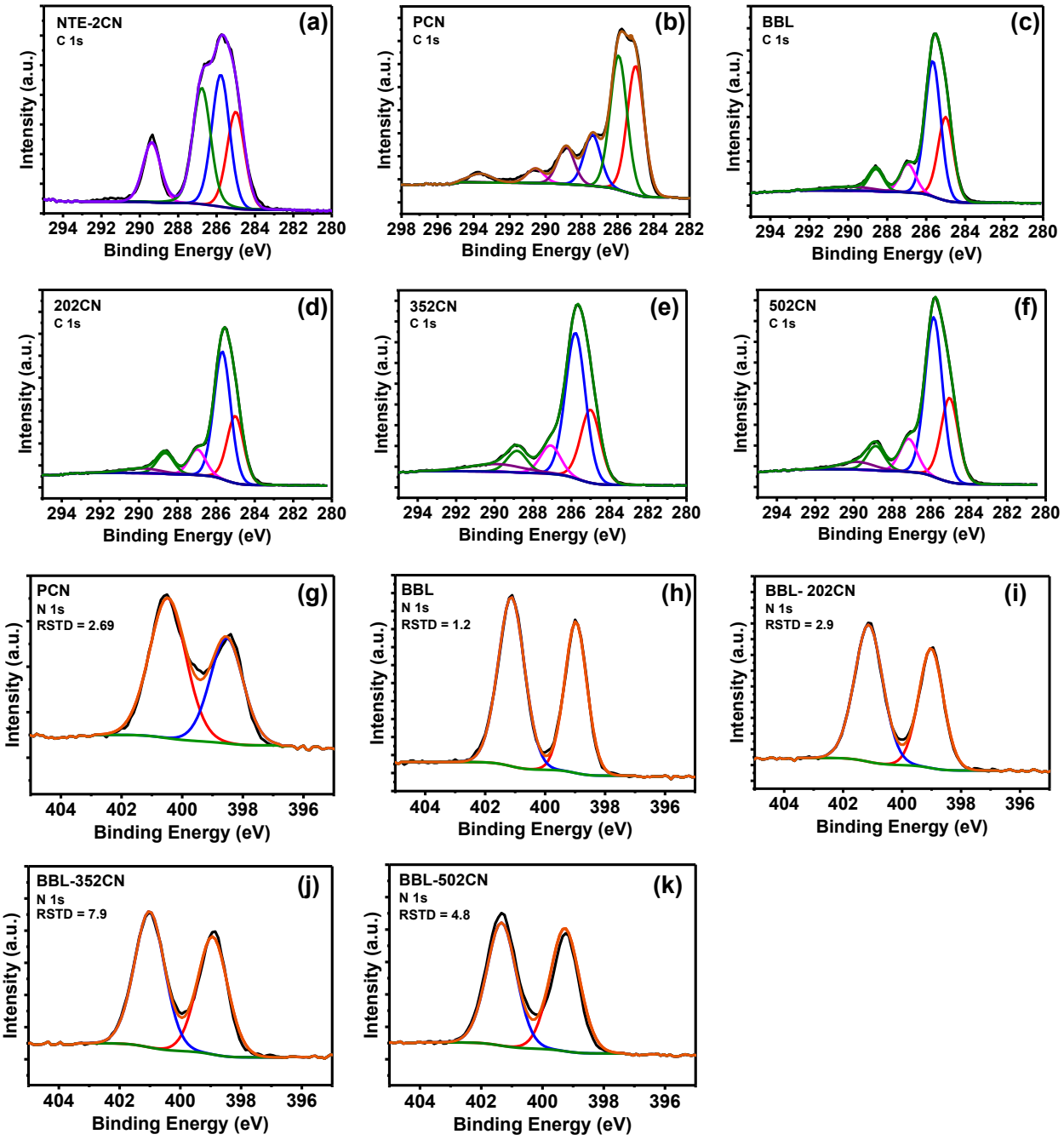

Figure B.12. XPS spectra of the C 1s peaks and their optimal fits of the (a) NTE-2CN monomer, (b) PCN model compound, and (c-f) the copolymers. N 1s spectra showing a two-peak fit with residual standard deviations (RSTD) for PCN (g) and (h-k) the copolymers.

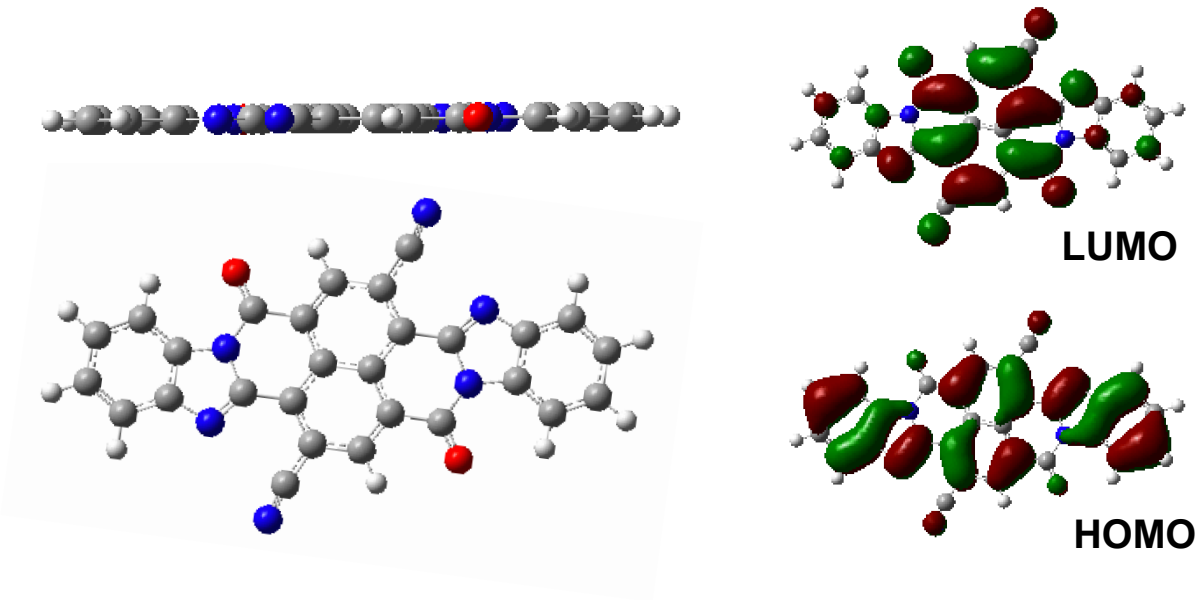

Figure B.13. DFT calculations of the optimized ground-state molecular geometry of PCN, and the pictoral representation of the ground-state frontier molecular orbitals. Calculations were performed at the ωB97XD/6-31G(d,p) level of theory.

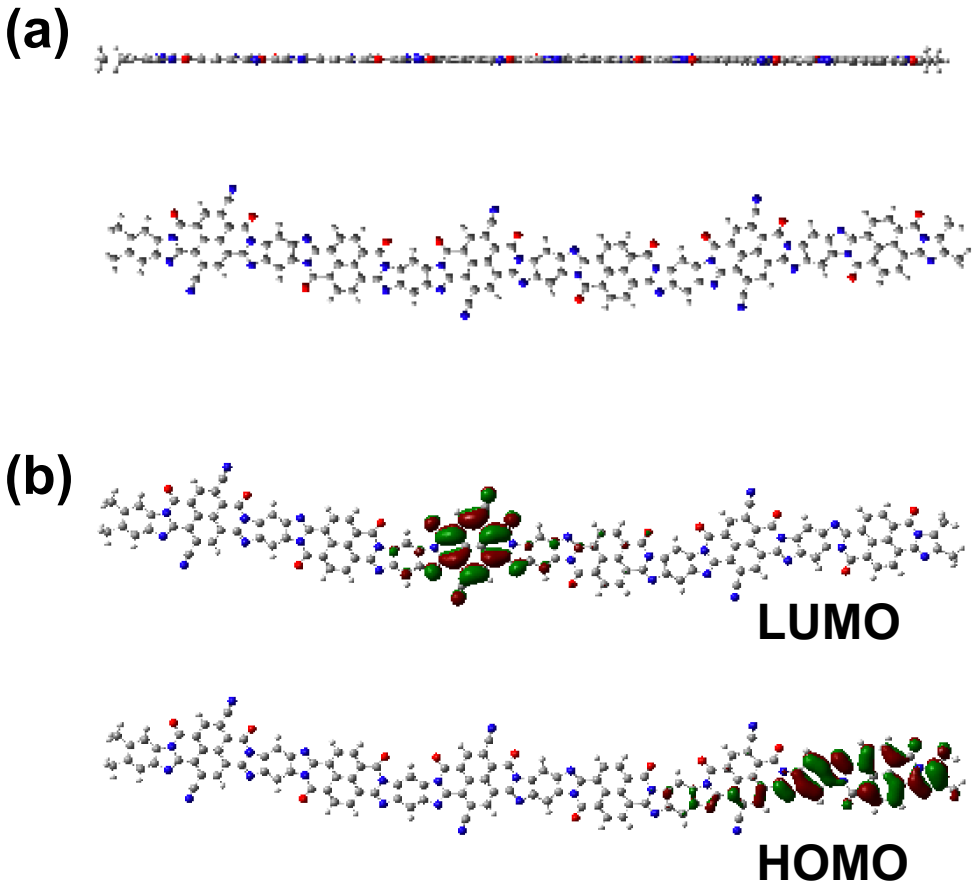

Figure B.14. DFT calculations of the optimized (a) ground-state molecular geometry of the representative BBL-502 oligomer comprised of 6 repeat units, and (b) the pictoral representation of the ground-state frontier molecular orbitals. Calculations were performed at the ωB97XD/6-31G(d,p) level of theory.

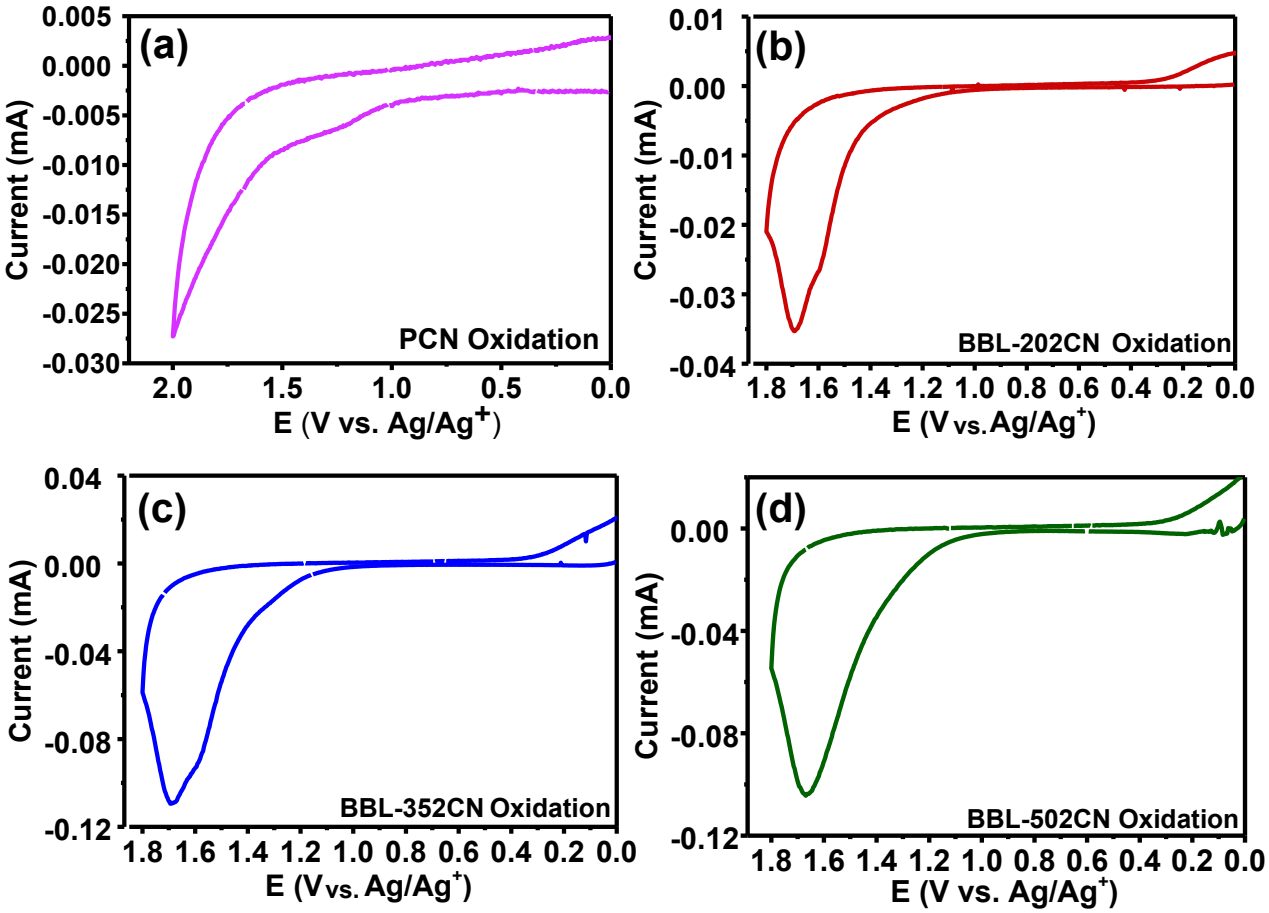

Figure B.15. Oxidation scans of (a) PCN (b) BBL-202CN, (c) BBL-352CN, and (d) BBL-502CN as thin films coated on platinum electrodes vs. Ag/Ag^{+} in anhydrous acetonitrile. The scan rate was 15 mV/s.

B.3 Supplementary Tables

Table B.1. Crystal Data and Structure Refinement for NTE-2CN.

Identification code	shelx	
Empirical formula	C24 H22 N2 O8	
Formula weight	466.43	
Temperature	100(2) K	
Wavelength	0.71073 Å	
Crystal system	Monoclinic	
Space group	C 2/c	
Unit cell dimensions	a = 15.2471(10) Å	α= 90°.
	b = 18.2854(13) Å	β= 98.299(4)°.
	c = 8.4312(6) Å	γ = 90°.
Volume	2326.0(3) $Å^3$	
Z	4	
Density (calculated)	1.332 Mg/m^3	
Absorption coefficient	0.101 mm^{-1}	
F(000)	976	
Crystal size	0.260 x 0.050 x 0.050 mm^3	
Theta range for data collection	1.750 to 25.154°.	
Index ranges	-18<=h<=18, -21<=k<=21, -10<=l<=10	
Reflections collected	36582	
Independent reflections	2018 [R(int) = 0.0342]	
Completeness to theta = 25.154°	96.7 %	
Refinement method	Full-matrix least-squares on F^2	
Data / restraints / parameters	2018 / 288 / 250	
Goodness-of-fit on F^2	1.039	
Final R indices [I>2sigma(I)]	R1 = 0.0597, wR2 = 0.1587	
R indices (all data)	R1 = 0.0672, wR2 = 0.1677	
Largest diff. peak and hole	0.425 and -0.414 e.$Å^{-3}$	

Table B.2. Atomic Coordinates (x 10^4) and Equivalent Isotropic Displacement Parameters ($Å^2$ x 10^3) for NTE-2CN. U(eq) is Defined as One Third of the Trace of the Orthogonalized U^{ij} Tensor.

	x	y	z	U(eq)
N(1)	5983(2)	2384(1)	6368(4)	75(1)
C(1)	5344(1)	5252(1)	5297(2)	27(1)
C(2)	6145(1)	4969(1)	6180(2)	33(1)
C(3)	6268(1)	4235(1)	6367(3)	35(1)
C(4)	5594(1)	3740(1)	5770(2)	34(1)
C(5)	4789(1)	3982(1)	4994(2)	31(1)
C(6)	5782(2)	2976(1)	6072(3)	49(1)
O(1)	3313(1)	3590(1)	5246(2)	36(1)
O(2)	4196(1)	2838(1)	4083(3)	40(1)
C(7)	4004(2)	3458(1)	4764(4)	35(1)
C(8)	3507(2)	2280(2)	3886(5)	46(1)
C(9)	3835(3)	1661(2)	3064(6)	57(1)
O(3)	6561(1)	5959(1)	8010(2)	34(1)
O(4)	7610(2)	5251(3)	7195(6)	48(1)
C(10)	6787(2)	5452(1)	7251(3)	28(1)
C(11)	8332(3)	5724(3)	7830(7)	65(1)
C(12)	8796(4)	5446(3)	9315(8)	90(2)
O(1A)	3922(4)	3525(4)	2625(7)	40(2)
O(2A)	4062(5)	2904(4)	4962(8)	44(1)
C(7A)	4228(6)	3446(4)	4017(8)	39(2)
C(8A)	3424(7)	2346(6)	4374(17)	45(2)
C(9A)	3864(12)	1724(7)	3770(20)	65(3)
O(3A)	7165(4)	5830(4)	5201(7)	69(2)
O(4A)	7547(5)	5233(5)	7563(10)	45(1)
C(10A)	7015(4)	5433(4)	6273(8)	50(1)
C(11A)	8241(4)	5643(5)	8492(9)	46(2)
C(12A)	9108(4)	5500(4)	8014(12)	55(2)

Table B.3. FTIR Absorption Bands and Their Peak Assignments for the Monomer NTE-2CN and the Model Compound PCN**.**

NTE-2CN FTIR Absorption Bands (cm^{-1})	PCN FTIR Absorption Bands (cm^{-1})	Assignment
2236	-	ν(CN), nitrile stretch
1721	1701	ν(C=O), carbonyl stretch
-	1590	ν(C=N), imine carbon-nitrogen stretch
1471, 1406	1541, 1476	Aromatic carbon-carbon skeletal stretches
-	1446	ν(C-N), carbon-nitrogen amide stretch
-	1374, 1335	ν(C-N), carbon-nitrogen single bond stretch
1198, 1153	1206, 1142	Mixed skeletal vibrations
1253, 1018	-	ν(C-O), carbon-oxygen ester stretch

Table B.4. FTIR and Raman Absorption Bands and Their Peak Assignments for the Random Copolymers.

BBL-*x*2CN FTIR Absorption Bands (cm^{-1})	BBL-*x*2CN Raman Absorption Bands (cm^{-1})	Assignment
-	-	ν(CN), nitrile stretch
1705	1706	ν(C=O), carbonyl stretch
1581	1594	ν(C=N), imine carbon-nitrogen stretch
1564, 1502	1530, 1381	Aromatic carbon-carbon skeletal stretches
1423	-	ν(C-N), carbon-nitrogen amide stretch
1373, 1304	1401	ν(C-N), carbon-nitrogen single bond stretch
1235, 994	1271, 1307, 988	Mixed skeletal vibrations

Table B.5. C 1s Binding Energies (B.E.) of the High-resolution Scans in Figure B.12.

Compound	C 1s/C-H B.E. (eV)	C 1s/C=C B.E. (eV)	C 1s/C-N B.E. (eV)	C 1s/C=N/C=O B.E. (eV)	C 1s/π-π* satellite B.E. (eV)
NTE-2CN	285.0	285.8	-	289.3	-
PCN	285.0	285.6	287.4	288.9	290.7
BBL	285.0	285.7	286.9	288.6	290.3
BBL-202CN	285.0	285.7	287.0	288.6	290.0
BBL-352CN	285.0	285.8	287.1	288.8	288.9
BBL-502CN	285.0	285.8	287.2	288.9	290.0

.

Table B.6. N 1s Binding Energies (B.E.), Full-Width at Half-Maximum (FWHM), and the Residual Standard Deviation (RSTD) of the 2 Peak and 3 Peak Fits of the High-resolution Scans in Figures 3.3 and B.12.

Compound	N 1s amide B.E. (eV)	N 1s Imine/nitrile B.E. (eV)	N 1s 3-peak fit FWHM (eV)	RSTD 2 peaks	RSTD 3 peaks
NTE-2CN	-	399.5	-	-	-
PCN	400.6	398.4	1.2	2.7	1.4
BBL	401.4	398.9	1.0	1.2	-
BBL-202CN	401.1	399.0	1.0	2.9	2.1
BBL-352CN	401.0	399.0	1.1	7.9	1.6
BBL-502CN	401.3	399.3	1.1	4.8	1.5

B.4 Supplementary References

1. Bruker **2007**, APEX2 (Version 2.1-4), SAINT (version 7.34A), SADABS (version 2007/4), BrukerAXS Inc, Madison, Wisconsin, USA.

2. Sheldrick G. M. A Short History of SHELX. *Acta. Cryst.* **2008**, A64, 112-122.

3. Sheldrick G. M. SHELXT - Integrated Space-Group and Crystal-Structure Determination. *Acta. Cryst.* **2015**, A71, 3-8.

4. Altomare, A.; Burla, C.; Camalli, M.; Cascarano, G. L.; Giacovazzo, C.; Guagliardi, A.; Moliterni, A. G. G.; Polidori, G.; Spagna, R. SIR97: A New Tool for Crystal Structure Determination and Refinement *J. Appl. Crystallogr*. **1999**, *32*, 115-119.

5. Altomare, A.; Cascarano, G. L.; Giacovazzo, C.; Guagliardi, A. Completion and Refinement of Crystal Structures with SIR 92. *J. Appl. Crystallogr*. **1993**, *26*, 343-350.

6. Sheldrick, G. M. SHELXL-97, Program for the Refinement of Crystal Structures. **1997,** University of Göttingen, Germany.

7. Sheldrick, G. M. Crystal Structure Refinement with SHELXL. *Acta. Cryst.* **2015**, C71, 3–8.

8. Waasmaier, D.; Kirfel, A. New Analytical Scattering Factor Functions for Free Atoms and Ions. *Acta. Cryst. A.* **1995***, 51*, 416-430.

Appendix C

Appendix C presents supplementary information to Chapter 3.2: Random Copolymers and Model Compound of Ladder Poly(benzimidazobenzophenanthroline) Featuring Dithiinotetracarbonitrile Groups: Synthesis and Electronic Structure

C.1 Additional Experimental Methods

X-ray Photoelectron Spectroscopy Experimental Setup

All XPS spectra were taken on a Kratos Axis-Ultra DLD spectrometer. This instrument has a monochromatized Al Kα X-ray and a low energy electron flood gun for charge neutralization. X-ray spot size for these acquisitions was on the order of 700 x 300 μm. Pressure in the analytical chamber during spectral acquisition was less than $5x10^{-9}$ Torr. Pass energy for survey and detailed spectra (composition) was 80 eV. Pass energy for the high-resolution spectra was 20 eV. The take-off angle (the angle between the sample normal and the input axis of the energy analyzer) was 0˚(0 degree take-off angle ~ 100 Å sampling depth). The Kratos Vision2 software program was used to determine peak areas and to calculate the elemental compositions from peak areas. CasaXPS was used to peak fit the high-resolution spectra. For the high-resolution spectra, a Shirley background was used and all binding energies were referenced to the C 1s C-C bonds at 285.0 eV.

Preparation of Polymer Thin Films on Glass Substrates.

The polymers was dissolved in methanesulfonic acid (MSA) at a concentration of 20 – 25 mg/mL and stirred at 125˚C for at least a week to ensure complete dissolution. Soda lime glass substrates or indium tin oxide (ITO) substrates were cleaned sequentially in detergent, DI water, acetone, and isopropyl alcohol. The cleaned substrates were treated with air plasma for 10 mins. The polymer solutions were spun on substrates at 1000 rpm for 30 seconds, and the wet films

were baked at 120˚C for 12 hours. At this stage, the thin films were sufficiently dried and showed a shiny gold surface. The resulting thin films showed dark brown color with a shiny gold surface and were used for further characterizations (XPS, UV-Vis).

Fabrication of Freestanding Films.

Films of the polymers were prepared on initial supporting glass substrates where the polymer solution (10 mg/mL – 15 mg/mL) in MSA was drop cast onto glass substrates, and the films were baked at 170˚C for 10 minutes. The polymer thin films were slowly cooled down to room temperature and submerged in DI water. Upon exposure to water, the polymer films can be peeled from the supporting substrate, floated on water surface, lifted off, and dried under vacuum to form freestanding films. These freestanding films were used for further characterizations (FTIR and Raman spectroscopy).

C.2 Supplementary Figures

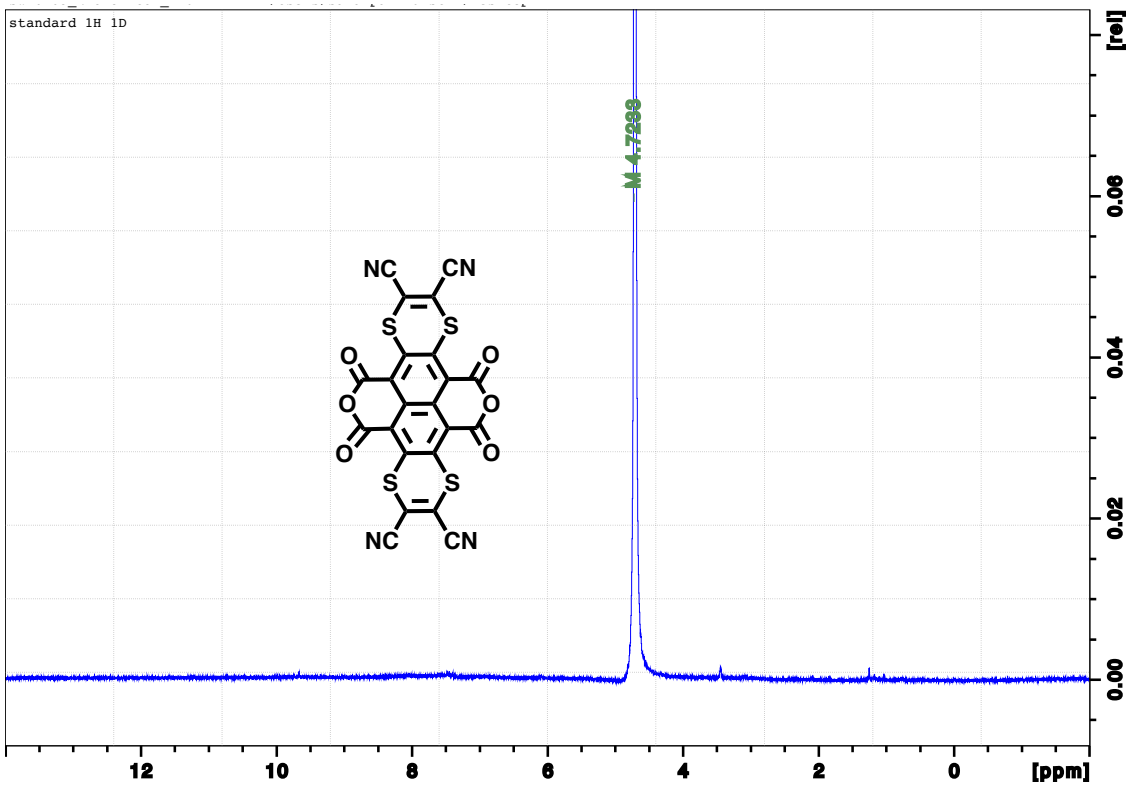

Figure C.1. Proton NMR of the NTA-TCN monomer dissolved in D_2O+NaOH.

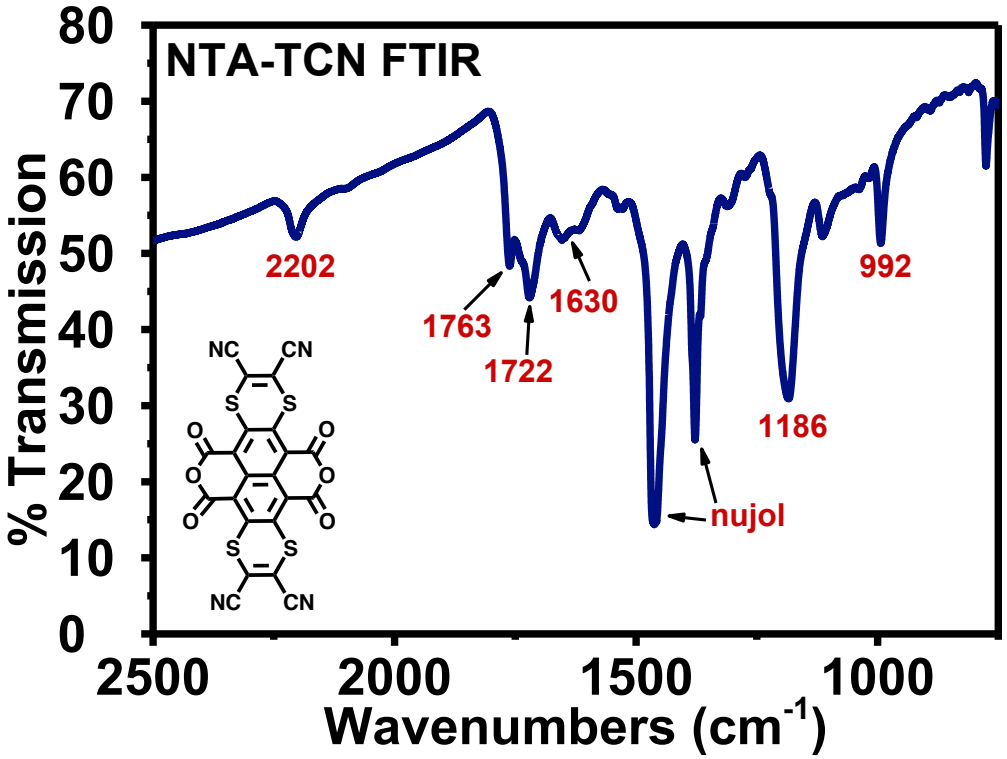

Figure C.2. FTIR spectrum of the NTA-TCN monomer in a Nujol mull. The peak at 2202 cm^{-1} is the nitrile stretch.

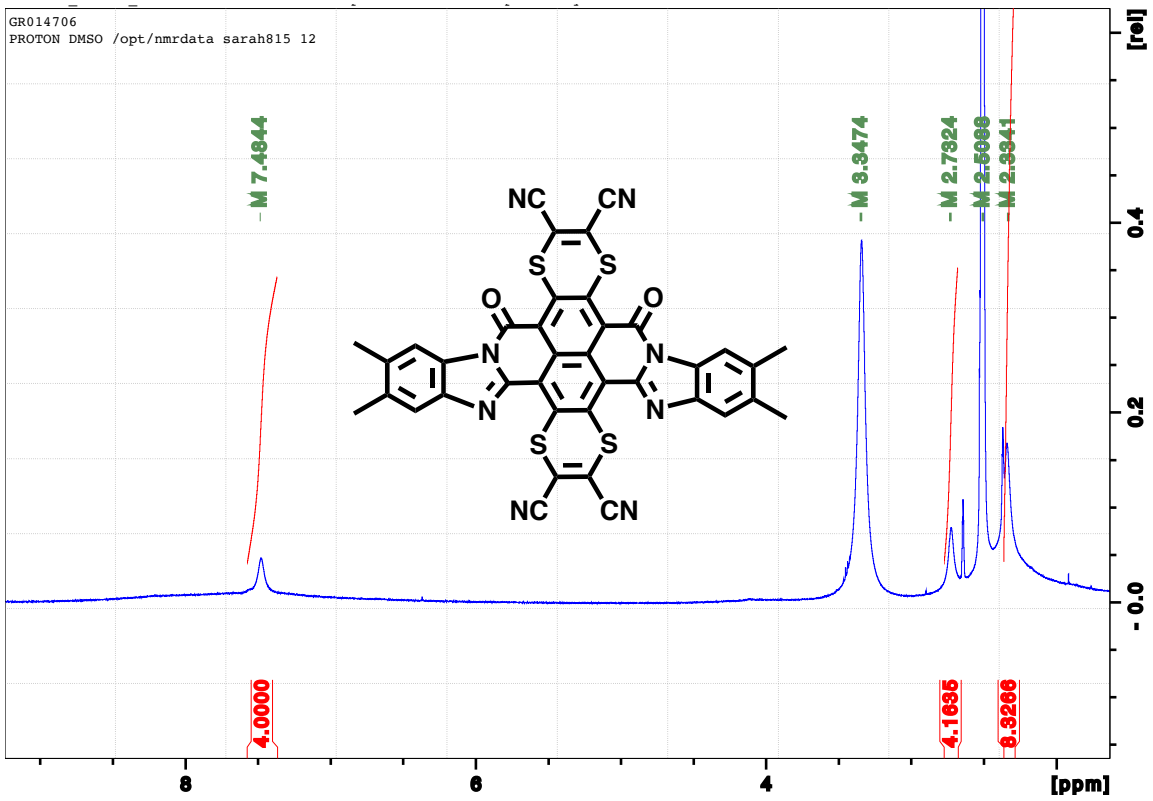

Figure C.3. Proton NMR of PTCNMe dissolved in DMSO-d6. The methyl groups are overlapping with the satellite peaks of DMSO-d6.

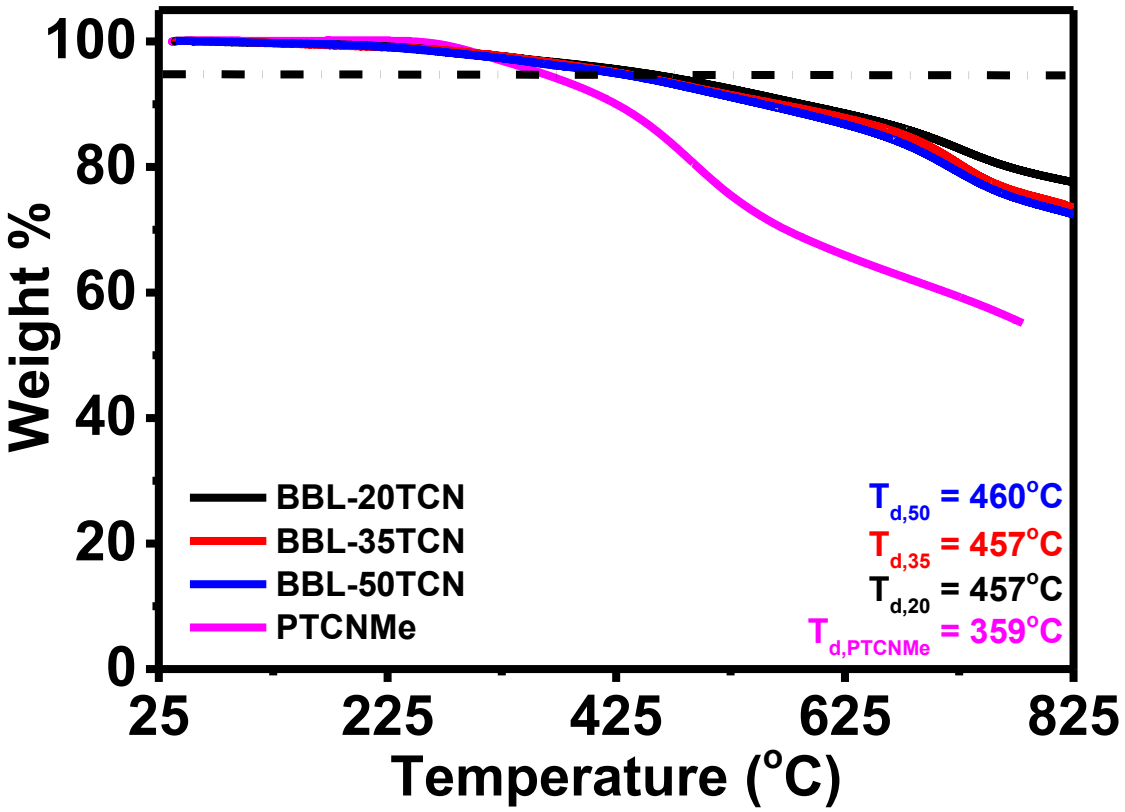

Figure C.4. Thermogravimetric analysis (TGA) scans of the BBL-*x*TCN random copolymers and model compound under N_2 at a heating rate of 10˚C/min. The dashed line marks 5% weight loss.

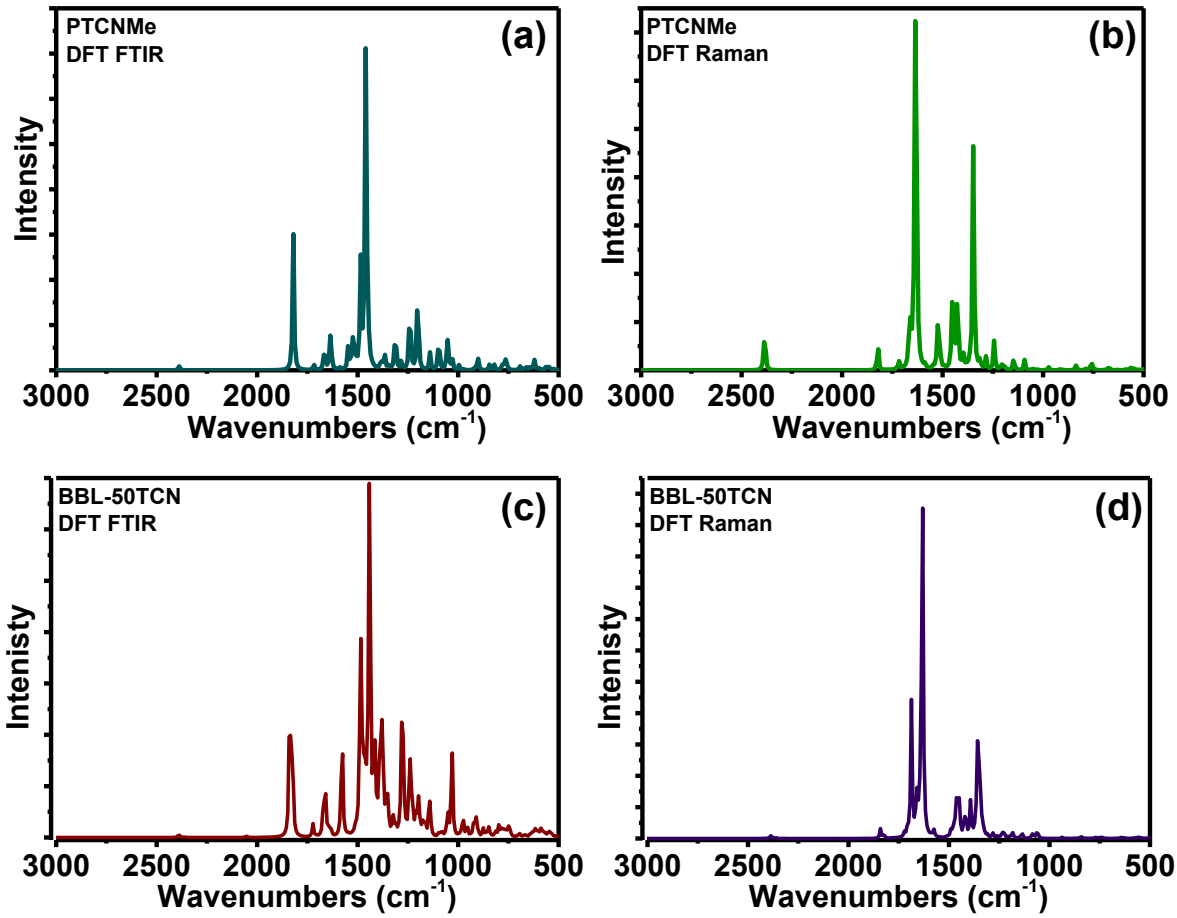

Figure C.5. The DFT-predicted (a,c) FTIR and (b,d) Raman spectra for PTCNMe and BBL-50TCN. The calculations were performed at the ωB97XD/6-31G(d,p) level of theory.

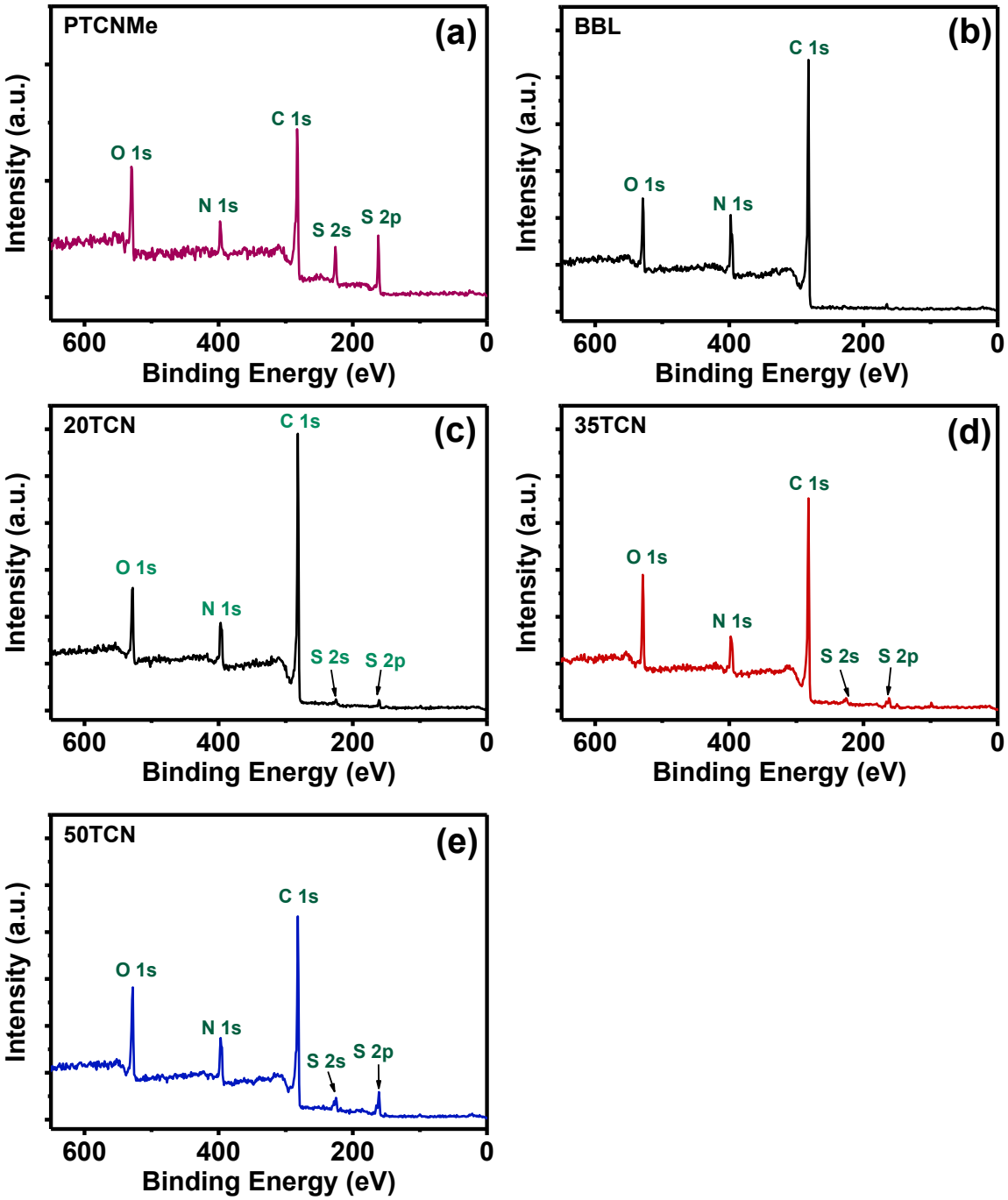

Figure C.6. XPS survey scans of thin films on silicon substrates of the (a) PTCNMe, (b) BBL, (c) BBL-20TCN, (d) BBL-352CN, and (e) BBL-50TCN.

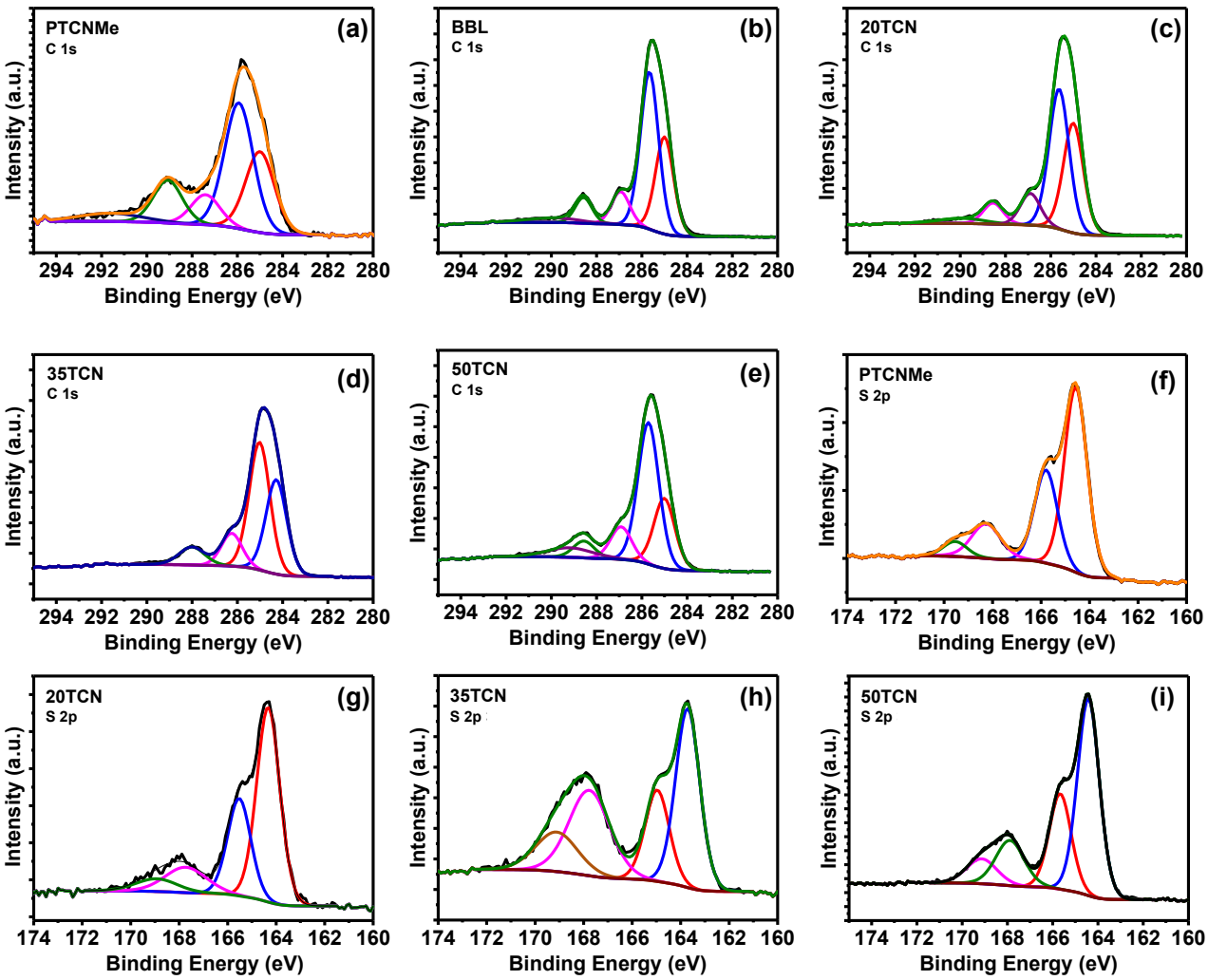

Figure C.7. XPS spectra of optimally fit C 1s and S 2p emissions for (a,f) PTCNMe, (b) BBL, (c,g) BBL-20TCN, (d,h) BBL-352CN, and (e,i) BBL-502CN. The peaks at ~ 168 eV in the S 2p spectra are due to an oxidized sulfur species, likely from residual methanesulfonic acid.

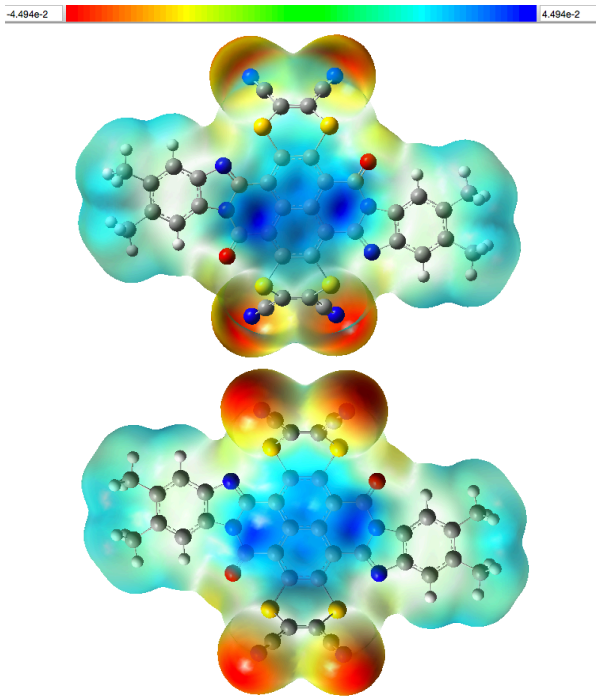

Figure C.8. Electrostatic potential map of PTCNMe showing top and bottom views calculated at the DFT ωB97XD/6-31G(d,p) level of theory.

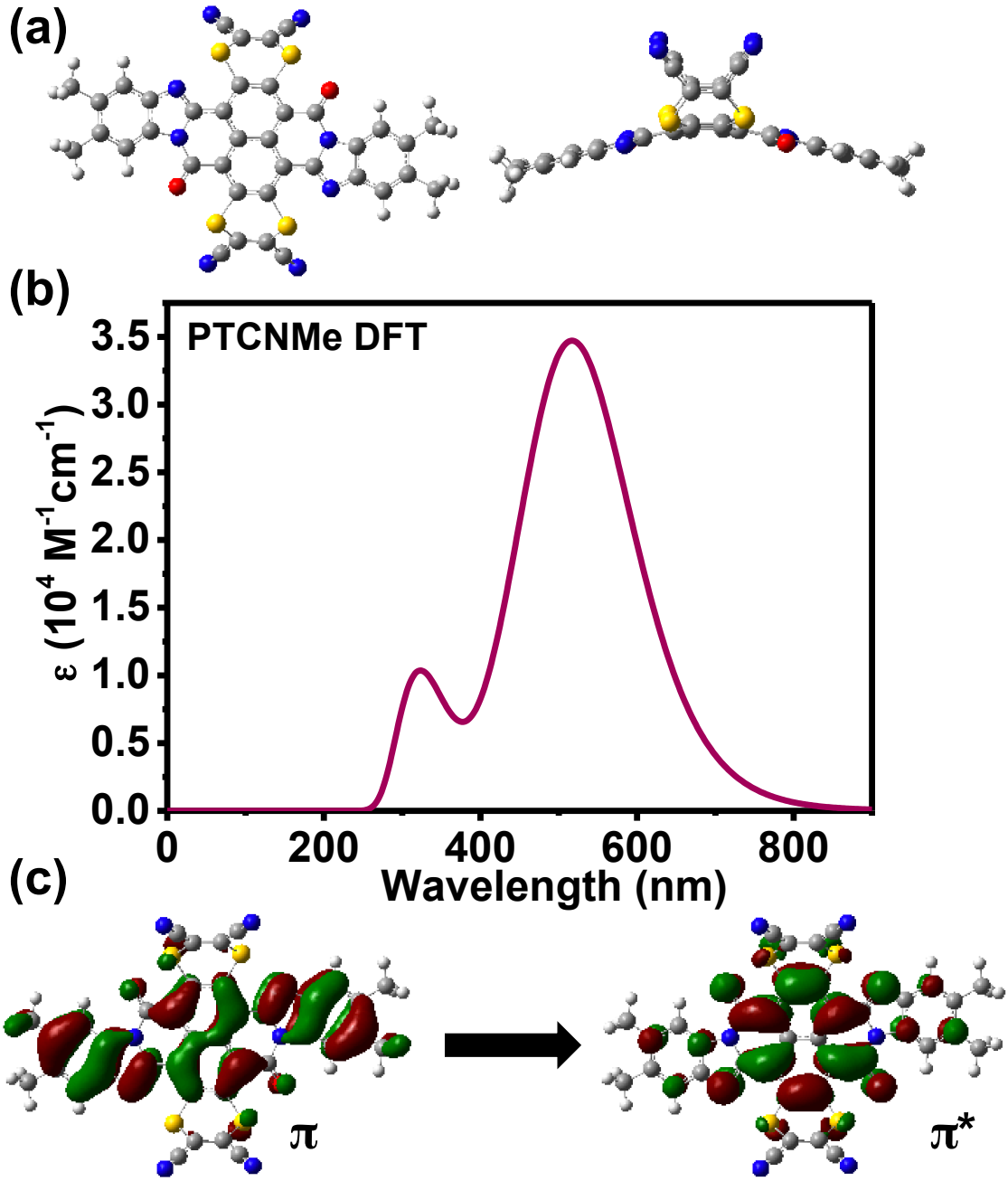

Figure C.9. TD-DFT calculations performed at the ωB97XD/6-31G(d,p) level of theory on the model compound showing (a) the excited state geometry, (b) simulated absorption spectra, and (c) the pictoral representations of the hole and electron orbital distributions show the lowest energy transition (π-π*) at 576 nm. The calculations were run for n = 12 excited states.

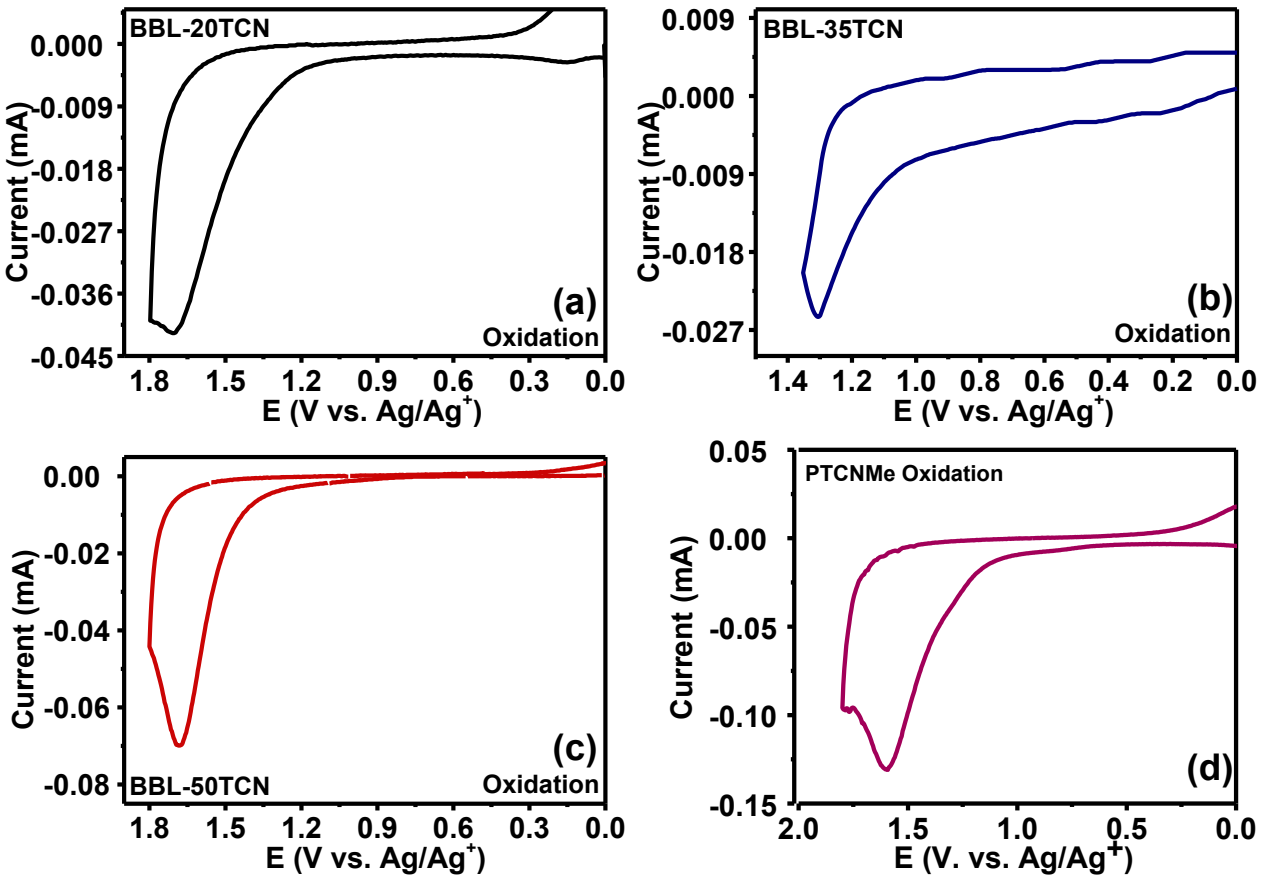

Figure C.10. Cyclic voltammetry oxidation scans for (a) BBL-20TCN, (b) BBL-35TCN, (c) BBL-50TCN, and (d) PTCNMe vs. $Ag/AgNO^3$ in acetonitrile with 0.1 M Bu_4NPF_6 at a scan rate of 15 mV/s.

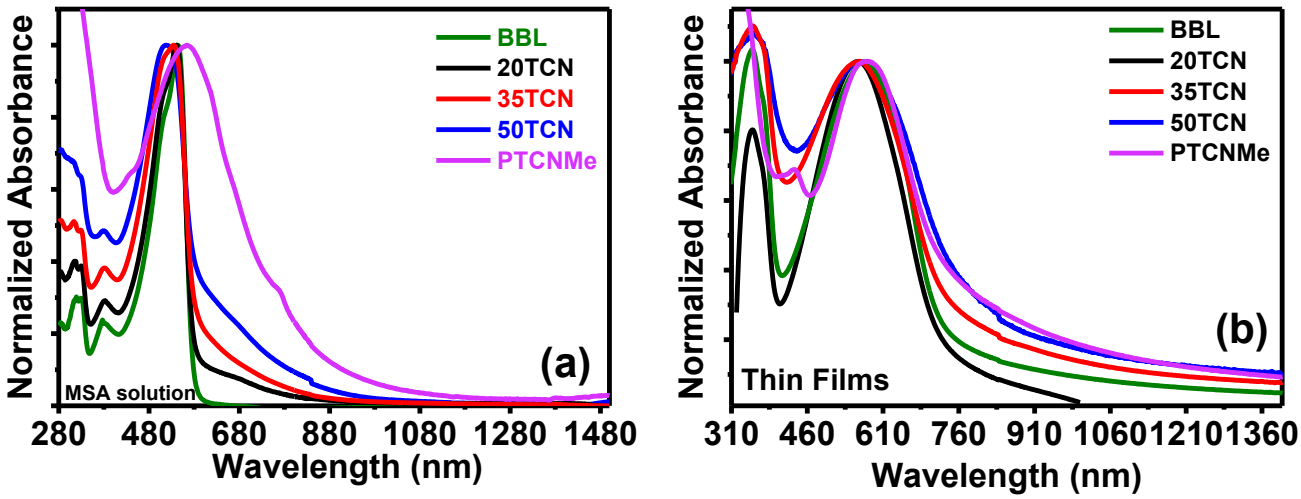

Figure C.11. Normalized optical absorption spectra of PTCNMe and the BBL-*x*TCN random copolymers (a) in dilute MSA solutions (10^{-5}M) and (b) as thin films on glass substrates.

C.3 Supplementary Tables

Table C.1. FTIR and Raman Absorption Bands and Peak Assignments for PTCNMe.

FTIR Absorption Band (cm^{-1})	Raman Absorption Band (cm^{-1})	Assignment
-	2458	ν(CN), nitrile stretch
1760	1761	ν(C=C), alkene stretch
1697	1713	ν(C=O), carbonyl stretch
1654	1582	ν(C=N), imine carbon-nitrogen stretch
1540, 1415	1555, 1414	Aromatic carbon-carbon skeletal stretches
1325	-	ν(C-N), carbon-nitrogen single bonds
1177	1256, 1189	Mixed skeletal vibrations
-	1099	C-H bending and wagging
996	1042	ν(C-S), carbon-sulfur stretch

Table C.2. FTIR and Raman Absorption Bands for the BBL-*x*TCN Random Copolymer Freestanding Films.

FTIR Absorption Band (cm^{-1})	Raman Absorption Band (cm^{-1})	Assignment
1705	1704	ν(C=O), carbonyl stretch
1632	1590	ν(C=N), imine carbon-nitrogen stretch
1503, 1466	1535, 1382	Aromatic carbon-carbon skeletal stretches
1417	-	ν(C-N), carbon-nitrogen amide bonds
1380, 1305	-	ν(C-N), carbon-nitrogen single bonds
1239, 1180	1267, 1020, 990	Mixed skeletal vibrations
-	725	C-H bending and wagging
949	-	ν(C-S), carbon-sulfur stretch

Table C.3. C 1s Binding Energies (B.E.) and the Corresponding Full-width at Half-maximum (FWHM) for the Fitted Peaks for PTCNMe, BBL, and the BBL-*x*TCN Random Copolymers

Compound	[a]C 1s, B.E. (eV)	[a]C 1s, B.E. (eV)	[a]C 1s B.E. (eV)	[a]C 1s B.E. (eV)	[b]FWHM (eV)
PTCNMe	285.0	285.9	287.4	289.1	1.5
BBL	285.0	285.7	286.9	288.6	0.9
20TCN	285.0	285.6	288.6	286.9	1.0
35TCN	285.0	285.7	287.0	288.7	1.1
50TCN	285.0	285.7	286.9	288.6	1.1

[a]Peaks corresponding to 1s bonds. [b] FWHM of the individual fitted peaks corresponding to Figure C.7.

Table C.4. N 1s, S 2p, and O 1s Binding Energies for PTCNMe and the BBL-*x*TCN Random Copolymers Calibrated to the Lowest Energy Carbon Peak at 285.0 eV.

Compound	N 1s, imine/nitrile B.E. (eV)	N 1s, amide B.E. (eV)	N 1s FWHM (eV)	S 2p B.E. (eV)
PTCNMe	401.0/399.5	402.8	1.7	164.6
BBL	399.0	401.1	1.0	-
20TCN	399.1	401.1	1.1	164.3
35TCN	399.1	401.3	1.2	163.9
50TCN	399.0	401.1	1.2	164.4

Appendix D

Appendix D presents supplementary information to Chapter 4: p-Type Semiconducting Ladder Poly(pyrrolobenzothiazine)s: Effects of N-Alkyl Side Chains on the Chain Conformation, Electronic Structure, and Charge Transport Properties.

D.1 Additional Experimental Methods

Fabrication of Thin Films.

Films of LPBT and LPBT-Me were prepared on glass substrates where LPBT and LPBT-Me thin films were deposited by spin-coating from their respective MSA solutions (25 mg/mL) at 4500 - 5000 rpm for 30 seconds. The acidic solvent was removed by dipping the films in a mixture of isopropanol (IPA) and ethylene glycol (EG) (1:1, v:v) several times for 12 hours. Afterwards, films were submerged in 100% IPA for several times before subjected to drying in vacuum oven at 60^{o}C overnight. Finally, the LPBT and LPBT-Me films were annealed at 170˚C on a hot plate for 10 min.

Fabrication of Freestanding Films.

Films of LPBT and LPBT-Me were prepared on initial supporting glass substrates using a similar procedure as described above where the polymer solution (25 mg/mL) drop-cast onto a hot substrate and baked overnight at 120˚C. Instead of additional annealing at higher temperature, the thin films were then slowly cooled down to room temperature and submerged in water. Thus, films can be peeled from the supporting substrate, floated on water, lifted off using a copper wire, and dried at 120˚C to form freestanding films. These freestanding films were used for further characterizations (FT-IR and Raman Spectroscopies).

Fabrication and Characterization of OFETs.

p-channel organic field-effect transistors (OFETs) were fabricated in a bottom-gate top-contact device architecture with a polymer buffer layer. The substrate is comprised of heavily p-doped silicon (< 0.005 S/cm; 500 cm) with a 300 nm-thick silicon oxide layer. The substrates were cleaned by sequentially sonicating in DI water, acetone, and isopropyl alcohol. The cleaned substrates were then treated with air plasma for 10 min. Insulating polystyrene (PS) was dissolved in anhydrous toluene (5 mg/mL) and stirred at room temperature overnight. The PS solution was spin-coated onto the substrates at 3000 rpm for 60 seconds to produce a 17.0 nm (± 0.12 nm) thick layer, followed by drying in vacuum at 60˚C overnight. On top of the PS-coated substrates, the LPBT and LPBT-Me thin films were deposited by spin-coating from their respective MSA solutions (25 mg/mL) at 4500 - 5000 rpm for 30 seconds. The acidic solvent was removed by dipping the films in a mixture of isopropanol (IPA) and ethylene glycol (EG) (1:1, v:v) several times for 12 hours. Afterwards, films were submerged in 100% IPA for several times before subjected to drying in vacuum oven at 60˚C overnight. Finally, the LPBT and LPBT-Me films were annealed at 170˚C on a hot plate for 10 min in a nitrogen-filled glovebox. Source and drain electrodes were defined by thermal evaporation of gold electrodes (50 nm). Channel width (W) and length (L) were 1000 μm and 100 μm, respectively. The transistors were tested by using two Keithley 2400 Sourcemeters inside a nitrogen atmosphere. The field-effect electron mobility was extracted by analyzing the current – voltage data with the saturation-region equation:

$$I_{ds} = \frac{\mu W C_i}{2L}(V_G - V_T)^2$$

where I_{DS} is the source-drain current, μ is field-effect mobility, C_i is the capacitance of gate insulator (10.6 nF/cm^2), V_{GS} is source-gate voltage bias, and V_T is threshold voltage.

D.2 Supplementary Figures

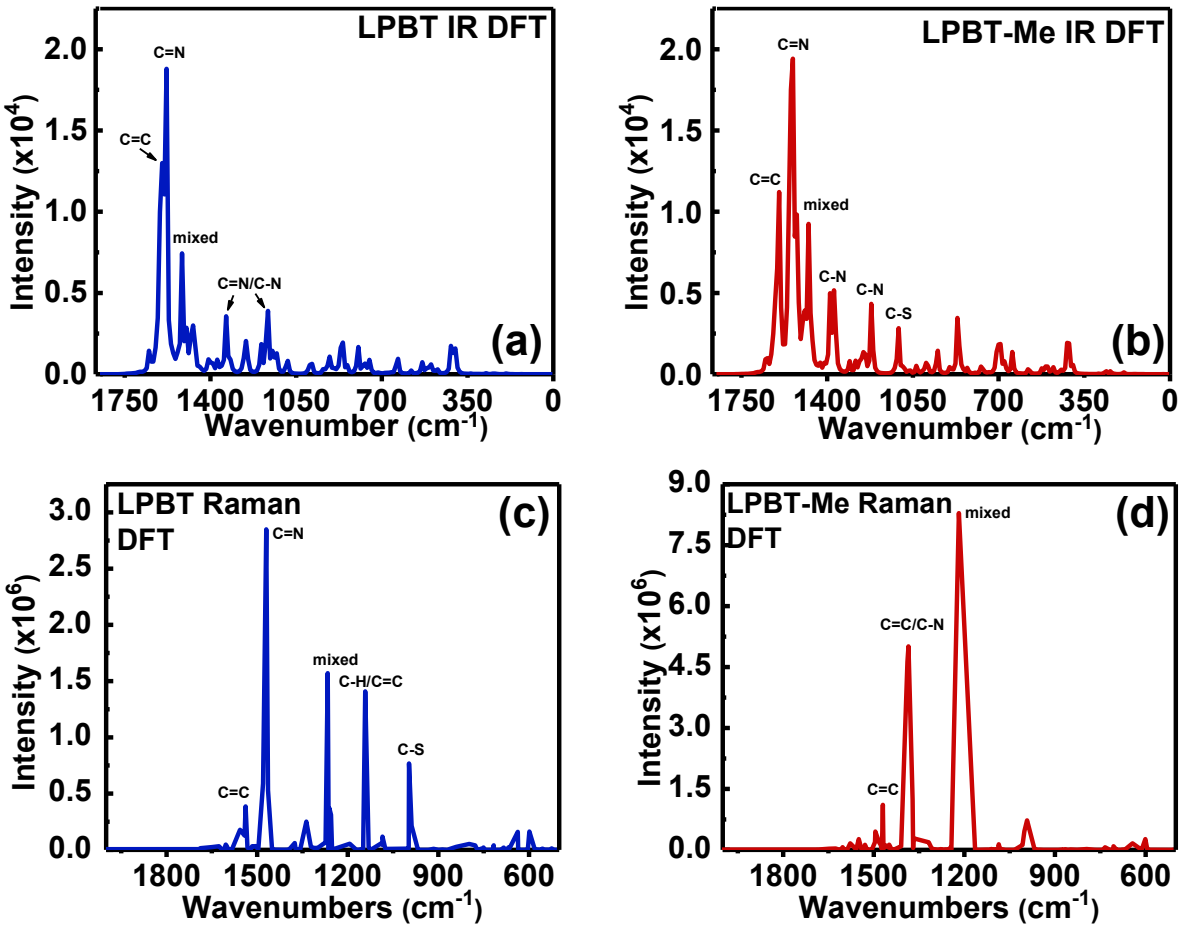

Figure D.1. DFT ωB97XD/6-31G(d,p) level of theory calculated IR spectra for (a) LPBT and (b) LPBT-Me. DFT-calculated Raman spectra for (c) LPBT and (d) LPBT-Me. The peak assignments and corresponding vibrational modes are in Tables D.1 and D.2.

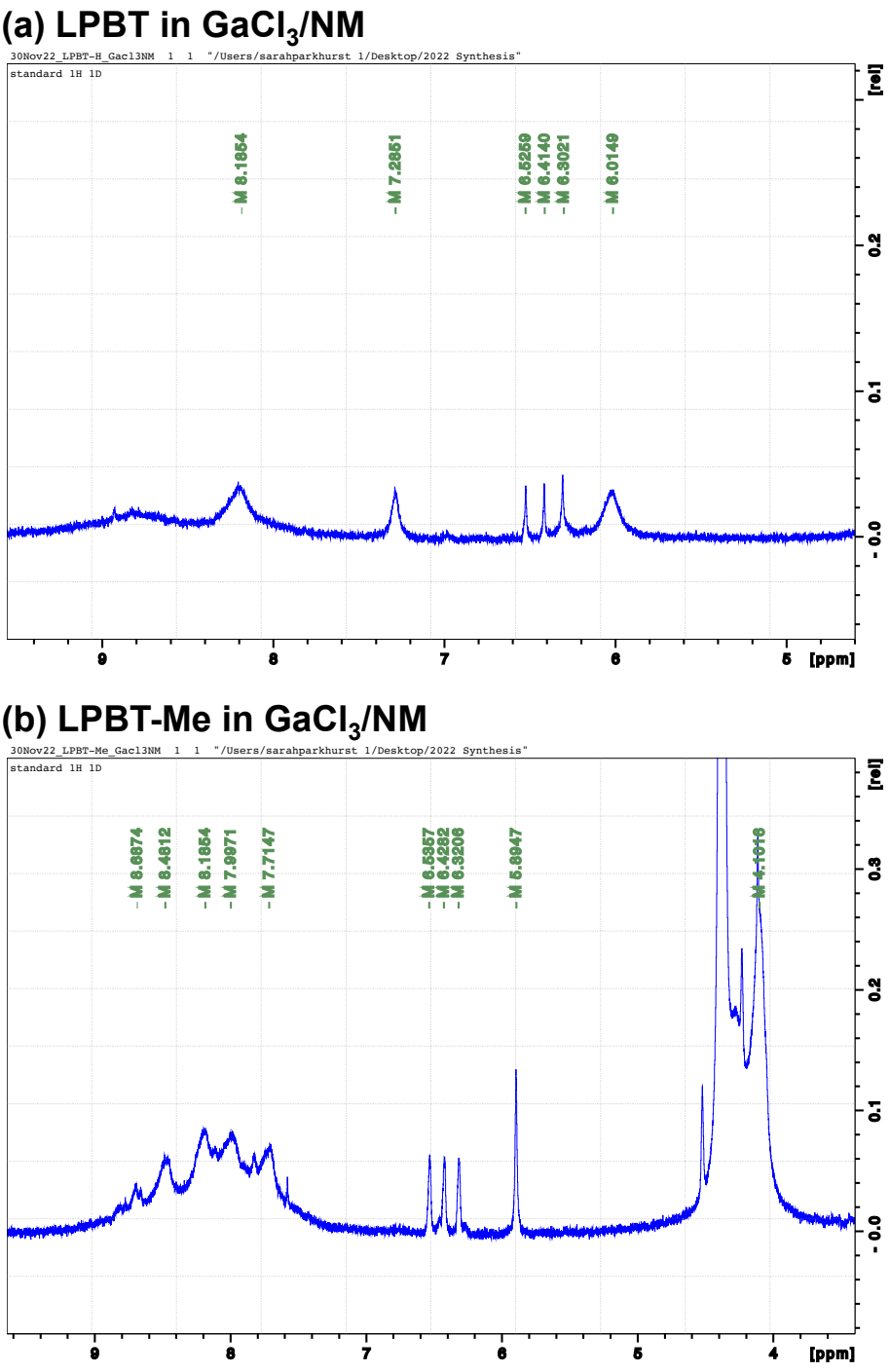

Figure D.2. Proton NMR spectra of (a) LPBT and (b) LPBT-Me in $GaCl_3$/nitromethane-d3.

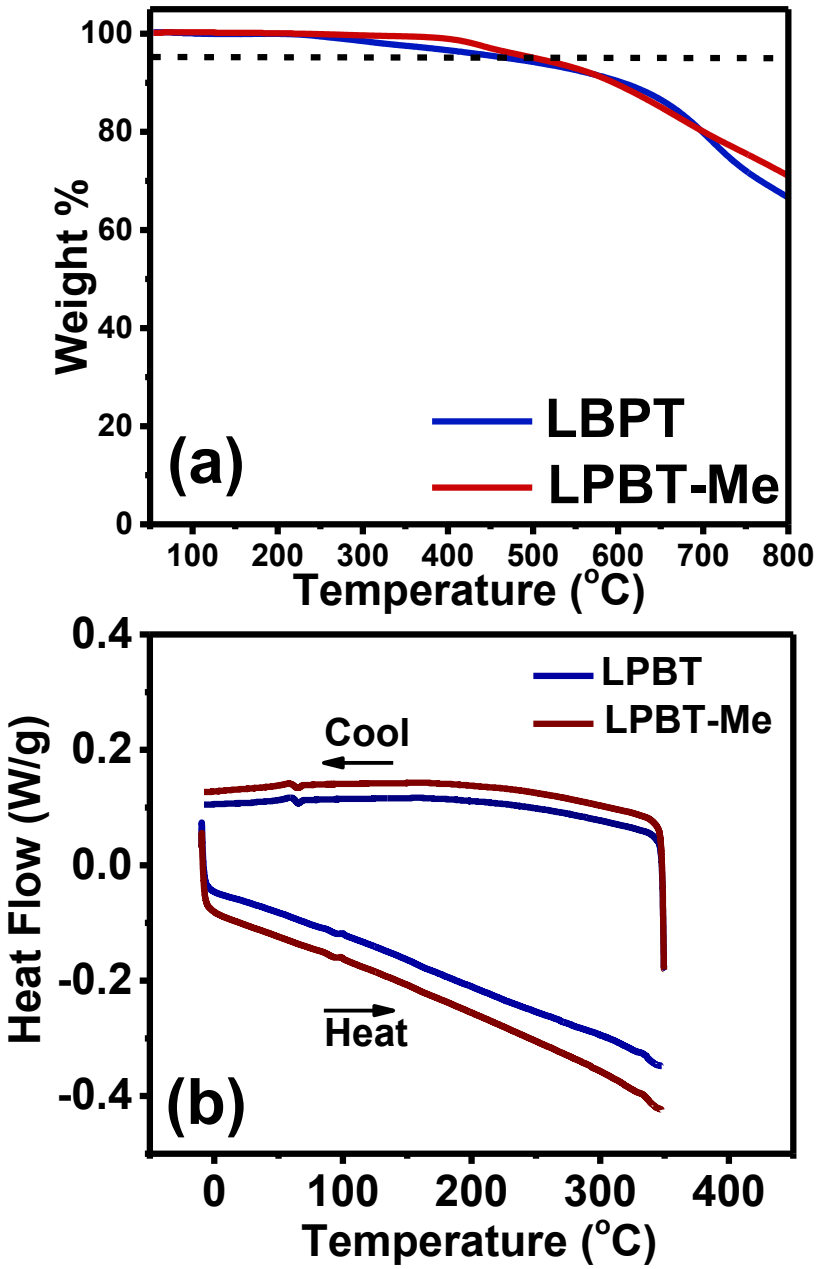

Figure D.3. (a) TGA (at 10˚C/min under N_2) of LPBT and LPBT-Me under nitrogen with 5% weight loss of 475˚C and 508˚C for LPBT and LPBT-Me, respectively, and (b) DSC heating and cooling scans of LPBT and LPBT-Me with a heating and cooling rate of 10˚C/min under N_2 gas flow.

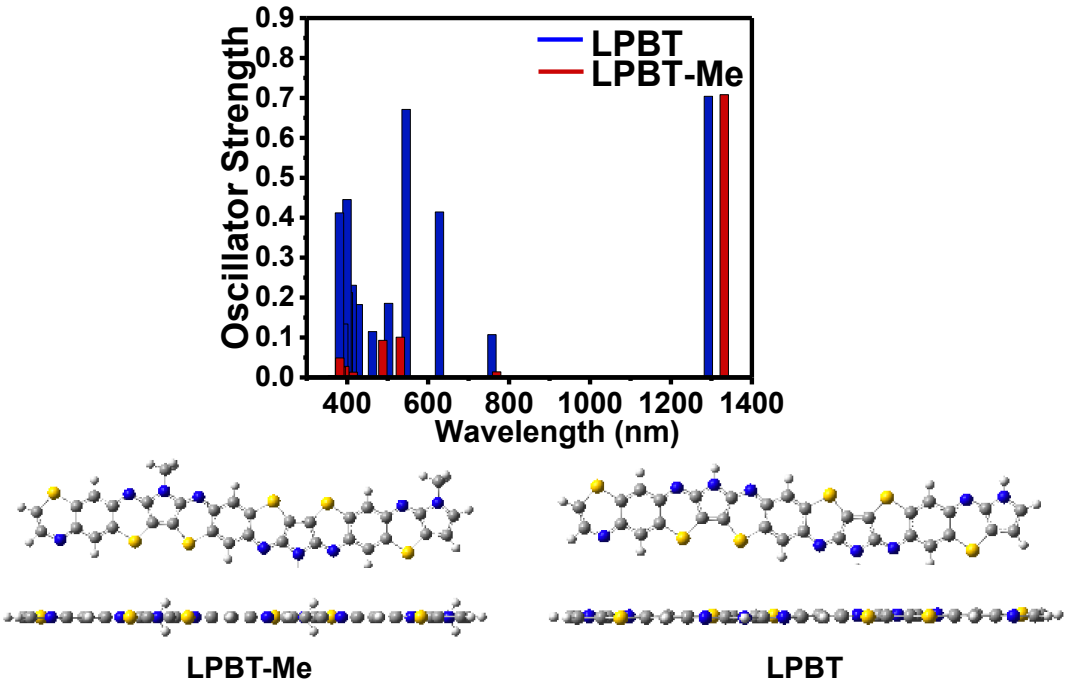

Figure D.4. TD-DFT-calculated vertical electronic transitions and excited state geometries of LPBT and LPBT-Me oligomers. Calculated at the TD-DFT ωB97XD/6-31G(d,p) level of theory for n=12 excited states.

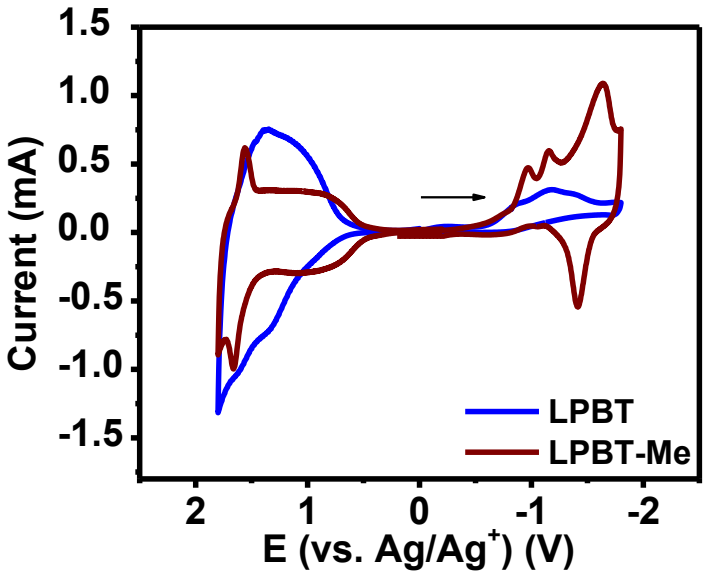

Figure D.5. Additional CV scans of the LPBT and LPBT-Me thin films measured in 0.1 M Bu_4NPF_6 electrolyte solution using $Ag/AgNO_3$ as the reference electrode. The scan rate was 100 mV/s and the arrow indicates the direction of charging.

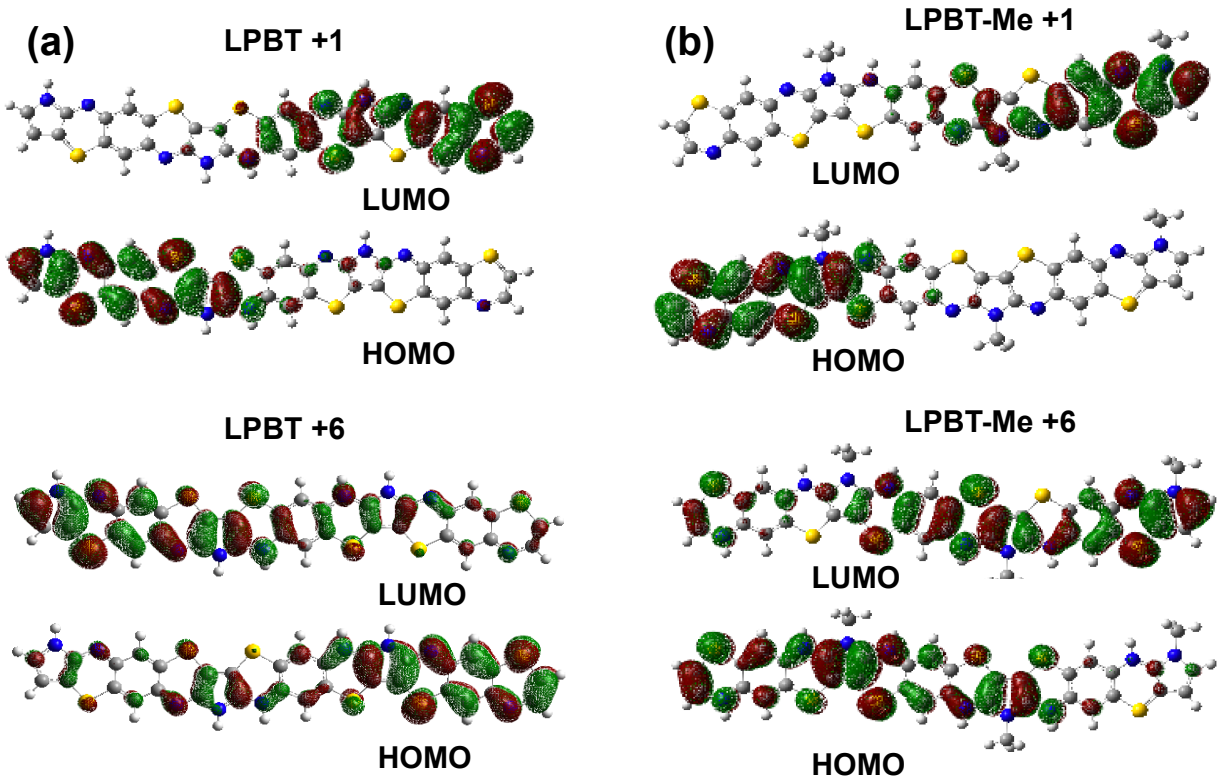

Figure D.6. HOMO and LUMO orbital distributions calculated using DFT at the ωB97XD/6-31G(d,p) level of theory for (a) LPBT and (b) LPBT-Me for oligomers bearing +1 and +6 charges. The oligomers were protonated at the same imine nitrogens.

D.3 Supplementary Tables

Table D.1. Fourier-Transform Infrared Spectroscopy (FT-IR) and Raman Absorption Bands of LPBT Free Standing Films and Their Peak Assignments.

FT-IR Absorption Band (cm^{-1})	Raman Absorption Band (cm^{-1})	Assignment
1698	1611, 1482	ν(C=C), carbon-carbon stretches
1600	1545	ν(C=N), imine carbon-nitrogen stretch
1459,1360	1349	Pyrrole stretch, mixed aromatic stretches
1225	-	ν(C-N), carbon-nitrogen stretch
-	1235	Mixed skeletal vibrations
1124	-	ν(C-N), amine carbon-nitrogen stretch
1085	1032, 743	ν(C-S), carbon-sulfur stretch

Table D.2. Fourier-Transform Infrared Spectroscopy (FT-IR) and Raman Absorption Bands of LPBT-Me Free Standing Film and Their Peak Assignments.

FT-IR Absorption Band (cm^{-1})	Raman Absorption Band (cm^{-1})	Assignment
1613	1619, 1488	ν(C=C), carbon-carbon stretch
1577	1542	ν(C=N), imine carbon-nitrogen stretch
1452	1428	Pyrrole stretch, mixed aromatic stretches
1239	-	ν(C-N), carbon-nitrogen stretch
-	1362	ν(C=C), ν(C-N), pyrrole stretches
-	1253	Mixed skeletal vibrations
-	1138	CH_3 rocking
1046	1026, 737	ν(C-S), carbon-sulfur stretch

Appendix E

Appendix E presents a supplementary information to accompany Chapter 5: Ladder Poly(Thienobenzothiazine): Synthesis, Electronic Structure, Optical Properties, and p-Doped Electrical Conductivity of a Narrow Bandgap p-Type Ladder Polymer

E.1 Additional Experimental Methods

Fabrication of Thin Films.

Films of LTBT were prepared on glass substrates where LTBT thin films were deposited by spin-coating from their respective MSA solutions (13 mg/mL) at 4500 - 5000 rpm for 30 seconds. The acidic solvent was removed by soaking the films in isopropanol (IPA) for 12 hours. Afterwards, films were dried in vacuum oven at 60^{o}C overnight. Finally, the LTBT films were annealed at 170˚C on a hot plate for 10 min.

Fabrication of Freestanding Films.

Freestanding films of LTBT were prepared on initial supporting glass substrates using a similar procedure as described above where the polymer solution (15 mg/mL) drop-cast onto a hot substrate and baked overnight at 120˚C. Instead of additional annealing at higher temperature, the thin films were then slowly cooled down to room temperature and submerged in water. Thus, films can be peeled from the supporting substrate, floated on water, lifted off using a copper wire, and dried at 120˚C to form freestanding films. These freestanding films were used for further characterizations (FTIR and Raman Spectroscopies).

Experimental Details of X-Ray Crystallography.

A red needle, measuring 0.60 x 0.04 x 0.005 mm^3 was mounted on a loop with oil. Crystal diffraction data was collected at -173˚C on a Bruker APEX II single crystal X-ray diffractometer, Mo-radiation, equipped with a Miracol X-ray optical collimator. Crystal-to-detector distance was

40 mm and exposure time was 30 seconds per frame for all sets. The scan width was 0.75°. 257 Data collection was 100.0% complete to 25° in ϑ. A total of 10370 reflections were collected covering the indices, h = -21 to 21, k = -25 to 25, l = -4 to 4. 2698 reflections were symmetry independent and the R_{int} = 0.1668 indicated that the data was of better than average quality (0.07). Indexing and unit cell refinement indicated an orthorhombic lattice. The space group was found to be $Pna2_1$ (No. 33). The data was integrated and scaled using SAINT, SADABS within the APEX2 software package by Bruker.[1] Solution by direct methods (SHELXT[2-3] or SIR97[4-5]) produced a complete heavy atom phasing model consistent with the proposed structure. The structure was completed by difference Fourier synthesis with SHELXL.[6-7] Scattering factors are from Waasmair and Kirfel[8]. Hydrogen atoms were placed in geometrically idealised positions and constrained to ride on their parent atoms with C---H distances in the range 0.95-1.00 Angstrom. Isotropic thermal parameters U_{eq} were fixed such that they were $1.2U_{eq}$ of their parent atom Ueq for CH's and $1.5U_{eq}$ of their parent atom U_{eq} in case of methyl groups. All non-hydrogen atoms were refined anisotropically by full-matrix least-squares.

E.2 Supplementary Figures

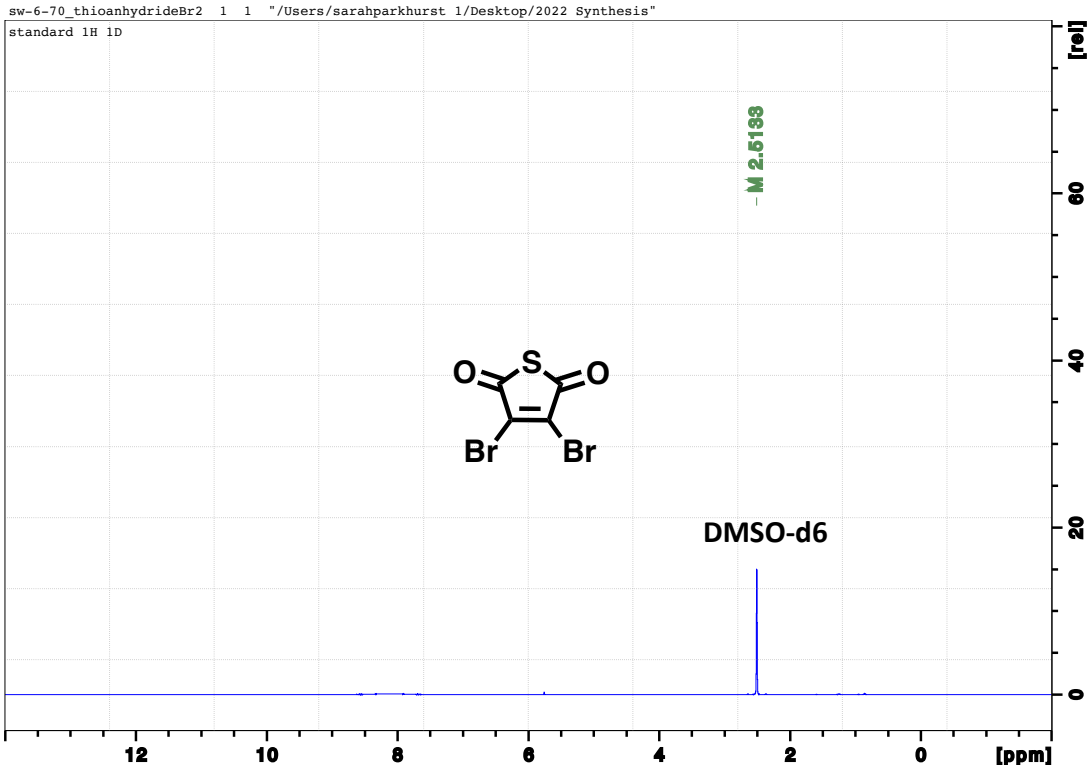

Figure E.1. Proton NMR of the monomer 3,4-dibromothiophene-2,5-dione in DMSO-d6.

.

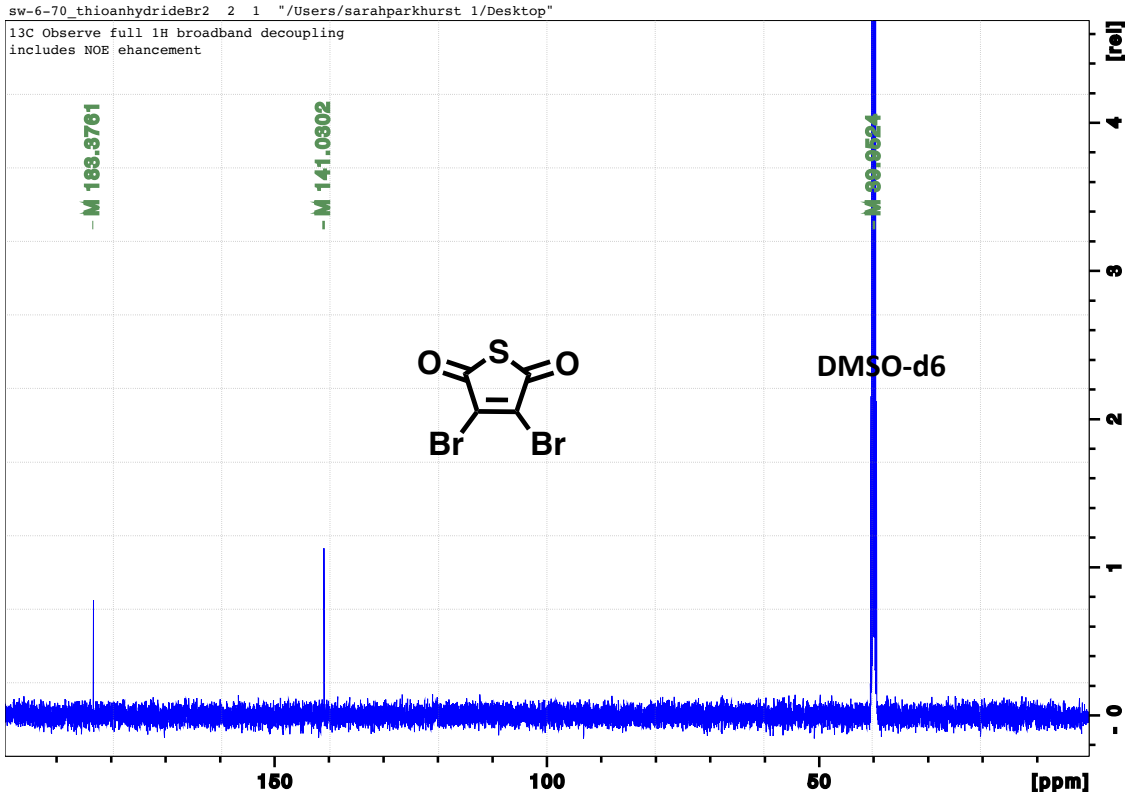

Figure E.2. Carbon NMR of monomer 3,4-dibromothiophene-2,5-dione in DMSO-d6.

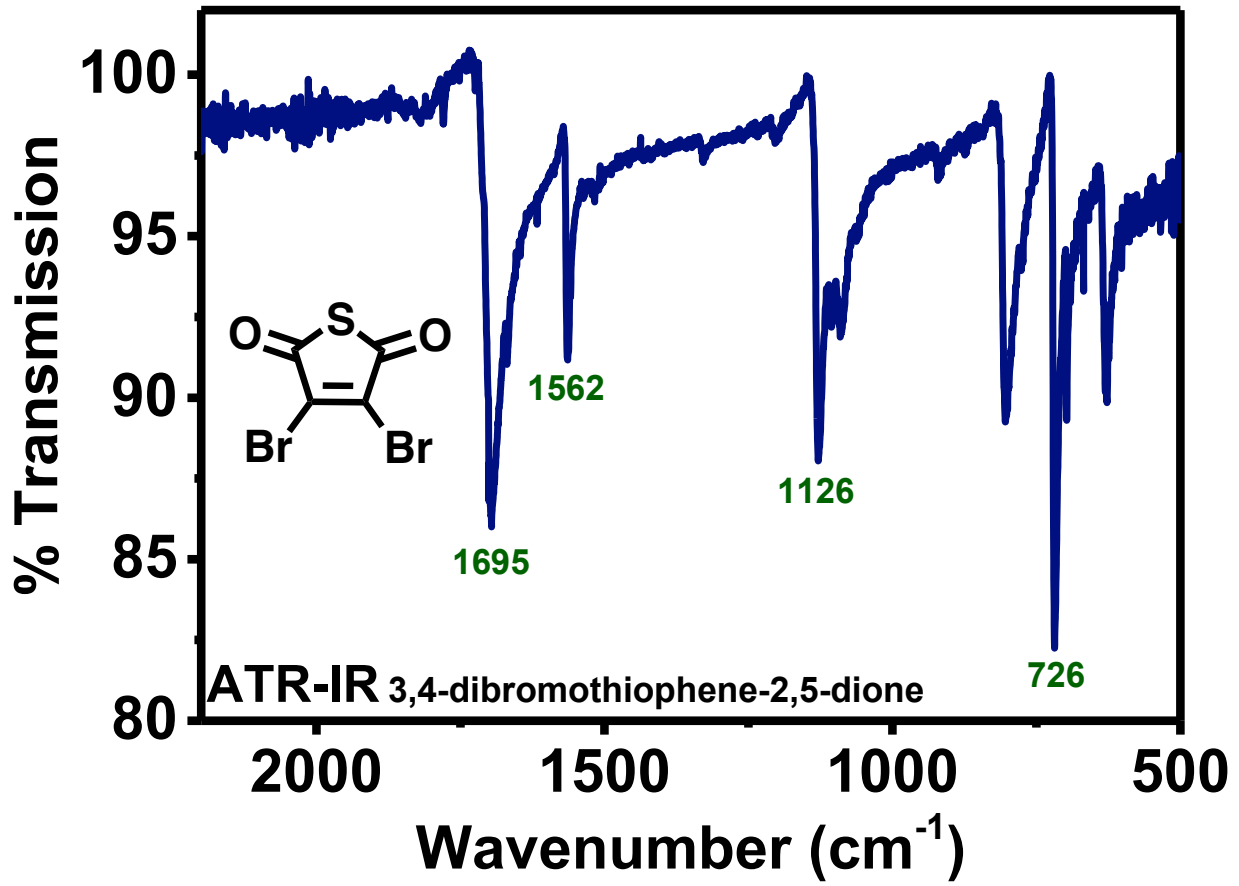

Figure E.3. Attenuated Total Reflectance Fourier-transform Infrared (ATR-FTIR) spectrum of the neat monomer, 3,4-dibromothiophene-2,5-dione.

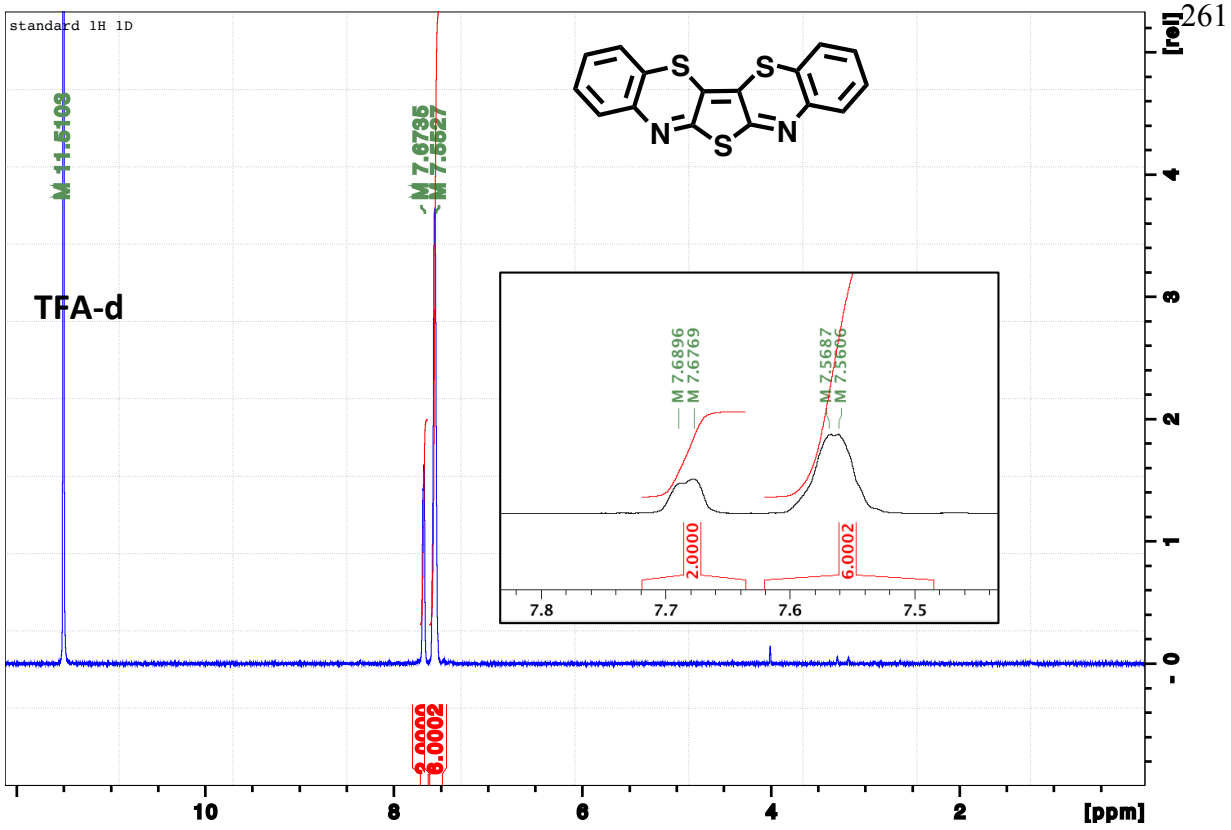

Figure E.4. Proton NMR of TBBT in TFA-d. Insert shows the peak integration for the benzene moiety.

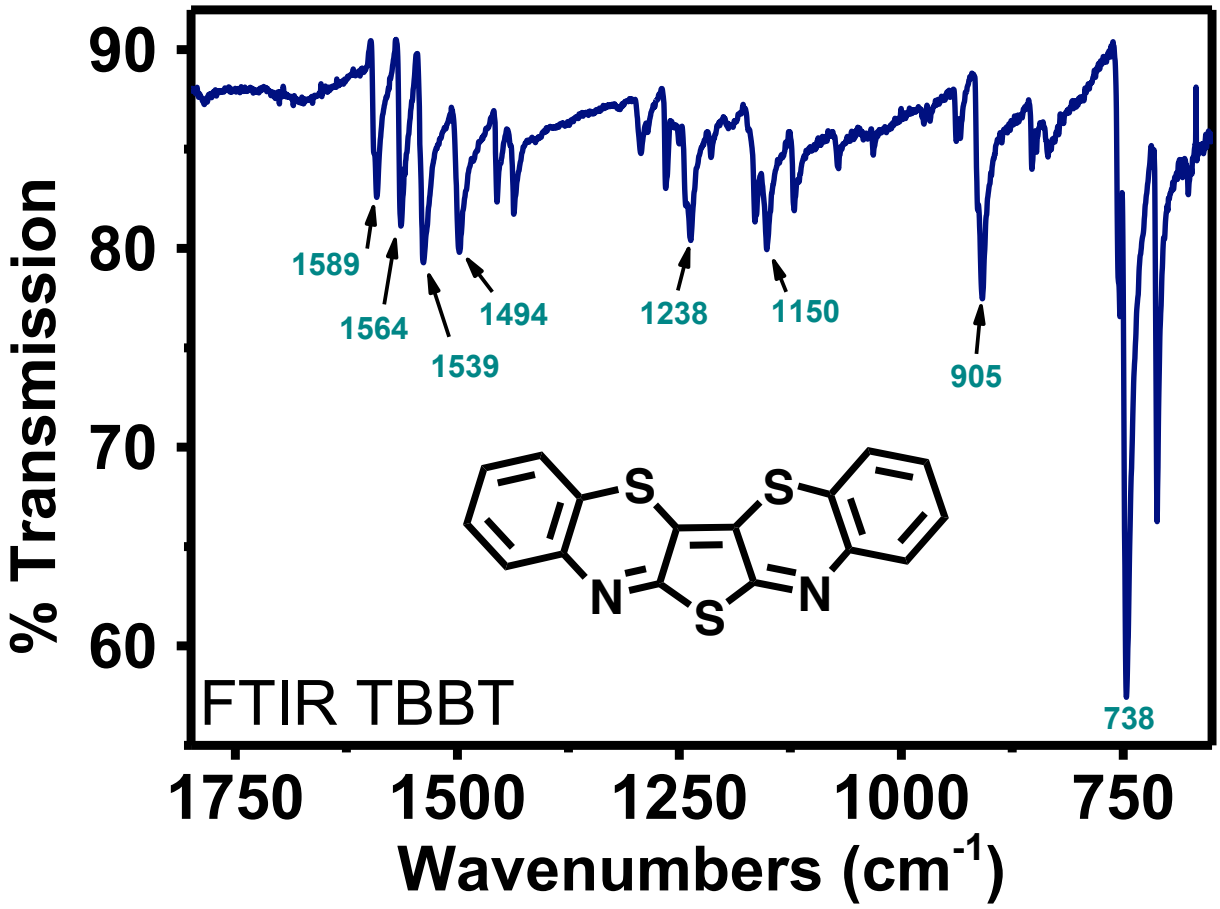

Figure E.5. FTIR spectrum of TBBT.

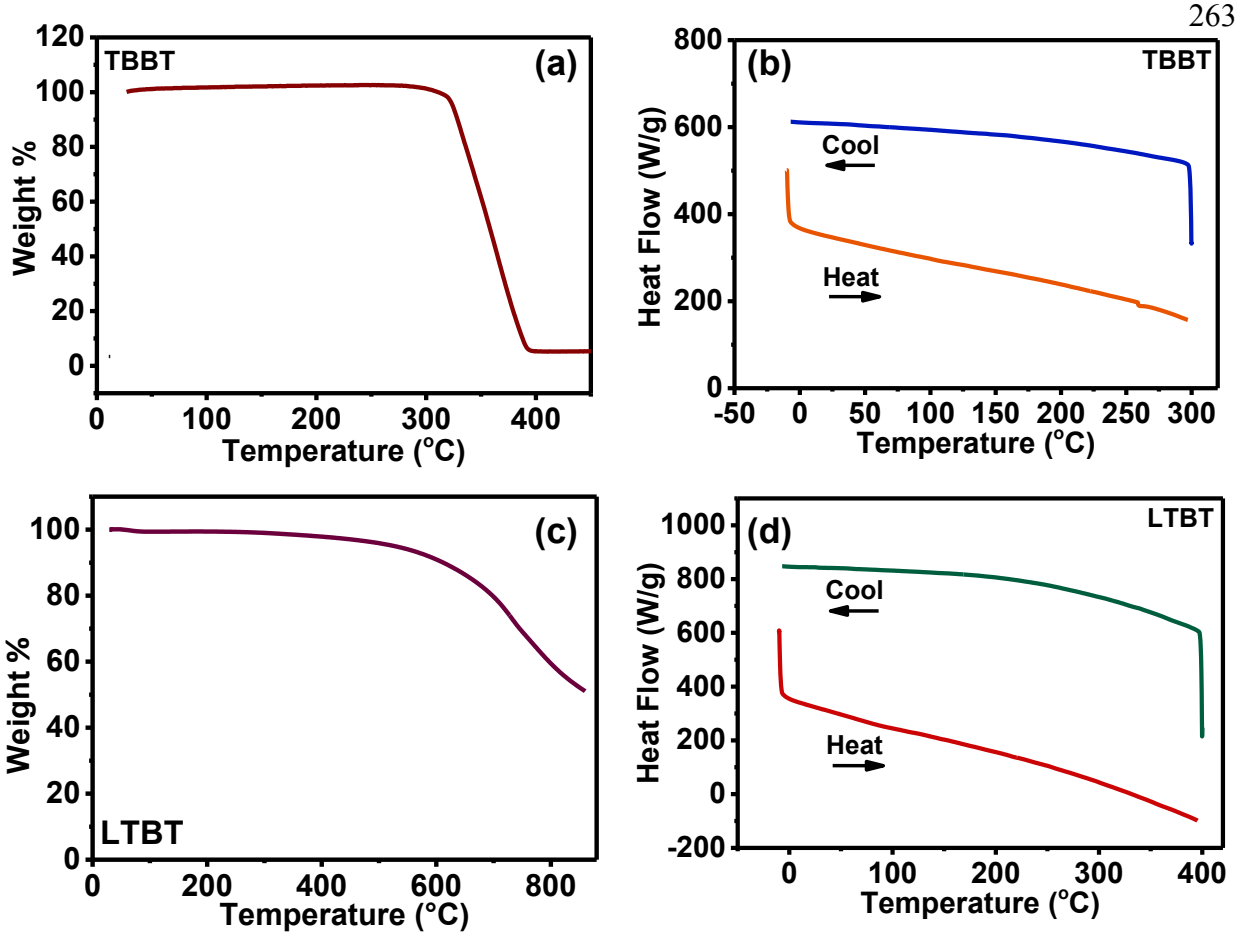

Figure E.6. Thermal gravimetric analysis (TGA) scans of (a) TBBT and (c) LTBT under nitrogen at a scan rate of 10˚C/min. Differential scanning calorimetry (DSC) scans of (b) TBBT and (d) LTBT at a scan rate of 10˚C/min under nitrogen.

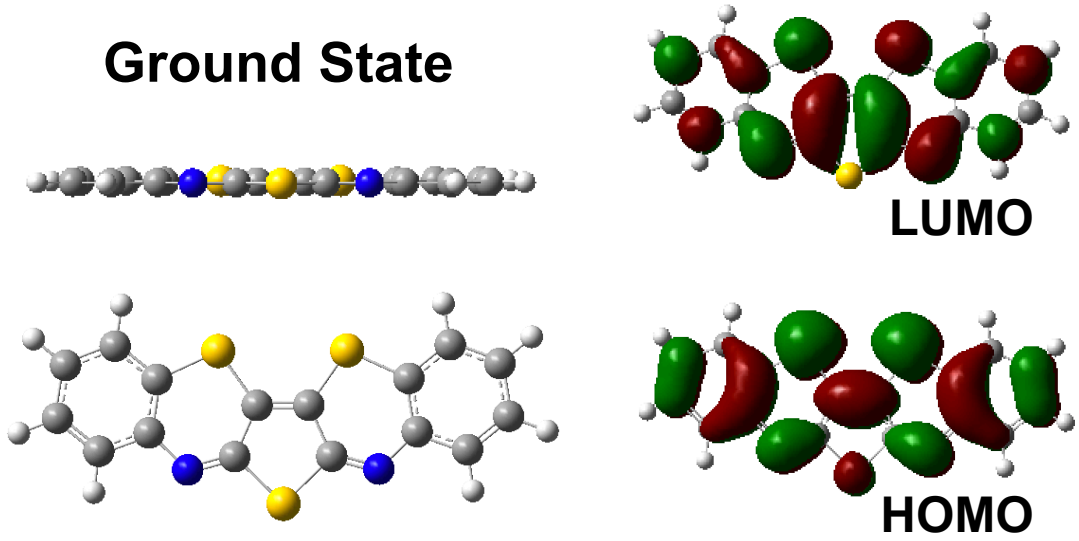

Figure E.7. Ground state geometry and molecular orbital distributions of TBBT calculated using DFT ωB97XD/6-31G(d,p) level of theory.

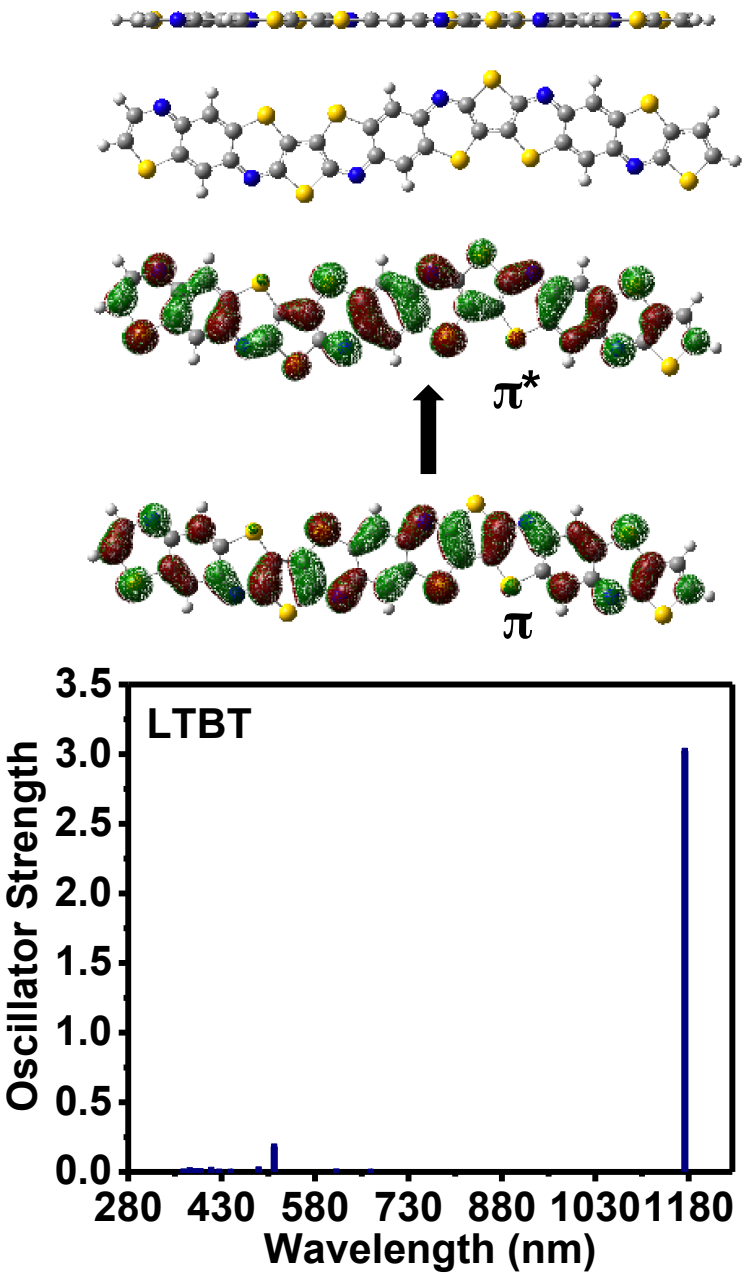

Figure E.8. Excited state geometry and simulated vertical excitations of the gas phase LTBT oligomer, and the corresponding hole and electron wavefunctions for the lowest energy transition (π-π*) at 1170 nm calculated using TD-DFT ωB97XD/6-31G(d,p) level of theory for n=12 excited states (λ_{max} = 1170 nm).

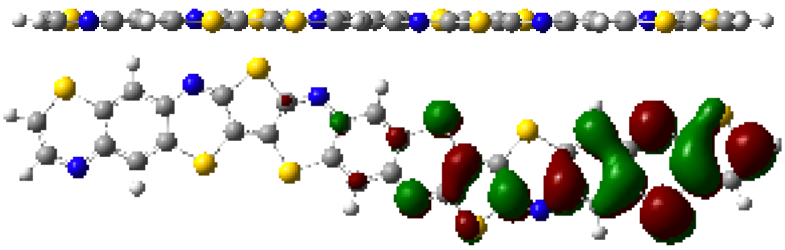

Figure E.9. Cationic LTBT oligomer geometry and polaron orbital distribution calculated at the DFT ωB97XD/6-31G(d,p) level of theory.

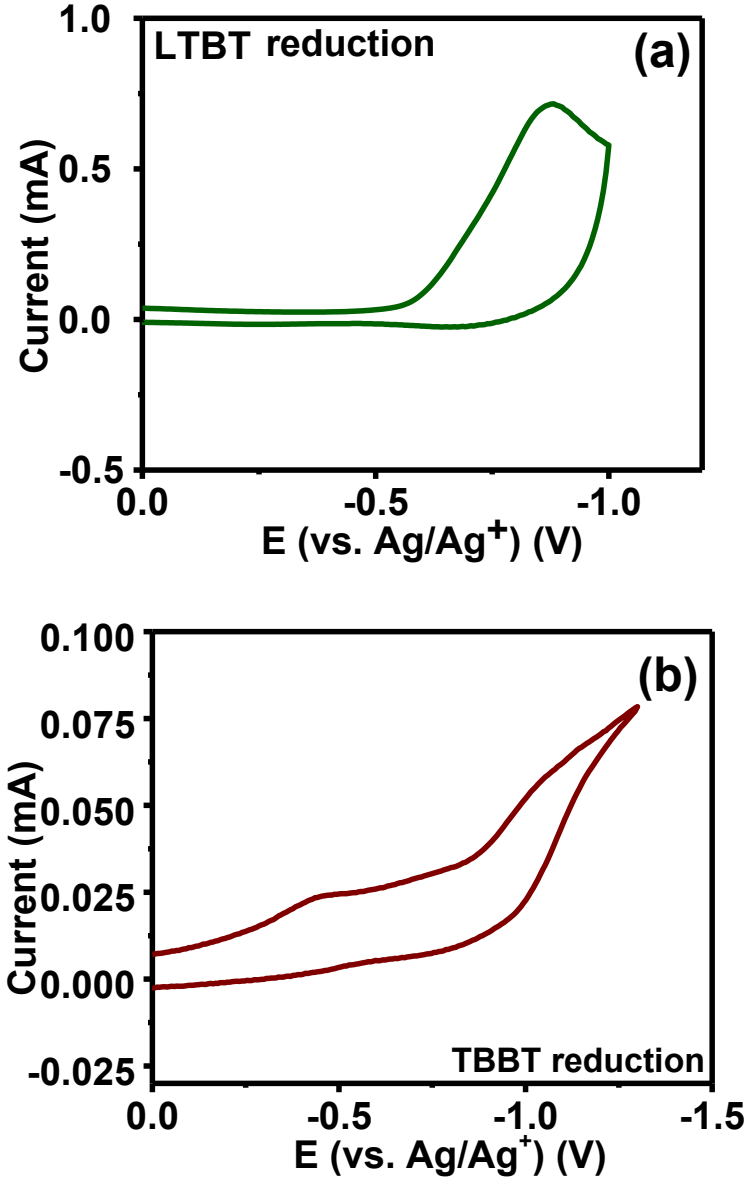

Figure E.10. The reduction scans of (a) LTBT and (b) TBBT in 0.1 M Bu_4NPF_6 acetonitrile solution vs. Ag/Ag^+. The scan rate was 100 mV/s.

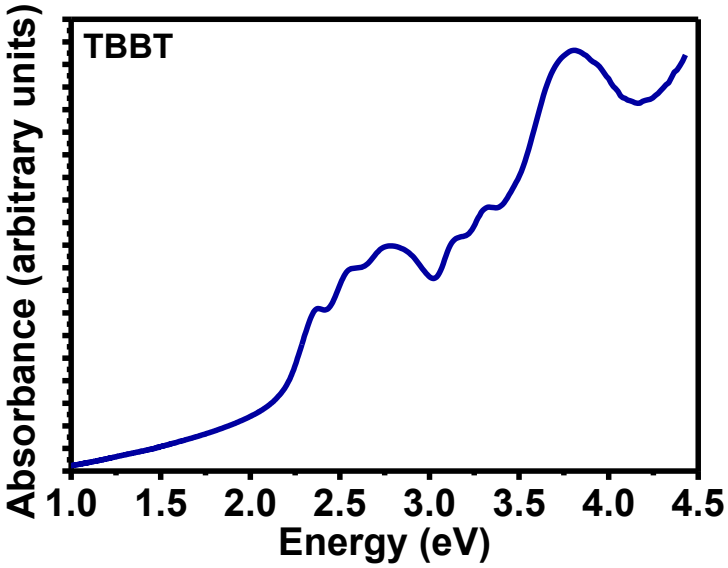

Figure E.11. Thin film absorption spectra of TBBT plotted vs. eV to determine the optical bandgap from the onset of absorption.

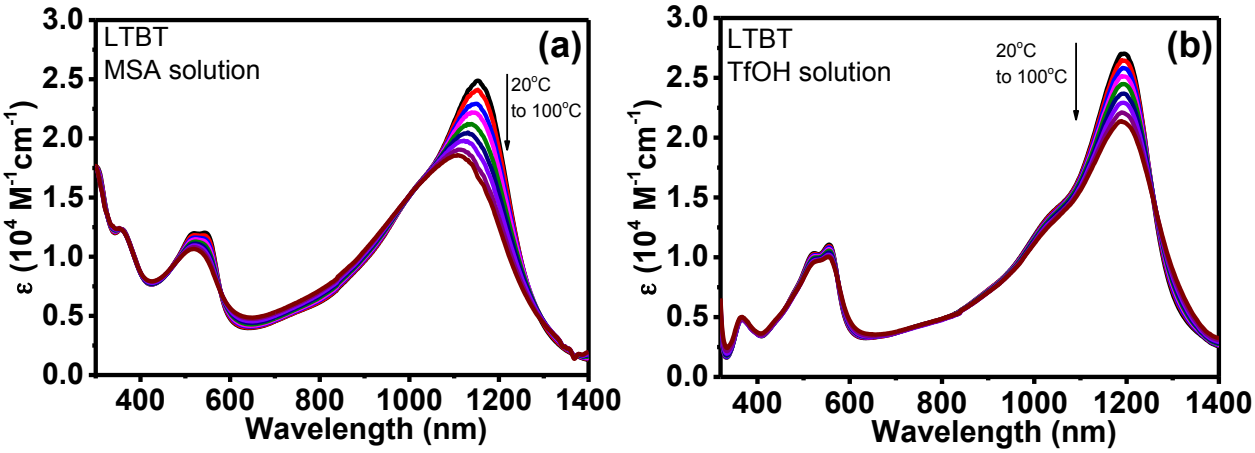

Figure E.12. Optical absorption spectra of LTBT in (a) dilute (10^{-5} M) MSA solution (λ_{max} = 1151 nm) and (b) triflic acid solution (λ_{max} = 1192 nm)**.**

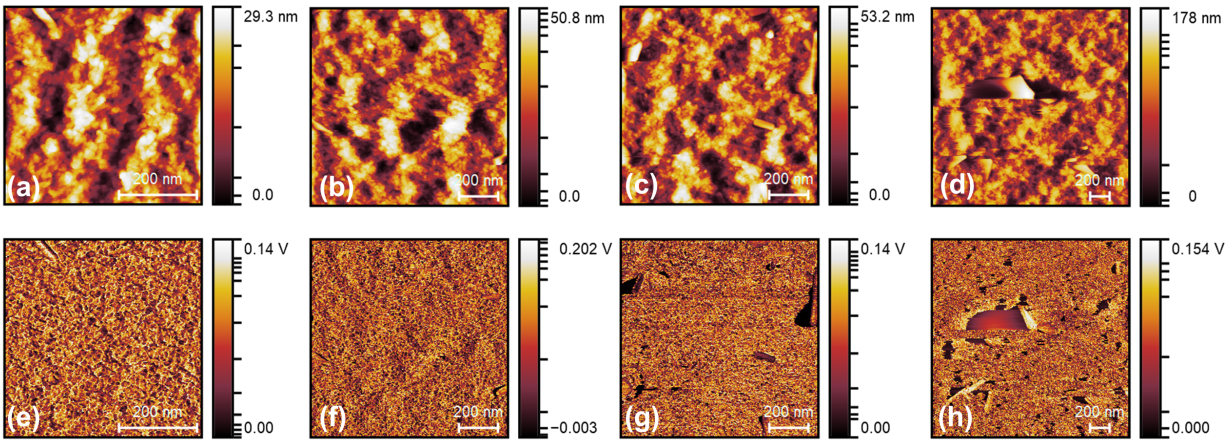

Figure E.13. (a - c) Atomic force microscopy (AFM) height images of neat LTBT thin films deposited on glass; (d -f) AFM phase images of neat LTBT films.

E.3 Supplementary Tables.

Table E.1. Fourier-Transform Infrared Spectroscopy (FTIR) and Raman Absorption Bands of LTBT Freestanding Films and Their Peak Assignments.

FTIR Absorption Band (cm^{-1})	Raman Absorption Band (cm^{-1})	Assignment
1601	1614, 1462	ν(C=C/C-C)/(Я band), carbon-carbon stretches
1534	1592, 1530	ν(C=N), imine carbon-nitrogen stretches
1443, 1300	1487	Thiophene stretches, mixed aromatic stretches
1226	-	ν(C-N), carbon-nitrogen stretch
1150	1073	ν(C-S), carbon-sulfur stretch
908, 800	1268, 1155	Intraring vibrations

Table E.2. Fourier-Transform Infrared Spectroscopy (FTIR) Absorption Bands of TBBT Needles and Their Peak Assignments.

FTIR Absorption Band (cm^{-1})	Assignment
1589, 1564	ν(C=C), carbon-carbon stretch
1539	ν(C=N), imine carbon-nitrogen stretch
1494, 1456, 1291	Thiophene stretches, mixed aromatic stretches
1238	ν(C-N), carbon-nitrogen stretch
1150	ν(C-S), carbon-sulfur stretch
905, 738	Mixed skeletal vibrations

Table E.3. Crystallographic Data for TBBT.

Empirical formula	C16 H8 N2 S3	
Formula weight	324.42	
Temperature	100(2) K	
Wavelength	0.71073 Å	
Crystal system	Orthorhombic	
Space group	P n a 21	
Unit cell dimensions	a = 17.198(9) Å	α= 90°.
	b = 20.222(12) Å	β= 90°.
	c = 3.782(2) Å	γ = 90°.
Volume	1315.3(13) $Å^3$	
Z	4	
Density (calculated)	1.638 Mg/m^3	
Absorption coefficient	0.555 mm^{-1}	
F(000)	664	
Crystal size	0.600 x 0.040 x 0.005 mm^3	
Theta range for data collection	1.554 to 26.533°.	
Index ranges	-21<=h<=21, -25<=k<=25, -4<=l<=4	
Reflections collected	10370	
Independent reflections	2698 [R(int) = 0.1668]	
Completeness to theta = 25.000°	100.0 %	
Refinement method	Full-matrix least-squares on F^2	
Data / restraints / parameters	2698 / 1 / 191	
Goodness-of-fit on F^2	0.976	
Final R indices [I>2sigma(I)]	R1 = 0.0524, wR2 = 0.1000	
R indices (all data)	R1 = 0.0990, wR2 = 0.1168	
Absolute structure parameter	-0.08(12)	
Extinction coefficient	0.012(2)	
Largest diff. peak and hole	0.485 and -0.473 $e.Å^{-3}$	

Table E.4. Atomic coordinates (x 10^4) and equivalent isotropic displacement parameters ($Å^2$x 10^3) for TBBT. U(eq) is defined as one third of the trace of the orthogonalized U^{ij} tensor.

	x	y	z	U(eq)
S(2)	4868(1)	7032(1)	7865(6)	23(1)
S(3)	5706(1)	5535(1)	7436(5)	24(1)
S(1)	7167(1)	7077(1)	3171(6)	25(1)
N(1)	6124(3)	8017(3)	4460(15)	24(1)
N(2)	7371(3)	5782(3)	3676(15)	22(1)
C(5)	4020(4)	8870(3)	8030(20)	25(2)
C(4)	4117(4)	8196(3)	8362(19)	23(2)
C(3)	4803(4)	7890(3)	7240(18)	20(2)
C(2)	5782(4)	6874(3)	6129(18)	23(2)
C(10)	6129(4)	6264(3)	5930(18)	20(2)
C(11)	6436(4)	4962(3)	6281(18)	23(2)
C(12)	6291(4)	4303(3)	7160(20)	26(2)
C(13)	6850(4)	3820(3)	6410(20)	27(2)
C(14)	7551(4)	3989(4)	4839(19)	29(2)
C(6)	4608(4)	9241(4)	6472(19)	31(2)
C(7)	5294(4)	8947(3)	5334(19)	26(2)
C(8)	5407(4)	8260(3)	5730(18)	23(2)
C(1)	6271(4)	7395(3)	4733(18)	22(2)
C(9)	6896(4)	6264(3)	4347(18)	23(2)
C(16)	7149(4)	5136(3)	4651(18)	24(2)
C(15)	7693(4)	4638(3)	3949(19)	25(2)

E.4 Supplementary References

1. Bruker **2007,** APEX2 (Version 2.1-4), SAINT (version 7.34A), SADABS (version 2007/4), BrukerAXS Inc, Madison, Wisconsin, USA.
2. Sheldrick, G. M. A Short History of SHELX. *Acta. Cryst.* **2008**, A64, 112-122.
3. Sheldrick, G. M. SHELXT - Integrated Space-Group and Crystal-Structure Determination. *Acta. Cryst.* **2015**, A71, 3-8.
4. Altomare, A.; Burla, C.; Camalli, M.; Cascarano, G. L.; Giacovazzo, C.; Guagliardi, A.; Moliterni, A. G. G.; Polidori, G.; Spagna, R. SIR97: A New Tool for Crystal Structure Determination and Refinement *J. Appl. Crystallogr*. **1999** *32***,** 115-119.
5. Altomare, A.; Cascarano, G. L.; Giacovazzo, C.; Guagliardi, A. Completion and Refinement of Crystal Structures with SIR 92. *J. Appl. Crystallogr.* **1993** *26***,** 343-350.
6. Sheldrick G. M. SHELXL-97, Program for the Refinement of Crystal Structures. **1997**, University of Göttingen, Germany.
7. Sheldrick G. M. Crystal Structure Refinement with SHELXL. *Acta Cryst*. **2015**, C71, 3–8.
8. Waasmaier, D.; Kirfel, A. New Analytical Scattering Factor Functions for Free Atoms and Ions. *Acta. Cryst. A*. **1995**, *51*, 416-430.

VITA

Sarah M. West was born in Lakewood, Washington. She was homeschooled up until she attended her local community college through the running start program. While at Pierce College, she earned her high school credits and graduated high school while simultaneously completing the pre-requests for the veterinary technician program at Pierce College. After earning her Associates of Veterinary Technology, she worked as a veterinary technician for three years during which she discovered her love of science. She then went back to Pierce College part time to earn her Associates of Science that will enable her to transfer to the University of Washington to complete a Bachelors of Science in Chemistry. At the University of Washington she worked in the lab of Professor Joshua C. Vaughan as an undergraduate researcher synthesizing fluorophores for microcopy while simultaneously working as an intern at the biotech startup company PhaseRX where she synthesized new water-soluble monomers for biomimetic polymers. She then joined Professor Samson A. Jenekhe's lab at the University of Washington where she studied ladder polymers for organic electronic device applications in graduate school. Her research has been published in peer reviewed scientific journals such as *Macromolecules* and *Chemistry of Materials*, and received support as a Fellow of the Clean Energy Institute at the University of Washington. The following is a list of the author's publications during her studies at the University of Washington.

1. Sarah M. West, Duyen K. Tran, Werner Kaminsky, and Samson A. Jenekhe, "Cyanated and Noncyanated Conjugated Ladder Copolymers and Model Compound of Poly(benzimidazobenzophenanthroline): Synthesis, Electronic Structure, and n-Doped Electrical Conductivity" *manuscript in preparation*.

2. Sarah M. West, Duyen K. Tran, Sung-Joo Kwon, David S. Ginger, and Samson A. Jenekhe, "Random Copolymers and Model Compound of Ladder Poly(benzimidazobenzophenanthroline) Featuring Dithiinotetracarbonitrile Groups: Synthesis, Electronic Structure, and Electrical Conductivity". *manuscript in preparation*.

3. Sarah M. West, Duyen K. Tran, Werner Kaminsky, and Samson A. Jenekhe, "Ladder Poly(Thienobenzothiazine): Synthesis, Electronic Structure, Optical Properties, and p-Doped Electrical Conductivity of a Narrow Bandgap p-Type Ladder Polymer" *manuscript in preparation*.

4. Duyen K. Tran, Sarah M. West, Elizabeth M. K. Speck, and Samson A. Jenekhe, "Super-Nernstian Proton-Coupled Electron Transfer and Nature of Charge Carriers in a Multiredox Conjugated Polymer" *Chem. Sci.* **2024**, *under revision*.

5. Duyen K. Tran, Sarah M. West, Jiajie Guo, Shinya E. Chen, David S. Ginger, and Samson A. Jenekhe, "Electron Transport Physics of Rigid Rod Poly(Benzimidazobenzophenanthrolinedinoe) (BBL) Ladder Polymer" *J. Am. Chem. Soc.* **2024**, *146* (2), 1425-1446.

6. Sarah M. West, Duyen K. Tran, Jiajie Guo, Shinya E. Chen, David S. Ginger, and Samson A. Jenekhe, "p-type Semiconducting Ladder Poly(pyrrolobenzothiazine)s: Effects of N-alkylation on the Chain Conformation, Electronic Structure, and Charge Transport Properties" *Macromolecules* **2023**, *56* (24), 10222-10235.

7. Sarah M. West, Duyen K. Tran, Jiajie Guo, Shinya E. Chen, David S. Ginger, and Samson A. Jenekhe, "Phenazine-Substituted Poly(benzimidazobenzophenanthrolinedione): Electronic Structure, Charge Transport, and Mechanical Properties of an n-Type Semiconducting Ladder Polymer" *Macromolecules* **2023**, *56* (5), 2081-2091.

8. Nagesh B. Kolhe, Sarah M. West, Duyen K. Tran, Xiaomei Ding, Daiki Kuzuhara, Noriyuki Yoshimoto, Tomoyuki Koganezawa, and Samson A. Jenekhe, "Designing High Performance Nonfullerene Electron Acceptors with Rylene Imides for Efficient Organic Photovoltaics" *Chem. Mater.* **2020**, *32* (1), 195-204.